(12) **LEVEL** 6 AD-E300 252

DNA 4507F

AD A056390

HARDENED REENTRY VEHICLE DEVELOPMENT PROGRAM

Erosion-Resistant Nosetip Technology

Prototype Development Associates, Inc.

1740 Garry Avenue, Suite 201

Santa Ana, California 92705

January 1978

Final Report for Period December 1974—September 1976

CONTRACT No. DNA 001-75-C-0054

| APPROVED FOR PUBLIC RELEASE; |
| DISTRIBUTION UNLIMITED. |

D D C
RECEIVED
JUL 20 1978
B

Prepared for

Director

DEFENSE NUCLEAR AGENCY

Washington, D. C. 20305

Best
Available
Copy

REPORT DOCUMENTATION PAGE		READ INSTRUCTIONS BEFORE COMPLETING FORM
1 REPORT NUMBER DNA 4507F	2. GOVT ACCESSION NO.	3. RECIPIENT'S CATALOG NUMBER
4. TITLE (and Subtitle) HARDENED REENTRY VEHICLE DEVELOPMENT PROGRAM, Erosion-Resistant Nosetip Technology		5. TYPE OF REPORT & PERIOD COVERED Final Report for Period Dec 1974–Sep 1976
		6. PERFORMING ORG. REPORT NUMBER PDA-TR-1031-90-58
7. AUTHOR(s) M. M. Sherman, et al.		8. CONTRACT OR GRANT NUMBER(s) DNA 001-75-C-0054
9. PERFORMING ORGANIZATION NAME AND ADDRESS Prototype Development Associates, Inc. 1740 Garry Avenue, Suite 201 Santa Ana, California 92705		10. PROGRAM ELEMENT, PROJECT, TASK AREA & WORK UNIT NUMBERS NWED Subtask N99QAXAC312-14
11. CONTROLLING OFFICE NAME AND ADDRESS Director Defense Nuclear Agency Washington, D.C. 20305		12. REPORT DATE January 1978
		13. NUMBER OF PAGES 236
14. MONITORING AGENCY NAME & ADDRESS(if different from Controlling Office) Space and Missile Systems Organization Worldway Postal Center, P. O. Box 92960 Los Angeles, California 90009		15. SECURITY CLASS (of this report) UNCLASSIFIED
		15a. DECLASSIFICATION/DOWNGRADING SCHEDULE

16. DISTRIBUTION STATEMENT (of this Report)

Approved for public release; distribution unlimited.

17. DISTRIBUTION STATEMENT (of the abstract entered in Block 20, if different from Report)

18. SUPPLEMENTARY NOTES

This work sponsored by the Defense Nuclear Agency under RDT&E RMSS
Code B342075464 N99QAXAC31214 H2590D.

19. KEY WORDS (Continue on reverse side if necessary and identify by block number)

Nosetip	Instrumentation
Ablation	Thermal Stress Analysis
Erosion	
Materials	

20. ABSTRACT (Continue on reverse side if necessary and identify by block number)

A series of programs has been conducted to develop erosion-resistant nosetip (ERN) concepts to provide an all-weather flight capability for high-performance reentry vehicles. In a previous effort, two ERN designs utilizing monolithic (solid) tungsten subtips were designed for flight tests on Advanced Nosetip Test (A. N. T.) vehicles. In the present program, ground tests were conducted in a rocket motor test facility to evaluate the thermal and structural performance of full-scale models of these flight designs. The results of these tests indicate a low probability of survival for

20. ABSTRACT (Continued)

monolithic tungsten subtips in ICBM flight environments. Therefore, additional studies were performed to develop an improved subtip concept that would be more resistant to thermal stress failures. These studies resulted in a segmented construction approach that will reduce the applied thermal stresses to acceptable levels and provide a high probability of survival in flight. Two segmented and two monolithic tungsten subtips were then designed, fabricated, and tested on HEARTS and FLAME flight test vehicles. All four nosetips survived to impact with no evidence of thermostructural failure and with no development of vehicle trim angles-of-attack at low altitudes. Additional tests at more severe conditions are required to verify the improvement in thermal stress performance provided by the segmented construction technique.

Two new types of ablation sensors were investigated for possible use in obtaining in-flight measurements of the recession performance of tungsten nosetips. These sensors were: 1) an ultrasonic ablation gage that measures the resonant frequencies in the nosetip to obtain an indication of the remaining length, and 2) a radioactive gage that uses bremsstrahlung radiation to activate the tungsten. Laboratory versions of both sensors were built and found to give promising results that warranted further development.

PREFACE

The studies described in this report were performed by Prototype Development Associates, Inc. (PDA), Santa Ana, California, for the Defense Nuclear Agency (DNA) under Contract Number DNA001-75-C-0054. Major T. W. Swartz was the DNA Contracting Officer's Representative. The work also was sponsored by the Space and Missile Systems Organization (SAMSO), Air Force Systems Command, Los Angeles, California. The SAMSO Project Officers were Captains J. E. Green and M. W. Elliott. Mr. P. J. Legendre of the Aerospace Corporation served as the principal technical monitor for SAMSO.

The PDA Program Manager was Mr. M. M. Sherman. Principal contributors to this study and report included: J. C. Schutzler (structural analyses and nosetip design), J. R. Stetson (design verification test program), J. L. Deleget (structural analyses), L. S. Groener (ablation testing and ablation gage development), and H. L. Moody (ablation gage development).

RE: Classified references, DNA-4507F
References should be deleted per Ms.
McCleary, DNA

Conversion factors for U. S. customary to metric (SI) units of measurement.

To Convert From	To	Multiply By
angstrom	meters (m)	$1.000\ 000 \times E -10$
atmosphere (normal)	kilo pascal (kPa)	$1.013\ 25 \times E +2$
bar	kilo pascal (kPa)	$1.000\ 000 \times E +2$
barn	meter^2 (m^2)	$1.000\ 000 \times E -28$
British thermal unit (thermochemical)	joule (J)	$1.054\ 350 \times E +3$
calorie (thermochemical)	joule (J)	$4.184\ 000$
cal (thermochemical)/cm^2	mega joule/m^2 (MJ/m^2)	$4.184\ 000 \times E -2$
curie	giga becquerel (GBq)*	$3.700\ 000 \times E +1$
degree (angle)	radian (rad)	$1.745\ 329 \times E -2$
degree Fahrenheit	degree kelvin (K)	$T_K = (t^o f + 459.67)/1.8$
electron volt	joule (J)	$1.602\ 19 \times E -19$
erg	joule (J)	$1.000\ 000 \times E -7$
erg/second	watt (W)	$1.000\ 000 \times E -7$
foot	meter (m)	$3.048\ 000 \times E -1$
foot-pound-force	joule (J)	$1.355\ 818$
gallon (U. S. liquid)	meter^3 (m^3)	$3.785\ 412 \times E -3$
inch	meter (m)	$2.540\ 000 \times E -2$
jerk	joule (J)	$1.000\ 000 \times E +9$
joule/kilogram (J/kg) (radiation dose absorbed)	Gray (Gy)**	$1.000\ 000$
kilotons	terajoules	4.183
kip (1000 lbf)	newton (N)	$4.448\ 222 \times E +3$
kip/inch^2 (ksi)	kilo pascal (kPa)	$6.894\ 757 \times E +3$
ktap	newton-second/m^2 (N-s/m^2)	$1.000\ 000 \times E +2$
micron	meter (m)	$1.000\ 000 \times E -6$
mil	meter (m)	$2.540\ 000 \times E -5$
mile (international)	meter (m)	$1.609\ 344 \times E +3$
ounce	kilogram (kg)	$2.834\ 952 \times E -2$
pound-force (lbf avoirdupois)	newton (N)	$4.448\ 222$
pound-force inch	newton-meter (N·m)	$1.129\ 848 \times E -1$
pound-force/inch	newton/meter (N/m)	$1.751\ 268 \times E +2$
pound-force/foot^2	kilo pascal (kPa)	$4.788\ 026 \times E -2$
pound-force/inch^2 (psi)	kilo pascal (kPa)	$6.894\ 757$
pound-mass (lbm avoirdupois)	kilogram (kg)	$4.535\ 924 \times E -1$
pound-mass-foot^2 (moment of inertia)	kilogram-meter^2 (kg·m^2)	$4.214\ 011 \times E -2$
pound-mass/foot^3	kilogram/meter^3 (kg/m^3)	$1.601\ 846 \times E +1$
rad (radiation dose absorbed)	Gray (Gy)**	$1.000\ 000 \times E -2$
roentgen	coulomb/kilogram (C/kg)	$2.579\ 760 \times E -4$
shake	second (s)	$1.000\ 000 \times E -8$
slug	kilogram (kg)	$1.459\ 390 \times E +1$
torr (mm Hg, 0° C)	kilo pascal (kPa)	$1.333\ 22 \times E -1$

*The becquerel (Bq) is the SI unit of radioactivity; 1 Bq = 1 event/s.
**The Gray (Gy) is the SI unit of absorbed radiation.

A more complete listing of conversions may be found in "Metric Practice Guide E 380-74," American Society for Testing and Materials.

TABLE OF CONTENTS

TABLE OF CONTENTS (Continued)

4

TABLE OF CONTENTS (Continued)

LIST OF ILLUSTRATIONS

LIST OF ILLUSTRATIONS (Continued)

9

LIST OF ILLUSTRATIONS (Continued)

LIST OF ILLUSTRATIONS (Continued)

LIST OF TABLES

1.0 INTRODUCTION AND SUMMARY

Prototype Development Associates, Inc. (PDA   is been developing erosion-resistant nosetips (ERN) to provide an all-weather flight capability fc   eentry and interceptor vehicles. The ERN designs are comprised of a graphitic (carbon-carbon or   alk graphite) external, or primary, nosetip and an erosion-resistant inner nosetip, or subtip. The g, aphitic primary nosetip provides minimum recession and shape change during clear air flight, while the subtip assures vehicle survival to impact in erosive weather environments. In the Erosion-Resistant Nosetip Technology (ERNT) program (Reference 1), the basic ERN concept was defined, tungsten was selected as the optimum state-of-the-art subtip material, and concept feasibility was demonstrated in a ground test program.

Plans were then made to evaluate the ERN concept in actual flight environments. A series of flight tests was designed to measure flight performance in increasingly severe aerothermal environments, both in clear air and in weather. Tungsten subtips and/or complete ERN assemblies were designed and fabricated for flight tests on SAMS, FLAME, HEARTS, and A.N.T. vehicles.

SAMS (Sandia-Air Force Materials Study) was an on-going program that offered an early opportunity to obtain flight ablation and erosion performance data for tungsten. The SAMS vehicles consist of a three-stage rocket and a payload section containing the nosetip, a recovery system, instrumentation, and telemetry equipment. Most of the test period occurs during the powered portion of the flight, and the peak velocities are slightly in excess of 10,000 ft/sec. The nosetips are recovered for post-test measurements and evaluation.

Four tungsten nosetips were designed, built, and flight-tested on SAMS vehicles. One of the nosetips was made from commercially pure tungsten, and three were made from tungsten' 2-percent thoria, $(W/2ThO_2)$. (Ground tests had shown that the ablation performance of these two types of tungsten is identical, but that the thoriated material offers potentially superior thermo-structural performance.) To identify the effects of particle impacts on ablation performance, two of the nosetips were flown in weather and two were flown in clear air. All four nosetips were recovered intact and subjected to detailed post-flight examination and analyses.

The most significant observation from the recovered nosetips was in regard to the effects of the weather environment on the tungsten ablation characteristics. Both clear air nosetips had smooth, flat stagnation regions; while the two nosetips flown in erosive weather environments were characterized by a sharper, biconic forward region with deep surface scallop patterns. The total axial recession of the weather nosetips was approximately twice that of the clear air nosetips. The scallop patterns are believed to have been initiated by weather particles impacting on the soft, melting tungsten surface. Once formed, the patterns tended to persist and cause increased local surface heating and recession rates. No scallop or crosshatch patterns were found on the conical frustum where no melting of the tungsten occurred.

No differences were observed in the ablation and shape change behavior of the commercially pure tungsten and the $W/2ThO_2$ nosetips that were flown in clear air environments.

Post-flight examination of the recovered nosetips revealed the presence of extensive fracture patterns in both clear air and weather nosetips. However, detailed metallographic examinations of the nosetips indicated that all of the fractures were initiated after the period of aerody namic heating. That is, all fractures could be attributed either to cool-down stresses or to residual stresses that were relieved by the sectioning process.

13

The conclusions of the metallographic analyses were confirmed qualitatively by post-flight thermostructural analyses. Calculations were performed to compare the predicted thermal stresses in the SAMS/ERN flight test nosetips with the stresses in similar tungsten models tested in the AFFDL 50 megawatt arc-jet and in a rocket motor facility. The peak stresses computed for the ground test models were equal to, or greater than, the peak stresses in the flight environment; and no thermostructural failures occurred during the ground tests. However, it was noted that both the ground and flight test models were computed to be marginal during the period of heat-up stresses.

Following the SAMS/ERN program, tungsten nosetips were designed and built for flight tests on the FLAME (Fighter-Launched Advanced Materials Experiment) and the HEARTS (Hydro-meteor Erosion And Recession Test System) vehicles, both of which provide flight conditions that are intermediate between the SAMS environments and ICBM flight environments. These flight test programs were performed concurrently with an intensive design, development, and fabrication effort to provide complete ERN designs for final evaluation on full-scale ICBM flight tests on the A.N.T. (Advanced Nosetip Test) vehicles.

Two configurations were specified for the A.N.T. flight tests: 1) a sharp (0.75-inch radius), high ballistic coefficient (β) vehicle; and 2) a blunt (1.25-inch radius) lower-β vehicle. Both vehicles (along with two other vehicles) were to be launched on a single booster, and each configuration was to be flown once in clear air and once in a weather environment. To permit accurate definition of the effects of the erosive environment on the tungsten recession performance, the A.N.T./ERN nosetips were designed so the tungsten subtips would be exposed at nearly the same altitude (35 kft) in clear air and in weather. It was further specified that the external shape and materials be the same for the clear air and weather flights and that the total shape change should be minimized. To satisfy these requirements, it was necessary to design a complex primary nosetip structure of graphite that would: 1) transmit axial aerodynamic loads from the external surface to the tungsten subtip, 2) support the external shell in a free-standing condition to minimize thermal stresses, and 3) assure a controlled fracture and removal of the external shell at the burn-through/ removal altitude. The subtip was designed for thermal and structural survival to impact following sudden exposure at the primary nosetip removal altitude of 35 kft.

All of the results of the SAMS/ERN flight test program and a complete description of the design/development effort for the A.N.T./ERN nosetips through the Critical Design Review (CDR) were summarized in Reference 2. The present report describes the final tasks accomplished in support of the A.N.T./ERN program, as well as the work performed in several related efforts, including the FLAME/ERN and HEARTS/ERN flight tests.

After the A.N.T./ERN CDR, the final nosetip flight designs were evaluated in a design verification test program performed at the Rocket Exhaust Test Facility at the Air Force Rocket Propulsion Laboratory (AFRPL). In this program, described in Section 2.0, full-scale nosetips were built and tested in a high performance exhaust flow environment. The tests were run with a model stagnation pressure of 100 atmospheres using a new benzonitrile/liquid oxygen propellant system. The resultant flow conditions produced an ablative and thermal stress environment for the nosetips that was representative of actual ICBM flight conditions. The test results indicated that the primary nosetip could be expected to perform satisfactorily in all respects, but that the tungsten subtips had an excessively high probability of experiencing thermal stress failures in flight.

The thermal stress problem for tungsten subtips had been of increasing concern after the post-flight analyses of the SAMS/ERN nosetips. All the early subtip designs were monolithic configurations that were machined from large billets of extruded or swaged material. As mechanical

1-4

property data for these billets gradually became available, it was found that the strength properties in the transverse plane were unsuitably low due to grain orientation characteristics and flaws. This poor transverse strength, coupled with the existence of a large volume of highly stressed material at temperatures below the ductile-brittle transition temperature (DBTT), resulted in the prediction of high probabilities of failure for many flight cases.

As a result, studies were begun to develop an improved subtip concept that would be more resistant to thermal stress failures. This task, which was conducted as a parallel effort to the A.N.T./ERN detailed design studies, involved a segmented construction approach that had the objective of reducing the applied thermal stresses to acceptable levels. With the segmented construction technique, the subtip is manufactured in the same external shape as the monolithic designs but is made from a number of smaller components. This results in lower thermal stress levels in the nosetip because: 1) the smaller components experience smaller temperature gradients, and 2) the segments can accommodate the stresses by deforming under the influence of the temperature gradient. The probability of failure also is reduced by the smaller unit volumes of highly stressed material in individual components. Because a fracture in one segment cannot propagate across the segment boundaries, any fracture that does occur will not result in a catastrophic failure of the assembly, thereby providing a form of artificial fracture toughness.

Several analytical and test programs were performed to develop and validate the segmented design concept. These included analyses to define the optimum segment configuration and arc-jet tests to determine if the segmented construction would affect the ablation performance of the assembly. The results indicated that segmented nosetips could be designed with a very low probability of thermostructural failure in flight and that the segmented construction has no detectable effect on the ablation performance.

Because of the favorable preliminary results obtained in the segmented nosetip development task (Section 3.0), segmented tungsten nosetips were designed and fabricated for evaluation on the HEARTS and FLAME flight test vehicles. The HEARTS vehicles were launched on Athena C and Athena D boosters and attained entry velocities of approximately 18,200 ft/sec. The HEARTS payloads were not recovered. One monolithic tungsten nosetip and one segmented nosetip were built and flight tested in clear air environments. Each nosetip was covered with a teflon glove designed to burn through and expose the tungsten at an altitude of around 35 kft. Both HEARTS/ERN nosetips survived to impact with no evidence of thermostructural failure and with no development of vehicle trim angle-of-attack at low altitudes. The HEARTS/ERN design analyses and results are summarized in Section 4.0.

The FLAME vehicles were air-launched, two-stage rockets that reached peak velocities in excess of 13,000 ft/sec. The payloads were designed for recovery to permit post-flight examination and analyses. One monolithic tungsten nosetip and one segmented nosetip were built and tested on FLAME vehicles in clear air flights. Both nosetips survived to impact with no unusual aerodynamic behavior. The monolithic design was recovered intact and found to be in excellent condition. The total recession depth was within predicted limits and no evidence of thermostructural failure was found. Section 5.0 describes the FLAME/ERN design and flight test analyses.

The HEARTS/ERN and FLAME/ERN flight tests provided valuable information regarding the performance of tungsten nosetips in hypersonic flight. Data were obtained to: 1) verify the clear air ablation performance of tungsten, 2) demonstrate the aerodynamic behavior of tungsten nosetips, and 3) verify the thermal stress behavior at sub-ICBM flight conditions. It also was shown that the segmented construction did not degrade the aerodynamic, structural, or ablation performance of

tungsten nosetips. However, since the HEARTS and FLAME flight environments were not sufficiently severe to produce thermal stress failures in the monolithic nosetips, no verification was obtained of the improvement in thermostructural performance provided by the segmented construction. Therefore, additional work was recommended to evaluate the thermostructural response of a full-scale segmented tungsten nosetip in a high performance rocket motor exhaust flow and to obtain final verification of the concept in an ICBM flight test.

Another major problem associated with flight test evaluation of tungsten nosetips has been the difficulty of obtaining in-flight surface recession measurements. Since the A.N.T. vehicles will not be recovered for post-flight inspection, all information regarding nosetip performance must be obtained from on-board instruments. However, the physical properties of tungsten are such that most of the measurement techniques developed for graphitic and resinous nosetips cannot be used. For example, gamma-ray backscatter sensors are not practical because the high density and attenuation characteristics of tungsten limit the effective measurement range to a fraction of an inch. The use of embedded discrete radioactive sources is prevented because the instrumentation holes critically degrade the thermostructural integrity of tungsten.

In the earlier ERN development studies (Reference 2), two new types of tungsten recession sensors were considered. These were: 1) the K West pulse/echo ultrasonic ablation gage (developed previously and flight tested successfully on graphite nosetips), and 2) a radioactive backscatter sensor utilizing neutrons (which are not attenuated by tungsten as significantly as are gamma rays).

Although mixed results were obtained in several ground tests and in one SAMS flight test, it was concluded that the pulse/echo ultrasonic ablation gage is unsatisfactory for measuring the surface recession of melting tungsten. The apparent reason is attenuation of the acoustic wave in the surface melt layer. The neutron backscatter gage was found to be capable of measuring tungsten thicknesses only slightly greater than 1.0 inch. Even though it was believed that this range could be extended somewhat (possibly to as much as 2.0 inches) with additional development effort, the performance still would not be satisfactory for most nosetip lengths of interest. This performance, along with the difficult safety and handling problems associated with neutron sources, resulted in the decision to discontinue further work on the neutron backscatter sensor.

In the present effort, two additional sensor concepts were investigated (Section 6.0). One of the concepts is a variation of the pulse/echo ultrasonic gage that measures the resonant frequencies in the nosetip to obtain an indication of the remaining length. The principal advantage of this concept over the conventional pulse/echo sensor is the fact that the low frequencies corresponding to the resonances were expected to have relatively low attenuation coefficients. The resonance sensor was designed in a laboratory development program and then demonstrated successfully in an ablation test of a tungsten model in the AFFDL 50 megawatt arc-jet facility. (No successful tests of the pulse/echo sensor had been obtained in this facility.)

The second tungsten recession sensor concept investigated in the present program was the bremsstrahlung-activation ablation gage (BAAG). With this concept the tungsten is activated by high energy electrons that produce high energy bremsstrahlung photons. The photons then convert the tungsten into the isotope ^{182}Ta with no physical alterations to the nosetip. Tungsten components were irradiated with this process, and a nosetip, collimator, and detector assembly was fabricated to determine the ablation measurement sensitivity of the instrumentation system. The count rate was found to be a nearly linear function of material thickness for nosetip lengths up to 8.0 cm (3.15 inches). The high count rate produced in the tungsten, along with the linear variation with length,

resulted in a detector system with good accuracy. All required electrical components were developed and the basic detector design has been flight tested extensively. Thus, it was concluded that the BAAG system is a feasible concept for obtaining in-flight recession measurements of tungsten nosetips. However, additional work is required to complete development of some components, optimize the nosetip activation procedures, and modify the calibration procedures.

2.0 A.N.T./ERN NOSETIP DEVELOPMENT

2.1 INTRODUCTION AND OBJECTIVES

This section describes the final design verification tests of the Advanced Nosetip Test/ Erosion-Resistant Nosetip (A.N.T./ERN) program that were conducted at the Air Force Rocket Propulsion Laboratories (AFRPL), Edwards Air Force Base, California, during the period May – November, 1975 (Reference 3).

The basic PDA erosion-resistant nosetip concept consists of a primary, or outer, nosetip and a secondary, or backup, subtip which assures survival to impact in an operational weather environment. The primary nosetip material consists of either graphite or carbon-carbon, while the erosion-resistant subtip is fabricated from an alloy of tungsten. A key objective of the A.N.T./ERN flight tests is evaluation of the subtip and phenolic carbon skirt/heatshield ablation performance in combined ablation/erosion environments. To accomplish this, it is necessary to remove the primary nosetip at an altitude characteristic of the removal altitude in an operational weather environment. Originally, an internally slotted carbon-carbon solid shell configuration, designed to burn through and separate from the vehicle at the selected removal altitude (35 ± 5 kft), was the concept to be flight tested. The results of design development tests on 0.7 scale models (also performed at the Air Force Rocket Propulsion Laboratory) to evaluate this concept indicated that an improved design was required to better control removal performance (Reference 2). It was decided to switch to a graphite nosetip design to provide better material homogeneity, reduce porosity, and improve confidence in the predictability of performance. An axisymmetric shell concept was designed to provide a predictable removal time based on burn-through rather than on fracture. (A detailed discussion of the final A.N.T./ERN design is contained in Reference 2). The present test series was the culmination of the design and material changes instituted after the initial 0.7 scale development tests. In addition to the nosetip changes discussed above, AFRPL also changed the rocket chemical reactants to a benzonitrile/liquid oxygen system to improve its reentry simulation.

The design verification tests discussed herein for the 994 graphite, thin, hollow shell primary nosetips and monolithic tungsten subtips were run in the AFRPL/ABRES 1-52-C test facility, described in Reference 4, using the benzonitrile/liquid oxygen propellant system. The specific test objectives were to:

1. Evaluate the removal characteristics of the redesigned outer tip.
2. Determine wall thickness and stagnation pressure conditions at the time of removal of the redesigned primary tip.
3. Expose the subtip to reentry thermal stress conditions.
4. Evaluate the performance of the acoustic recession sensor on tungsten.

2.2 APPARATUS

2.2.1 Test Facility Description

The ABRES RPL Reentry Nosetip Test Facility is rocket engine test stand 1-52-C with a hot gas combustion chamber and a remotely controlled model insertion mechanism. The high enthalpy gas generator is a 50,000-pound thrust equivalent liquid rocket engine. Liquid oxygen and benzonitrile (C_6H_5CN) propellants are burned in a combustor at 3000 psia chamber pressure at an

oxidizer-to-fuel mixture ratio (O/F) of 2.80. Both mixture ratio and chamber pressure are closed-loop controlled to maintain the desired environment. In addition, the chamber pressure can be varied during a run from 500 to 3000 psia according to a predetermined program.

The insertion mechanism consists of a rotating radial arm mounted on a carriage that can be moved both axially and radially. The test item may be swept in and out of the flowfield at preprogrammed rates. Although the engine can be started and stopped with the model/holder either in or out of the stream, the A.N.T./ERN tests were performed with the model rotated into place at the 'vernier" or 500 psi chamber pressure level. Additional details of the facility capability and instrumentation are given in Reference 4.

The combustion flame temperature variation with propellant mixture ratio predicted by the ODE (One-Dimensional Equilibrium) chemistry program (Reference 5) is shown in Figure 1. The present test point at a mixture ratio of 2.80 is an oxygen-rich environment. A summary of the ideal theoretical performance for the 100-atmosphere and the 50-atmosphere nozzle configurations, calculated by the ODE code, is given in Table 1. The nozzle contour data were extracted from Reference 6 and used in the calculations.

CHAMBER PRESSURE = 3000 PSIG
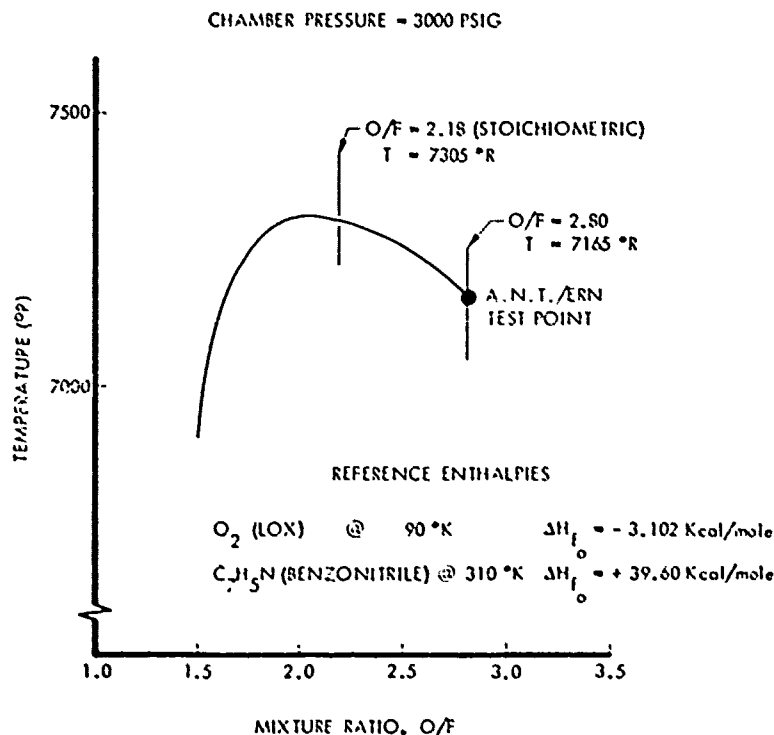
Figure 1. Combustion flame temperature variation with O/F mixture ratio, AFRPL/ABRES 1-52-C rocket motor.

Table 1. AFRPL nosetip test facility cell 1-52-C
environment* ideal theoretical performance.

PROPELLANT	LOX/BZN	LOX/BZN
MIXTURE RATIO, O/F	2.80	2.80
NOSETIP STAGNATION PRESSURE, (ATM)	100	50
NOZZLE AREA RATIO	2.76**	6.00**
NOZZLE EXIT MACH NUMBER	2.26	2.76
NOZZLE STATIC TEMPERATURE, (^{o}R)	5797	5353
NOZZLE STATIC PRESSURE (PSF)	36367	12977
NOZZLE STAGNATION TEMPERATURE (^{o}R)	7165	7165
NOZZLE GAS MOLECULAR WEIGHT	31.95	32.76
NOZZLE GAS STAGNATION ENTHALPY (BTU/LB)	53.3	53.3
NOZZLE GAS DENSITY (LB$_m$/Ft^3)	0.1297	0.0514
NOZZLE EXIT VELOCITY (FT/SEC)	7161	8302
NOZZLE EXIT DIAMETER (IN.)	5.80	8.66
GAMMA, γ (CHAMBER)	1.13	1.13
CHAMBER PRESSURE (PSIG)	3000	3000
TOTAL DRIVING ENTHALPY, ΔH (BTU/LB)	3906	3906

*ODE COMPUTER CODE (REFERENCE 5) EQUILIBRIUM
**CALCULATED FROM NOZZLE CONTOUR DATA PROVIDED IN REFERENCE 6

The present test point, O/F 2.80, for benzonitrile (BZN) and liquid oxygen (LOX) was characterized completely and a full Mollier description of the environment as a function of enthalpy and pressure was generated for use in the PDA NOHARE and NOSEC computer programs (Reference 7) from modified ODE computations. Carbon and tungsten wall materials in the same environment also were characterized, and tables were generated of gas-wall enthalpy and ablation potential (B-value) as functions of temperature and pressure. The universally accepted JANAF reference state of 298^oK (536^oR) was used throughout the calculations. These tabulated data were presented in Reference 3.

2.2.2   Calibration Models

Since the BZN/LOX propellant system had not been used for any test program prior to the present test series, calibration data did not exist. Hence, a series of pressure and heat flux calibration models were used to characterize the exhaust environment at chamber pressures of 500, 1500 and 3000 psia for the 50- and 100-atmosphere nozzle configurations. The RPL facility provided all calibration models except for a special biconic model supplied by PDA. The RPL models all

20

were sphere-cone copper models with cone half-angles of 7.0 degrees and nose radii of 0.5, 1.0, and 2.0 inches using Aerotherm null-point calorimeters. The special PDA biconic heat flux calibration model had the same external configuration as the sharp primary nosetip model (described later). The calibrations at the various chamber pressure levels were necessitated by the requirement for model insertion prior to steady-state operation to: 1) simulate high altitude preheat effects on the primary nosetip, and 2) avoid high model side loads encountered at the higher chamber pressures.

A surface pressure calibration model with a nose radius of 1.0 inch and a cone half-angle of 7.0 degrees was tested to confirm analytical prediction techniques. The calibration models with calorimeter locations indicated are shown in Figures 2 through 5. Table 2 summarizes, for each model, the axial locations of the sensors measured from model stagnation point.
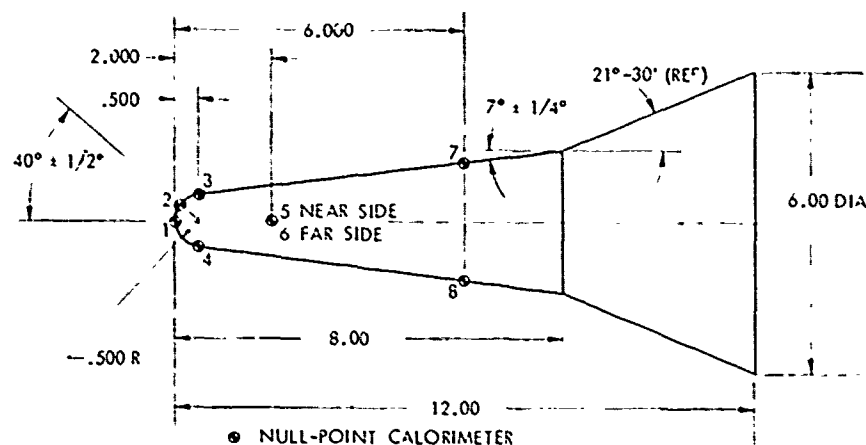
Figure 2. RPL 0.50-inch nose radius calorimeter model.
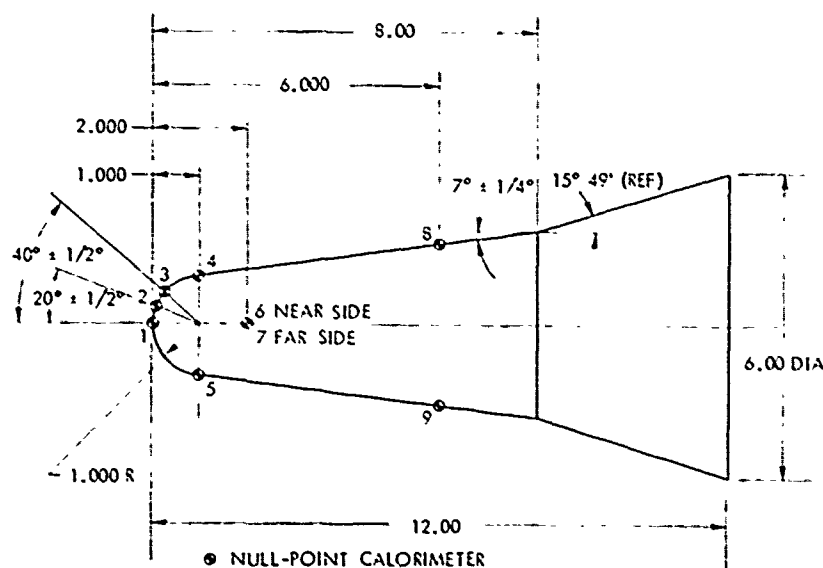
Figure 3. RPL 1.00-inch nose radius calorimeter model.
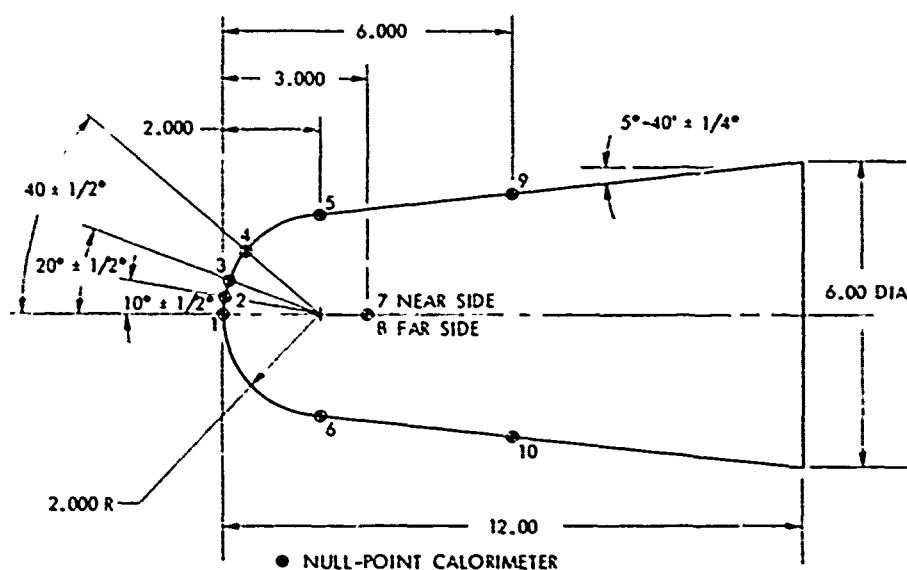
Figure 4. RPL 2.00-inch nose radius calorimeter model.
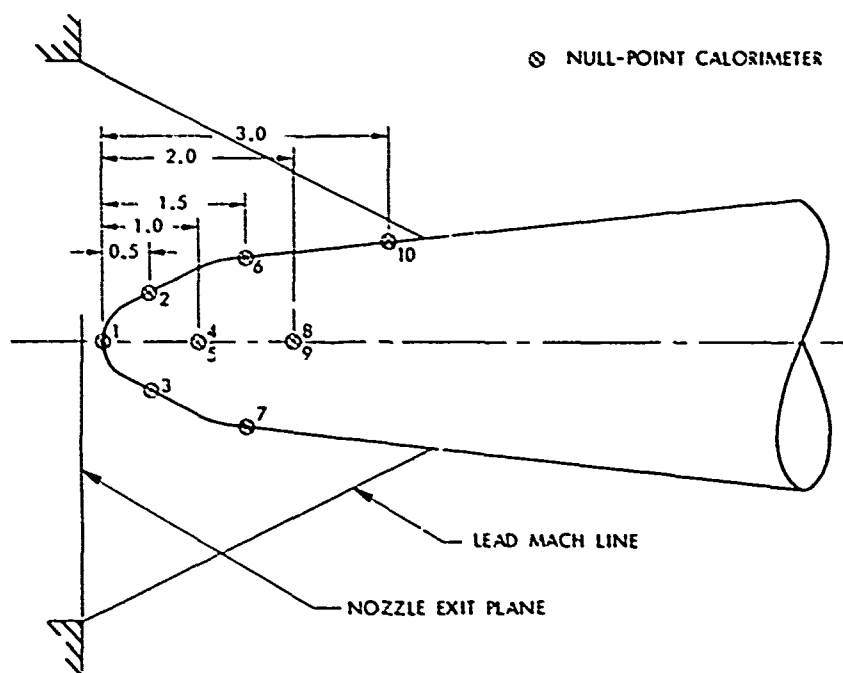
Figure 5. PDA sharp biconic calorimeter model.

Table 2. Calorimeter location summary.

Model Configuration	$R_N = 0.50, \theta_c = 7$ Degrees		$R_N = 1.0, \theta_c = 7$ Degrees		$R_N = 2.0, \theta_c = 7$ Degrees	
Sensor	Axial Location (Inches)	Circumferential Location (Degrees)*	Axial Location (Inches)	Circumferential Location (Degrees)	Axial Location (Inches)	Circumferential Location (Degrees)
1	0	0	0	0	0	0
2	0.117	0	0.068	0	0.030	0
3	0.50	0	0.234	0	0.121	0
4	0.50	180	1.0	0	0.465	0
5	2.00	270	1.0	180	2.0	0
6	2.00	90	2.0	270	7.0	180
7	6.00	0	2.0	90	3.0	270
8	6.00	180	6.0	0	3.0	90
9	--	--	6.0	180	6.0	0
10	--	--	--	--	6.0	180

*Looking into nozzle

2.2.3 Graphite Ablation Models

Three ablation reference models were fabricated and tested by PDA. The results were correlated with analytical results from the PDA NOHARE NOSEC computer programs. Two sharp models and one blunt model, each identical in exterior profile to the respective shell removal models, were tested to define the ablation response of graphite in the BZX 1OX propellant system. Accurate characterization of the ablation rates was critical because of the necessity to predict burn-through times accurately for the shell removal models. The ablated shape was of as much interest as the overall stagnation point or sidewall recession, since proper thickness contouring was necessary to assure initial burn-through at the stagnation point location.

Each model had a 994-2 graphite plug nosetip held in a steel substructure insulated with carbon phenolic and silica phenolic. The external profiles were identical to the shell removal models discussed in Section 2.2.4. The sharp graphite ablation model is shown in Figure 6. A second sharp model was required because the first model was subjected to an off-nominal mixture ratio of 4.1 because of a propellant system valve failure. The resultant high recession rate was not characteristic of recession at the design mixture ratio of 2.5; hence, the second model was fabricated and tested.

2.2.4 Shell Removal Models

The A.N.T./ERN RPL test models were full-scale models of the proposed flight designs with a modification to the primary nosetip configuration intended to inhibit thermostructural failure due to the sudden high heat flux encountered during insertion of the cold nosetip into the exhaust flow.

The modification consisted of removing material on the spherical nosecap to reduce the wall thickness at the sonic region. The resultant biconic shape reduced the thermal gradient and, therefore, the probability of thermostructural failure prior to burn-through-induced removal. Two test model configurations, representing the "sharp" and "blunt" flight models, were tested. The sharp and blunt configurations are shown schematically in Figures 7 and 8, respectively.
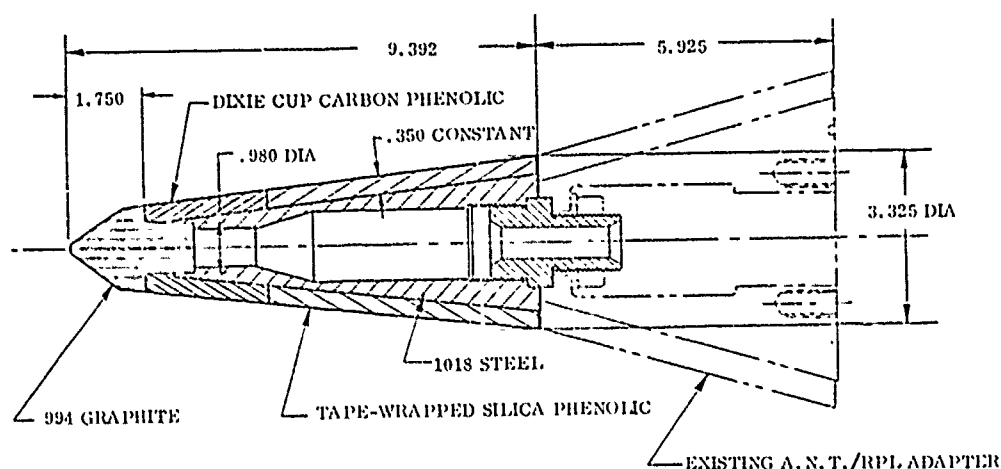
Figure 6. Sharp graphite ablation model.
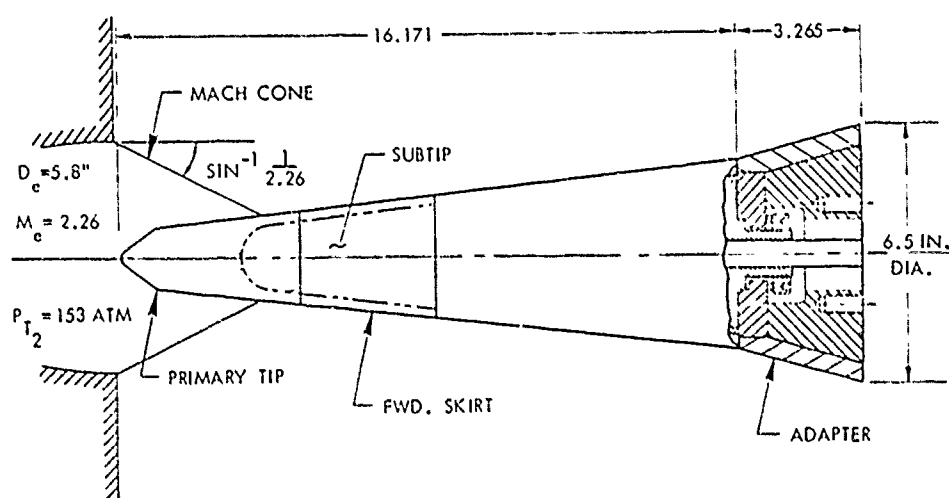
Figure 7. A.N.T. sharp test configuration.
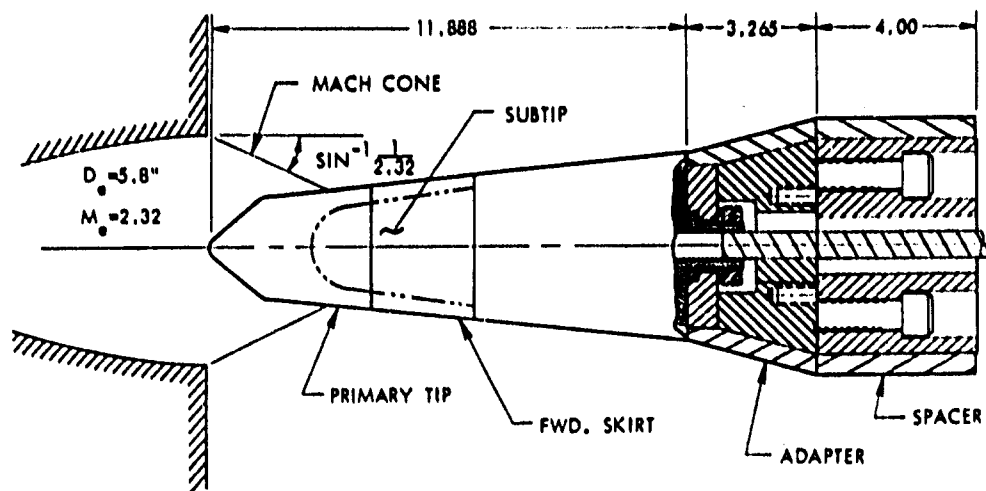
Figure 8. A.N.T. blunt test configuration.

The sharp model consisted of a 994-2 graphite primary tip with a 0.40-inch nose radius, 26-degree (half-cone) initial conic section, followed by a 6.0-degree cone. The stagnation point thickness was nominally 0.30 inch (versus 0.41 inch for the flight design). The forward portion of the shell was in intimate contact with a thin insulating pyrolytic graphite cap which was supported by an ATJ-S graphite cruciform block which, in turn, transmitted the loads through a graphite bearing cap to the tungsten subtip. Grafoil insulation was used between the 994 shell and the ATJ-S cruciform on the sidewall. The blunt primary tip had a 0.60-inch nose radius with 40-degree initial conic section faired to a 6.0-degree cone. The stagnation point wall thickness was 0.25 inch (versus 0.31 inch for the flight design), and the sidewall thickness was 0.15 inch. The load path and insulation were the same as for the sharp design.

The sharp tungsten subtip consisted of a 0.75-inch nose radius with a 6.69-degree cone and 5.0 inch overhang. The blunt subtip had a 1.0-inch nose radius with an 8.42-degree cone and 4.0 inch overhang. Both subtips included a 0.05-inch thick flame-sprayed coating of molybdenum as an overlay. An exploded view of the primary nosetip components is shown in Figure 9.

2.2.5   Subtip Thermostructural Models

The subtip thermostructural test models were essentially identical to the subtip models in the shell removal configurations except for the following component deletions:

1.   Primary tip and supports,
2.   forward skirt, and
3.   subtip overlay.

The blunt tungsten subtip model (Figure 10) was installed with a 0.15-inch thick teflon glove to delay subtip exposure until steady-state operation was achieved in the motor. The model was placed into the rocket exhaust at low pressure to preclude losing the subtip due to entry side loads. Upon removal of the teflon glove, the bare tungsten subtip would experience minimum thermostructural margin-of-safety (i.e., peak thermal gradient).

A. CROSS-SECTIONAL VIEW

SECTION A-A   SECTION B-B

B. EXPLODED VIEW

PYROLYTIC GRAPHITE CAP

994 GRAPHITE SHELL

GRAFOIL INSULATION

SPLIT GRAPHITE SUPPORT

GRAPHITE BEARING RING

SUBTIP AND INSULATION
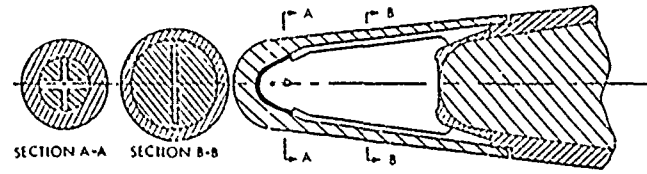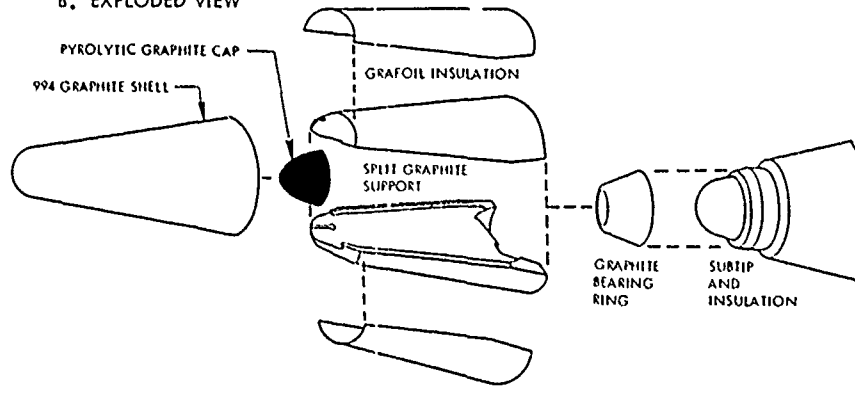
Figure 9. A.N.T./ERN primary nosetip concept.

MACH CONE

$SIN^{-1}\frac{1}{2.32}$

TEFLON CAP (UNBONDED)

$D_e = 5.8"$

$M_e = 2.26$

$P_{T_2} = 103$ ATM

0.25"

SUBTIP

9.588

3.265

6.5 IN. DIA.

MODIFIED A.N.T./RPL ADAPTER
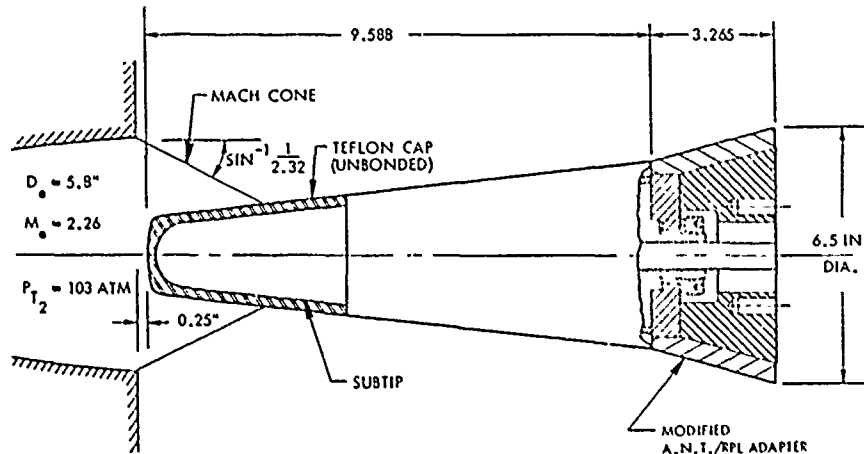
Figure 10. Blunt subtip thermostructural test configuration.

26

The sharp tungsten subtip model had an additional modification, consisting of a special teflon primary nosetip, as shown in Figure 11. The teflon noset was evaluated as a possible alternate primary tip for flight in place of the 994 graphite shell configuration. The actual teflon nosetip used in the RPL ground test extended to the subtip overhang shoulder.
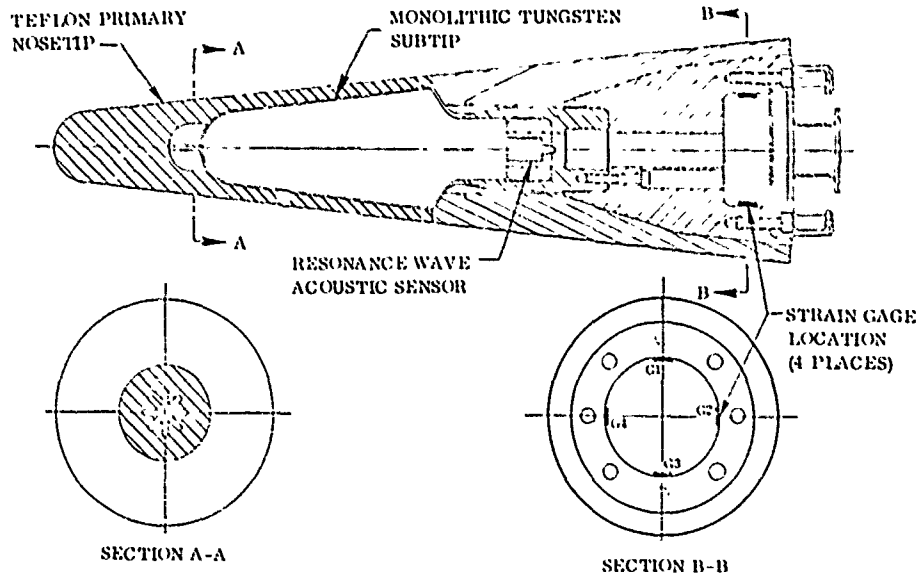
Figure 11. Sharp subtip configuration with teflon primary nosetip.

2.2.6   Instrumentation

Each A.N.T./ERN model was instrumented with Chromel-Alumel and tungsten-rhenium thermocouples, an Endevco Model 2292 shock accelerometer, and a K West acoustic recession gage. Table 3 gives the detailed description of the locations and types of thermocouples used on each design. Note that the thermocouples under the primary tip and the forward skirt were deleted on the subtip thermostructural test models.

Each A.N.T./ERN model was instrumented with an acoustic subtip recession gage provided and installed by K West under subcontract to PDA. The specific sensor type for each model is given in Table 4. Three of the models used the pulse/echo type of acoustic recession sensor that had been selected for use on the flight nosetip units (Reference 2). However, since recent ground and flight test results had indicated a low probability of success for this sensor, additional work was being performed to develop a new type of acoustic sensor that measured the length-dependent resonant frequency in the nosetip (Section 6.1). The fourth test model contained one of these resonance wave acoustic recession sensors.

Six pyrometers were used to measure the external surface temperatures of the models, and high speed motion picture coverage was provided by eight motion picture cameras.

Table 3. Summary of nosetip thermocouple functions.

| THERMOCOUPLE* NUMBER | TYPE | POSITION** (INCH) | | | | FUNCTION |
| | | SHARP | | BLUNT | | |
		AXIAL	RADIAL	AXIAL	RADIAL	
(A1)	0.032 Steel-Sheathed Cr/Al	9.67	0.00	13.23	0.00	Primary tip removal, stagnation point
(A2, B2)	0.032 Steel-Sheathed Cr/Al	9.88	0.55	13.50	0.70	Primary tip removal, sidewall
(A3, B3)	0.032 Steel-Sheathed Cr/Al	11.70	0.90	15.22	1.15	Forward heatshield stripback
(A4, B4)	0.032 Steel-Sheathed Cr/Al	12.97	1.06	16.12	1.29	Forward heatshield stripback
(A5, B5)	0.032 Steel-Sheathed Cr/Al	14.22	1.20	17.02	1.13	Forward heatshield stripback
A6, B6	0.032 Steel-Sheathed Cr/Al	14.90	0.91	17.60	1.04	Subtip temperature
A7	0.010 Tantalum-Sheathed W/W-26Re	15.82	0.72	18.52	0.84	Tantalum holder temperature (high temperature measurement)
B7	0.032 Steel-Sheathed Cr/Al	15.82	0.72	18.52	0.84	
A8, B8	0.032 Steel-Sheathed Cr/Al	16.77	0.89	18.52	0.97	Erosion guard performance
A9	28 Gage Glass-Wrapped Cr/Al	18.48	1.27	19.76	1.30	Aft heatshield stripback
A10	28 Gage Glass-Wrapped Cr/Al	19.38	1.55	20.68	1.60	Aft heatshield stripback
A11, B11	28 Gage Glass-Wrapped Cr/Al	20.28	1.80	21.60	1.90	Aft heatshield stripback
A12	0.032 Steel-Sheathed Cr/Al	16.34	0.35	19.00	0.35	Acoustic transducer, subtip backface
C1, D1	0.010 Tantalum-Sheathed W/W-26Re	16.65	1.60	19.66	1.85	Heatshield in-depth temperature
C2, D2	0.010 Tantalum-Sheathed W/W-26Re	16.25	1.40	19.14	1.59	Heatshield in-depth temperature
C3, D3	0.020 Steel-Sheathed Cr/Al	15.85	1.20	18.62	1.33	Heatshield in-depth temperature

(Left margin brackets: Nosetip Assembly — rows A1 through A8,B8; Aft Heatshield — rows A9 through A12; In-Depth Heatshield — rows C1,D1 through C3,D3)

* Thermocouples A are at 120°, B at 300°, C at 30°, and D at 210° (vehicle azimuth angles). Thermocouples in parentheses not installed on thermostructural test models.

** Axial position measured from theoretical vehicle apex.

Table 4. Acoustic sensor summary.

RPL TEST NUMBER	DATE	PDA SUBTIP MODEL	ACOUSTIC SENSOR	MODEL AND TYPE
165	7-2-75	BT-3	309-38 SN2	Shear Wave
169	7-17-75	BD-4	309-33 SN2	Compression (1.5 mHz)
186	10-21-75	BK-4	309-32 SN3	Shear Wave
189	11-14-75	BM-4	310-R	Resonance

2.3 TEST METHOD

Four A.N.T./ERN models and two graphite ablation models were tested, as summarized in Table 5. Each test model was mounted on the centerline of the rocket exhaust and mated to the RPL movable sting system using a common adapter provided by PDA. Each test was started with the model positioned 0.25 inch aft of the nozzle exit plane. Figures 7 and 8 show the relationship of the model to the Mach cone intersection and the nozzle exit plane for the sharp and blunt primary nosetip configurations, respectively, in the 100-atmosphere nozzle. The test continued with models in this position until burn-through or removal of the primary tip (if present) occurred, at which time the sting was moved forward to position the subtip 0.25 inch aft of the nozzle exit plane. Axial forward motion was 3.25 inches and 2.55 inches for the sharp and blunt nosetip models, respectively.

The forward motion was actuated by the RPL test conductor upon visual observation of the primary nosetip removal via remote color television. Visual observation was found to be a more reliable indication of removal than surface temperature changes monitored by the pyrometers because intermittent unburned fuel clouds (from excess fuel sprayed on the chamber walls for cooling) tended to mask the surface of the model.

Because of the excessively high bending loads which would result from model insertion into the flow at full stagnation pressure, it was necessary to insert the models at a reduced, or "vernier" level, operating condition which produced a stagnation pressure on the order of 12 to 18 atmospheres. The graphite primary nosetip models were protected by a polyethylene bag from the nozzle wall coolant flow during insertion. The tungsten subtip models had teflon covers to keep the tungsten from being exposed until steady-state, high pressure operating conditions were achieved. The teflon glove on the sharp subtip model was of a full-scale primary tip configuration (Figure 10).

The primary nosetip removal tests not only required insertion of the models at the vernier (500 psia chamber pressure) level, but, in addition, an extended preheat time was required at this level to alleviate the thermal gradient that would be induced at the higher pressure conditions. The preheat allowed for some bulk temperature rise to occur before ramping up to the high pressures and, thus, relieved the thermal shock response and inhibited thermostructural failure.

Table 5. Design verification test matrix.

TEST NO.	MODEL DESCRIPTION	PRIMARY TEST OBJECTIVE	NOSE RADIUS (INCH)	OVERALL LENGTH (INCH)	INSTRUMENTATION
1	Graphite Ablation Model (Sharp Biconic)	Measure Primary Tip Recession and Shape Change History in Benzonitrile/LOX	0.40	15.32	Backface Thermocouples
2	Graphite Ablation Model (Blunt Biconic)		0.60	11.04	Backface Thermocouples
3	A.N.T. Sharp Biconic Full A.N.T./ERN Design	Outer Tip Removal Performance Verification/Subtip Performance	0.40	19.44	Shear Wave Acoustic Sensor Thermocouples ENDEVCO Accelerometer
4	A.N.T. Blunt Biconic Full A.N.T./ERN Design	Outer Tip Removal Performance Verification/Subtip Performance	0.60	15.15	Compression Wave Acoustic Sensor Thermocouples ENDEVCO Accelerometer
5	A.N.T. Sharp (w/o Underlay)*	Subtip Thermostruc-tural Response	0.75	16.19	Resonance Wave Acoustic Sensor Thermocouples
6	A.N.T. Blunt (w/o Underlay)*	Subtip Thermostruc-tural Response	1.00	12.65	Shear Wave Acoustic Sensor Thermocouples

*Primary Tip and Forward Skirt will be Removed Before Test to Achieve Required Thermal Stress.

2.4 CALIBRATION RESULTS

2.4.1 Heat Flux and Pressure

A series of ten heat flux calibration runs and one pressure calibration run were made in the RPL 100-atmosphere and 50-atmosphere nozzles at chamber pressures of 500, 1500, and 3000 psia. The principal objective of the calibration runs was to correlate the measured and theoretical surface heat transfer distributions to provide a basis for accurate predictions of the ablation and thermostructural response histories of the A.N.T./ERN flight nosetip models.

All heating analyses were performed with the NOHARE code (Reference 7) and accounted for actual motor performance losses. Measurements by facility personnel (Reference 8) indicated that the performance (C*) efficiency was approximately 97 percent at the design operating condition of 3000 psia chamber pressure and propellant mixture ratio of 2.80. However, at the 500 psia vernier condition used for model preheat, the measured C* efficiency was only 90 percent.

Several possibilities were considered to account for the reduced efficiency at the low pressure condition. These included: 1) chemical kinetics, 2) boundary layer losses, 3) nozzle divergence losses, 4) mixture ratio maldistribution, and 5) energy release losses. A series of calculations and nozzle design evaluations were performed (Reference 3) to select the probable source(s) of the performance losses and to define the proper method for describing the exhaust flow conditions. The results of this study indicated that the first three possibilities would not be significant for this nozzle/propellant system. Thus, the most likely sources of the measured performance losses are some combination of incomplete energy release and mixture ratio maldistribution.

The energy release (i.e., combustion) process in a liquid propellant system involves a complex combination of thermodynamic, fluid dynamic, and chemical processes. A review of the analytical capabilities for describing these processes was performed by the Interagency Chemical Rocket Propulsion Group (ICRPG) for JANAF (Reference 9). This review concluded that the energy release phenomena cannot be described adequately by current analytical techniques. As a result of this conclusion, the ICRPG committee adopted an empirical technique, known as the energy release model (Reference 10), as an interim procedure for predicting energy release inefficiencies. Basically, this procedure models incomplete energy release analytically by reducing the total energy of the system available in the expansion by the use of effective propellant heats of formation that have been artificially lowered from their standard JANAF values. Prior to expansion, 100 percent of the propellant is presumed to be in thermodynamic equilibrium at the reduced enthalpy level. The chemical and fluid dynamic calculations for the expanding combustion products are then made in their usual manner, and the calculated performance is reduced because of the lower energy available to the expansion process. The procedure is repeated iteratively until agreement is obtained with the measured C* value. It should be noted that, with this technique, all performance losses are attributed to a loss in energy release.

An alternate method of accounting for the lowered C* efficiency is to assume that the entire performance loss is caused by incomplete fuel vaporization (IFV model). The basis for the IFV model is the assumption that propellant vaporization is the rate controlling combustion process (Reference 11). The most important physical parameter in the vaporization process is the heat of vaporization. Thus, a propellant such as BZN, which has a high heat of vaporization, will require a relatively long combustion chamber to achieve complete vaporization. Furthermore, since the vaporization rate is pressure-sensitive, an engine operating at pressure levels substantially lower than the design values may exhibit reduced performance. The IFV model assumes that the

unvaporized fuel is inert, has no effect on performance, occupies no volume, and does not contribute to the chamber pressure. No other sources of performance losses are considered. This model provides a worst-case estimate of exhaust conditions in the sense that incomplete vaporization of the fuel will result in the presence of higher mole fractions of chemical species that are capable of oxidizing or reducing carbon (e.g., O_2, O, OH, and H_2O).

Nozzle heating and thermal response calculations were performed (Reference 3) using exhaust flow properties computed with the assumptions of ideal flow, the energy release model (ERM), and the IFV model. Stagnation point heating and recession rate histories were computed for carbon models with initial nose radii of 0.1, 0.2, and 0.4 inch for chamber pressures of 500 and 600 psia. The results, summarized in Table 6, show that increasing the chamber pressure over this range has small effect on all parameters. Similarly, very little effect was produced by the change in nose radius from 0.1 inch to 0.4 inch. However, there were significant differences between the results predicted with the three flow models. The energy release model calculations show a small (2 - 4 percent) decrease in surface recession rate relative to the ideal flow case, while the IFV model predicts a 15 percent increase in surface recession rate. The enthalpy driving potential and the surface temperature predicted with the energy release model are lower by about 27 percent and 35 percent, respectively, than in the ideal case. The IFV model causes a 14 percent reduction in the enthalpy difference and a 1 percent increase in surface temperature relative to the ideal calculations.

Preliminary correlations of the calorimeter model heat flux data (presented below) indicated better agreement with the energy release model. The actual flow conditions probably are represented by some combination of the energy release and IFV models. However, in the absence of any additional data with which to correlate the analytical predictions, the energy release model was selected for use in all of the data correlations and nosetip response predictions involving the vernier preheat condition.

The calibration tests performed during this test series are summarized in Table 7. The locations at which the Mach lines impinged on the calorimeter models are shown schematically in Figure 12 for the various combinations of nozzle and model configurations. The Mach line angle (θ) was computed from the expression

$$\theta = \sin^{-1} \frac{1}{M_e}$$

where M_e is the theoretical exit plane Mach number. The impingement location defines the point aft of which the heating is less well-defined, since it is outside the test rhombus, or region of constant freestream properties. The calorimeters aft of the impingement point were of special interest since they would define this environment.

Figures 13 through 18 present the calorimeter data superimposed on the best NOHARE computer program predictions, which accounted for the actual C* efficiencies measured during the tests, as discussed above. The calorimeter data aft of the Mach cone impingement locations were correlated initially by Aerotherm (Reference 12) by plotting the normalized heat flux quantity, $\dot{Q}/\dot{Q}_{MLI}$*, versus the axial distance from the Mach line impingement point. The Aerotherm correlation, however, showed more data points than were available from the A.N.T./ERN test series,

_____

*$\dot{Q}_{MLI}$ is the predicted heat flux at the Mach line intersection on the model (see Figure 13).

Table 6. Summary of predicted steady-state ablation results for preheat condition.

Model	P_c (psia)	P_{t_2} (atm)	h_{gw} (Btu/lb)	h_r (Btu/lb)	$|h_r - h_{gw}|$ (Btu/lb)	R_N (in)	T_s (°R)	B --	$\dot{S}$ (in/sec)	$\dot{S}/\dot{S}_{ideal}$ --
Ideal	500	18.35	-3853	53.3	3906	.1	5105	.351	.094	--
	500	18.35	-3853	53.3	3906	.2	5061	.350	.067	
	500	18.35	-3853	53.3	3906	.4	4998	.348	.047	
	600	22.0	-3853	53.3	3906	.1	5115	.351	.104	
	600	22.0	-3853	53.3	3906	.2	5071	.350	.073	
	600	22.0	-3853	53.3	3906	.4	5021	.349	.051	
ERM(a)	500	18.29	-3853	-1001.3	2851	.1	3335	.338	.091	.97
	500	18.29	-3853	-1001.3	2851	.2	3310	.338	.065	.97
	500	18.29	-3853	-1001.3	2851	.4	3285	.337	.046	.97
	600	21.95	-3853	-1001.3	2851	.1	3343	.338	.100	.96
	600	21.95	-3853	-1001.3	2851	.2	3320	.338	.071	.97
	600	21.95	-3853	-1001.3	2851	.4	3295	.337	.050	.98
IFVM(a)	500	17.6	-3330	12.1	3342	.1	5172	.425	.108	1.15
	500	17.6	-3330	12.1	3342	.2	5122	.424	.076	1.13
	500	17.6	-3330	12.1	3342	.4	5047	.422	.054	1.15
	600	21.4	-3330	12.1	3342	.1	5180	.425	.119	1.14
	600	21.4	-3330	12.1	3342	.2	5137	.424	.084	1.15
	600	21.4	-3330	12.1	3342	.4	5074	.423	.059	1.16

Note: (a) 90 percent C* efficiency

Table 7. A.N.T./RPL calibration test summary.

CHAMBER PRESSURE, PSI	3000		1500	500
MODEL STAGNATION PRESSURE, ATM	100	50	50	17
NOZZLE DIAMETER, IN	5.8	8.6	5.8	5.8
NOSE RADIUS, IN (a)	RPL TEST NUMBER			
0.50	#158	#180, #183	---	#182
1.0	#157, #168 #163 (b)	#179	#157	---
2.0	#171	---	---	---
0.40, 26° BICONIC	---	---	---	#178.2

NOTES: (a) Heat flux distribution calibration unless otherwise noted
         (b) Pressure distribution calibration

TIP RADIUS (IN.)	NOZZLE	•IMPINGEMENT PT. (IN.)
0.50	50 ATM	7.30
0.50	100 ATM	3.75
1.00	50 ATM	6.45
1.00	100 ATM	3.05
2.00	50 ATM	4.75
2.00	100 ATM	1.60

• MEASURED FROM MODEL STAGNATION POINT
  ASSUMING 0.25-INCH POSITION
  AFT OF EXIT PLANE

MODEL STAG. PT. POSITION

$\theta = \sin^{-1}\frac{1}{2.77} = 21.2°$

50 ATM NOZZLE MACH CONE

$\theta_c = 7°$ CONE ANGLE

$\theta = \sin^{-1}\frac{1}{2.25} = 26.4°$

100 ATM NOZZLE MACH CONE

DISTANCE FROM CENTERLINE (INCHES)

AXIAL DISTANCE FROM NOZZLE EXIT PLANE (INCHES)

Figure 12. Mach line impingement locations on calorimeter models.

34
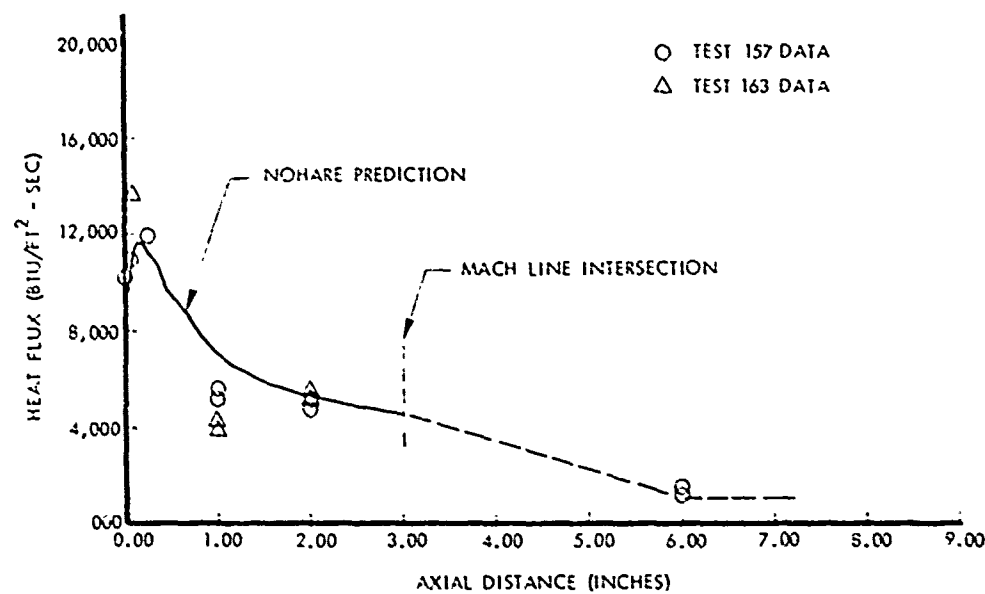
Figure 13. NOHARE/RPL heat flux correlation,
$R_N = 0.50$, $P_s = 100$ ATM, $P_c = 3000$.
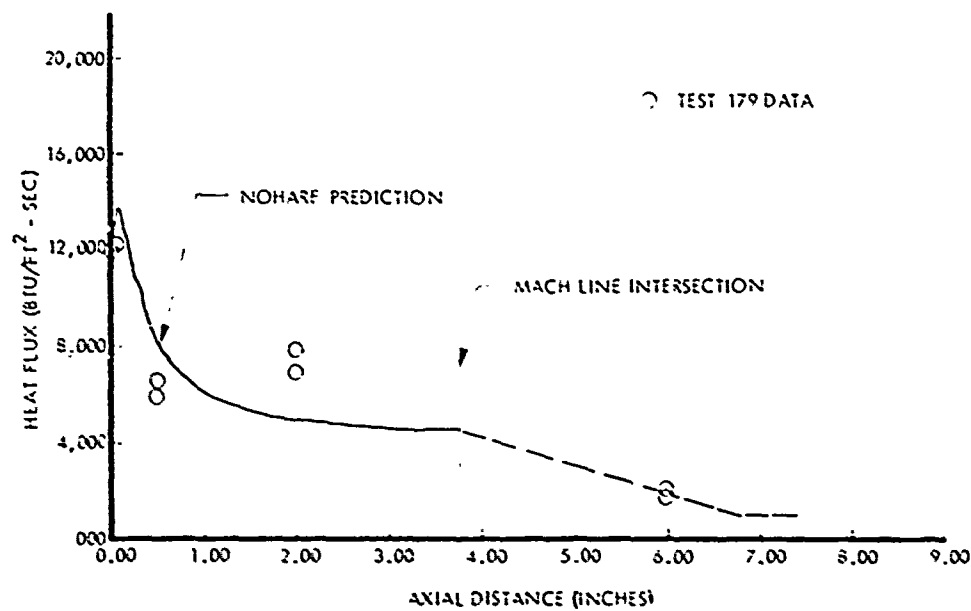
Figure 14. NOHARE/RPL heat flux correlation,
$R_N = 1.0$, $P_s = 100$ ATM, $P_c = 3000$.
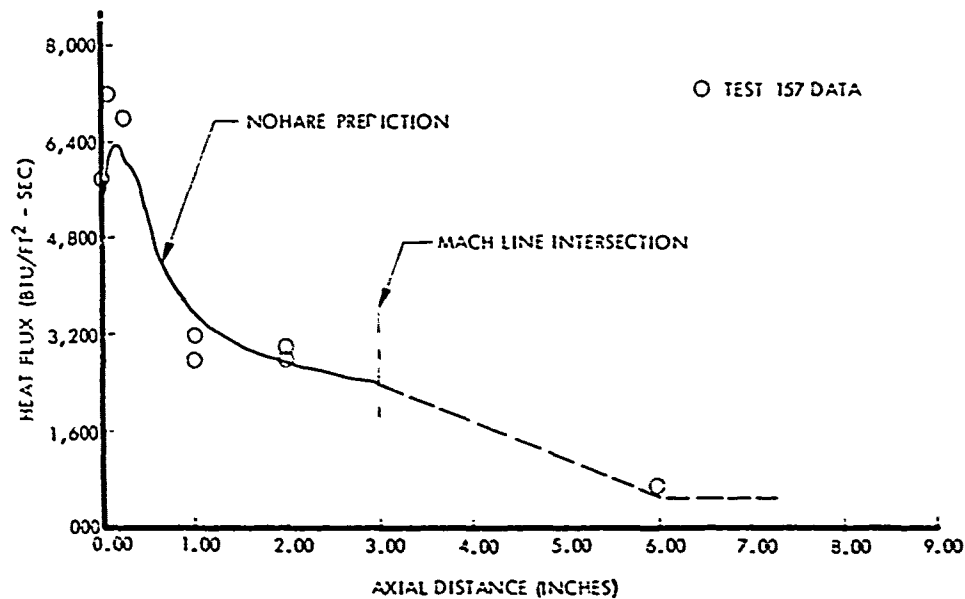
Figure 15. NOHARE/RPL heat flux correlation,
$R_N = 1.0$, $P_s = 50$ ATM, $P_c = 1500$.
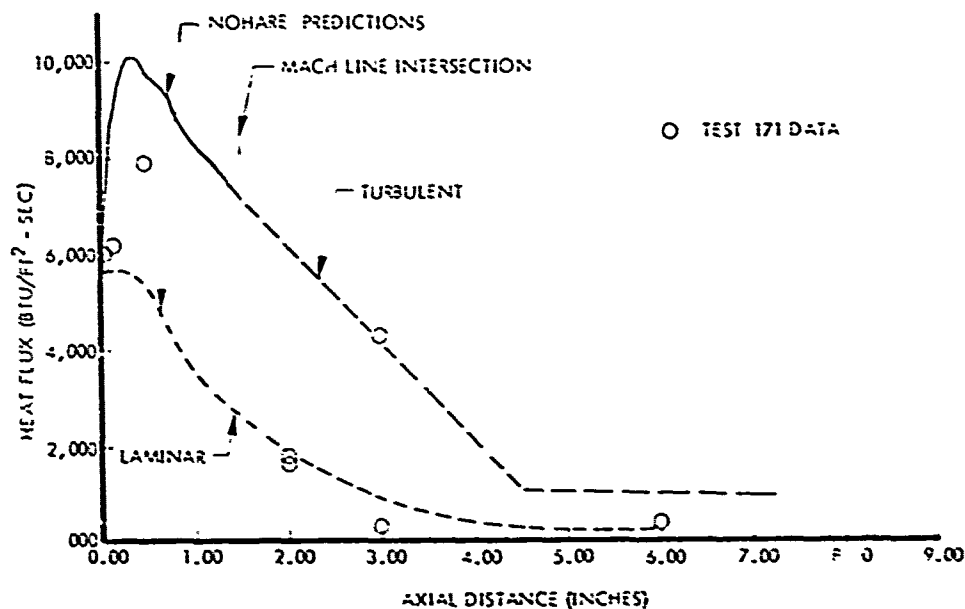
Figure 16. NOHARE/RPL heat flux correlation,
$R_N = 2.0$, $P_s = 100$ ATM, $P_c = 3000$.
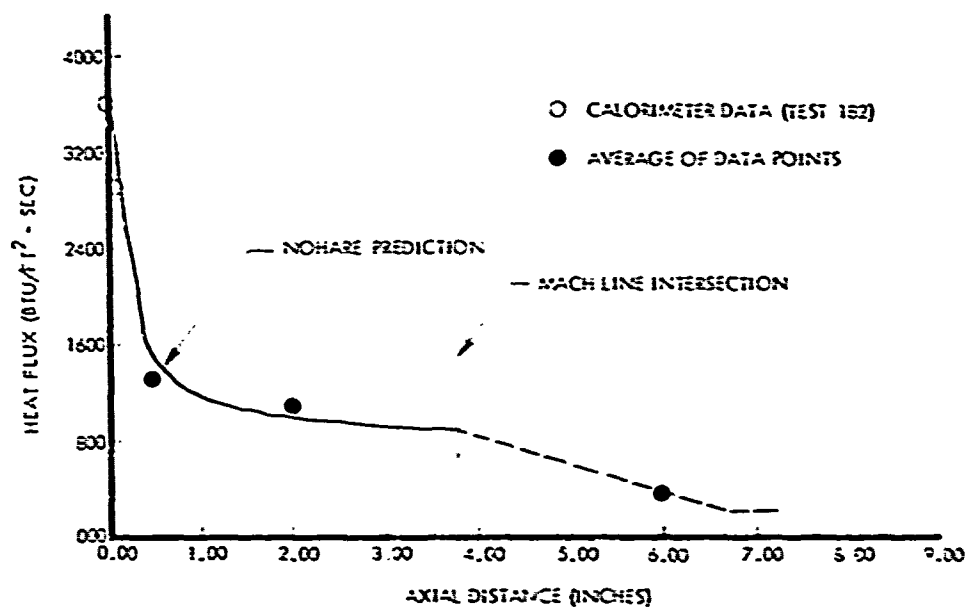
Figure 17. NOHARE/RPL heat flux correlation.
$R_N = 0.50$, $P_s = 17$ ATM, $P_c = 500$.
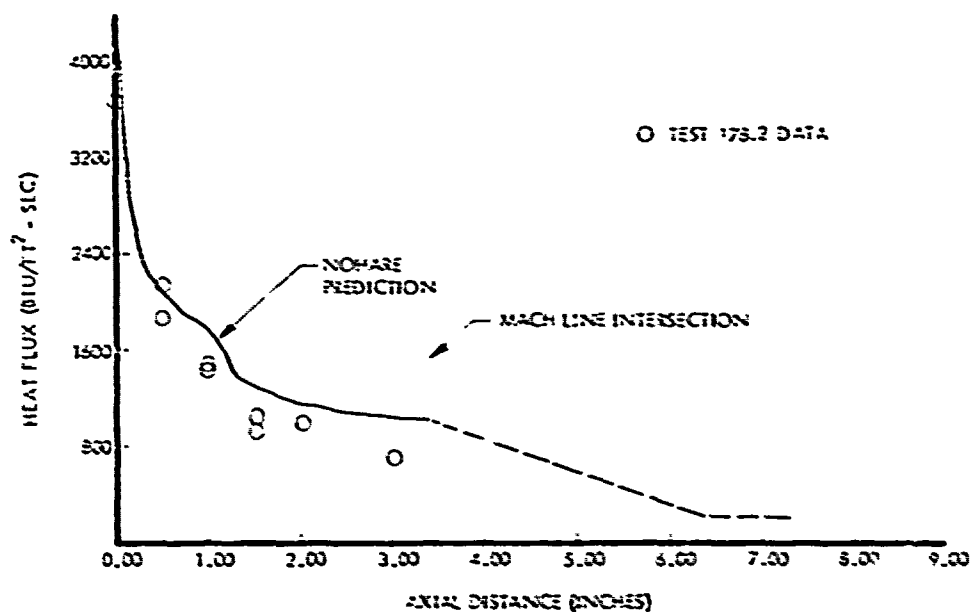
Figure 18. NOHARE/PDA biconic model heat flux correlation.
$R_N = 0.40$, $P_s = 17$ ATM, $P_c = 500$.

and the 2.0-inch nose radius calorimeter data were not included in the correlation. Figure 19 shows all the available data acquired from the heat flux calibration models. The conclusion that the heat flux decreases linearly to one-fourth the value at the impingement point at an axial distance 3.0 inches aft of the impingement point is valid except for the 2.0 inch calorimeter model results. Three of the data points on this model indicated laminar flow values, and this was confirmed by subsequent analysis. The blunt 2.0-inch radius calorimeter model thus experienced asymmetric heating. This linearly decreasing heat flux was incorporated into all analyses performed after October 15, 1975. Prior to this date the heat flux was reduced to one-fourth the value at the impingement location at a distance 0.50 inch aft. The correlation of NOHARE prediction to the data for the pressure calibration is shown in Figure 20.

SYM	RPL TEST NO.	P_s (ATM)	R_N (IN)	P_c (psig)
O	158	100	0.5	3000
□	157	100	1.0	3000
●	171	100	2.0	3000
■	157	50	1.0	1500
△	168	100	1.0	3000
+	A-50/N_2O_4 178	100	1.0	3000
▽	(VERNIER)	17	0.50	500
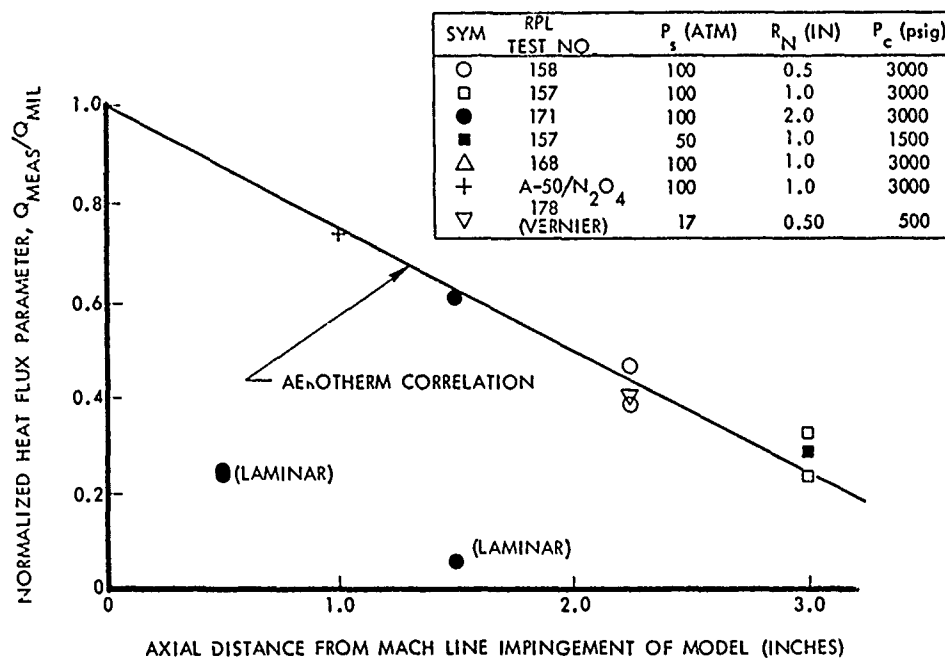
Figure 19. Heat transfer correlation outside model test rhombus.

2.4.2 Graphite Ablation Results

Three 994 graphite ablation models were fabricated and tested by PDA during the Design Verification Test Series of the A.N.T. program (Reference 2). The primary objective of the graphite ablation tests was to calibrate the graphite recession in the BZN/LOX propellant system which previously had not been used at AFRPL. The nature of the A.N.T./ERN nosetip design required accurate characterization of the graphite shell recession to assess the overall removal mechanics of the design. Specifically, burn-through location (desired at the shell stagnation point) and burn-through time were critical parameters in assessing the removal characteristics of the shell and in facilitating pretest planning and analyses.

Two models were planned originally, but a third model was needed when the first sharp model was exposed to an abnormal mixture ratio condition. The graphite recession results are summarized in Table 8. Comparisons of the NOHARE computer code predictions with the measured
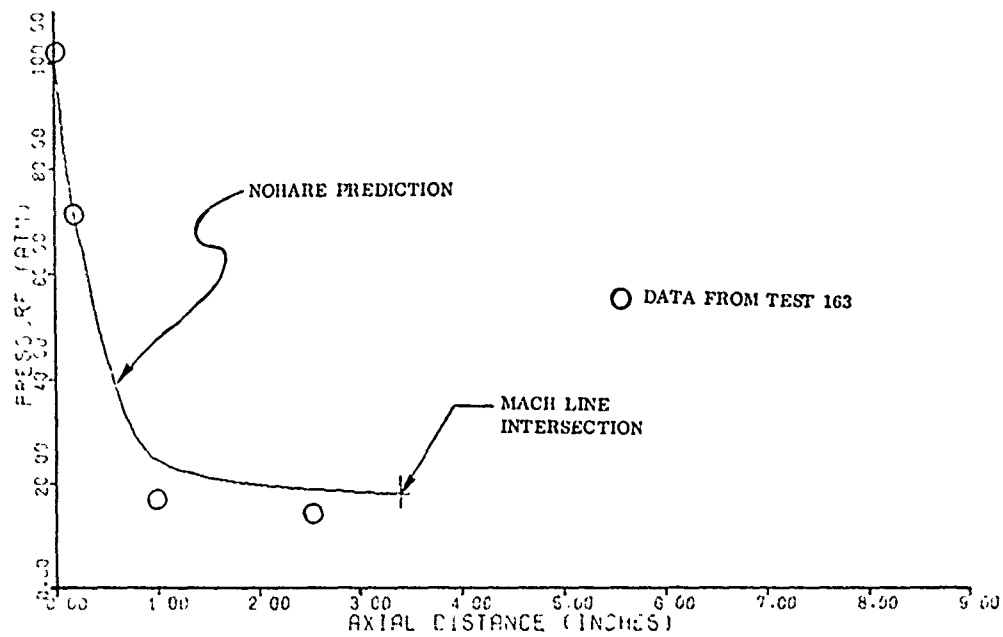
Figure 20. NOHARE/RPL pressure calibration correlation.

Table 8. Summary of graphite ablation calibrations.

TEST NO.	MODEL $\theta_c = 7$ DEG	EXPOSURE TIME (SEC)	$\Delta s_{MEASURED}$ (IN)	$\Delta s_{CALCULATED}$[1] (IN)	$\dfrac{\Delta s_{CALC.} - \Delta s_{MEAS.}}{\Delta s_{MEAS.}}$	REMARKS
160	RPL BLUNT[3] $R_N = 1.60$ (Sphere-Cone)	6.1	0.94	1.00[2]	0.061	RPL ATJ Graphite Model
161	A.N.T. BLUNT (40 Deg Biconic)	3.07	0.48	0.55	0.15	Model Broke Off C_L At 2.0 Sec
164	A.N.T. SHARP (26 Deg Biconic)	2.46	0.46	0.53	0.18	Retest

Notes: 1. Using Heat Flux Calibration Data for 0.5 R_N Model; $\gamma = 1.13$

2. Preliminary Heating Data Used with an Estimated Value for γ of 1.2

3. Model Supplied and Tested by AFRPl

data from the two valid graphite ablation tests are shown in Figures 21 and 22 for the blunt and sharp models, respectively. These predictions incorporated the latest refinements based on the calibration results of Section 2.4.1 and the code refinements incorporated after the blunt A. N. T. 'ERN shell removal test (Section 2.5).
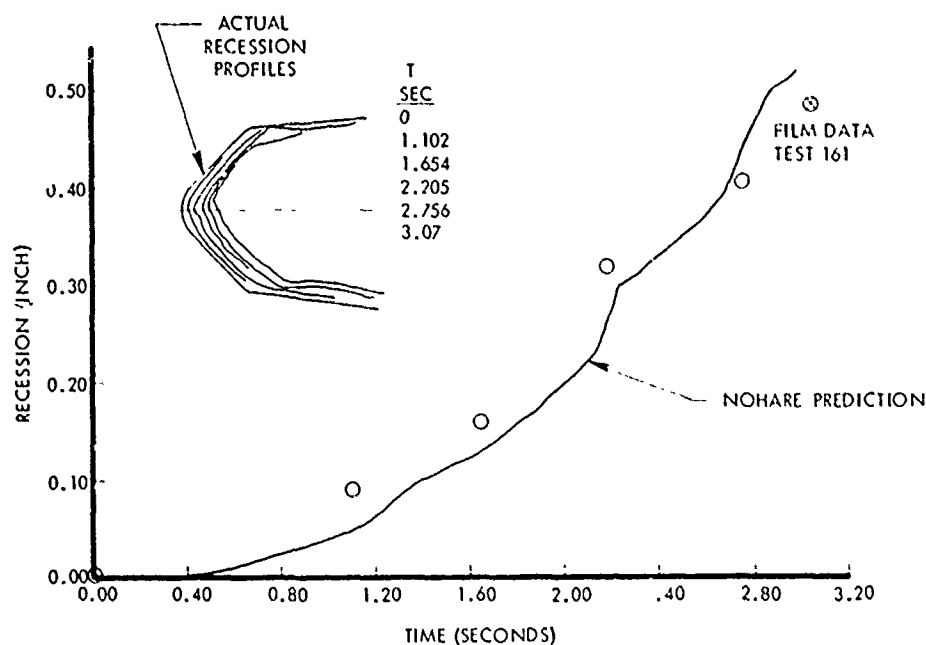
Figure 21. Blunt graphite ablation model correlation.
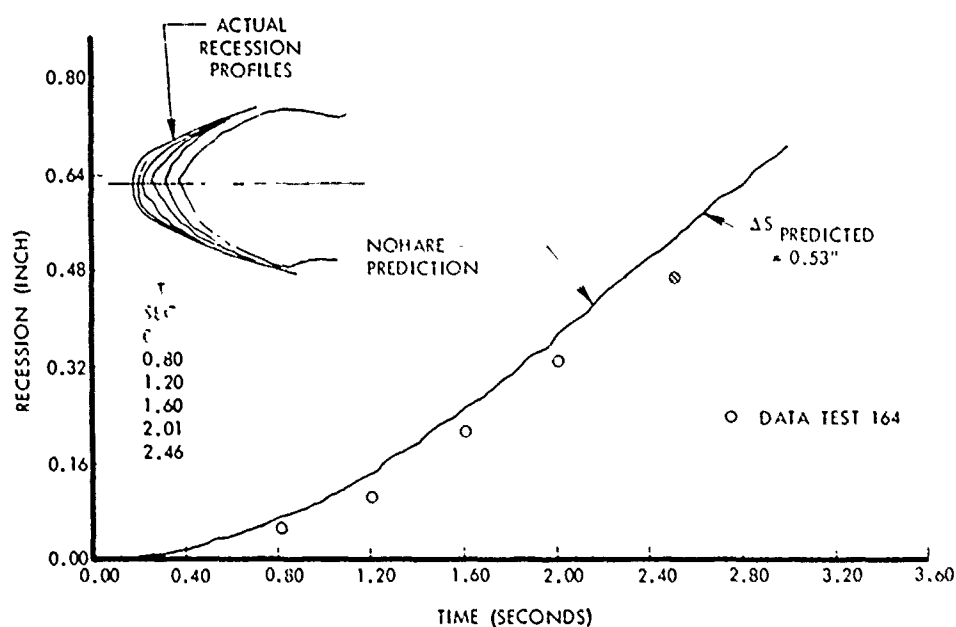
Figure 22. Sharp graphite ablation model correlation.

The NOHARE correlations for both graphite ablation model tests were good. The computer code tended to overpredict the recession by 15 to 18 percent (see Table 8), which was conservative. Pre-test and post-test photographs of the sharp and blunt models are shown in Figures 23 through 25. The blunt model showed an area of apparently higher recession on the 270 degrees side of the model (visible on the left side of the 0-degree view). This anomaly was attributed to a thermo structural failure of the graphite from improper support (Reference 13). The failure precipitated a loss of material that accounted for the asymmetric shape. This support problem was corrected for the second sharp model. Except for this problem, the ablated profiles showed good agreement with theory.
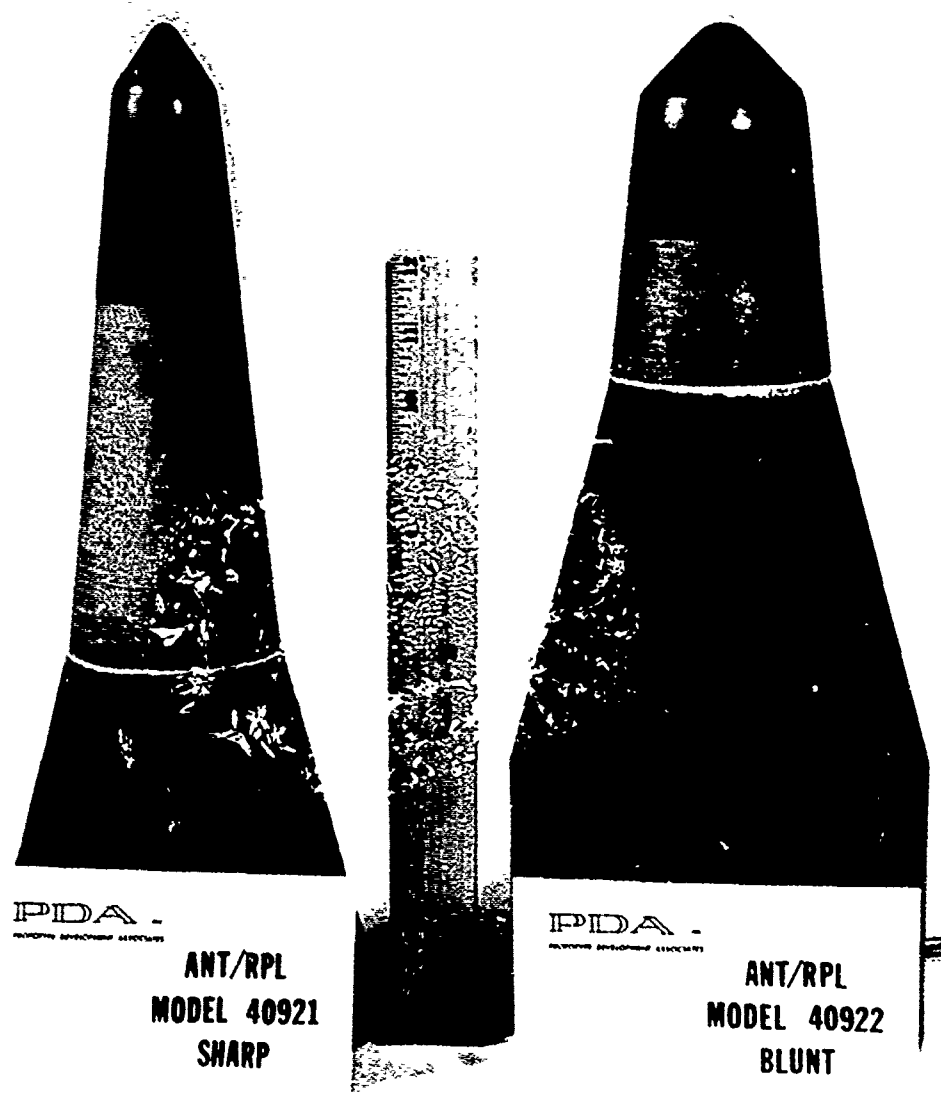
Figure 23. Pre-test photographs of sharp and blunt graphite ablation models.
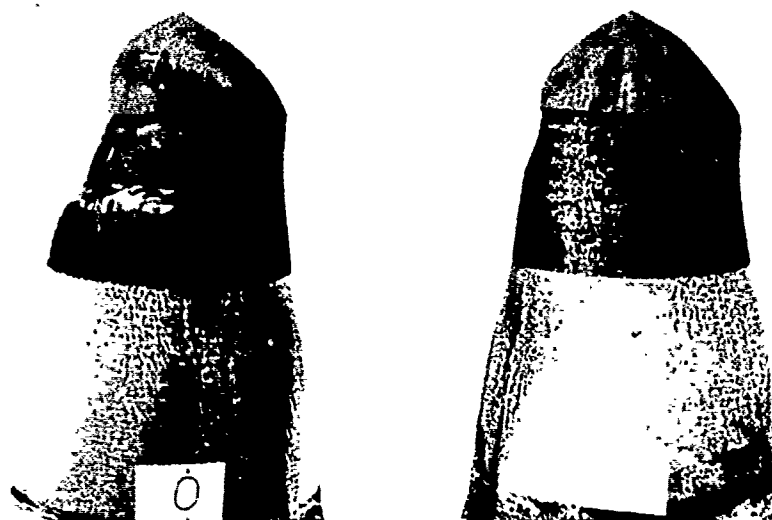
Figure 24. Post-test photographs of blunt graphite ablation model.
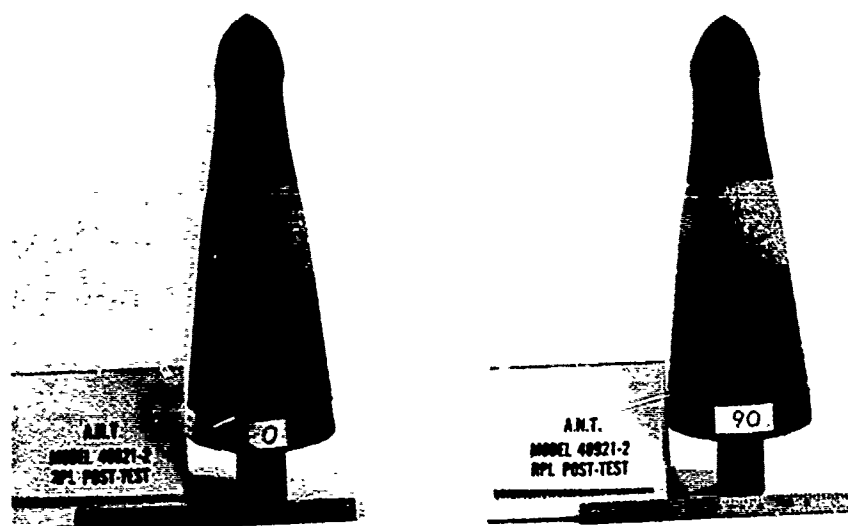
Figure 25. Post-test photographs of sharp graphite ablation model.

The second sharp model test produced an excellent axisymmetric specimen with a stable equilibrium profile and excellent agreement with predicted recession rates and profiles. The test confirmed recession rates and probable equilibrium shapes, which enabled final contouring of the shell removal model internal and external shape and thickness configurations.

2.5 RESULTS OF MODEL TESTS

Two graphite shell removal tests and two tungsten subtip thermostructural tests were completed during the Final Design Verification Test Series from July through November 1975. Table 9 summarizes the principal test results, including shell or glove removal time, subtip exposure time, and total recession. Table 10 gives the times of each major event and the respective chamber pressure at that time. All times were taken from the high speed digital data or measured from analysis of the high speed films. The chamber pressure profiles for each test are shown in Figures 26 through 29. The events summarized in Tables 9 and 10 are also shown on these figures. From the pressure calibration data and the theoretical calculations, the steady-state values of stagnation pressure actually were 103 and 53 atmospheres for the "100" atmosphere and the "50" atmosphere nozzles, respectively, at a steady-state chamber pressure of 3000 psig.

Table 9. A.N.T./RPL design verification test summary.

PDA MODEL NUMBER	BT-3	BD-4	BK-4	BM-4
MODEL DESCRIPTION	BLUNT SUBTIP	FULL-SCALE (PRESHAVED) BLUNT ANT/ERN NOSETIP	FULL-SCALE (PRESHAVED) SHARP ANT/ERN NOSETIP	SHARP SUBTIP
RPL TEST NO.	165	169	186	189
TEST DATE	7-2-75	7-17-75	10-21-75	11-14-75
STEADY STATE STAGNATION PRESSURE (ATM)	103	90	103	53
TOTAL TIME IN JET (SEC)	4.49	6.37	8.46	9.78
TIME OF SHELL OR GLOVE REMOVAL (SEC)	0.66	0.99	3.85	2.24
TOTAL TIME OF TUNGSTEN EXPOSURE (SEC)	3.83	5.39	4.61	7.54
TOTAL TUNGSTEN RECESSION (IN)	1.00	1.34	2.0	1.80

* TEFLON GLOVE INSTALLED ON SUBTIP UNITS BT-3 AND BM-4
** 50 ATMOSPHERE NOZZLE

Table 10. A.N.T./RPL design verification test events. *

RPL TEST NUMBER PDA MODEL NUMBER	165 BT-3	169 BD-4	186 BK-4	189 BM-4
Model Enters Jet (Sec) Chamber Pressure (PSIG)	12.87 1566	7.536 486	6.485 465	6.722 540
Model on C_L (Sec) Chamber Pressure (PSIG)	13.00 1680	7.942 501	6.800 596	6.875 575
Shell or Glove Removed (Sec) Chamber Pressure (PSIG)	13.53 2750	8.528 1491	10.333 2021	9.01 2850
Subtip Moves Forward (Sec) Chamber Pressure (PSIG)	Model in position at insertion	2590	2750	2974
Subtip in Forward Position (Sec) Chamber Pressure (PSIG)		10.757 2570	11.324 2796	10.883 2994
Subtip Fragmentation Time (Sec) Chamber Pressure (PSIG)	None	13.37 2595	13.55-13.63 2998	15.42-16.03 2959-2951
Subtip Moves Back (Sec) Chamber Pressure (PSIG)	17.28 2792	13.320 2600	14.246 2997	16.413 2959
Subtip Leaves Jet (Sec) Chamber Pressure (PSIG)	17.36 242	13.906 436	14.945 258	17.086 350

*Time in Seconds from Facility Fire Signal
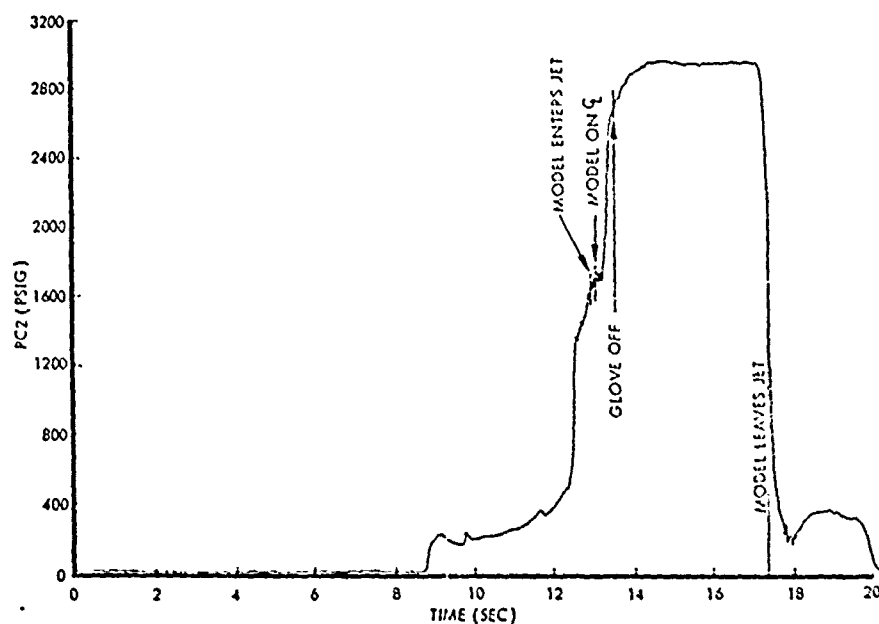
Figure 26. Chamber pressure history — RPL Test 165 (blunt subtip).
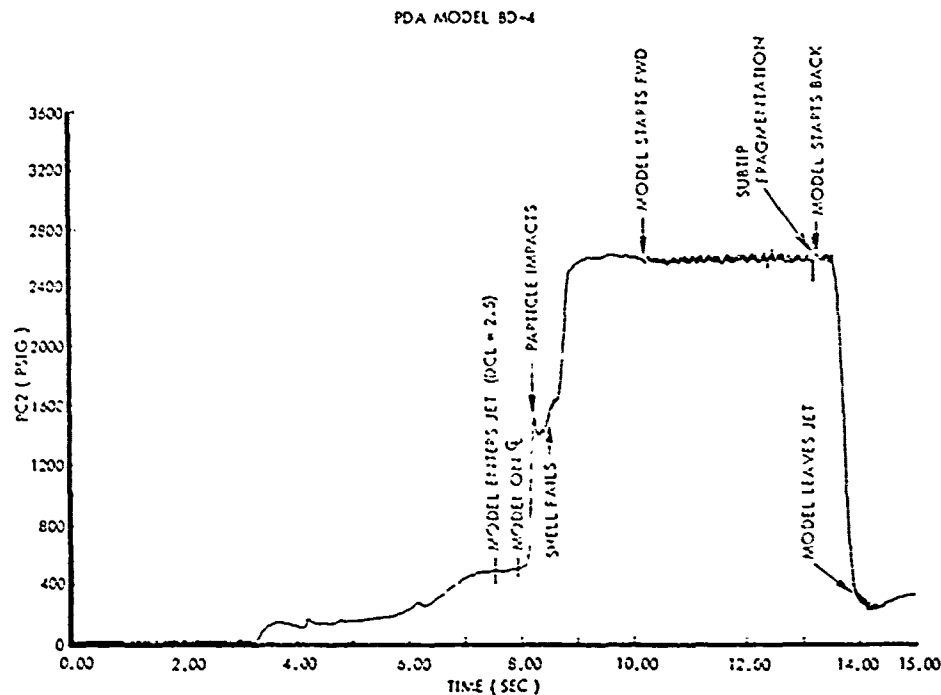
Figure 27. Chamber pressure history — RPL Test 169 (blunt removal test).
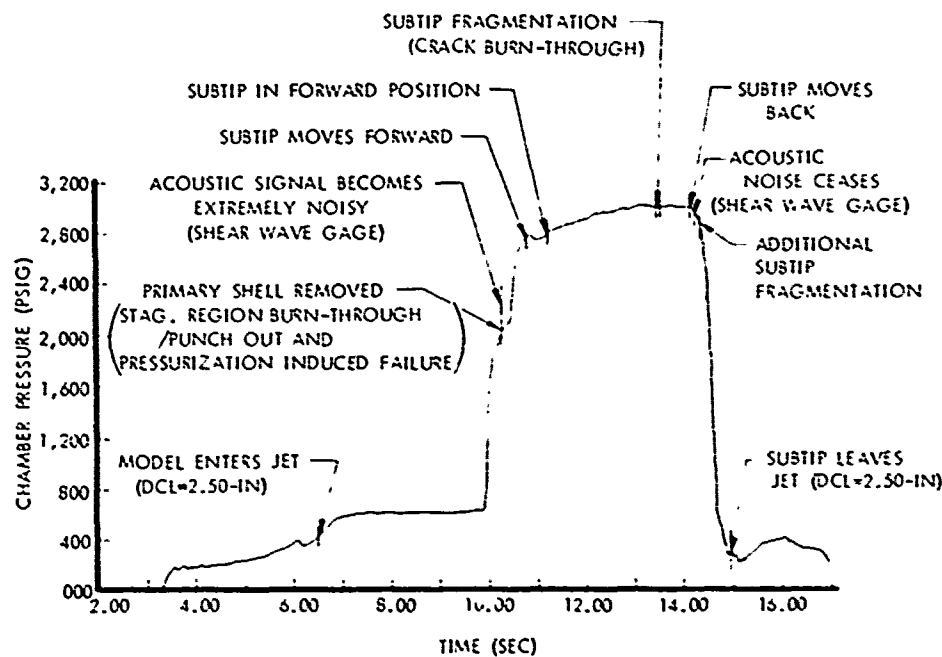
Figure 28. Chamber pressure history — RPL Test 186 (sharp removal test).
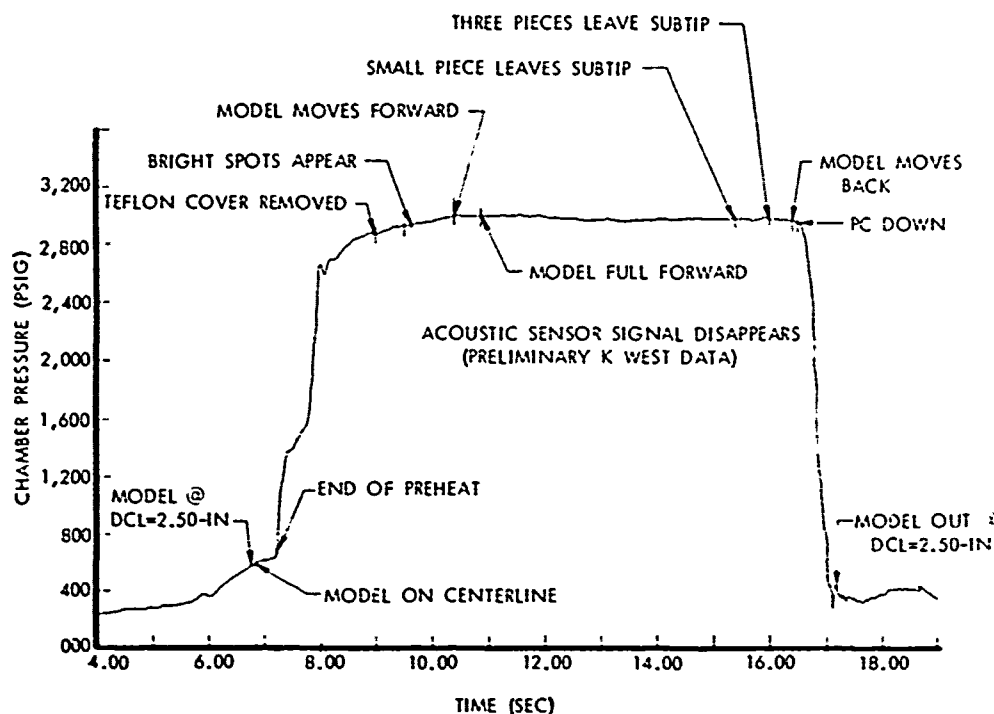
Figure 29. Chamber pressure history — RPL Test 189 (sharp subtip test).

2.5.1 Test 165, Model BT-3, Blunt Subtip

This blunt thermostructural subtip model was tested without the molybdenum overlay and without the forward heatshield skirt. A teflon cover was used to delay exposure of the model until steady-state motor conditions were achieved. Figure 30 shows the pre-test photograph of the model. The model entered the exhaust jet 12.87 seconds after fire signal. The teflon glove was removed 0.66 second later at 13.53 seconds from fire signal. A review of the test films indicated melting over the spherical portion of the model with rivulets of molten tungsten flowing off the nosecap along the sidewall and onto the heatshield. Roughened, longitudinal groove-like patterns were formed on the sidewall, possibly formed from vortex shedding of flow from the rivulets of molten tungsten at the model shoulder or, alternatively, from the flow of molten tungsten over the softened tungsten. Additionally, crosshatching was evident over the sidewall areas with regions of fully developed scallop patterns. No fragmentation or loss of tungsten was observed during the test, although the model was found to be cracked upon post-test inspection. Later analysis, discussed in Section 2.6.2, substantiated that internal cracking probably occurred during the test. The test model showed an appearance of asymmetric flow in both the stagnation region and the sidewall. The 0- to 90-degree region (looking into the nozzle) of the subtip indicated a region of high heating, possibly the boundary layer transition location aft of the tangent point. The stagnation region assumed a blunter profile for this region. The other rays tended to show a high probability of transition on the shoulder or sonic region because of the sharper equilibrium profile. These rays did not show a pronounced increase in heating and recession on the sidewall.

Cracks were visible upon post-test inspection on the RPL sting. The cracks appeared much as indicated in the photographs in Figure 31. Note the segmented nature of the cracks. The shear wave acoustic sensor failed to function and no recession data were acquired.

46
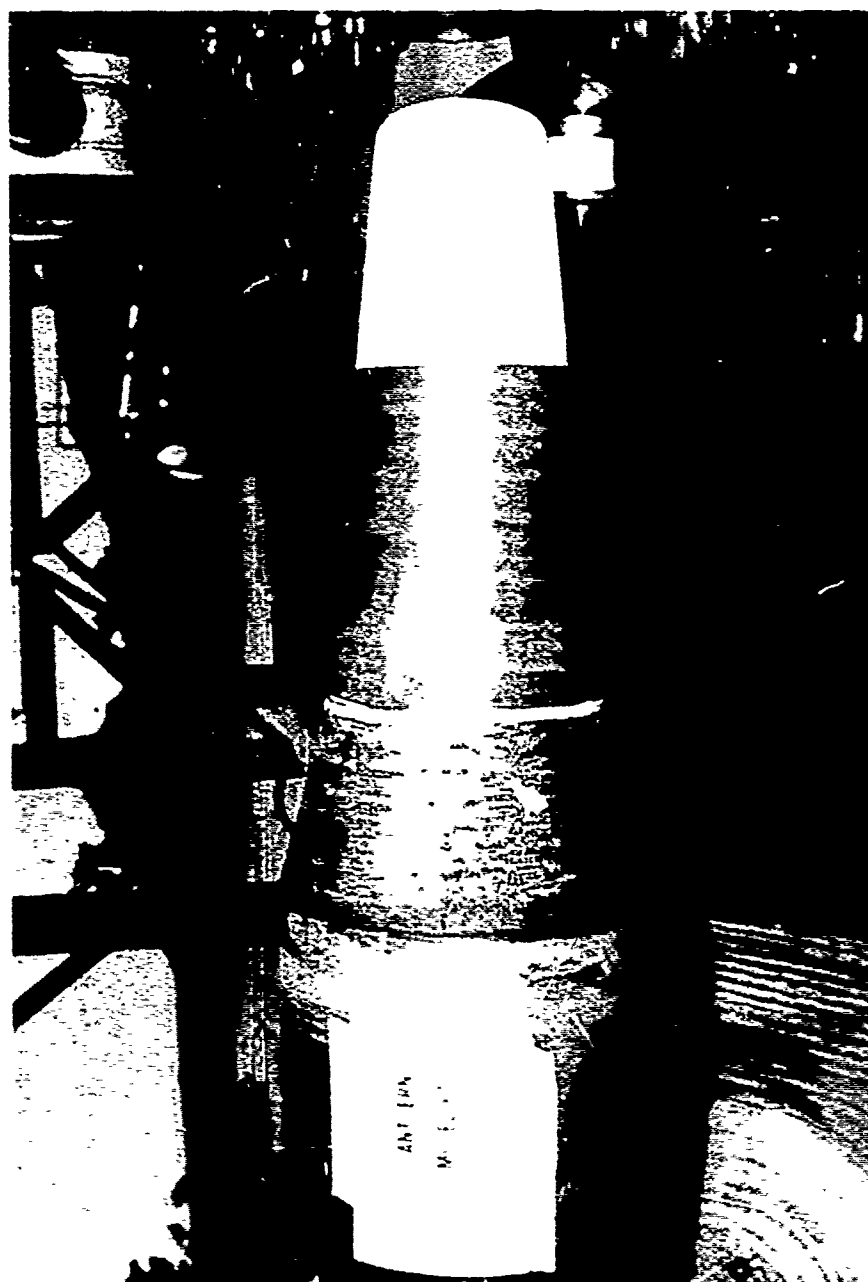
Figure 30. Pre-test photograph of blunt subtip model BT-3.
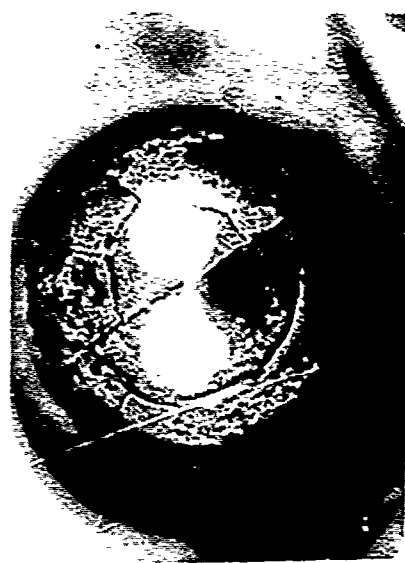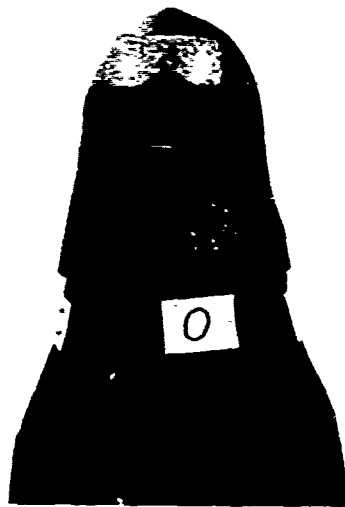
Figure 31. Post-test photographs of blunt subtip model BT-3.

2.5.2   Test 169, Model BD-4, Blunt A.N.T./ERN Tip

The blunt shell removal model was tested with the full-scale shell configuration, forward skirt, and overlay components intact. The shell differed from the flight design only in that the shell was preshaved to a biconic shape to reduce the thickness in the sonic region and thereby lower the probability of thermostructural failure. Figure 32 shows a pre-test photograph of this blunt shell removal model.
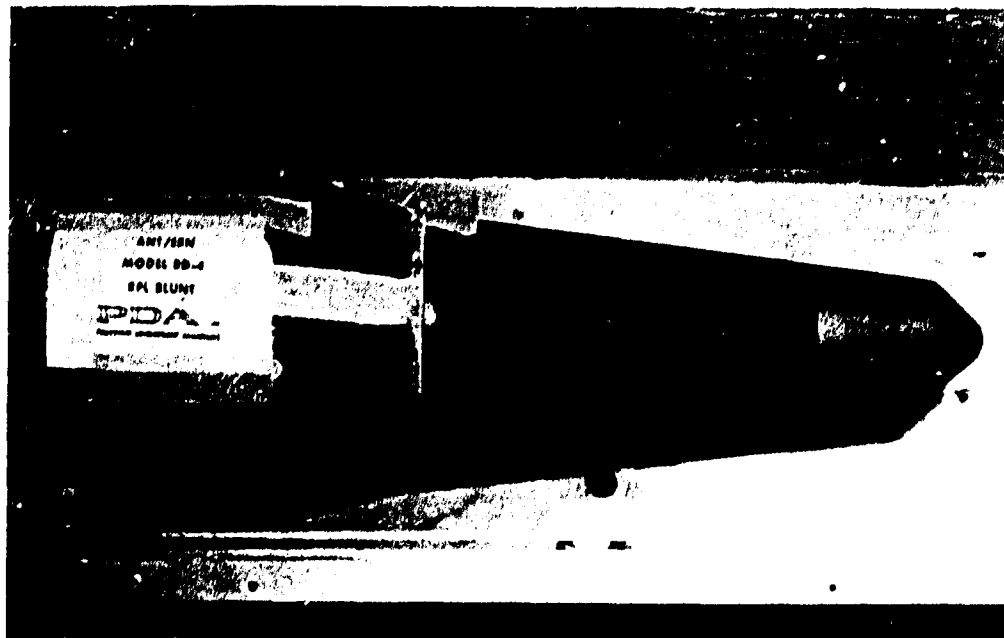
Figure 32.   Pre-test photograph of blunt shell removal model BD-4.

The primary nosetip entered the exhaust at 7.536 seconds after the fire signal. At 8.23 to 8.25 seconds, high speed motion picture coverage indicated particle impacts on the shell. The shell was observed to crack at 8.523 seconds. Pyrometer and thermocouple data indicated the shell was completely removed by 8.528 seconds. The subtip moved forward at 10.272 seconds and was determined to be full-forward at 10.757 seconds. The model started back at 13.320 seconds and rotated out of the exhaust at 13.906 seconds. Review of the motion pictures indicated tungsten subtip failure approximately 0.25 second before shutdown, or 13.37 seconds. The best evidence of this appeared on the facility cameras which captured the trajectory of three segments that were ejected from the model. The loss of subtip material was from the third quadrant; i.e., from 180 to 270 degrees (looking into the nozzle). The photographs in Figure 33 clearly show the extent and location of the loss.

The post-test photographs of this model (Figure 33) show a different picture of the tungsten from the first thermostructural test (Figure 31). The segmented fracturing is similar to the first test; however, the nature or character of the melt layer, sidewall roughness, and crosshatch pattern formation is modified, being less pronounced in this test.

A significant occurrence observed in the film coverage was the appearance of a shock induced within the nozzle, resulting in a standing shock impingement on the spherical portion of the model during the preheat transient. Further discussion of this shock formation is presented in Section 2.6.1.

Figure 33. Post-test photographs of blunt shell removal model BD-4.

2.5.3.   Test 186, Model BK-4, Sharp A.N.T./ERN Tip

The sharp A.N.T./ERN shell removal model, designated BK-4, was identical in configuration and components to the sharp flight model with the exception of a pre-shaved biconic shape for the shell to lower the probability of thermostructural failure. A pre-shaved thickness of 0.30 inch at the stagnation point was selected to ensure burn-through at the stagnation point. Figure 34 shows a pre-test view of Model BK-4. Table 11 is an event summary of Test 186.

The model entered the exhaust at 6.485 seconds after the facility fire signal. The model was in the preheat condition until 9.933 seconds. Motion picture coverage indicated particles impinging on the model during this preheat phase, causing some material loss on the shell. The extent of surface damage or material loss was not completely discernible, although bright spots were evident where impingement losses occurred. One area on the 0-degree meridian near the stagnation point showed an indentation in profile on two cameras. Later frames seemed to indicate that burn-through occurred in this general area. The evidence of burn-through or "punch-out" of the shell near the stagnation point was captured on film at 10.333 seconds and is shown in the photographic sequence shown in Figure 35, taken from individual movie frames. After punch-out occurred, the flow entered the interior of the shell at near-stagnation pressure. The unequal force that was immediately generated tended to thrust the shell forward as seen in Frame Number 2. The forward thrust was arrested as flow proceeded out the increasing annular area created at the aft bond area of the shell and, concurrently, the shell failed as anticipated from the internal pressurization. The shell shattered explosively and the small pieces were carried clear of the afterbody by the exhaust flow. The ATJ-S cruciform section and bearing cap were seen to rotate clear in the fifth frame. The final frame showed the exposed tungsten subtip with its attendant bow shock. This entire sequence was accomplished in 0.005 second. The stagnation pressure at the time of burn-through was approximately 69 ± 1 atmospheres, which was lower than the 90 atmospheres predicted in pre-test calculations. The lower pressure was the result of the earlier burn-through time, which may have been precipitated by the early particle impingement and material loss in the stagnation region.

Figure 34. Pre-test photograph of sharp shell removal model BK-4.

Table 11. Event summary of RPL/A.N.T. Test 186, sharp 994, model BK-4.

EVENT	TIME (REFERENCED TO FIRE SIGNAL)		MEASURED CHAMBER PRESSURE (PSIG)	REMARKS
	PLANNED (SEC)	ACTUAL* (SEC)	PC AVERAGE	
Model Enters Jet (DCL = 2.50 In)	6.5	6.4+5	465.	
Model on C_L	6.8	6.400	506.	
End of Preheat	9.5	9.503	667.	
Shell Removal	10.6**	10.333	2021.	P_s = 69 ± 1 atm***
				Note: Pyro #1, 2, 5, 6 Indicate Removal at 10.333 Sec. T/C A1 and B2 Indicate Removal at 10.336 Sec. Data from K West
Acoustic Sensor Signal Disappears Due to Noise		10.35	2062.	
Schtlp Moves Forward	10.8	10.452	2759.	
Schtlp at Forward Position	11.3	11.334	2786.	
Schtlp Fragmentation ("Crack Burn-through")	---	13.55-13.63	2894.	Film Data: S = 1.1 ± .1 In Measured Fragment
T/C #B5 Burnout		13.64-13.65	2944.	S = 1.04 "
Schtlp Moves Back	14.2	14.296	2997.	T/C's on 200 Deg Ray 'correlates
Chamber Pressure Starts Down	14.2	14.392	2917.	Fragmentation
Additional Schtlp Fragmentation	---	14.435	2462.	Film Data
Schtlp Leaves Jet (DCL = 2.50 In)	14.7	14.945	254.	

* Digital Timing Data Unless Otherwise Specified
** Changed from 10.6 Sec due to Change in Preheat Insertion Time
*** Assumes P_c = 3000 psig at P_s = 103 atm

51

3. ×47 SEC   3. ×46 SEC   3. ×45 SEC

3. ×50 SEC   3. ×49 SEC   3. ×48 SEC

*Time from primary tip insertion into exhaust

Figure 35. Primary tip removal sequence — Test 156.

Figure 34.   Pre-test photograph of sharp shell removal model BK-4.

Table 11.   Event summary of RPL/A.N.T. Test 186, sharp 994, model BK-4.

EVENT	TIME (REFERENCED TO FIRE SIGNAL)		MEASURED CHAMBER PRESSURE (PSIG)	REMARKS
	PLANNED (SEC)	ACTUAL.* (SEC)	PC AVERAGE	
Model Enters Jet (DCL = 2.50 In)	6.5	6.485	165.	
Model on C	6.8	6.800	596.	
End of Preheat	9.8	9.933	667.	
Shell Removal	10.8**	10.333	2021.	P_s = 69 ± 1 atm***
				Note: Pyro #1, 2, 5, 6 Indicate Removal at 10.333 Sec. T/C A1 and B2 Indicate Removal at 10.339 Sec.
Acoustic Sensor Signal Disappears Due to Noise		10.36	2062.	Data from K West
Subtip Moves Forward	10.8	10.852	2750.	
Subtip at Forward Position	11.3	11.324	2796.	
Subtip Fragmentation ("Crack Burn-through")	---	13.55-13.63	2998.	Film Data S = 1.1 ± .1 In Measured Fragment
T C #B5 Burnout		13.64-13.65	2988.	S = 1.04 In
Subtip Moves Back	14.2	14.296	2997.	T/C's on 300 Deg Ray Correlates
Chamber Pressure Starts Down	14.2	14.392	2917.	Fragmentation
Additional Subtip Fragmentation	---	14.135	2862.	Film Data
Subtip Leaves Jet (DCL = 2.50 In)	11.7	14.915	258.	

*   Digital Timing Data Unless Otherwise Specified

**   Changed from 10.6 Sec due to Change in Preheat Insertion Time

***   Assumes P_c 3000 psig at P_s = 103 atm

The subtip was moved forward 10.852 seconds after the fire signal. From film coverage, subtip fragmentation was seen to occur 13.55 to 13.63 seconds after fire signal, and this was substantiated by thermocouple data. Figure 36 shows tungsten fragment losses taken from the motion film frames. Additional fragmentation occurred during the shutdown phase as the subtip was being rotated from the exhaust. The acoustic sensor signal disappeared at 10.36 seconds, immediately after the shell removal, and no data were acquired during subtip recession and failure. Post-test views of the model are shown in Figure 37.
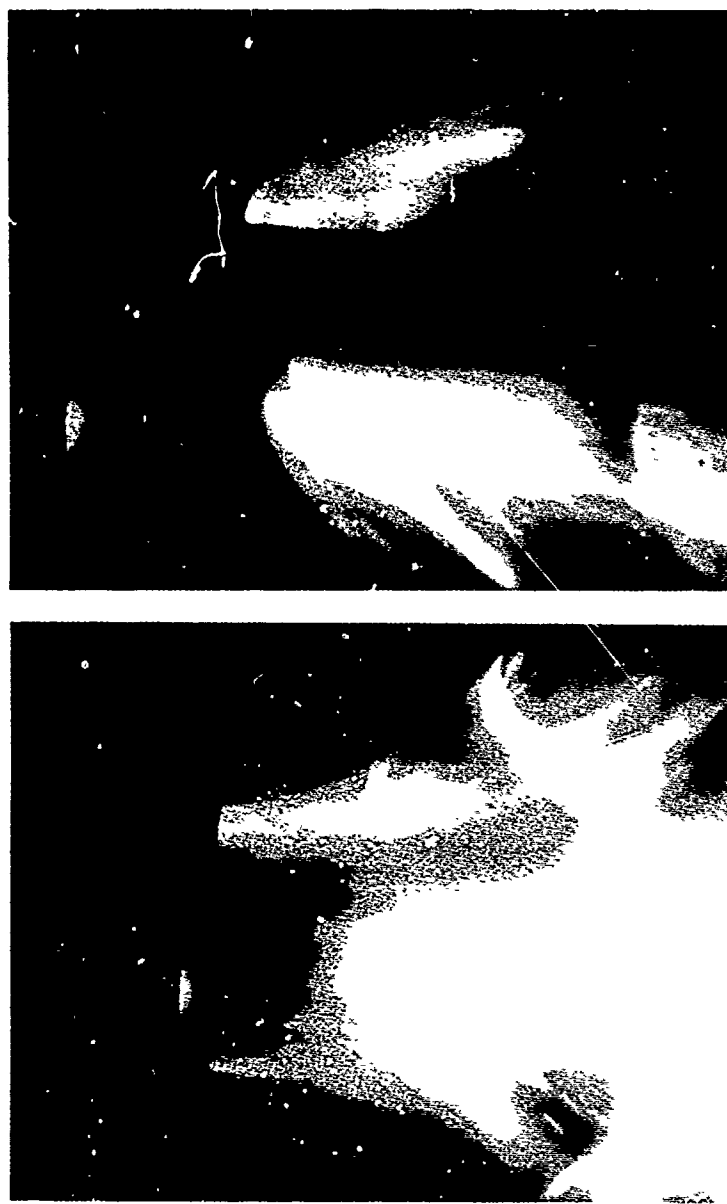
Figure 36. Tungsten subtip fragmentation during Test 186.
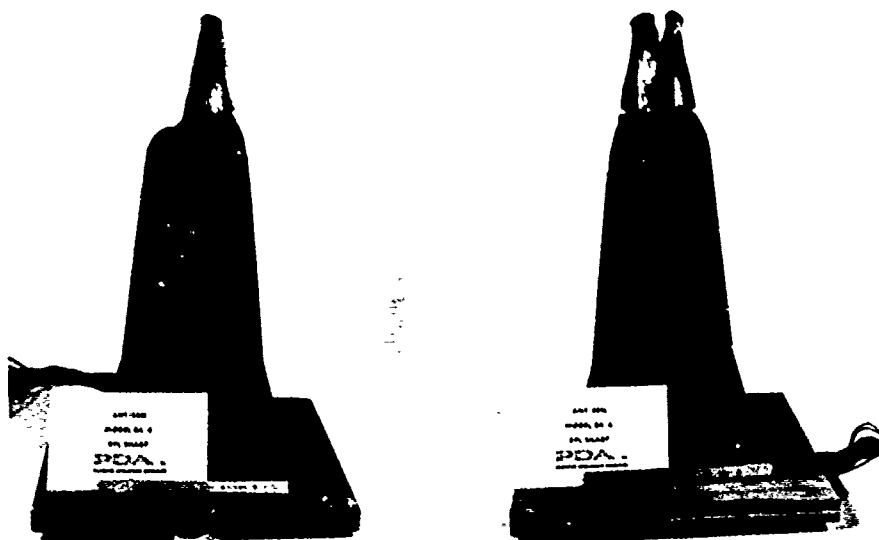
Figure 37. Post-test photographs of sharp model BK-4.

2.5.4   Test 189, Model BM-4, Sharp Subtip

The sharp tungsten subtip was tested using the RPL 50-atmosphere nozzle (all other tests were performed with the 100-atmosphere nozzle). Calculations of the subtip response at the 50-atmosphere condition predicted approximately the same probability of crack initiation as in the clear air flight; hence, the decision was made to test at the less severe condition. It was to be understood that the probability of crack burn-through was significantly higher in the ground test than in the clear air flight. The primary difference in the crack burn-through probabilities was the result of the preheat on the flight subtip ensuring a ductile-brittle transition temperature (DBTT) location penetration into the material, whereas the RPL thermostructural tests produce a nearly instantaneous heat-up of a cold tip and, hence, have a much reduced penetration of the DBTT location. A complete discussion of the analysis is given in Section 2.6.2. A pre-test photograph of Model BM-4 is shown in Figure 38. Table 12 summarizes the events of Test 189.

The model entered the exhaust at 6.722 seconds after the facility fire signal. The teflon glove was removed at 9.01 seconds. The film data showed the appearance of bright spots on the sidewall at an axial location of 2 to 2.5 inches from the stagnation point at 9.63 seconds. The spots were distributed circumferentially over 360 degrees at this general location. Fractures appeared soon afterward on the sidewall. The subtip was moved forward and in position at 10.883 seconds. Small pieces were observed to leave the shoulder area at 15.42 seconds and additional pieces, further aft, were removed at 16.03 seconds. The subtip was moved aft at 16.413 seconds and rotated out of the exhaust at 17.086 seconds. Post-test views of the tungsten subtip are shown in Figure 39.
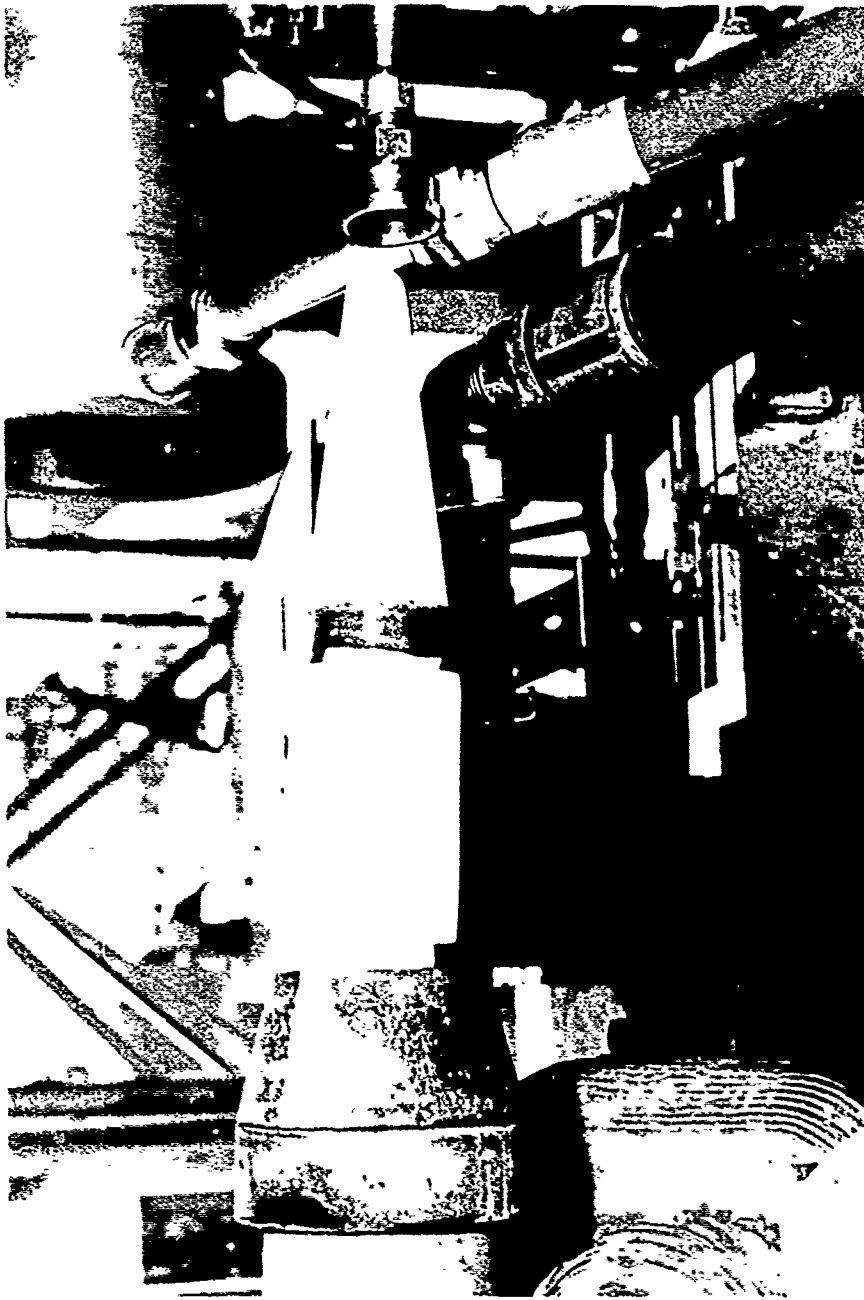
Figure 3-. Pre-test view of sharp subtip model BM-4.

Table 12. Event summary of RPL/A.N.T. Test 189, sharp subtip, model BM-4.

EVENT	TIME (REFERENCED TO FIRE SIGNAL)		MEASURED CHAMBER PRESSURE (PSIG)	REMARKS
	PLANNED (SEC)	ACTUAL (a) (SEC)	$PC_{AVERAGE}$	
Model Enters Jet (DCL = 4.7 In)	6.7 (Ref)	6.722	540	
Model on C_L	6.8	6.875	575	
End of Preheat	7.2	7.20	637	
TFE Glove Removal (T_1)	9.7 - 11.7	9.01 (b)	2850	P_s = 50.4 atm (c)
Acoustic Sensor Signal Disappears		9.5 ± 0.1	2910	Preliminary Data From K West
Bright Spots Appear		9.63 (b)	2921	
Subtip Moves Forward (T_2)	11.7 (d)	10.402	2974	
Subtip at Forward Position	T_2 + 0.5	10.883	2994	
Small Piece Leaves Subtip Shoulder		15.42 (b)	2959	Film Data
Three More Pieces Leave		16.03 (b)	2951	Film Data
Subtip Moves Back	T_2 + 5.5	16.413	2959	
Chamber Pressure Starts Down	T_2 + 6.0	16.500	2950	
Subtip Leaves Jet (DCL = 4.7 In)	T_2 + 6.0	17.086		

Notes: (a) Digital Timing Data Unless Other Specified
(b) Film Data
(c) Assumes P_c - 3000 psig at P_s = 53 atm
(d) Manual Override to be Used if Glove Removed Early

56

Figure 39. Post-test photographs of sharp subtip model BM-4.

2.6   DISCUSSION OF RESULTS

        This section discusses the results of the verification test series as a whole. Rather than discuss the results of each test separately, the results, as they affect each A.N.T./ERN component, are addressed as follows:

- Primary Nosetip Performance
- Subtip Performance
- Heatshield Performance
- Instrumentation Performance

2.6.1   Primary Tip Removal Performance

        One objective of the design verification tests was to evaluate the removal characteristics of the blunt and sharp 994-2 graphite shells in a thermostructural environment approximating flight severity. The sharp and blunt nosetip shells were critical components in the flight test nosetips designed to provide recession data for the monolithic tungsten subtips beginning at a specified altitude (35 ± 5 kft) at which weather may be encountered by an operational vehicle. For the flight test program, the desired operational sequence leading to subtip exposure was as follows: 1) ablation burn-through near the stagnation point at 35 ± 5 kft, followed by 2) internal pressurization, and 3) shell fragmentation and positive separation and expulsion from the vehicle. The primary nosetip configuration is illustrated in Figure 9.

        Initial pre-test thermostructural analyses were performed for exposure of the flight-design graphite shells in the ABRES/AFRPL rocket motor facility with the BZN/LOX propellant system. The results of these analyses indicated a probable thermostructural failure before burn-through due to the sudden exposure to the extremely high heating rates in this facility. To increase the thermostructural margins-of-safety, both sharp and blunt nosetip shells were modified by removing material on the spherical nosetip to reduce the wall thickness in the sonic region. The

resultant biconic shapes were found to have thermostructural margins-of-safety similar to, but lower than, those predicted for clear air flight. The purpose of the following discussion is to compare the results of the thermostructural analyses with the observed response of these shells and to assess the performance capability of the flight designs.

2.6.1.1 Method of Analysis

All thermostructural analyses were performed with the finite element SAAS III code (Reference 14). These analyses accounted for: 1) temperature-dependent material properties; 2) time-dependent shapes, pressure loads, and internal temperatures; and 3) differences in tension/compression properties. The graphite material properties used in the pre-test thermostructural analyses were the same as those used in the detailed design studies (Reference 2), with the exception of slightly higher free thermal strains. The properties, shown in Table 13, were the best properties data available at the start of the design verification test program.

In modeling the reaction forces of the split internal structure against the nosetip surface, it was assumed that the epoxy adhesive at the aft end of the nosetip would pyrolyze fully during the rocket motor pre-heat phase to leave a free-standing shell. Pressures of the form $P_o\sin\theta$ were applied on the forward interior shell surface; where θ is the local slope of the shell boundary measured from the horizontal axis, and P_o is a constant. At each rocket motor exposure time, P_o was chosen so that reaction forces of the internal support structure balanced the total nosetip airload in the axial direction.

Nosetip margins-of-safety were based on 95/95 strain allowables for truncated 994-2 graphite. These allowable across-grain and with-grain strains are shown as functions of temperature in Figures 40 and 41 (Reference 15). A biaxial failure strain criterion developed successfully in the LORN program (Reference 16) was used to calculate margins-of-safety according to:

$$MS = \left(\frac{1}{\sqrt{\left(\frac{\epsilon_{max}}{A}\right)^2 + \left(\frac{\epsilon_{WG}}{B}\right)^2}} - 1 \right) 100 \tag{1}$$

ϵ_{max} = maximum principal strain in RZ plane

A = 95/95 allowable strain in maximum principal strain direction

ϵ_{WG} = with-grain strain

B = 95/95 allowable strain in with-grain direction

It should be noted that the above formula accounted both for the maximum principal RZ strain predicted on a nosetip shell and for the allowable strain in that direction.

All pre-test analyses were made using the methodology described above. For the blunt-design shell, a minimum thermostructural margin-of-safety of +18 percent prior to burn-through was predicted when the nosetip is inserted into the test stream 0.5 second before the end of the

Table 13. Mechanical properties of 994-2 graphite.

MATERIAL NUMBER 1   MCIVER GRAPHITE TENSION PROPERTIES   MARCH 10 1975   DENSITY = .0615 LB/CU INCH

TEMP-DEG F	EN-PSI	ES-PSI	ET-PSI	GNS-PSI	NU-MS	NU-NT	NU-ST	THETA-N	THETA-S	THETA-T
70.0000	1.5000+06	1.0000+06	1.5000+06	5.5000+05	.1310	.1190	.0900	0.00000	0.00000	0.00000
500.0000	1.5100+06	1.0000+06	1.5100+06	5.9000+05	.1350	.1150	.0930	6.0000-04	8.5000-04	6.0000-04
1000.0000	1.5200+06	1.0000+06	1.5200+06	5.7000+05	.1410	.1200	.0970	1.5000-03	2.3500-03	1.5000-03
1500.0000	1.5600+06	1.0000+06	1.5600+06	6.0000+05	.1460	.1250	.1020	2.4500-03	3.4500-03	2.4500-03
2000.0000	1.6100+06	1.0400+06	1.6100+06	6.5000+05	.1510	.1300	.1070	3.6000-03	4.9000-03	3.6000-03
2500.0000	1.6500+06	1.0900+06	1.6900+06	7.0000+05	.1570	.1350	.1120	4.8500-03	6.8500-03	4.6500-03
3000.0000	1.7800+06	1.1800+06	1.7800+06	7.5000+05	.1590	.1400	.1160	6.2000-03	8.3500-03	6.2000-03
3500.0000	1.0500+06	1.2600+06	1.4500+06	7.5000+05	.1580	.1450	.1210	7.6500-03	1.0200-02	7.6500-03
4000.0000	1.5500+06	1.0500+06	1.5500+06	7.4000+05	.1710	.1500	.1250	9.1000-03	1.2100-02	9.1000-03
4500.0000	1.0100+06	1.0200+06	1.1000+06	5.5000+05	.1930	.1630	.1430	1.0700-02	1.4100-02	1.0700-02
5000.0000	7.7000+05	7.8000+05	7.7000+05	4.0000+05	.1960	.1770	.1620	1.2300-02	1.6200-02	1.2300-02
5500.0000	5.1000+05	5.7000+05	5.1000+05	2.5000+05	.2000	.1900	.1860	1.4000-02	1.8000-02	1.5000-02
6000.0000	3.2000+05	3.0000+05	3.2000+05	1.0000+05	.2000	.1940	.1870	1.5700-02	2.0700-02	1.5700-02
6500.0000	2.5000+05	2.5000+05	2.5000+05	1.0000+04	.2000	.1970	.1930	1.7400-02	2.3200-02	1.7400-02
7000.0000	2.5500+05	2.5000+05	2.5000+05	3.0000+04	.2000	.2000	.2000	2.0100-02	2.5400-02	2.0100-02

MATERIAL NUMBER 2   MCIVER GRAPHITE COMPRESSION PROPERTIES   MARCH 10 1975   DENSITY = .0615 LB/CU INCH

TEMP-DEG F	EN-PSI	ES-PSI	ET-PSI	GNS-PSI	NU-MS	NU-NT	NU-ST	THETA-N	THETA-S	THETA-T
70.0000	1.5200+06	9.6000+05	1.5200+06	5.5000+05	.0670	.0650	.0650	0.00000	0.00000	0.00000
500.0000	1.5300+06	9.7000+05	1.5300+06	5.9000+05	.0950	.0740	.0590	6.0000-04	8.5000-04	6.0000-04
1000.0000	1.5600+06	1.0000+06	1.5600+06	5.7000+05	.1010	.0740	.0740	1.5000-03	2.3500-03	1.5000-03
1500.0000	1.5600+06	1.0000+06	1.5300+06	6.0000+05	.1050	.0780	.0780	2.4500-03	3.4500-03	2.4500-03
2000.0000	1.6200+06	1.0700+06	1.6200+06	6.5000+05	.1130	.0420	.0420	3.6000-03	4.9000-03	3.6000-03
2500.0000	1.6800+06	1.1500+06	1.6800+06	7.0000+05	.1160	.0460	.0860	4.8500-03	6.8500-03	4.8500-03
3000.0000	1.7200+06	1.2100+06	1.7200+06	7.5000+05	.1250	.0700	.0900	6.2000-03	8.3500-03	6.2000-03
3500.0000	1.7100+06	1.2300+06	1.7100+06	7.5000+05	.1320	.0900	.0950	7.6500-03	1.2000-02	7.6500-03
4000.0000	1.3600+06	1.1500+06	1.3600+06	7.6000+05	.1360	.1000	.1000	9.1000-03	1.2000-02	9.1000-03
4500.0000	1.1500+06	1.0200+06	1.1500+06	4.5000+05	.1850	.1500	.1500	1.0700-02	1.4100-02	1.0700-02
5000.0000	9.5700+05	8.6500+05	9.6000+05	2.5000+05	.2560	.2000	.2000	1.2300-02	1.6200-02	1.2300-02
5500.0000	6.6200+05	6.2000+05	6.6000+05	2.5000+05	.3070	.2500	.2500	1.4000-02	1.8000-02	1.4000-02
6000.0000	3.6900+05	3.8000+05	3.8000+05	1.0000+05	.3650	.3170	.3170	1.5900-02	2.0700-02	1.5900-02
6500.0000	1.7000+05	1.7000+05	1.7000+05	7.0000+04	.3850	.3850	.3850	1.7900-02	2.3200-02	1.7900-02
7000.0000	1.5000+05	1.5000+05	1.5000+05	3.0000+04	.6500	.4500	.4500	2.0100-02	2.5400-02	2.0100-02

59

Figure 41. Strain-to-failure versus temperature, with-grain direction, truncated 994 graphite.

Figure 40. Strain-to-failure versus temperature, across-grain direction, truncated 994 graphite.

rocket motor pre-heat igniter phase (Reference 17). The pre-test conclusion was that there was a high probability of obtaining an accurate evaluation of the primary nosetip removal mechanism in the design verification test.

On July 17, 1975, the blunt-design shell was tested in the ABRES/AFRPL Rocket Exhaust Facility. Test pyrometer and thermocouple data showed that the nosetip shell fractured 0.99 second after entering the rocket exhaust stream. Post-test reviews of the facility camera data showed conclusively that the shell failed thermostructurally near the nosetip shoulder well before ablation burn-through. Post-test analyses were directed at finding reasons for the thermostructural failure of the nosetip shell. These analyses included a review of the structural analysis methodology, particularly possible deficiencies in the failure criterion which could explain the observed shell failure. To establish an improved failure criterion for these nosetip shells, the Priddy stress-based theory for brittle anisotropic materials (Reference 18) was adapted to 994-2 graphite using tensile test data obtained for the Material Requirements Definition (MRD) program (Reference 19). This theory accounted for multiaxial loading including shear, stress interactions, and volume and statistical effects. A detailed description of the Priddy criterion and its application to 994-2 graphite nosetips is presented in Appendix A. Comparisons of post-test results using both the Priddy criterion and the LORN criterion are described in the following section.

2.6.1.2   Results

The blunt-design nosetip shell was tested in the RPL facility on July 17, 1975. The model was rotated into the rocket exhaust stream about 0.5 second before the end of the rocket motor pre-heat igniter phase. Facility camera, pyrometer, and thermocouple data showed a fracture of the graphite shell initiating near the shoulder region after approximately 0.99 second of exposure. Post-test reviews of the camera data showed positive separation and expulsion of the nosetip and internal support structure within 0.005 second after observed crack initiation with no visible damage to the remaining components of the test model. From the test chamber pressure history it was determined that the shell fracture occurred during ramping from the reduced "vernier" pressure level to the final steady-state pressure. Figure 42 shows the stagnation point recession predictions based on actual test conditions, including the start transient. At the observed failure time, the nosetip was exposed to approximately 50 atmospheres stagnation pressure and had ablated approximately 0.025 inch of the original 0.250-inch stagnation thickness (see Figure 42). In other words, the thermostructural failure occurred well before planned ablation burn-through and was attributed to a build-up of internal multiaxial stresses in the nosetip following sudden exposure to the exhaust flow environment.

To investigate the thermostructural failure, LORN-based and Priddy-based margins-of-safety for the nosetip shell were calculated. The thermal boundary conditions were computed using a revision to the pre-test analysis that corrected an error discovered in the reference state used to define the solid-wall enthalpy. The error was found to cause an under-prediction of the surface temperature by about 500 - 800°F. The thermal analysis also accounted for the effects of a nozzle-induced shock wave that impinged on the shell model, as shown in Figure 43. The results of these post-test analyses are presented in Figure 44 and are summarized below:

1. Shock wave heating augmentation from nozzle wall discontinuities was not found to affect the thermostructural response of the nosetip shell.

2. Margins-of-safety based on the Priddy criterion were found to be similar to, but lower than, margins-of-safety based on the LORN
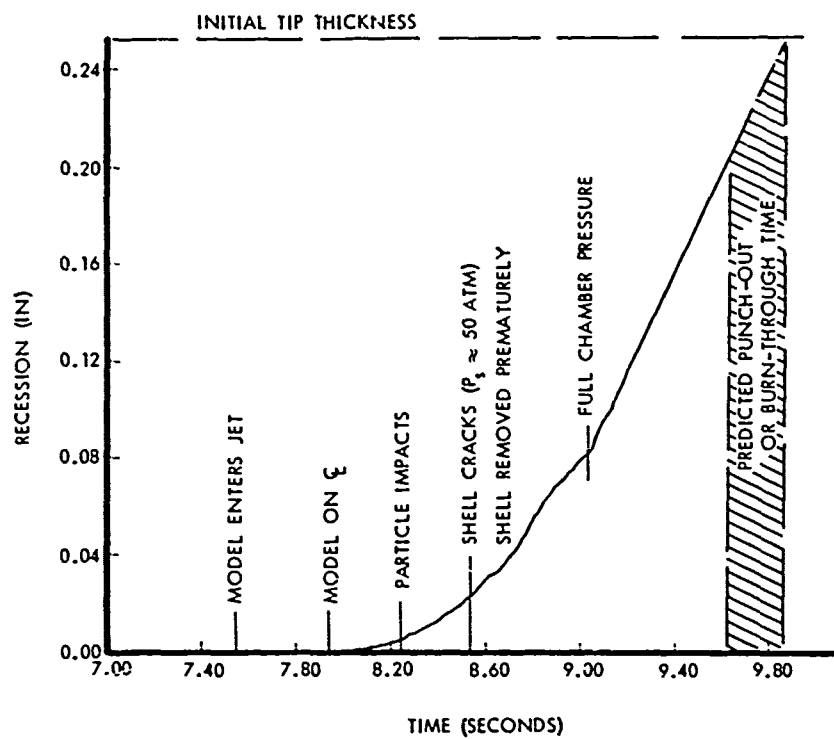
Figure 42.   Recession and event history for Test 169 — blunt shell.
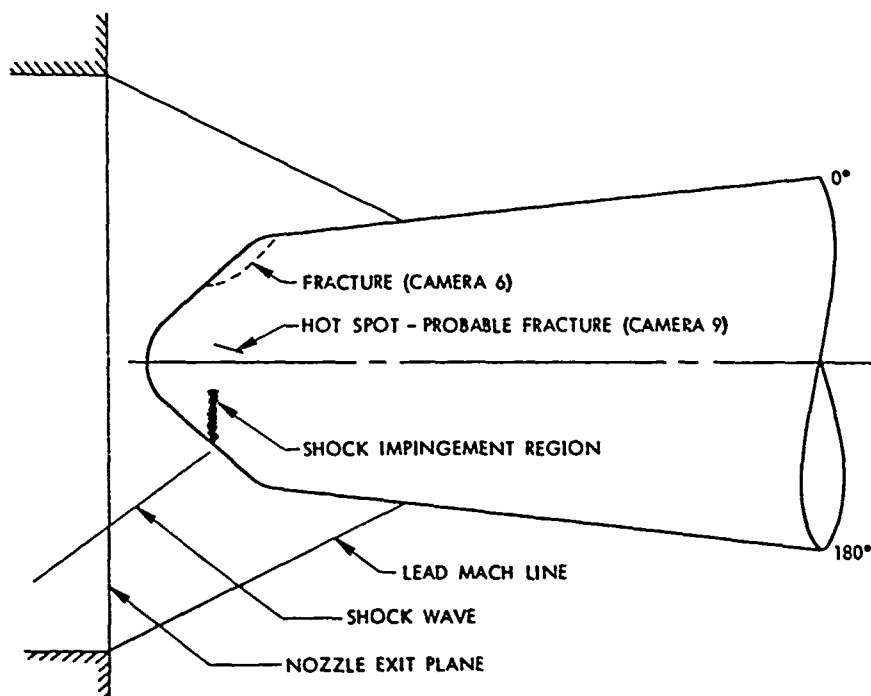
Figure 43.   Shock impingement on the blunt graphite shell model.
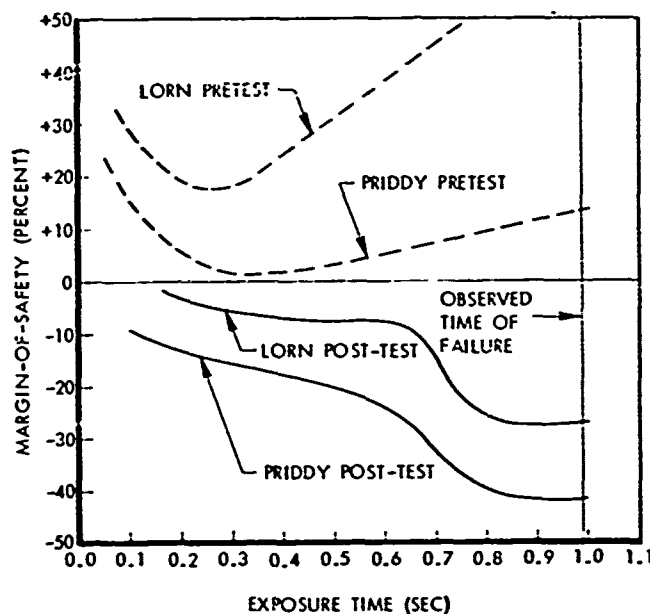
Figure 44. Margins-of-safety for blunt shell.

criterion. Differences in the calculated margins-of-safety were
not enough to explain the thermostructural failure.

3. Much lower margins-of-safety were calculated using the post-
test thermal analysis with the corrected enthalpy reference
state. These lower margins-of-safety were a consequence of
the higher graphite surface temperatures predicted in the revised
analysis.

Post-test analyses with the improved structural analysis methodology and reference enthalpy correc-
tion were found to provide a reasonable explanation of why the thermostructural failure occurred,
as well as the approximate time and mode of failure. The overall conclusion from the post-test anal-
yses was that the blunt-design graphite shell was exposed to a thermostructural environment of
greater severity than had been indicated by the pre-test analyses.

For design verification testing of the sharp-design shell, an extended rocket motor pre-
heat of at least 3 seconds was recommended to increase the survivability of the shell prior to ablation
burn-through. Pre-test analyses that included the effects of a 3-second preheat period at the vernier
operating condition indicated margins-of-safety similar to, but slightly lower than, in flight
(Figure 45). A maximum probability of thermostructural failure of less than 1 percent for this test
was predicted after 0.5 second of exposure. It was concluded that the revised design verification
test would provide an accurate evaluation of the primary nosetip removal mechanism.

On October 21, 1975 the sharp-design biconic shell was tested in the ABRES AFRPL
Rocket Exhaust Facility. The nosetip shell entered the exhaust stream approximately 3.51 seconds
before the end of the rocket motor preheat igniter phase, in general agreement with pre-test recom-
mendations. Facility cameras showed that during this preheat period, rocket motor particles im-
pacted the nosetip shell causing some material loss to the nosetip. Bright spots in the film could be
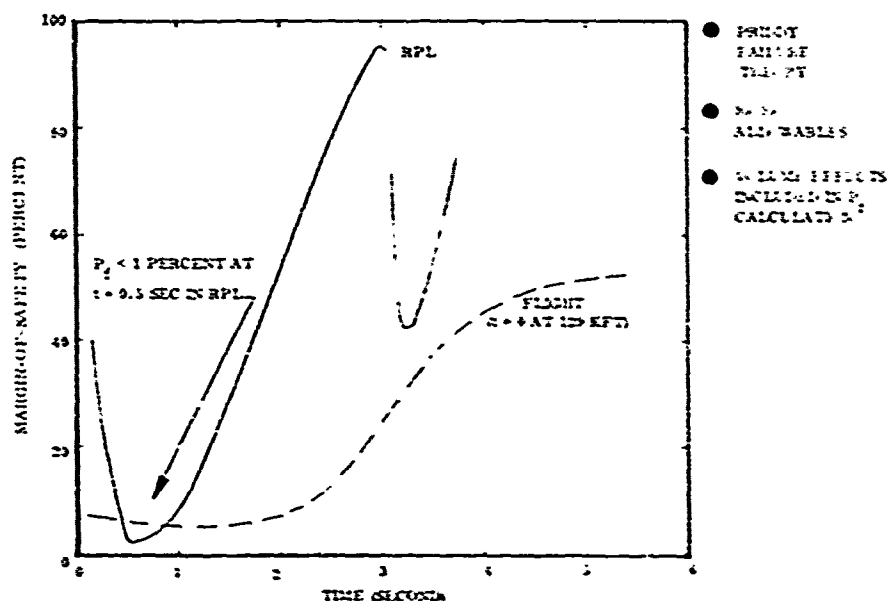
Figure 45. Thermostructural response predictions
for sharp primary nosetip.

seen where impingement losses had occurred and one area near the stagnation point showed an inden-
tation in profile on two cameras. Facility cameras showed no evidence of thermostructural damage
to the nosetip shell during the extended preheat period or on facility ramping to the final steady-state
stagnation pressure. Figure 46 shows the stagnation point recession predictions based on actual
test conditions, including the preheat transient. The nosetip shell remained intact up to a stagnation
pressure of approximately 69 atmospheres when ablation burn-through, or "punch-out," was observed.
In other words, the nosetip shell survived thermostructurally until ablation burn-through, as required
for the flight test models. Following ablation burn-through, exhaust flow entering the internal cavity
caused shell fragmentation and expulsion with no visible damage to the remaining components of the
test model. The elapsed time between observed ablation burn-through and complete shell removal,
including the internal split structure and bearing cap, was approximately 0.005 second. The shell
thickness at ablation burn-through, or punch-out, estimated from the post-test recession analysis,
was approximately 0.070 inch (see Figure 46). It is believed that this remaining thickness at shell
punch-out may have contained some material irregularities from particle impingement during the
rocket motor preheat. The damage depth at the time of ablation burn-through is estimated to be less
than 0.050 inch, based on surface roughness observed from the film data. In other words, the ob-
served particle impingement may have influenced the shell removal time. Although the resulting
stagnation pressure at burn-through was less than the pre-test objective, it is believed that the test
provided an accurate evaluation of the removal mechanism leading to subtip exposure in flight. It
was concluded that the graphite shell can be removed in a clean, predictable fashion without adverse
effects on downstream components, thereby proving the viability of the shell removal concept.

2.6.2   Subtip Performance

The blunt design tungsten subtip was first tested as a bare nosetip (S/N BT-3) on July 3,
1975. A second blunt subtip was tested as a component of a full-scale model of the proposed flight

POST TEST T-186
C* DEGRADED ENERGY RELEASE MODEL
NOSEC PREDICTED RECESSION
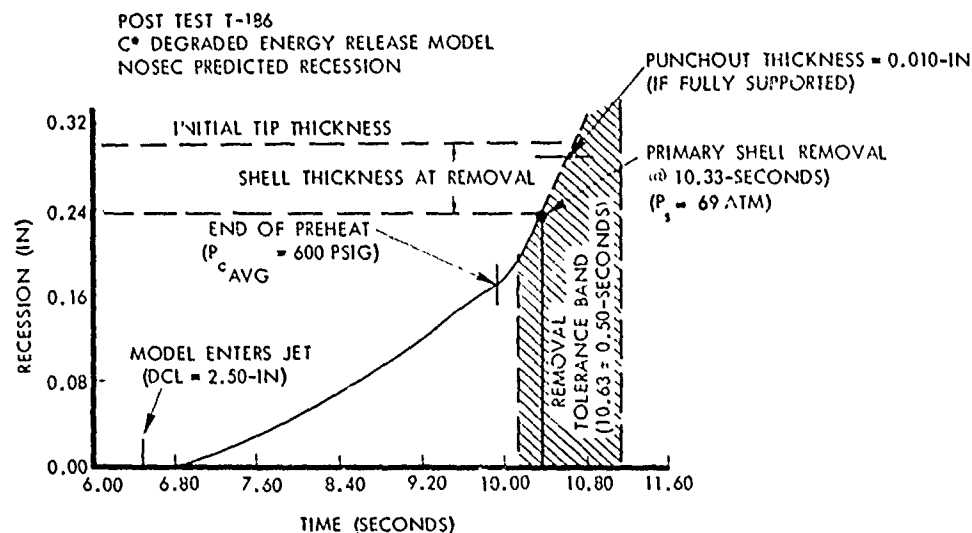
Figure 46. Stagnation point recession history of sharp
primary biconic nosetip, Test 186.

design in the shell removal test on July 17, 1975 (S/N BD-4). The sharp subtip design was tested
as a bare nosetip on November 14, 1975 (S/N BM-4). The steady-state recession rates of the tungsten
subtips, as measured from the high speed film data for each test, are given in Figures 47 through 50,
respectively. In the remainder of this section, the results of thermostructural analyses are compared
with the observed response of these monolithic subtips to assess their performance capability for
flight.
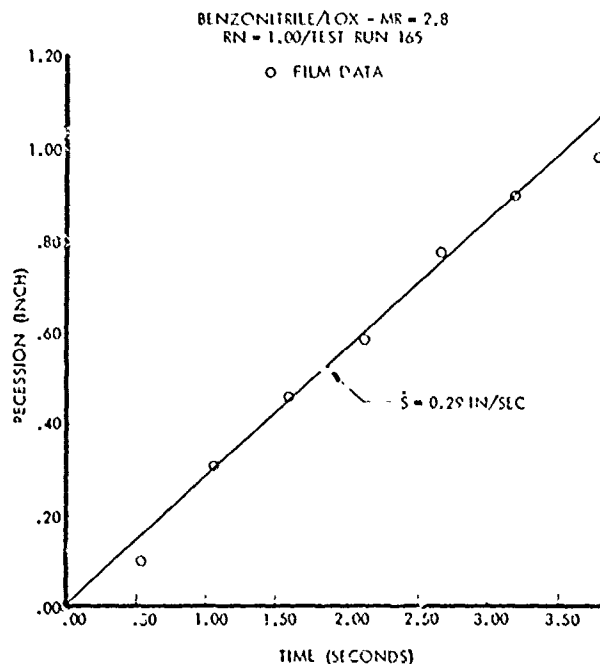
Figure 47. Blunt tungsten subtip axial
recession history — Test 165.
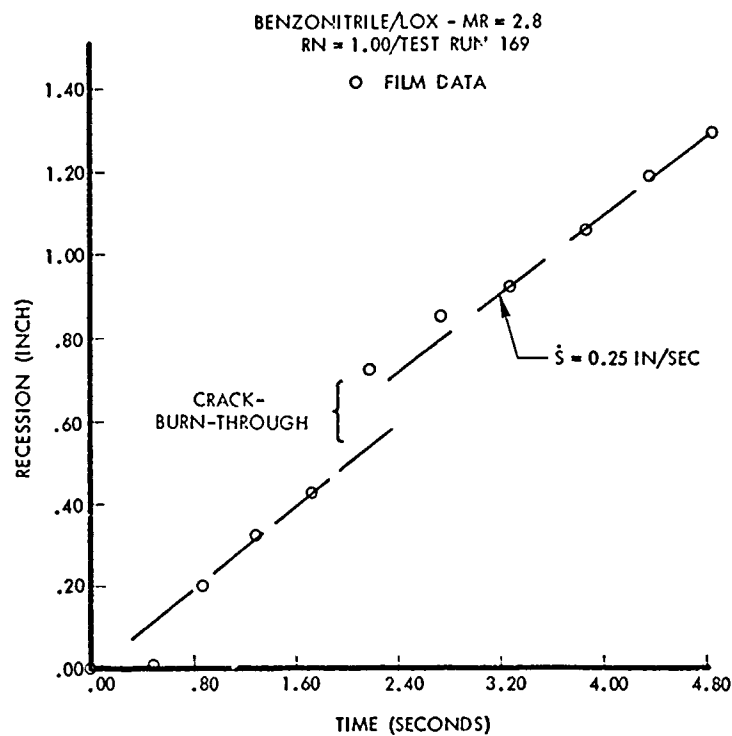
Figure 48. Blunt tungsten subtip axial recession history — Test 169.
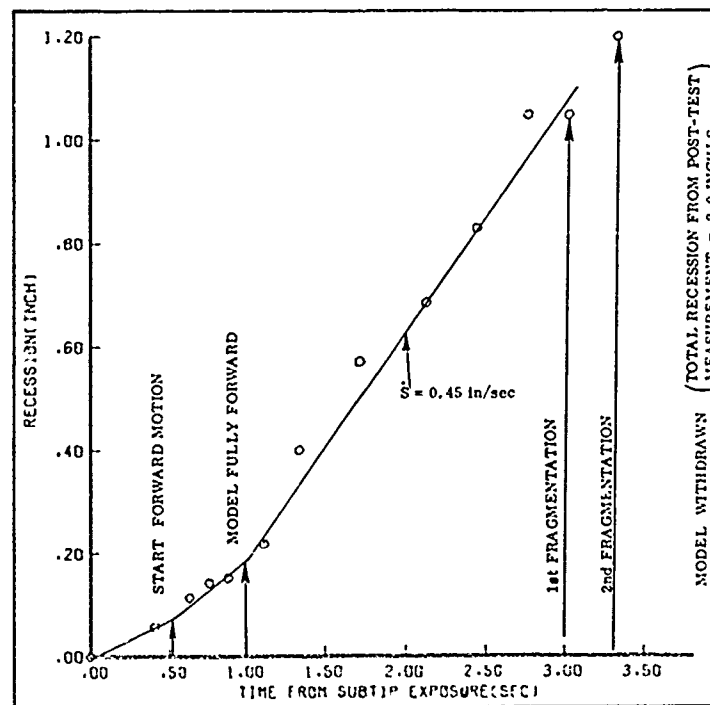
Figure 49. Sharp tungsten subtip axial recession history — Test 186.
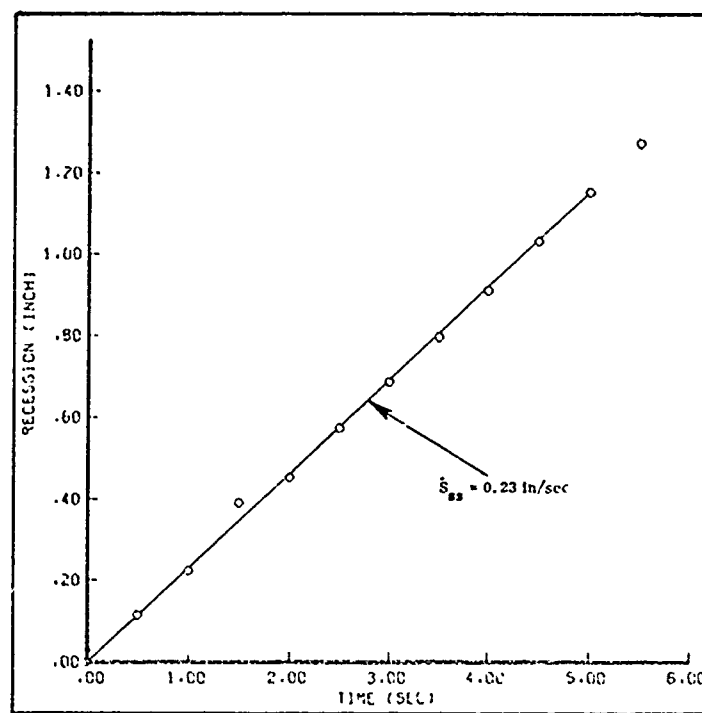
Figure 50. Sharp tungsten subtip axial recession history — Test 189.

2.6.2.1 Method of Analysis

All thermostructural analyses of the tungsten subtips were made using the SAAS III code (Reference 14) with temperature-dependent material properties. All analyses accounted for time-dependent shapes, pressure loads and internal temperatures. The most important consideration in predicting the response of these subtips was the extremely brittle behavior of tungsten below the ductile-brittle transition temperature (DBTT). At the start of the A.N.T./ERN program, the material data that were required to account for the brittle behavior below the DBTT and for inelastic yielding above the DBTT were not available. Just as important, no proven failure criterion had yet been developed for tungsten nosetips.

At the start of the A.N.T./ERN program, properties for tungsten were based on limited modulus of elasticity data, axial direction strengths, and free thermal strain data that were characteristic of tungsten as a generic material. At that time, thermostructural analyses were made with linear-elastic material properties. Stresses from these analyses were greatly overpredicted and, as a result, generally exceeded an assumed 100 ksi allowable stress. For this reason, only comparisons of relative response severity were meaningful, and absolute indications of thermostructural performance capability had to be based on ground test results.

During the A.N.T./ERN detailed design studies, analysis methodology was modified to account for inelastic yielding in material above an assumed DBTT of 400°F. In addition, the Priddy stress-based failure criterion for anisotropic materials was adopted for tungsten, using limited axial direction strength data and two measured transverse strengths at 500°F. These major improvements in analysis methodology, described in Reference 2, gave brittle margins-of-safety, based on 50/50

67

allowable strengths, that accounted for multiaxial stress interactions, including shear. Since that time, the results of a large tungsten characterization program conducted at Southern Research Institute (SoRI) and at the Illinois Institute of Technology Research Institute (IITRI) for the A.N.T./ERN program became available (References 20 and 21). Transverse strengths near room temperature measured in this characterization program were much lower than had been estimated previously. All final design properties obtained from the characterization program were incorporated into all subsequent thermostructural analyses. The final mechanical properties used in the SAAS III analyses are shown in Table 14; the matrix of nine strengths required by the Priddy failure criterion are shown in Table 15.

All pre-test analyses for the design verification tests of the sharp- and blunt-design subtips were made using the methodology just described. Analyses based on the A.N.T./ERN program characterization data with the Priddy failure criterion indicated small but positive margins-of-safety for exposure in the AFRPL facility at 100-atmospheres pressure with the BZN/LOX propellant system at an oxidizer-to-fuel mixture ratio of 2.8. Since margins-of-safety were calculated for the worst-case finite elements using average strength allowables, it was concluded that the probability of thermostructural survival was in excess of 50 percent.

Internal heat-up fractures in the first blunt subtip test and catastrophic failure in the second blunt subtip test demonstrated conclusively that the monolithic designs had much lower performance capabilities than had been indicated by the pre-test analyses. For this reason, the thermostructural analysis methodology was modified to account for: 1) volume effects believed to have had an important influence on the test results, and 2) the propagation of cracks caused by transverse stresses and subsequent ablation burn-through to these cracks. These improvements in analysis methodology were made during the design verification test program in the period of July through September 1975, and are described in the following paragraphs.

2.6.2.2   Results

On July 2, 1975, a blunt-design subtip was tested in the ABRES/RPL facility (Test Number 165). Although no catastrophic failure was observed during 3.83 seconds of rocket motor exposure at 103 atmospheres stagnation pressure, post-test metallographic examination revealed internal (heat-up) fractures induced by transverse (hoop) stresses. It is believed that for a slightly longer exposure test, ablation burn-through to the cracks would have caused major losses of subtip material. A second blunt subtip, tested on July 17, 1975 (RPL Test Number 169) as a component in the primary shell removal test, was exposed to 90 atmospheres stagnation pressure for 5.39 seconds and failed catastrophically from transverse direction (hoop) stresses. Post-test data reduction of acoustic sensor data obtained from Test 169 indicated internal crack initiation in the subtip after 1.15 seconds of rocket motor exposure. Film data from facility cameras showed ablation burn-through to these internal fractures and subsequent loss of subtip material after 4.84 seconds of exposure.

Post-test thermostructural analyses, including the effects of film-observed shock impingement and corrections to the thermochemistry model, did not alter the pre-test prediction. Margins-of-safety in excess of plus 6 percent were predicted for worst-case subtip elements (Figure 51). In other words, the observed failures in these subtips could not be explained with the analysis methodology used at the start of the design verification test program. It was postulated at this time that catastrophic failures in these subtips were the result of volume effects in material below the ductile-brittle transition temperature. For brittle materials, allowable strengths are dependent on the stressed volume. Since the critically stressed volumes in the monolithic subtips are much greater

Table 14. Thermostructural properties for extruded 2 percent thoriated tungsten.

TEMP (°F)	MODULUS (PSI)	POISSON'S RATIO	FREE THERMAL EXPANSION	YIELD STRENGTH (PSI)	STRAIN • HARDENING
70	57,500,000.	0.30	0.0	500,000.	0.630
400	54,100,000.	0.30	0.000725	500,000.	0.470
401	54,100,000.	0.30	0.000725	51,000.	0.470
482	53,400,000	0.30	0.000906	49,000.	0.433
750	50,600,000.	0.30	0.001550	39,200.	0.330
932	48,800,000.	0.30	0.001950	34,100.	0.272
1352	44,300,000.	0.30	0.003100	25,000.	0.164
1832	39,800,000.	0.30	0.004350	18,400.	0.095
2252	35,400,000.	0.30	0.005750	14,000.	0.056
2732	31,000,000.	0.30	0.007250	10,300.	0.032
3162	26,500,000.	0.30	0.008900	7,300.	0.019
3632	22,100,000.	0.30	0.010700	5,000.	0.012
4000	18,500,000.	0.30	0.012250	2,680.	0.009
5000	6,500,000.	0.30	0.016850	2,120.	0.005
6000	1,000,000.	0.30	0.021440	1,560.	0.005
7000	100,000.	0.30	0.026040	1,000.	0.005

*RATIO OF SECONDARY MODULUS TO INITIAL MODULUS

Table 15. Low temperature average strengths for extruded 2 percent thoriated tungsten (ksi).

NOSETIP	V^1	γ^2	β^3	R^4	θ^5	L^6	H^7	W^8
994-2 Primary Shell	25000	-40	2000	2.96	8	2.75	300	Clear
2-2-3 C/C Primary Shell								
Design Sequence 2	25000	-30	2000	2.96	8	3.88	300	Clear
Design Sequence 3^B	25000	-30	2000	2.96	8	4.63	300	Clear
Design Sequence 4	25000	-30	2000	2.96	8	1.38	300	Clear
TZM Subtip								
Design Sequence 7	25000	-30	2000	1.60	19.33	5.00	33	ESI 5.8
Tungsten Segmented Subtip								
Design Sequence	25000	-30	2000	1.60	30	4.05	30	ESI 5.8

1   Reentry Velocity ft/sec

2   Reentry Angles degrees

3   Ballistic Coefficient psf

4   Nose Radius inches

5   Cone Angle degrees

6   Overhang Length inches

7   Exposure Altitude kft

8   Weather
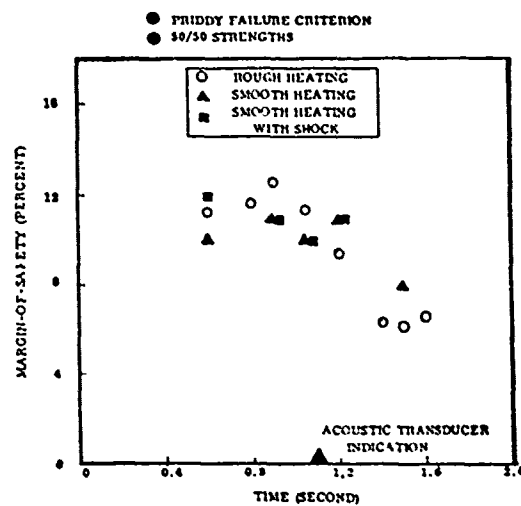
Figure 51. Margin-of-safety predictions
for blunt subtip in RPL.

than the tensile volumes of the test specimens used to obtain the strength data base, the allowable strengths for these subtips should be degraded substantially. In order to account for the dependence of allowable strengths on stressed volume, a Weibull distribution was fit through all of the low temperature uniaxial strength data that had been obtained from the recent characterization program (Figure 52). The distribution was used to correct the brittle allowable strengths to finite element volumes. Using the Weibull statistics, the probability of crack initiation in any fine element volume was calculated from the proximity of the stress vector to the Priddy failure surface. The overall probability of crack initiation in the subtip was then calculated from the cumulative product of finite element survival probabilities over all brittle elements.
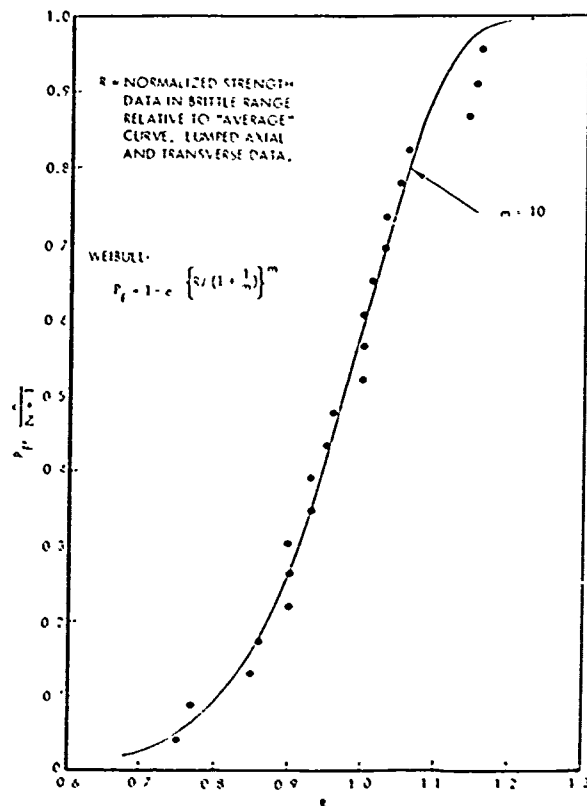
Figure 52. Weibull model of brittle strength of thoriated tungsten.

The post-test analyses then were re-evaluated using this methodology, and the results indicated very high probabilities of crack initiation in the blunt subtips (Figure 53). In the case of Test Number 165, these predictions are in reasonable agreement with a crack initiation indication from the acoustic-sensor attached to the subtip shank. For the first time, crack initiation in blunt monolithic subtips was correlated by the post-test analysis. The thermostructural failures in the blunt monolithic subtips were attributed to:

1. High multiaxial stresses,
2. low transverse direction strengths and,
3. large critically stressed volumes.
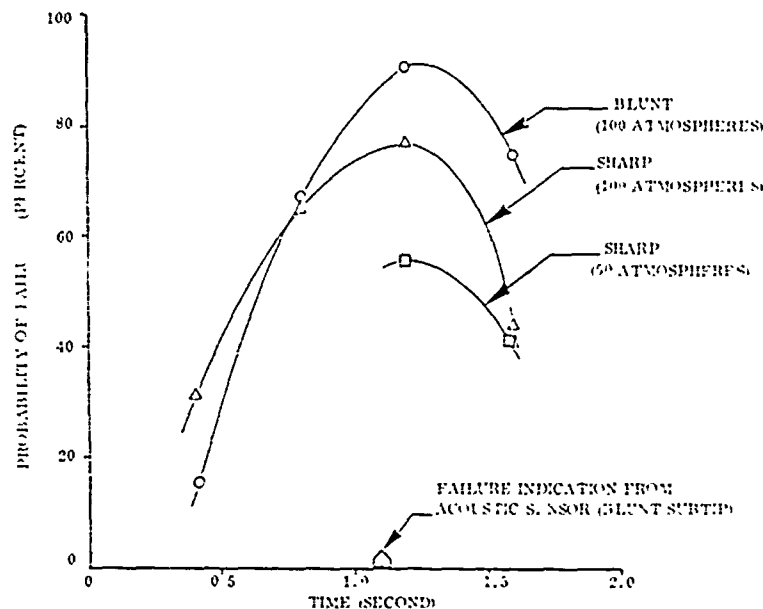
Figure 53. Predicted failure probabilities for
A.N.T./ERN subtips in RPL.

To further explain the test results, the analysis methodology was extended to include a prediction of when a catastrophic failure (i.e., loss of solid material) in a subtip would occur following assumed internal crack initiation. This extension was necessary because the thermostructural analysis methodology only gives a prediction of internal crack initiation in the subtip. Assuming that an internal crack resulting from transverse stresses does not progress forward beyond the DBTT location in the subtip, catastrophic failure will not occur until sometime later when the outer surface of the subtip ablates to that location. The delay between crack initiation and subsequent crack burn-through can be estimated from stagnation point recession histories and DBTT location histories in the thermal analyses.

To summarize, the following procedure was used to obtain probabilities of crack burn-through in the subtip:

1. Inelastic stresses in the nosetip during the test were calculated with the SAAS III code as functions of time.
2. Probabilities of crack initiation in each finite element were calculated with the Priddy stress-based criterion with statistical and volume effects included.
3. Overall probability of crack initiation P_F, was found by cumulative product over all brittle elements.
4. An internal crack initiating at any time, t_c, was assumed to propagate forward to the 400°F isotherm, Z_{DBTT}.
5. The subsequent crack burn-through time, t_{bt}, was found by observing when the ablation profile reaches Z_{DBTT}.
6. P_F versus t_{bt} points were plotted to obtain the probability of crack burn-through curve.

This method provides a comprehensive procedure for describing the thermostructural behavior of tungsten nosetips. It was first applied to results of ground tests of blunt subtips in Test Numbers 165 and 169 (Figures 54 and 55) and was found to explain: 1) the mode of failure, 2) the strong likelihood of failure in monolithic designs, 3) the sensor-determined time of crack initiation, and 4) the subsequent film-observed burn-through time.
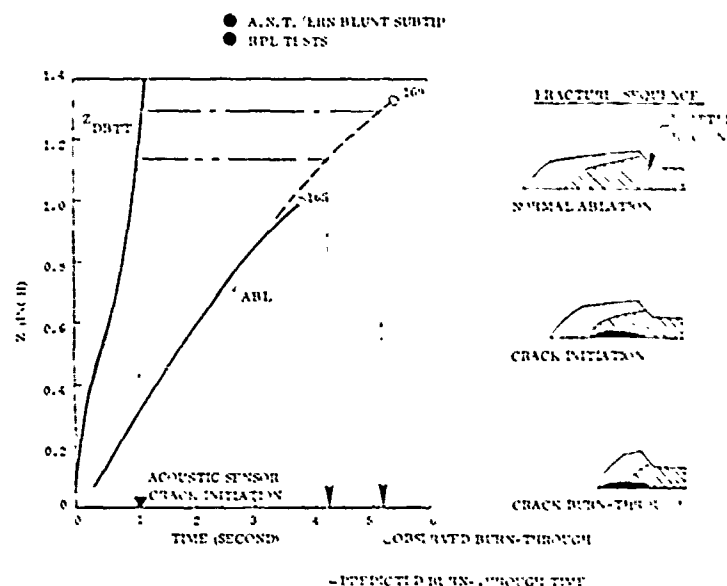
Figure 54. Ablation/DBTT location histories.
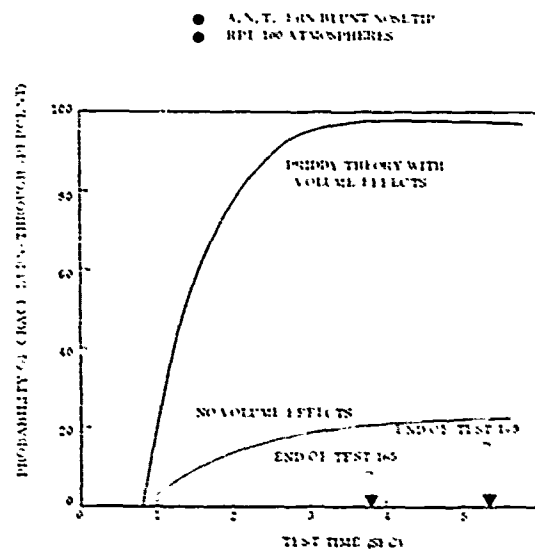
Figure 55. Probability of crack burn-through.

Subsequently, pre-test thermostructural predictions with the methodology described above were made for design verification tests of the sharp subtip in the ABRES/RPL facility. Probabilities of crack initiation for exposure at 50 atmospheres stagnation pressure are shown as a function of time on centerline in Figure 56 and are compared to clear air flight. The calculated peak probability of crack initiation was found to be approximately the same in ground test as for clear air flight (approximately 80 percent). On November 14, 1975, the sharp subtip model was tested in the RPL facility for 7.54 seconds of exposure at 53 atmospheres stagnation pressure (Test Number 189). Film data from facility cameras showed bright spots on the model sidewall two inches from the tip 0.6 second after teflon glove removal. These were believed to be the result of internal cracks generated by transverse (radial) stresses. The estimated probability of crack initiation at this time was approximately 75 percent.
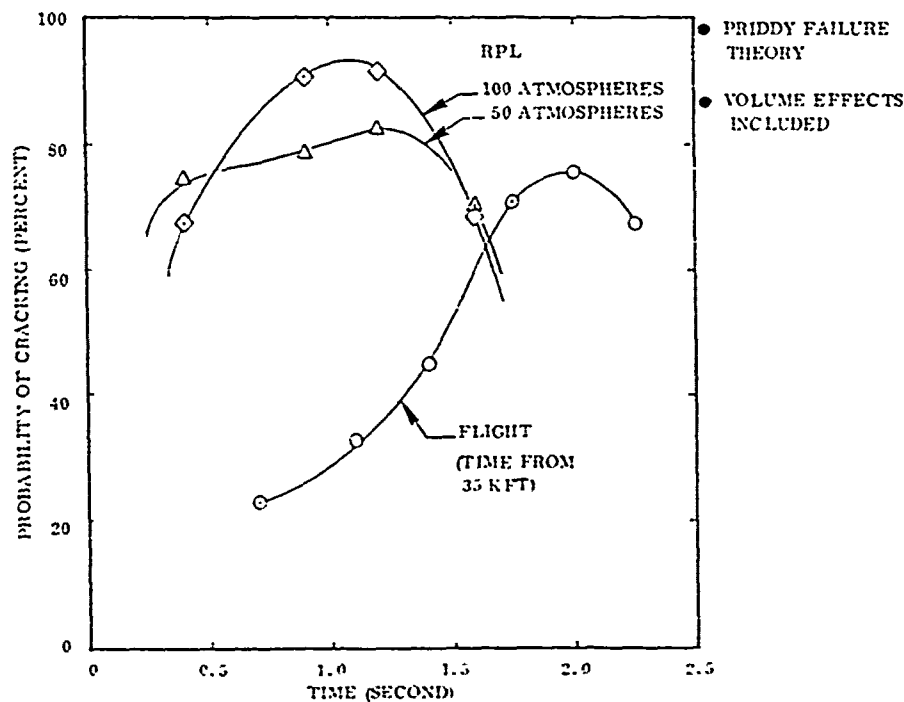
Figure 56. Sharp tungsten subtip thermostructural response.

2.6.2.3   Conclusions and Recommendations

The following conclusions and recommendations were made:

1. Monolithic subtips of thoriated tungsten tested at RPL had internal
    (heat-up) fractures induced by transverse direction stresses.
    Thermostructural analyses indicated high probabilities of crack
    initiation in these tests. Since the thermostructural response in
    a ground test exposure was comparable to that for clear air reentry,
    it was recommended that monolithic subtip designs not be flight
    tested.

74

2. Internal fractures in the subtips were attributed to large multiaxial stresses, low room-temperature strengths in the subtip material, and large critically stressed volumes.

3. The structural analysis methodology which evolved during the A.N.T./ERN program has been successfully applied to design verification ground test models; it is believed that these methods successfully describe all the essential features of the thermo-structural response of tungsten nosetips.

2.6.3   Skirt Heatshield Performance

The data summary given in Table 16 shows the maximum measured recession at the nosetip/heatshield interface region. Detailed post-test analysis of the heatshield recession perform-ance was not performed because no anomalous behavior of the skirts was observed. The nosetip/heatshield joint region experienced the largest recession in each test and therefore determined heat-shield thickness requirements in the design. Note that with the 100-atmosphere nozzle, the heatshield location of interest remained outside of the test rhombus in both the shell removal and the thermo-structural configurations. Since the model was moved forward in the shell removal tests, the heat-shield saw a varying heating environment based on the position of the interface location relative to the Mach line intersection as a function of time (see Section 2.4). Evidence from previous tests (Reference 2), as well as the present results, suggested that the int rface location experienced higher recession than was predicted from one-dimensional charring ablato. codes. The difference resulted not only from the two-dimensional conduction effects contributed from the hot subtip, but also from scouring of the char structure by a high shear environment. Further analyses would be required to characterize fully the response in any particular exhaust environment.

The higher sidewall recession on the heatshield for Test Number 189, which was run in the 50-atmosphere nozzle, was attributed to the larger test rhombus, which encompassed the location of interest. Hence, the heat flux was not reduced as in the 100-atmosphere nozzle tests.

Since no anomalous behavior of the heatshield was observed, it was concluded that the skirt heatshield configuration was adequate both structurally and thermally for the planned clear air flight test environment.

2.6.4   Instrumentation

The instrumentation on each test consisted of internal thermocouples, optical pyrometers, and an acoustic recession sensor. In addition, strain-gages were mounted on the aft structure of both sharp-design subtips to measure possible bending loads on the nosetip during primary nosetip removal (Test Numbers 186 and 189).

2.6.4.1   Thermocouple Instrumentation

The performance of the thermocouples on each test model is summarized in Table 17. On the average, data were obtained from 84 percent of the thermocouples that were installed. The remaining thermocouples either were defective after final model assembly or failed during the tests due to either vibration or shock loads. *

---

* It should be noted that all 26 thermocouples on each of two flight units that were deliv-ered survived acceptance vibration testing (0.1 g^2 Hz) successfully, and all were operating after installation on the flight vehicles.

Table 16. Summary of heatshield recession in A.N.T./ERN RPL tests.*

TEST NO.	P_s (ATM)	MAXIMUM RECESSION (NORMAL) (IN)**	TOTAL EXPOSURE (SEC)***	TOTAL STRIPBACK (IN)**	REMARKS
165	100	0.48	4.49	---	Teflon Glove Forward-Facing Step Mid Heatshield
169	100	---	6.37	2.96	Graphite Shell Forward Heatshield Step
196	100	---	8.46	4.27	Graphite Shell Forward Heatshield Step
189	50	0.59	9.78	---	Teflon Primary Nosetip Forward-Facing Step Mid Heatshield

* Because of the step created by removal of glove or shell, most of the recession was a combination of stripback and normal ablation. However, the cases with shell removal are reported as stripback because of the initial forward heatshield step.

** Determined from post-test and pre-test photographs and measurements

*** Includes all transient times including sting movement transients

76

Table 17. Summary of thermocouple operating performance.

	TEST NUMBER				TOTAL
	165	169	186	189	
No. of Thermocouples Installed	18	26	2(	18	88
T/C's Operating at Start of Test	16	24	24	17	81
No. of T/C's Giving Useful Data	16	20	22	16	74

Table 18 summarizes the performance of each individual thermocouple in each test. Either the failure time of each backface thermocouple is indicated, or the temperature at the end of the test is given in parentheses. The purpose of this table is to indicate the consistent response of the thermocouples at each location. The thermocouple locations for the design verification test units were identical to the locations in the respective flight units. For example, the primary tip removal thermocouples failed at 8.52 seconds and 10.34 seconds on the blunt and sharp shell removal tests, respectively. The film data indicated that shell removal actually occurred at 8.53 and 10.33 seconds, respectively. Confirmation of shell removal, therefore, was in excellent agreement for both designs. In addition, thermocouples A6 and B6 showed positive responses at the times of subtip fragmentation that occurred in Tests 169 and 186.

Additional data obtained from the heatshield backface thermocouples are shown in Table 19. From the data for Test 186, the forward heatshield stripback rate was deduced and correlated with the film data. The indicated stripback rate was 0.88 to 0.95 inch/sec. This technique for measuring heatshield stripback would be especially valuable during a weather reentry test.

2.6.4.2   Optical Pyrometer Instrumentation

The overall performance of the optical pyrometer data was disappointing and subject to large uncertainties in the indicated temperatures. The disappointing performance was due primarily to obscuration of the surface by clouds of unburned fuel. The chamber walls are cooled by the spraying of fuel which does not combust completely before exiting the nozzle. The fuel-rich region, with its attendant dark, carbon-rich cloud tends to obscure the model either continuously or intermittently. The pyrometer data were used primarily in these tests as a potential indicator of shell removal, since an abrupt change in the readings should signal the event. Correlation with the motion picture timing and thermocouple data was used to determine the actual removal time. AFRPL is actively pursuing facility refinements to alleviate the pyrometer obscuration problem.

2.6.4.3   Acoustic Recession Gage Instrumentation

The original intent of the RPL acoustic recession gage tests was to demonstrate the A.N.T./ERN flight ablation sensor on a full-scale nosetip under high heating conditions. Thus, only the sensor specified at the Critical Design Review (Reference 22), a 1.5-mHz shear wave pulse echo gage, was to have been tested. Two tests were planned with a sharp nosetip and two with a blunt nosetip.

Table 15. Summary of A. N. T. ERN thermocouple data
in design verification tests.

THERMOCOUPLE NUMBER	FUNCTION	BURN THROUGH TIME SOLUTION TEMPERATURE AT END OF TEST[c]			
		TEST NUMBER			
		1-2	1-3	1-4	1-5
A1	Primary tip removal, stagnation point		*, *2	16, 31	
A2	Primary tip removal, sidewall		*, *2	(a)	
B2			(a)	14, 34	
A3	Forward heatshield stagnation		9, 49	16, 44	
B3			9 7*	16.7*	
A4	Forward heatshield stagnation		11, 39		
B4			11, 42	12, 79	
A5	Forward heatshield stagnation		12, 47	13, 42	
B5			13, 44	13, 44	
A6	Solids temperature	.1	(a)	13, 73	9, 7*
B6		.26	13, 34	13, 43	*, 3*
A7	Insulator holder temperature (high temp. measurement)	*5	(a)	*7	*a
B7		.55	(a)	(a)	*7
A8	Pressure guard performance	.35	.45	.5*	.53
B8		.5*	.5*	.5*	.5*
A9	Aft heatshield stagnation	.55	.5*	.5*	.4*
A10	Aft heatshield stagnation	.5*	.5*	.5*	.5*
A11	Aft heatshield stagnation	.5*	.55	.53	.5*
B11		.5*	.55	.55	.5*
A12	Acoustic transducer, sidewall boundary	.5*	.5*	(a)	.5*
A13		.5*	X	.5*	.5*
C1	Heatshield in-depth temperature	.57	(a)	.5*	22, 5*
D1		.57	(a)	.5*	23, 3*
C2	Heatshield in-depth temperature	(a)	(a)	.5*	22, 1*
D2		(a)	(a)	(a)	22, 7*
C3	Heatshield in-depth temperature	.5*	.5*	.5*	22, 5*
D3		.5*	.5*	.5*	22, 75

NOTES:
(a) Thermocouple temperature at start of test
(b) Thermocouple output unreadable due to noise
"X" = No thermocouple installed
(c) Numbers in parentheses are temperatures

Table 19. Thermocouple data summary, Test 186 (model BK-4).

T/C	AXIAL LOCATION (FROM PRIMARY TIP STAGNATION POINT) (IN)	RAY (DEG)	EVENT RECORDED	TIME OF T/C BURNOUT (SEC)	HEATSHIELD STRIPBACK (IN/SEC)
A1	3.24	C_L (STAG. POINT)	Shell Removal	10.339	---
A2	3.45	120	Shell Removal	N.G.	---
B2	3.45	300	Shell Removal	10.339	---
A3	5.27	120	H/S Stripback	10.40	
B3	5.27	300	H/S Stripback	10.78	0.894
A4	5.54	120	H/S Stripback	---	
B4	6.54	300	H/S Stripback	12.20	0.868
A5	7.79	120	H/S Stripback	13.05	0.881
B5	7.79	300	H/S Stripback	13.64*	0.951
A6	8.47	120	Subtip Shank	13.75	---
B6	8.47	300	Region	13.65*	---

$\dot{S}_{H/S(300)} = 0.881$

$\dot{S}_{H/S(120)} = 0.951$

$\dot{S}_{H/S(AVE.)} = 0.916$

* Correlates Movie Data of Subtip Fragmentation

79

However, as model fabrication proceeded, new evidence on the performance of acoustic gages on tungsten nosetips became available. First, HEARTS flight test results indicated that recession data could not be obtained from shear wave gages bonded to tungsten. Then, in a May 1975 test series at the AFFDL 50 Megawatt arc-jet, it was found that: 1) a change from the shear wave to compression wave mode in pulse/echo gages did not result in any meaningful improvement in sensor performance on t, ٪sten, and 2) a resonance-type compression wave gage did show considerable promise, with good correlation obtained between gage recession measurements and motion picture data (see Section 6.1). As this new evidence became available, changes were made in the RPL model instrumentation where practical. Where model fabrication had proceeded beyond the point that transducer modifications could be made without major rework, the instrumentation was left unchanged.

The final ablation gage instrumentation tested was as indicated in Table 4 (Section 2.2.6). Two models were instrumented with shear wave pulse/echo gages: one with a compression wave pulse/echo gage and one with a resonance wave gage. All three pulse/echo gages had a nominal carrier frequency of 1.5 mHz.

Only the shear wave transducers were flight-qualified production type sensors. The other two transducers were, of necessity, prototype units. Furthermore, to meet the schedule requirements of the design verification test program, a "breadboard" resonance sensor was fabricated. The basic construction technique and materials were the same as for shear wave gages. However, with the tight model fabrication schedules, no time was available to optimize the new sensor designs for their particular applications. The performance of the prototype transducers was considered adequate to determine only the basic feasibility of the gages for tungsten ablation measurements.

By the time the actual tests were performed, the probability of obtaining recession data from any of the pulse/echo gages was considered remote. It was for this reason that the resonance gage was substituted on the last test unit. It may be noted that, even without recession measurements, the ablation gages would still be expected to function as crack detectors.

Pulse/Echo Gage Performance

In all three of the pulse/echo sensor tests, the transducer was excited with a laboratory-type pulser/receiver (Panametrics Model 5052). The output signal was monitored on an oscilloscope and recorded on a video tape recorder. With this approach (as opposed to using a flight-type signal conditioner), the complete bipolar signal was obtained, permitting detailed post-test analysis and processing. If desired, the output tape can be played through a breadboard flight processor unit at a later date to evaluate the overall ablation gage system.

The background noise produced by the RPL facility varied widely in the three tests using pulse/echo sensors. In Run No. 186 (shear wave transducer), the noise level was so high that the receiving equipment was completely saturated throughout the model on-centerline period. Neither the echo location nor the presence of crack signatures could be detected, even after post-test filtering. On the other hand, Run No. 169 (compression wave transducer) was exceptionally quiet with almost no increase in in-band noise associated with the model entering the flow. Run No. 165 (shear wave transducer) was typical, with an increase in baseline noise by a factor of about two when the model entered the flow. Wide variations in the RPL noise environment had been noted in previous tests involving acoustic gages. However, to date, no explanation for these variations has been offered, nor has a correlation been found between the apparent noise level (as detected by the ablation gage) and facility performance data.

Because of the high noise level, the most that can be said about the test results of Run No. 186 is that the echo pulse was gone when the model rotated out of the flowfield (removing the background noise interference). However, the relative performance of the shear wave and compression pulse/echo sensors could be obtained from the results of Runs 165 and 169. In both of these tests, the echo pulse decayed to the noise level in about 0.5 second. Comparable decay times were obtained in previous flight and ground tests of pulse/echo gages on tungsten nosetips.

Numerous noise bursts, probably associated with crack formation and propagation, occurred during and immediately after Run 165. However, the earliest noise burst, occurring approximately 0.15 second after model insertion, was of much shorter duration than the typical bursts previously associated with crack formation (about 15μS, as compared to perhaps 200μS). The short duration of this burst suggested the possibility of another source; e.g., impact of a particle on the subtip. The strongest noise burst was recorded at 1.15 seconds of exposure and is believed to indicate internal subtip fracture. Only one noise emission occurred during Test 169. This was a strong burst (400μS duration) occurring 0.6 second after insertion.

It was concluded that none of the pulse/echo sensors could measure tungsten recession. However, the basic acoustic unit should still function as a crack detector during the flight tests.

Resonant Frequency Gage Description and Performance

Figure 57 is a schematic of the test setup used for the resonance gage test (Run 189). The transducer included two crystals bonded together in a vertical stack. The crystal immediately adjacent to the nosetip (transmitter crystal) was driven by a wave generator, while the output of the rear-most crystal (receiver) was monitored. As indicated in Figure 57, the excitation frequency was varied linearly with time from 40 kHz to 10 kHz over a sweep time of 500 ms. The sweep was then repeated to form a sawtooth input signal.
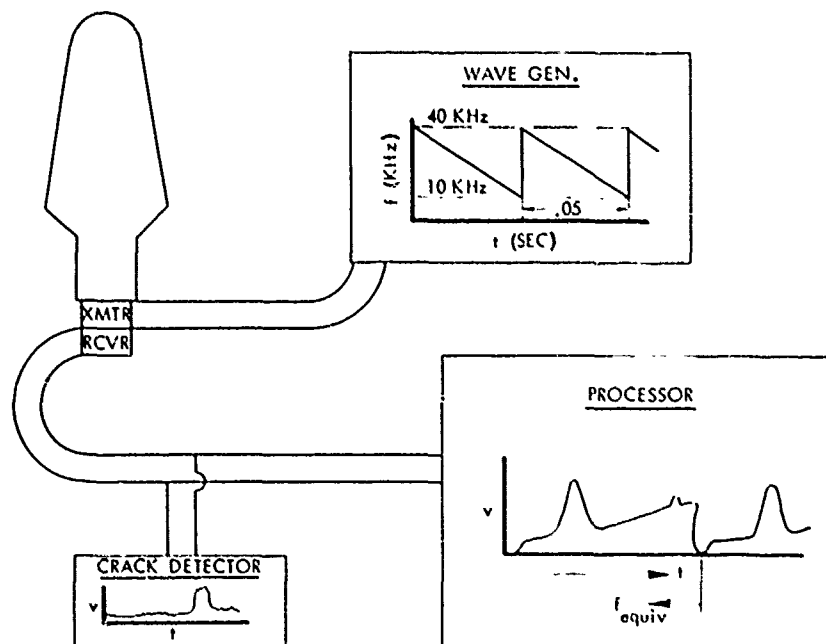
Figure 57. Test setup for resonance sensor.

For the pre-test subtip length, two resonances occurred in this frequency range: 1) a 1/2 wave resonance at about 11 kHz and 2) a 3/2 wave resonance at about 33 kHz. Both resonant frequencies would be expected to increase in inverse proportion to nosetip length during ablation.

Of the two resonances, the 3/2 wave peak was much stronger and more suitable for tracking. (The same was true in the earlier resonance sensor models used in the laboratory and the 50 MW tests.) The half-wave resonance was theoretically strong, but apparently the resonance was of such high "Q" as to be obscured by the slew rate limitations of the system. In an attempt to make the half-wave resonance as visible as possible so that it would be feasible to trace both resonances for comparison, the signal processor amplified the signal with a gain which increased logarithmically with decreasing frequency.

The processor block of Figure 57 includes a representation of the envelope of the output signal. In a given data frame, increasing time correlates directly with decreasing excitation frequency. Thus, the baseline signal increases logarithmically with time. The strong pulse represents the 3/2 wave resonance, while the small pulse near the end of the frame represents the 1/2 wave resonance. Both pulses would move to the left during ablation.

The unprocessed receiver output also was monitored and recorded on a video recorder. By filtering out the low frequency ablation gage signal, the wide band background noise history could be determined. The resulting signal served the same function as the "crack detector" on the pulse/echo ablation gage.

The performance of the gage in the actual test was disappointing. The signal became quite noisy at teflon glove removal, though the 3/2 wave resonance was still distinguishable. At 0.6 second after glove removal, the resonance pulse vanished suddenly for a single frame; at 1.0 second it vanished completely.

The crack detector showed a ramp increase in noise beginning at glove removal. Between 0.60 and 0.75 second after removal, the noise reached a maximum with two sharp peaks, followed by a sharp decline. For the remainder of the test, the noise level was comparatively low. As noted previously (Section 2.5), post-test inspection showed the nosetip to be cracked clear through across the axis. In the movies, the crack first became visible on the surface about 1.1 second after glove removal.

As the crack axial location was close to the subtip shank and "off-scale" for the ablation gage, it is tempting to associate the signal loss with the crack formation. According to this hypothesis, the crack first occurred about 0.6 second after glove removal and propagated for an additional 0.5 second. The ramp increase in crack detector noise could be attributed to a build-up in aerodynamic noise from the rocket motor flowfield. The two sharp peaks would be associated with crack formation, and the sudden decrease in noise could be attributed to isolation of the transducer from the flowfield noise as the crack propagated across the axis.

However, three facts strongly suggest that the loss in ablation gage signal actually was due to an internal transducer failure:

1. If the crack hypothesis were correct, it would be expected that the resonance pulses would simply disappear from the signal, with the baseline unchanged. However, in actual fact, the baseline voltage decreased sharply to about the level that would be expected from

82

background noise alone. A similar decrease was simulated in the laboratory by disconnecting one of the transmitter crystal terminal wires.

2. It also would be expected that some minor resonances would be present in the sensor frequency range even for a "short nosetip" due to various possible multiple reflection sound beam paths. In fact, such resonances were shown to be present in the laboratory when a new transducer was mounted on the remains of the test nosetip. On the other hand, during the test the signal was almost free of structure after the loss of the 3/2 wave resonance peak.

3. Finally, the temporary one-frame signal loss at 0.6 second after glove removal is most easily explained as a "loose wire" effect.

Thus, it was concluded that one of the two wire terminal junctions on the transmitter crystal failed due to vibration. Unfortunately, it was impossible to verify this conjecture, as the transducer could not be removed from the nosetip model without destroying the internal wiring. Since RPL schedule requirements precluded the use of flight-qualified design and construction procedures, no conclusion could be made from this test regarding the worthiness of a resonance gage for tungsten recession measurements.

2.6.4.4 Strain Gage Instrumentation

Strain gages were mounted on the aft substructure of the two sharp units. The purpose of the gages was to measure deflection of the nosetip through the substructure during the shell removal sequence. Figure 11 (Section 2.2.5) shows the location of the four strain gages, mounted 90 degrees apart, on both sharp units. The location of the gages were identical for the subtip and shell removal models. Each gage was a 350 ohm, 1/4 bridge, BLH foil strain gage number FAE 255-35-S6-ET, with a gage factor of 2.07. Bridge completion circuits were provided by AFRPL and a 1.7 MΩ calibration resistor was used for a maximum expected strain of 0.0001 in/in.

Figure 58 shows the responses of the four strain gages during the sharp shell removal test (Test 186). All gages show a response during the test, starting shortly after model insertion (6.5 seconds). Significant lateral pulses are indicated at 8.9 seconds (G4), 9.25 seconds (G2), 9.9 seconds (G3), and 10.9 seconds (G1). However, no significant pulses occur at the time observed for shell removal (10.33 seconds). Similarly, Figure 59 shows the responses of the gages during the sharp subtip test with the teflon glove (Test 189). All of these gages indicate an increasing (compressive) strain characteristic of model blunting during a test. Gages G2 and G3 show small pulses within 0.05 second of the time of teflon glove removal, but the pulses are no larger than others that occur during the test.

Based on the results of these two tests it was concluded that:

1. Aerodynamic pulses that may occur during shell or glove removal are small relative to other changing aerodynamic loads or vibration levels in a rocket motor test.

83
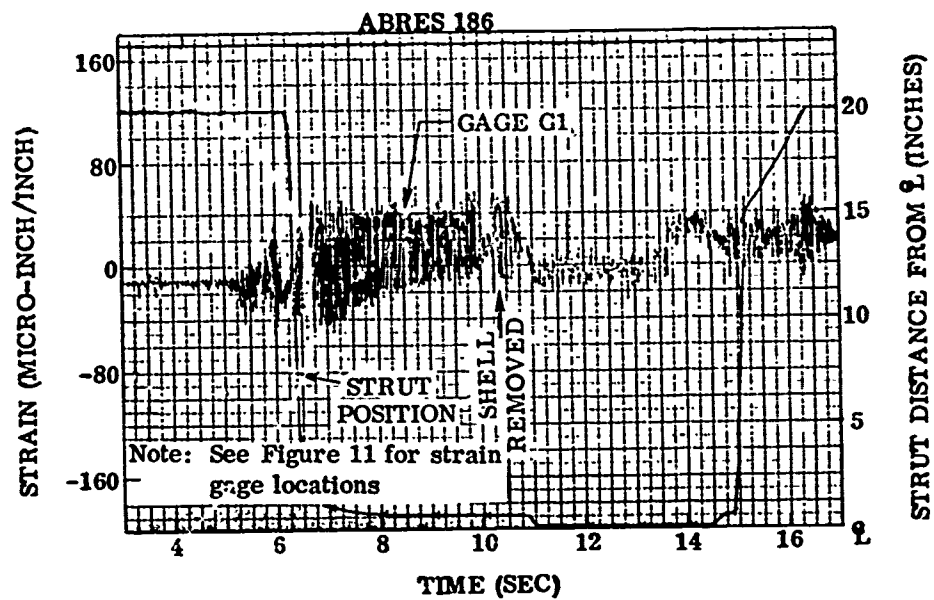
(a)
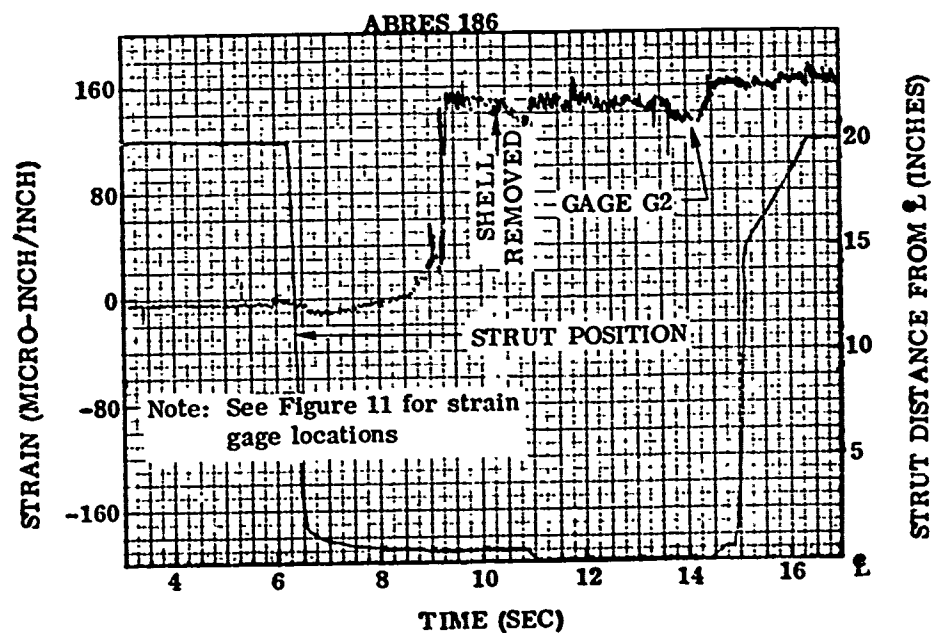
(b)

Figure 58. Strain gage response for Test 186.
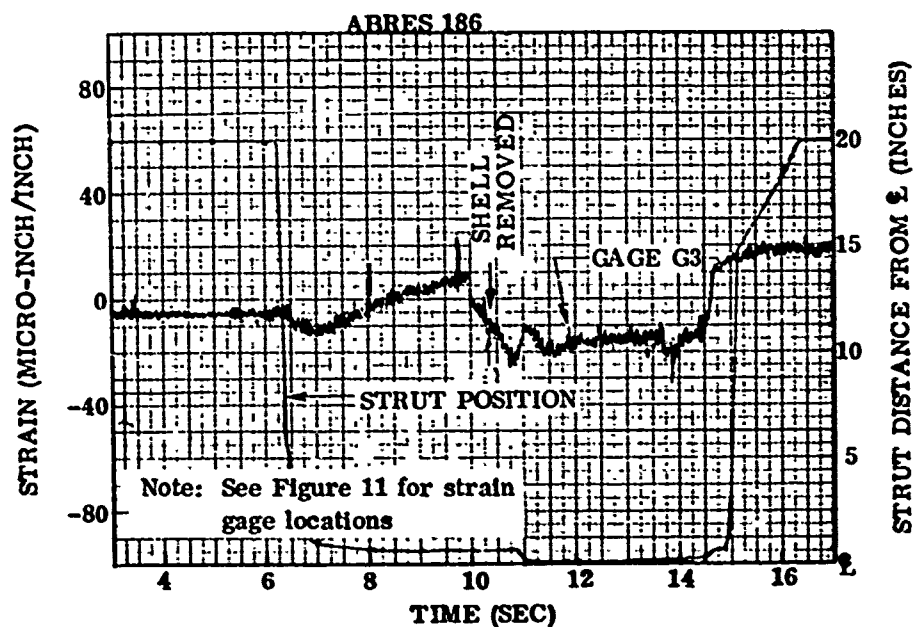
(c)
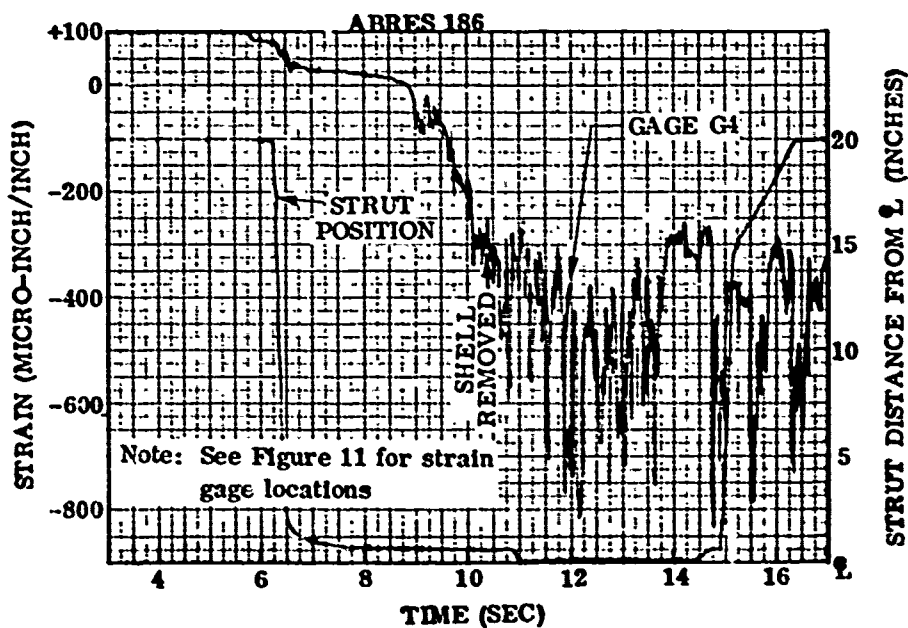
(d)

Figure 58 (continued). Strain gage response for Test 186.
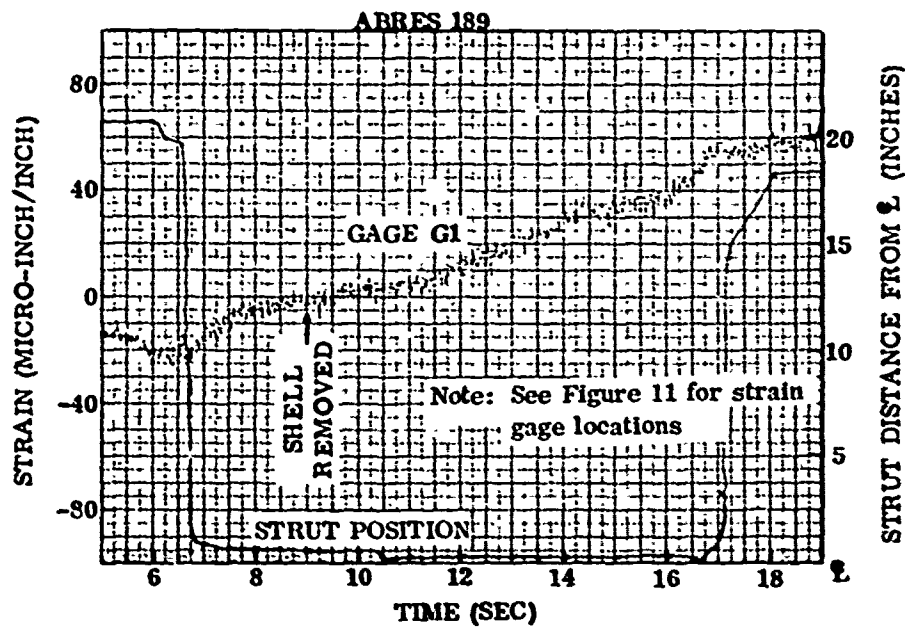
(a)
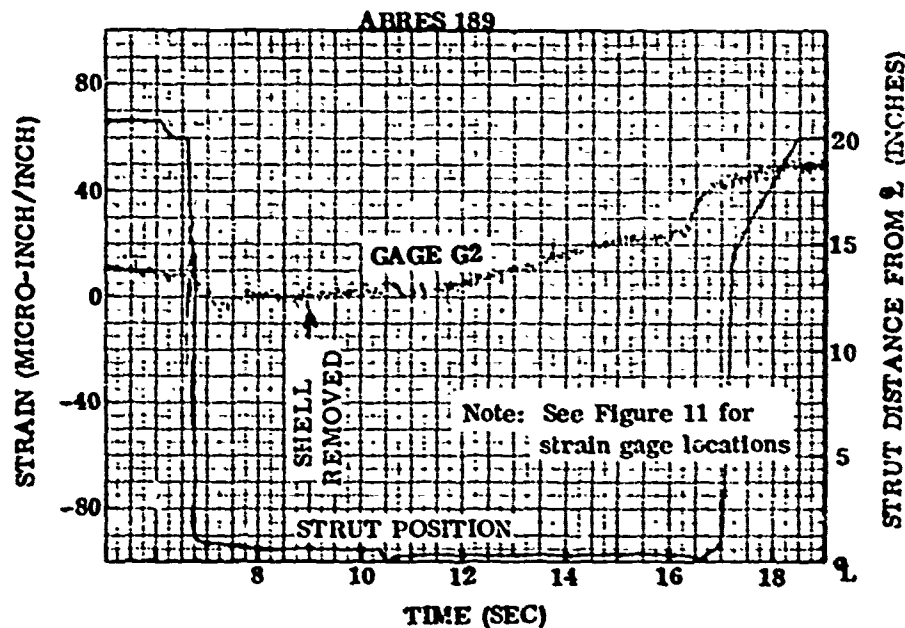
(b)

Figure 59. Strain gage response for Test 189.
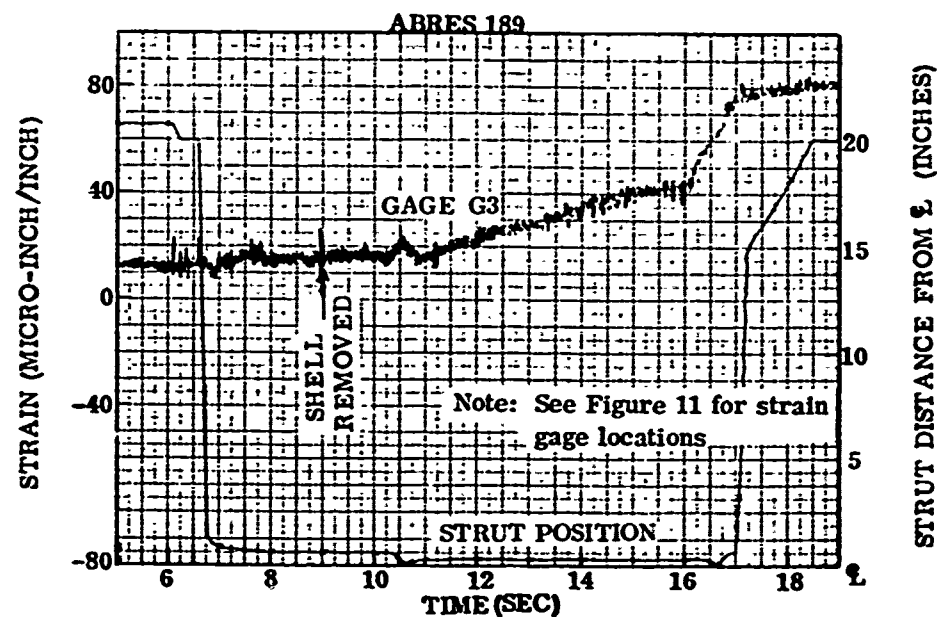
(c)
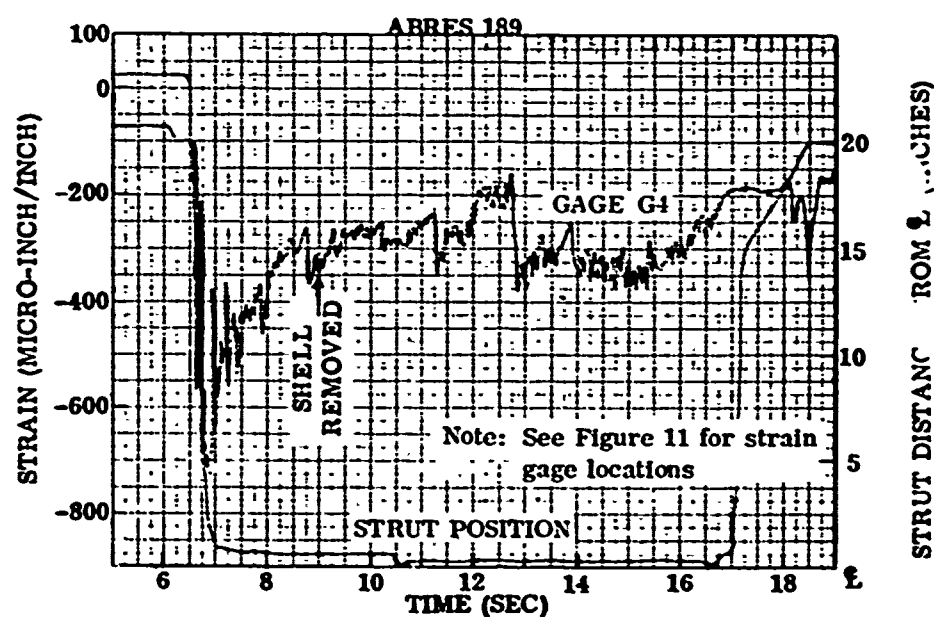
(d)

Figure 59 (continued). Strain gage response for Test 189.

2. Strain gages at this location in the substructure cannot detect
the nosetip response, if any, during primary tip removal in
a rocket motor test.*

2.7 CONCLUSIONS

The results of the A.N.T./ERN Design Verification Test program discussed in the pre-
ceding sections lead to the following conclusions:

With respect to the A.N.T./ERN nosetip designs:

1. A graphite shell primary nosetip, properly sized and designed,
can be removed in a clean, predictable fashion without adverse
effects on downstream components.
2. A monolithic tungsten subtip with a length of four to five inches
is not a viable erosion-resistant concept for the A.N.T. design
flight environment.
3. Acoustic recession sensor technology for tungsten applications
requires further development or concept modifications.
4. In-flight shell removal and heatshield stripback rates can be
measured successfully with backface thermocouples.
5. No significant aerodynamic load pulses during shell removal
could be measured by strain gages mounted on the aft substructure.

With respect to the use of the ABRES/AFRPL facility for full-scale performance verifi-
cation testing:

1. The AFRPL facility provided an excellent test vehicle for assessing
the thermostructural and recession capability of graphite, carbon,
and tungsten nosetip materials. Further operating refinements and
environment characterization should produce an excellent nosetip
material testing capability.
2. Present flowfield anomalies such as igniter particles in the pre-
heat and shock formations during operation at low chamber pressure
did not appear to compromise ultimate test results.
3. The presence of quantities of unburned fuel in the boundary layer
make interpretation of film data difficult and render surface
pyrometer measurements nearly useless.

2.8 RECOMMENDATIONS

The conclusions of the Design Verification Test series resulted in the following
recommendations:

1. Because of the high probability of crack initiation predicted for
monolithic tungsten subtips, the present A.N.T./ERN subtip
designs should not be flight-tested at this time.

---

* Subsequent to this experiment, a more sophisticated aerodynamic load measurement
experiment using strain gages was designed for flight test on A.N.T. II. Full-scale flight units have
been built and calibrated to measure axial forces and bending moments in the substructure (Reference 23).

2. The monolithic tungsten subtip should be replaced by a design, such as a segmented tungsten concept, that will enhance its thermostructural performance capability.

3. Future development or verification tests of similar concepts or designs should be tested in the refined AFRPL test facility with the present benzonitrile/liquid oxygen propellant system. The rocket exhaust flowfield should be improved by elimination of the boundary layer clouds.

3.0   SEGMENTED TUNGSTEN SUBTIP DEVELOPMENT

The segmented nosetip concept was conceived as an approach to reduce the high proba-
bilities of thermostructural failure associated with the monolithic tungsten designs. With this tech-
nique, the subtip is manufactured in the same external shape as the monolithic designs, but is
comprised of a number of small components. This results in lower thermal stresses in the segments
because of the smaller temperature gradients in the smaller components and because of the ability
of the segments to deform elastically under the influence of the temperature gradient. The probability
of failure also is reduced by the smaller unit volumes of highly stressed material. Because a frac-
ture in one segment cannot propagate across the segment boundaries, any fracture that does occur
will not result in a catastrophic failure of the assembly, thereby providing a form of artificial frac-
ture toughness.

Several analytical and experimental programs were performed to develop and validate
the segmented subtip concept. An early test program was run at the Air Force Flight Dynamics
Laboratory (AFFDL) 50 megawatt arc-jet facility in November 1974 (Reference 24) to evaluate the
basic feasibility of the segmented concept and to compare several preliminary designs. A particular
objective of the tests was to determine if the segmented models would experience increased heating
and surface recession at the segment boundaries. The results indicated that the segmented models
had about the same total recession as solid tungsten models, but that some configurations had a
greater tendency to form scallop patterns in regions of segment boundaries.

After concept feasibility was demonstrated in the initial ground test program, analyses
were performed to select optimum segment configurations and to improve design and construction
details. An additional test series was then run in the 50 megawatt facility to evaluate the improved
designs. This section describes the segment design analyses and the second 50 megawatt ablation
test program (Reference 25). Later sections present the results of flight test evaluations of seg-
mented nosetip designs.

3.1   SEGMENT DESIGN ANALYSES

Analyses were performed to predict the thern $_\Lambda$ stress response of subtip components
in a flight environment. The calculations were performed with the SAAS III finite element computer
code (Reference 14) using material properties for extruded billets of two-percent thoriated tungsten
(Section 2.6.2). The analyses accounted for temperature-dependent material properties with nonlinear
stress-strain curves. Time-dependent external shapes, pressure loads, and internal temperatures
were predicted with the NOSEC computer code (Reference 7) and were included in the analyses.

The probability of crack initiation was estimated from the Priddy stress-based failure
criterion for brittle anisotropic materials (Appendix A) using the predicted stress distributions.
This criterion accounts for arbitrary stress states and multiaxial stress interactions using nine mea-
surable strength parameters to describe the failure characteristics of a transversely isotropic mate-
rial. The nine strengths required by the Priddy criterion were based on characterization results for
extruded two-percent thoriated tungsten (Section 2.6.2). The probability of crack initiation at any
point in the subtip was calculated from the proximity of the stress vector to failure surfaces defined
for .arious probabilities of failure by application of the Priddy criterion to uniaxial data reduced by
Weibull statistics. Volume effect corrections also were applied to the failure probability of each
volume of material represented by a finite element in the computer code.

90

The overall probability of crack initiation in any component of the subtip was calculated from the cumulative product of finite-element probabilities over all brittle elements (below 400°F) expressed by:

$$P_F = 1 - \Pi \left(1 - P_f\right) \qquad (2)$$

where P_f is the probability of crack initiation in any single brittle element, and P_F is the overall probability of crack initiation for the entire component.

The thermostructural responses of the segment and stud components of the segmented subtip were calculated for the design shown in Figure 60 and expressed in terms of component probability of failure. These results were compared to results for a monolithic design of the same external shape. Segment thicknesses and cone angles were varied to establish guidelines for optimizing the design. Thick segments with shallow cone angles are less costly to manufacture, but generate higher thermal stresses because they are less compliant. That is, thermal gradients are accommodated more readily by deformation in thin segments with large cone angles. The computed failure probability is plotted in Figure 61 as a function of segment aspect ratio (defined as the ratio of thickness, t, to outside radius, R) for forward, middle, and aft segments with 35-degree cone angles. All cases analyzed fall close to a common curve, illustrating the dominating effect of aspect ratio. Low failure probabilities can be achieved by designing all segments with aspect ratios of 0.10 or below. This permits thicker segments to be utilized near the aft end of the segment stack for economy.
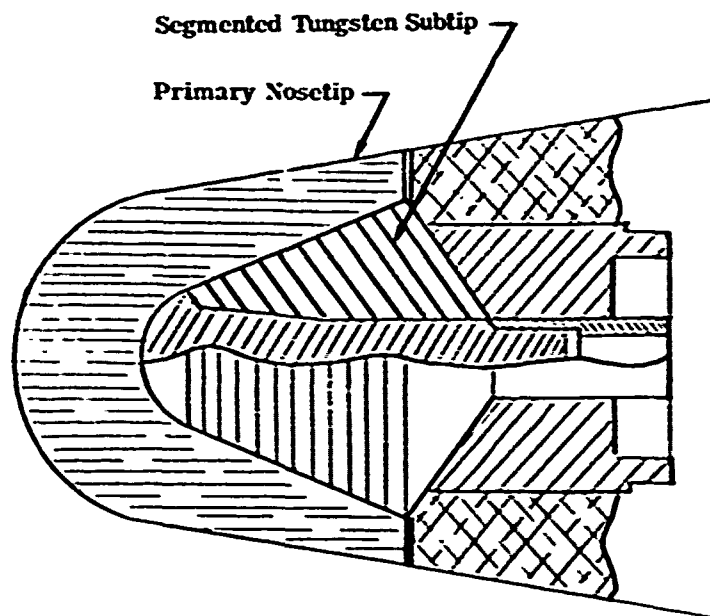
Figure 60. Segmented tungsten subtip design concept.

91
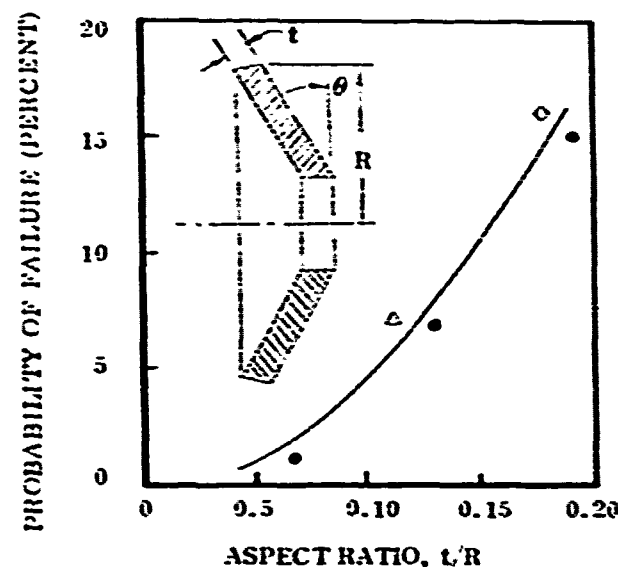
Figure 61. Effect of aspect ratio on thermostructural
response of subtip segments.

Figure 62 shows the effect of cone angle on the thermostructural response of the middle segment with a thickness of 0.250 inch. It can be seen that segment cone angles of about 35 degrees are required to achieve high survival probabilities by segment deformation under thermal gradients, but that larger cone angles have only marginal additional benefit. According to these figures, high segment survival probabilities are possible with reasonable design combinations of segment thickness and cone angle.

OUTSIDE DIAMETER
EQUALS 3.5 INCHES
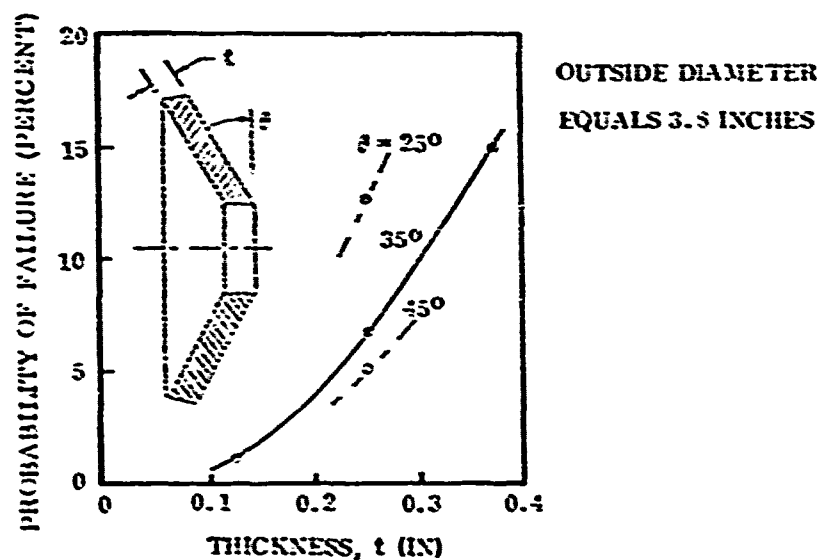
Figure 62. Effect of segment cone-angle on
thermostructural response.

Calculated failure probability histories for the segmented subtip components, including the stud, and for a monolithic subtip are shown in Figure 63. Although the stud generates maximum stresses of the same order as the monolithic subtip, the critically stressed volume is much lower and, with the lower transverse stress, results in a much lower probability of failure. The subtip segments are 0.250-inch thick and have 35-degree half-cone angles. The improvement in survival probability offered by the segmented construction approach is apparent.
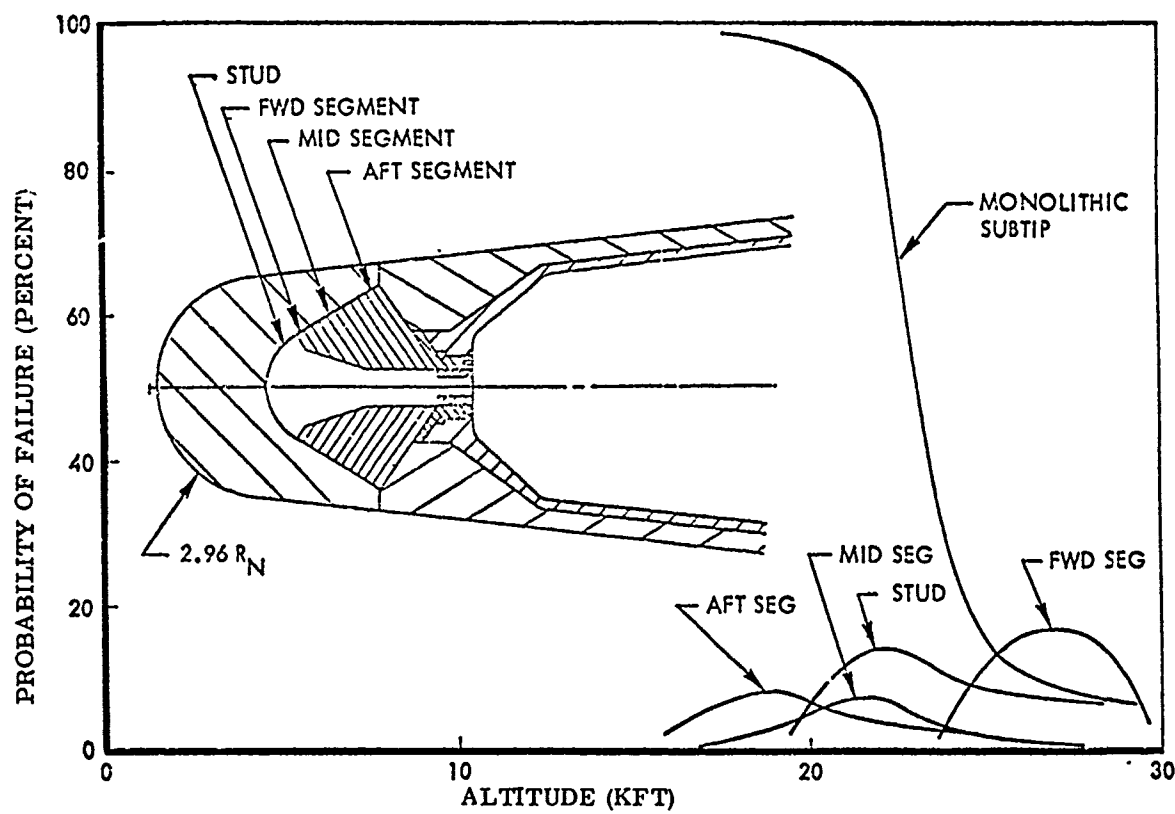
Figure 63. Tungsten subtip thermostructural response summary.

The failure probabilities shown in Figures 61, 62, and 63 were calculated using the failure characteristics of three-inch diameter extruded two-percent thoriated tungsten (Section 2.6.2) to provide a direct evaluation of the effect of the segmented design relative to the monolithic design. However, significant material improvements are available for the segmented design which make this comparison very conservative. It is probable that large additional improvements can be accomplished by optimizing the methods for fabricating the segments. For example, the segments could be coined from cross-rolled tungsten plate or forged and coined from pressed and sintered billets. Since these forms of tungsten generally are more flaw-free and have much more cold work than the large diameter extruded billets, the resultant segments should have significantly higher failure strengths and lower ductile-brittle transition temperatures (DBTT) than segments made from extrusions. Consequently, it is reasonable to expect much lower failure probabilities than those indicated in Figures 61, 62, and 63. In addition, the stud can be fabricated from a smaller diameter extrusion or swaging and, consequently, can be upset-forged to improve the transverse properties by producing a more equiaxial

grain structure. Since the monolithic subtips tested previously (Section 2.0) were critical with respect to transverse direction properties, it is also reasonable to expect that upset-forging of the small diameter billets will improve the thermostructural performance of the stud.

Artificial fracture toughness provided by segment boundaries, although not assessed quantitatively, is believed to be another major advantage of the segmented tungsten design concept. Cracks initiating in any component can propagate only to the nearest boundary. Because of the design geometry, several adjacent segments must fail to permit loss of material. Cracks in the stud resulting from transverse stresses can propagate only to the segment-stack boundary and the segments should restrict the crack from opening.

3.2 ABLATION TEST PROGRAM

After the initial ground test program (Reference 24), several important improvements were made in segmented nosetip designs. The new features, which were evaluated in the present test series, included:

1. Selection of forward-facing cones as the optimum segment configuration, based on evaluations of the test results and additional analyses (Section 3.1).
2. Addition of a tapered center stud to provide positive retention of the segments.
3. Use of forged segments to improve mechanical properties and to reduce material consumption.
4. Use of thermocouples between segments to provide an indication of the axial recession history.

The segmented tungsten subtip models tested in this series were designed primarily to investigate the ablation behavior relative to monolithic designs. No attempt was made to produce a specimen configuration that would provide a meaningful thermostructural test of the concept. In principal, this objective would be very difficult to achieve because of the size constraints and the heating distribution in the arc-jet environment.

Another erosion-resistant nosetip (ERN) design concept was also studied in the previous test program. The essential components in this design were a copper-infiltrated tungsten core and a surrounding solid tungsten sleeve. The purpose of the solid sleeve was to prevent loss of the melted copper infiltrant to the low-pressure sidewall region, which would reduce the transpiration cooling effectiveness in the stagnation region. This concept was tested in a cone-cylinder configuration and experienced lower recession rates than solid models of either pure tungsten or copper-infiltrated tungsten (Reference 26). This sleeve construction has since been adapted to the more conventional sphere-cone nosetip configuration. In addition, a design is being considered in which copper-infiltrated tungsten segments are used in conjunction with an infiltrated tungsten core. Models based on both of those infiltrated tungsten concepts were included in the current tests.

The test series also afforded an opportunity for ablation gage experiments. A shear wave pulse/echo ultrasonic gage had been selected previously for development as a tungsten ablation sensor (Reference 2). However, in the most recent flight and ground tests of the shear wave gage, unacceptable degradation of the echo signal strength occurred. Thus, two alternate ultrasonic ablation sensor concepts were tested in the current series:

94

1. A compression wave pulse/echo gage and,
2. a compression wave resonant frequency gage.

Both of these concepts were expected to benefit from the lower attenuation coefficient of compression waves (relative to shear waves) in hot tungsten (Reference 27). The resonant wave sensor had the added advantage of lower carrier frequencies.

3.2.1   Model Descriptions

3.2.1.1   Ablation Models

The ablation test models consisted of six different designs, illustrated in Figure 64, which were selected to evaluate various aspects of segmented nosetip design and fabrication. All models had the same external sphere-cone geometry to eliminate the effects of shape differences on ablation performance.
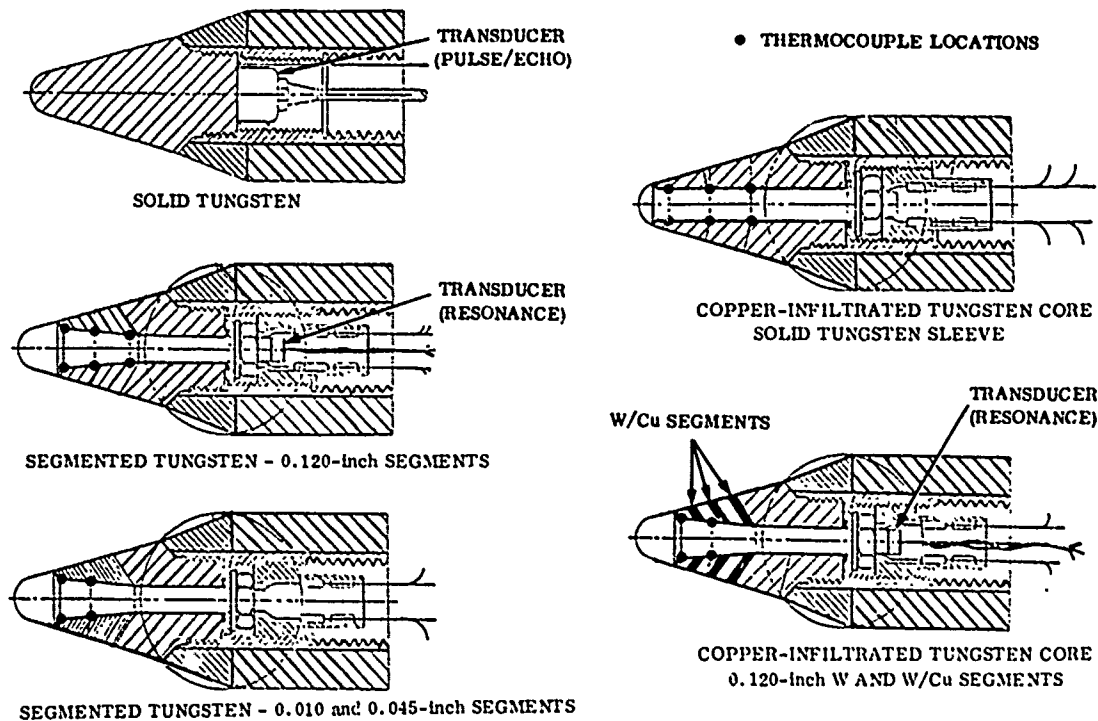
Figure 64.   Model configurations.

The solid (monolithic) configuration was included as a tare model to provide a reference basis for the ablation performance comparison. These models were machined from a 2 5/8-inch diameter billet of extruded commercially pure tungsten fabricated by the General Electric Company (G.E.), Cleveland, Ohio.

All three types of segmented tungsten models were of the same basic design, as indicated in Figure 64. Three different segment thicknesses were used to assess the effect of this parameter

on thermal and structural performance. The segmented models all utilized a tapered center stud to provide positive retention of the segments during ablation. The studs were all machined from three-inch diameter billets of extruded tungsten two-percent thoria fabricated by G.E., Cleveland. The large aft segment on all models was machined from the same commercially pure tungsten used for the solid tare models.

The 0.120-inch thick segments were constructed by first cutting 0.25-inch thick discs from the 2 5/8-inch diameter commercially pure tungsten billets. These discs were then upset-forged to 0.125-inch thickness, and then forged (coined) to the final conical shape, and finish-machined to the 0.120-inch thickness.

The 0.045-inch thick segments were constructed from 0.060-inch thick sheets of commercially pure tungsten supplied by Schwarzkopf Development Corporation. These segments were coined to the conical shape and then finish-machined to the final 0.045-inch thickness.

The 0.010-inch thick segments were coined from 0.010-inch thick sheets of commercially pure tungsten supplied by AMAX, Inc. These segments were brazed together and then machined as a unit to the final conical shape. The small thickness made all handling and machining operations for these thin segments very difficult.

Two types of models utilizing infiltrated tungsten were tested. Both types used infiltrated tungsten supplied by Teledyne Wah Chang of Albany, Oregon. This material was constructed by infiltrating approximately 10 percent (by weight) of copper into sintered billets of commercially pure tungsten. The "infiltrated core" models utilized a center stud of this infiltrated tungsten, and a surrounding sleeve made from the 2 5/8-inch diameter billets of G.E. commercially pure tungsten. The "infiltrated segments" models had a center stud of infiltrated tungsten surrounded by 0.120-inch thick segments. Alternate segments were made of commercially pure G.E. tungsten and the copper-infiltrated tungsten.

3.2.1.2 Model Instrumentation

One of each type of segmented model was instrumented with in-depth thermocouples. The 0.120-inch thick segmented tungsten and the infiltrated core models each had six thermocouples located along the stud as indicated in Figure 64. Each of the other segmented models had four thermocouples located at the two forward stations. The exact thermocouple stations are given in Table 20. Tungsten versus tungsten/26-percent rhenium thermocouples were used in the two most forward (hotter) locations, while the remaining thermocouples were platinum versus platinum/13-percent rhodium. The types and output ranges of the thermocouples on each model are summarized in Table 21.

Three models (one solid tungsten, one segmented tungsten, and one infiltrated segments) were instrumented with K West ultrasonic ablation sensor transducers bonded to the back surface as illustrated in Figure 64. A Chromel/Alumel thermocouple also was bonded to the back surface, adjacent to the transducer, to measure the approximate temperature history. The sensor on the solid tungsten model used a pulse/echo (compression wave) transducer with a frequency of 1.15 mHz. With this type of sensor, the instantaneous model length is proportional to the round-trip time of the acoustic signal (Reference 2). The other two sensors utilized a newly developed resonant frequency technique in which the model length is inversely proportional to the frequency at which resonance is observed to occur.

96

Table 20. Thermocouple locations in segmented models.

MODEL*	AXIAL DISTANCE FROM STAGNATION POINT (INCH)					
	TC 1	TC 2	TC 3	TC 4	TC 5	TC 6
1-2	0.570	0.882	1.320	0.525	0.917	1.318
1-3	9.620	0.985	1.430	0.600	0.970	1.410
1-4	0.537	0.913	0.552	0.912		
2-3	0.510	0.902	0.514	0.918		
3-3	0.555	0.899	0.568	0.955		

* See Table 22 for model number identifications.

Table 21. Thermocouple instrumentation summary.

RACK NO.	STRUT NO.	MODEL	THERMOCOUPLES		
			NO.	TYPE*	RANGE (MV)
1	1	Solid Tungsten	1	K	0 – 50
	2	Segmented: 0.120-inch segments	2	G	0 – 50
			4	R	0 – 25
	3	Infiltrated Core	2	G	0 – 50
			4	R	0 – 25
	4	Infiltrated Segments	2	G	0 – 50
			2	R	0 – 25
	5	Calorimeter	5	K	0 – 50
2	1	Segmented: 0.120-inch segments	1	K	0 – 50
	3	Thin Sheet: 0.010-inch segments	2	G	0 – 50
			2	R	0 – 25
	5	Calorimeter	5	K	0 – 50
3	1	Infiltrated Segments	1	K	0 – 50
	5	Thin Sheet: 0.015-inch segments	2	G	0 – 50
			2	R	0 – 25

*Thermocouple Types:

K   Chromel versus Alumel
G   Tungsten versus Tungsten 26 percent Rhenium
R   Platinum versus Platinum 13 percent Rhodium

97

3.2.1.3   Rotating Sting

One of each type of ablation model was modified for installation on a rotating sting assembly (Reference 28). In these tests, the models were rotated continuously throughout the test in an attempt to eliminate the effects of possible flowfield asymmetries on ablation and thermostructural performance. The rotating sting system is illustrated in Figure 65. The rotating hub, which serves as the specimen holder, is driven by a 1/3 horsepower compressed air motor. At design conditions, the motor consumes 15 cfm of air at a source pressure of 90 psi. The stall torque is 156 inch-pounds. The cold, expended air is routed around the motor case through passages in the front of the motor housing and exhausted out of the annular gap between the hub and the fixed sting assemblies. This delivers maximum cooling to the critical thrust bearing area and, at the same time, purges the sting interior of hot gases.
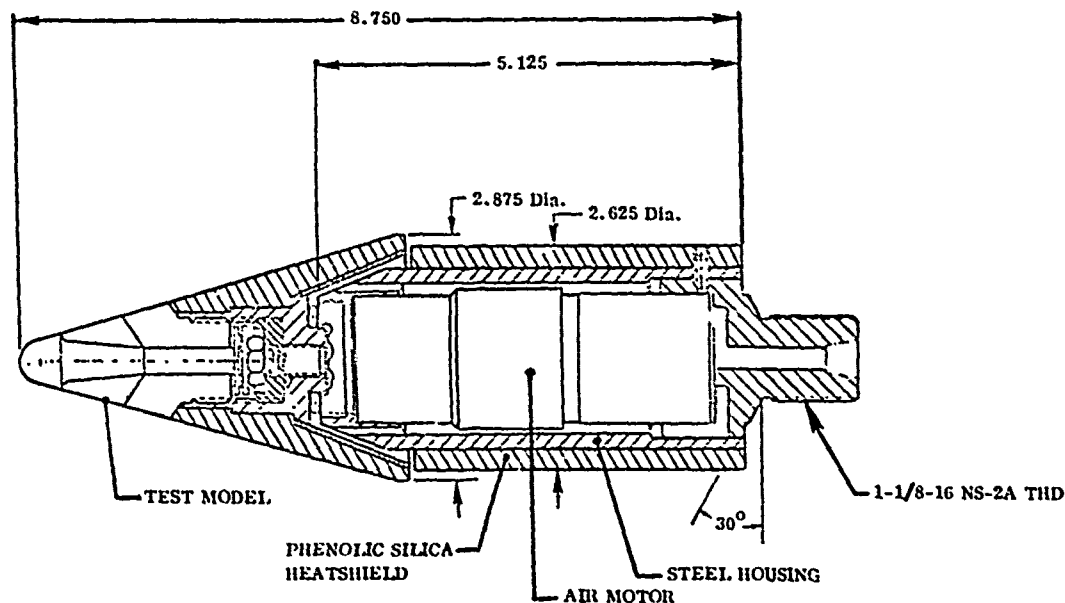
Figure 65. Rotating sting assembly.

The sting/ablation model assembly was 8.75 inches long from the specimen tip to the interface with the facility strut. It was designed to mate directly to the strut. The 1/4-inch copper tube airline passes through the instrumentation lead passage.

3.2.2   Test Description

3.2.2.1   Facility Description

The tests were performed in the Reentry Nosetip (RENT) leg of the Air Force Flight Dynamics Laboratory (AFFDL) 50 megawatt arc-jet facility. The general layout of the facility is illustrated in Figures 66 and 67. A complete description of the facility is given in Reference 29.

The models were mounted on a linear motion model carriage for sequential insertion into the test stream. The carriage has five struts laterally spaced one foot apart, as illustrated

98
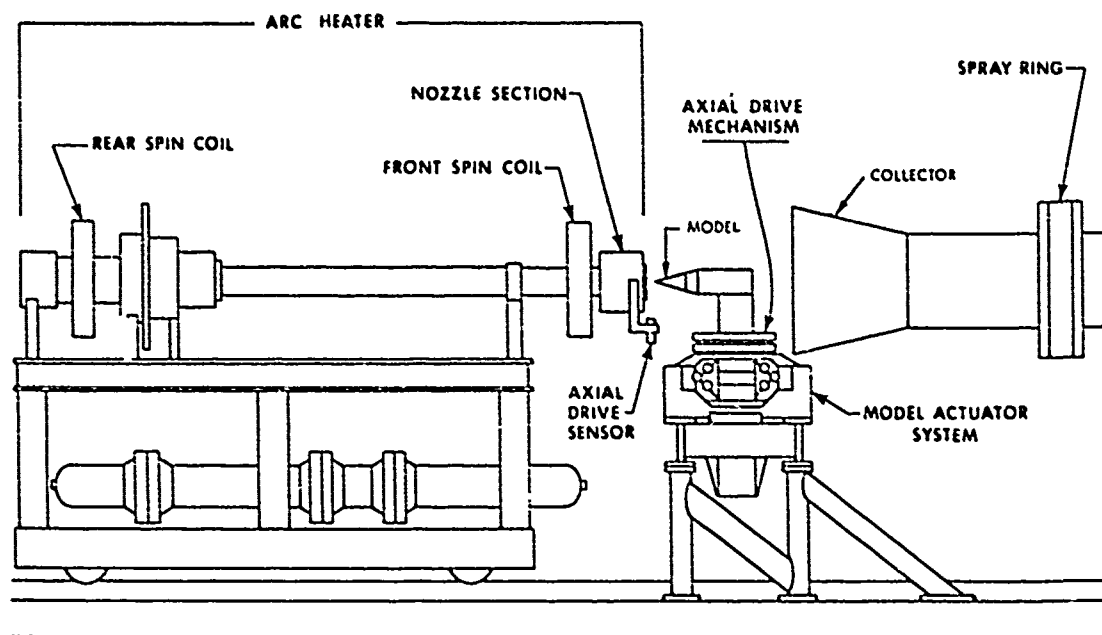
Figure 66. AFFDL 50 MW arc-jet RENT test leg schematic.
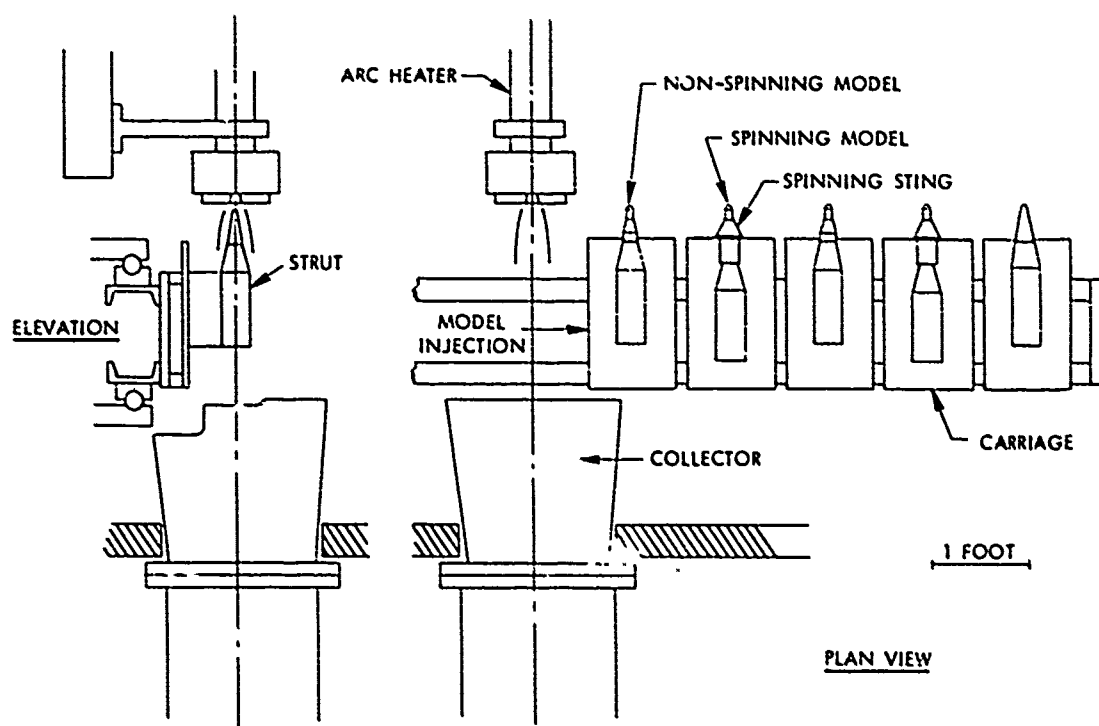
Figure 67. AFFDL 50 MW arc-jet RENT test section and model support.

99

in Figure 67. Each strut has a servo-controlled axial drive system, coupled to an infrared sensor, that can be used to control the models at a specified constant location. For the present tests, the models were maintained at a constant distance of approximately 0.1 inch from the nozzle exit plane.

3.2.2.2   Test Conditions

All of the runs were made with the 1.38-inch exit diameter flared nozzle (10138F) with a reservoir pressure of 1500 psig. The nominal dwell time (model on flow axis) was two seconds. The nozzle contour is shown in Figure 68. Since the flow leaving the nozzle is expanding, the pressure continues to decline along the test section centerline. At the test location of 0.1 inch from the nozzle exit plane, the model stagnation pressure is approximately 75 atmospheres. In the mode of operation used in these tests, there is a strong radial variation of enthalpy, with the peak value occurring at the centerline. Since the flow at the edge of the model boundary layer comes from the hot central core, this produces an effective stagnation enthalpy of about 6000 Btu/lb.
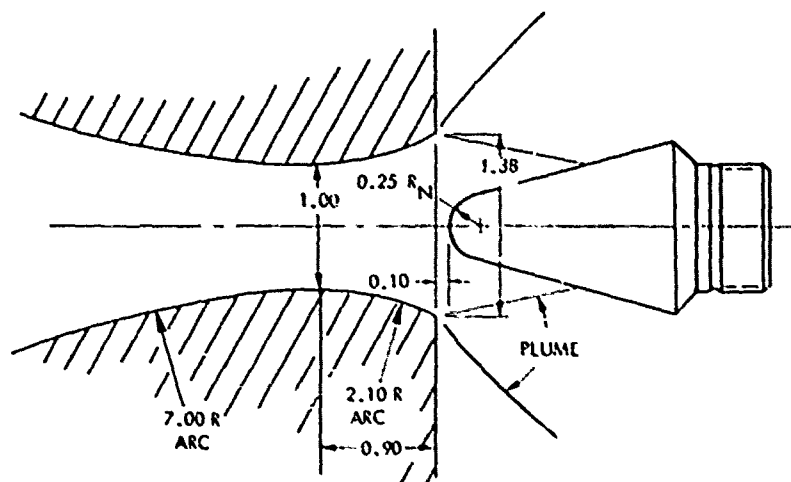
Figure 68.   AFFDL 50 MW arc-jet 1.00/1.38 solid nozzle.

3.2.2.3   Data Sources

Several ablation models were equipped with recession sensors and in-depth thermocouples, as described in Section 3.2.1.2. However, the principal source of ablation data was high-speed motion picture films. All runs were photographed by three cameras: two Photosonic cameras sighted from either side of the models, and one overhead Hycam camera. The Photosonic cameras used black-and-white film and were operated at approximately 1000 frames/second. The Hycam used color film and was operated at a nominal speed of 400 frames/second. Three pyrometers were focused as near as possible to the model stagnation point.

3.2.2.4   Test Matrix

The complete test matrix is summarized in Table 22. A total of 20 models were tested, consisting of two solid tungsten tare models, 16 segmented models, and two calorimeter models. The calorimeter model contained five null-point sensors (with Chromel/Alumel thermocouples) at

the locations indicated in Figure 69. This model was included on two of the racks to obtain both an indication of the consistency of the test conditions during this series and a comparison with previous tungsten ablation tests.

Table 22. Test matrix — segmented tungsten ablation test program.

| Heater Run No.	Strut No.	Model Type	Model Number	Number of Thermocouples	Ablation Gage	Rotating Sting	Actual Dwell Time (sec)
	1	Infiltrated Segments	3-1	1	Resonant	No	1.80
	2	Thin Sheet: 0.010 Segments	4-2	0	No	Yes	1.87
R62-006	3	Segmented: 0.120 Segments	2-1	1	Resonant	No	1.85
	4	Segmented: 0.120 Segments	3-2	0	No	Yes	1.74
	5	Calorimeter	Cal	5	No	No	Swept
	1	Solid Tungsten	1-1	1	Pulse/Echo	No	1.82
	2	Solid Tungsten	2-2	0	No	Yes	1.88
R62-007	3	Thin Sheet: 0.045 Segments	4-3	0	No	No	1.86
	4	Thin Sheet: 0.045 Segments	3-4	0	No	Yes	1.98
	5	Calorimeter	Cal	5	No	No	Swept
	1	Infiltrated Core	3-5	0	No	No	1.91
	2	Infiltrated Core	2-4	0	No	Yes	1.96
R62-008	3	Segmented: 0.120 Segments	4-1	0	No	No	1.90
	4	Infiltrated Segments	4-4	0	No	Yes	1.86
	5	Segmented: 0.120 Segments	1-2	6	No	No	1.81
	1	Thin Sheet: 0.010 Segments	4-5	0	No	No	1.87
	2	Thin Sheet: 0.010 Segments	3-3	4	No	No	1.90
R62-009	3	Thin Sheet: 0.045 Segments	2-3	4	No	No	1.90
	4	Infiltrated Segments	1-4	4	No	No	1.97
	5	Infiltrated Core	1-3	6	No	No	1.91
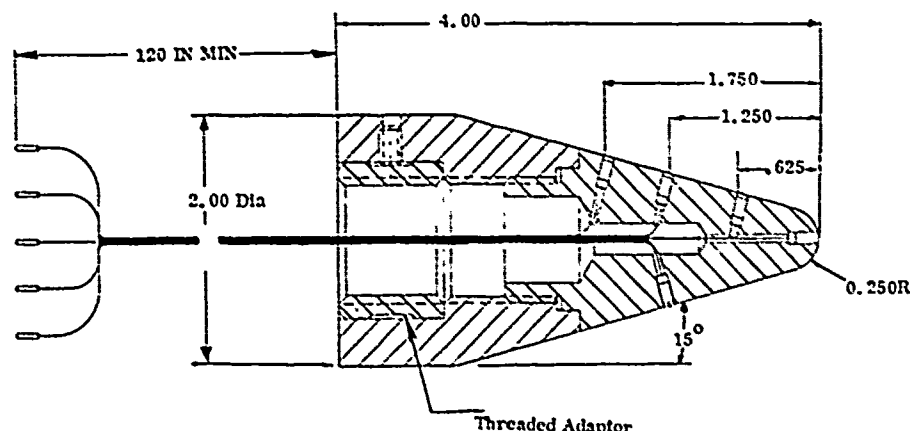
Figure 69. Calorimeter model.

101

3.2.3 Test Results

In this section, the physical data and evidence obtained during the program are presented. Post-test analyses and data interpretation are discussed in Section 3.2.4.

3.2.3.1 Ablation Performance

After completion of the tests, the models were inspected and photographed. Overall recession depths were obtained by comparisons of pre-test and post-test measurements. Recession histories were obtained from the motion picture films; the films were also reviewed for loss of solid material and other significant events.

Post-test photographs of the models, grouped according to type, are shown in Figures 70 through 75. The general appearance of the models can be summarized as follows:

1. All of the spinning models ablated symmetrically. The appearance of the ablating face of these rotating models also was superior, with a more uniform texture than the comparable non-spinning versions (e.g., Figures 70 and 72).
2. The segments of the non-spinning 0.010-inch thin-sheet models were separated and badly warped, especially in Model 4-5 (Figure 71).
3. The ablating faces of the infiltrated segment models were nearly planar (Figure 74). The faces of the two non-spinning versions were at an angle to the model axis. The face of Model 3-1 was slightly concave. _
4. The tungsten sleeves of all of the infiltrated core models ablated into a "turbulent shape" with scallop patterns (Figure 75). None of the other models had such patterns.

The motion pictures showed that the distortion in the two non-spinning thin-sheet (0.010-inch segments) models occurred upon exit from the jet. During the dwell period at the jet centerline, the models ablated in a normal fashion. However, as they moved laterally through the jet boundary, the segments spread apart and several segments were torn from each model. No similar spreading of segments occurred in the spinning version; however, the remnants of one 0.120-inch segment which had nearly ablated away, was torn from the model at exit. No solid material loss was observed from any of the other models tested.

The movies also revealed some unexpected behavior in the non-spinning infiltrated segment models. These models ablated normally until the forward pure tungsten segment ablated through at one point on the periphery. The nose caps then became asymmetric very rapidly due to the relatively high ablation rate of the locally exposed infiltrated tungsten. In the case of Model 3-1 (Figure 74), in particular, there was a strong coupling between the nose shape and flowfield, which promoted the asymmetry. About halfway through the two-second dwell period, the nose formed into a concave wedge, which deflected the hot enthalpy core, as indicated in Figure 76. Thereafter, there was almost no recession of the wedge leading edge. Thus, the angle between the face and the model axis continued to decrease throughout the test, while the overall model length remained nearly constant.

The axial recession histories obtained from the motion pictures, along with the indicated steady-state recession rates are shown in Appendix B. The recession results are summarized in Table 23.

MODEL 2-2
ROTATING STING

SOLID TUNGSTEN

MODEL 1-1
FIXED STING
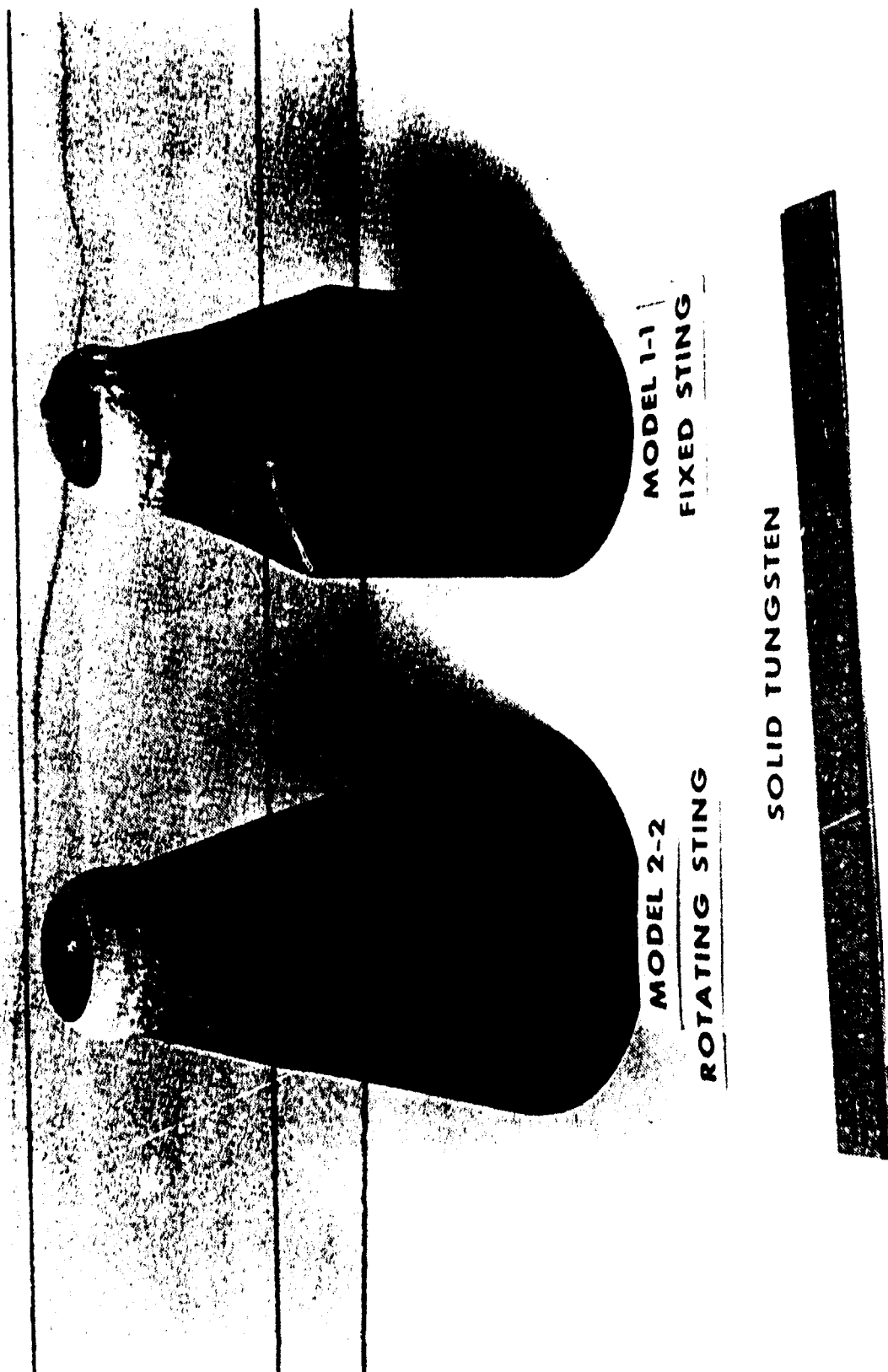
Figure 70. Post-test photograph, solid tungsten models.
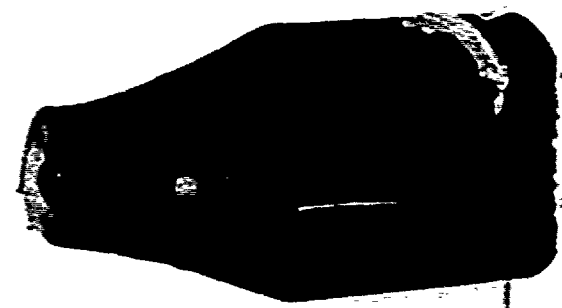
MODEL 3-3
FIXED STING

MODEL A-5

MODEL A-2
ROTATING STING
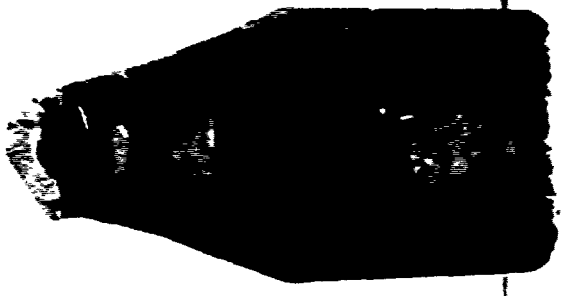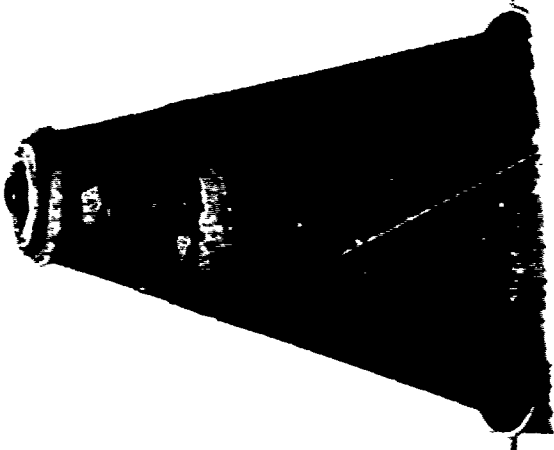
SEGMENTED TUNGSTEN
0.010 INCH SEGMENTS

Figure 71. Post-test photograph, 0.010-inch segment models.

MODEL 2-3　　MODEL 4-3　　MODEL 3-4

FIXED STING　　ROTATING STING

SEGMENTED TUNGSTEN

0.045-INCH SEGMENTS

Figure 72.　Post-test photograph, 0.045-inch segment models.

105
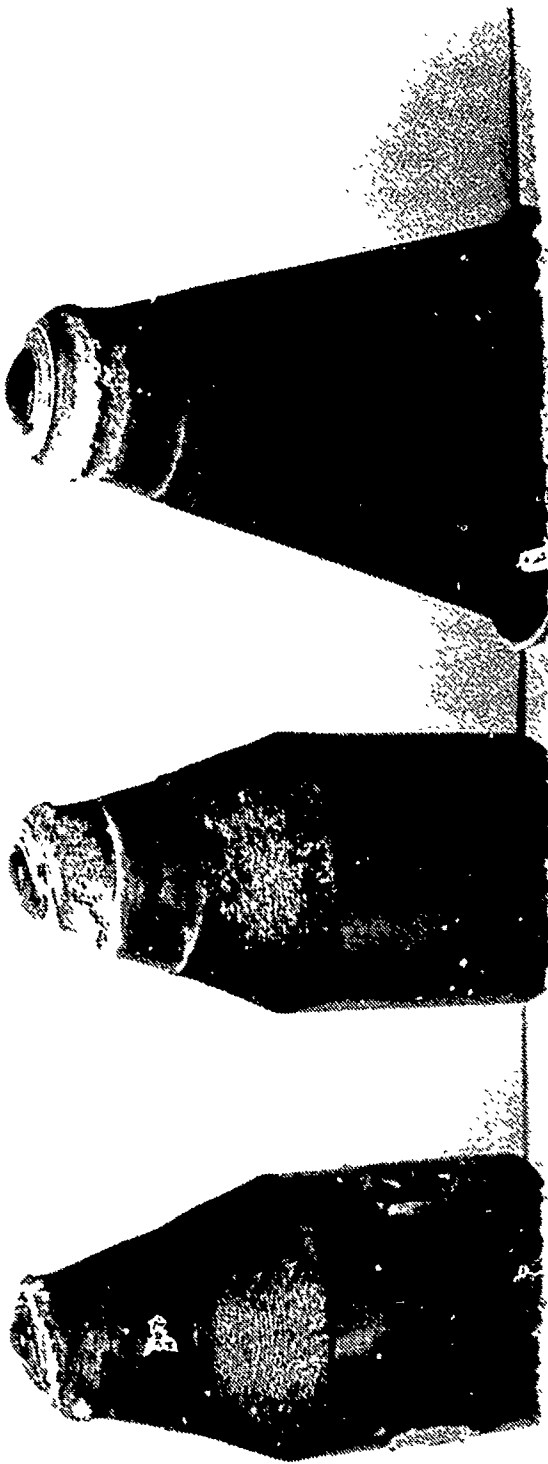
MODEL 1-2

MODEL 2-1
FIXED STING

MODEL 4-1

MODEL 3-2
ROTATING STING

SEGMENTED TUNGSTEN
0.120 INCH SEGMENTS

Figure 73. Post-test photograph, 0.120-inch segment models.

MODEL 1-4   MODEL 3-1   MODEL 4-4

FIXED STING   ROTATING STING
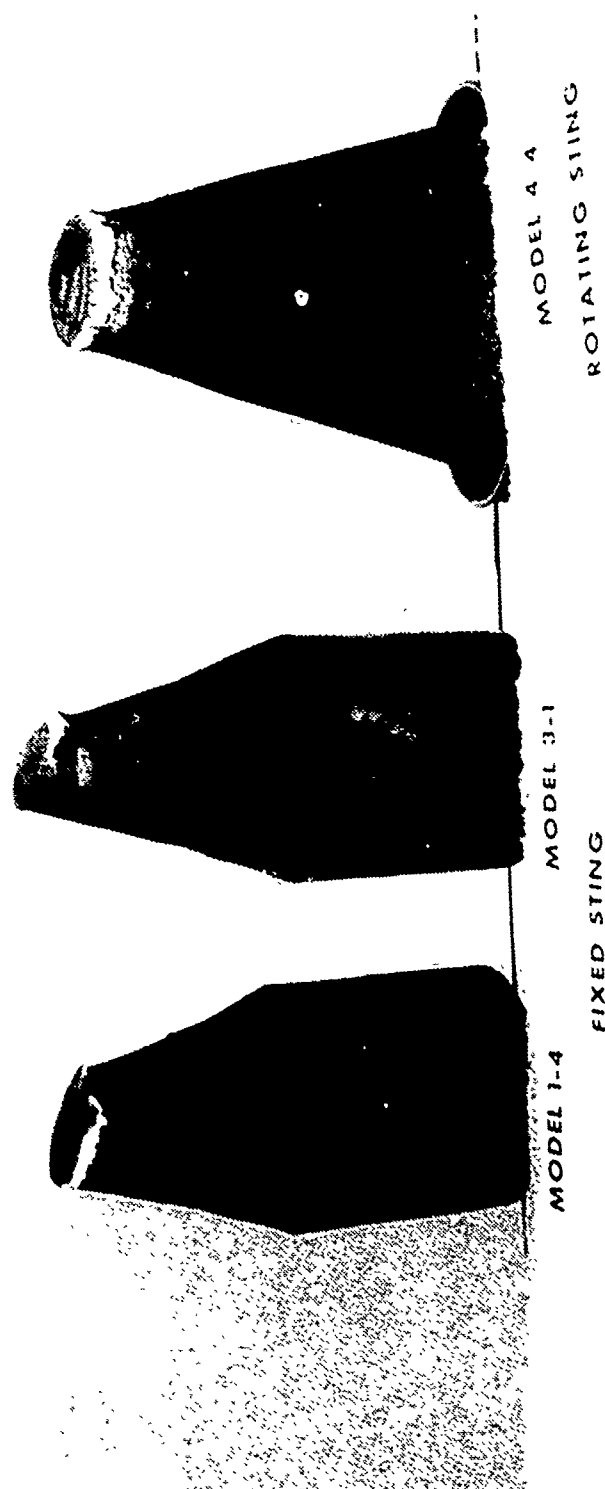
COPPER INFILTRATED
TUNGSTEN CORE

0.120 INCH W AND W CU SEGMENTS

Figure 74. Post-test photograph, infiltrated tungsten segment models.

MODEL 1-3

MODEL 3-5

MODEL 2-4

FIXED STING

ROTATING STING

COPPER-INFILTRATED
TUNGSTEN CORE

SOLID TUNGSTEN SLEEVE
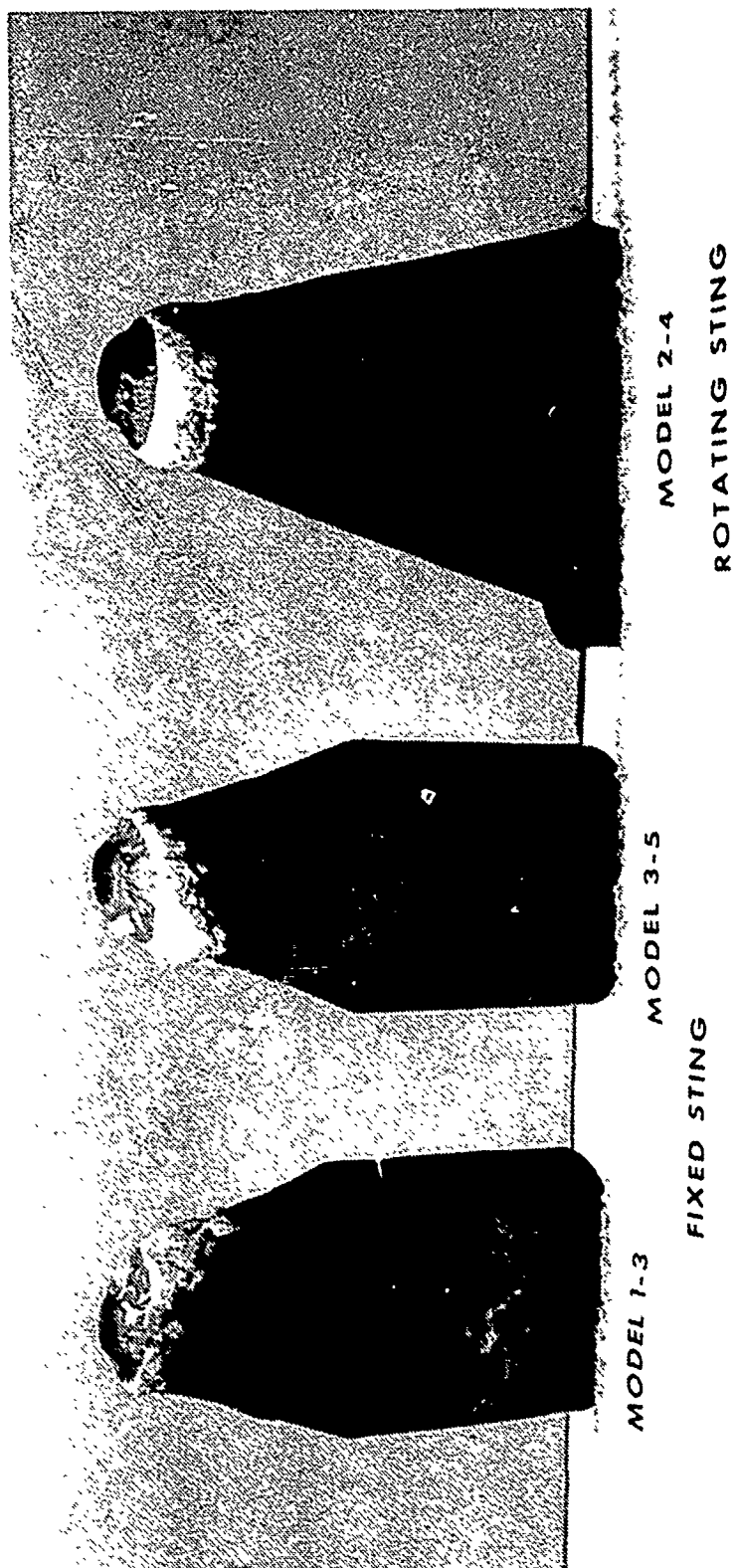
Figure 75. Post-test photograph, infiltrated tungsten core models.

HIGH ENTHALPY CORE (LUMINESCENT)

NOSETIP MODEL
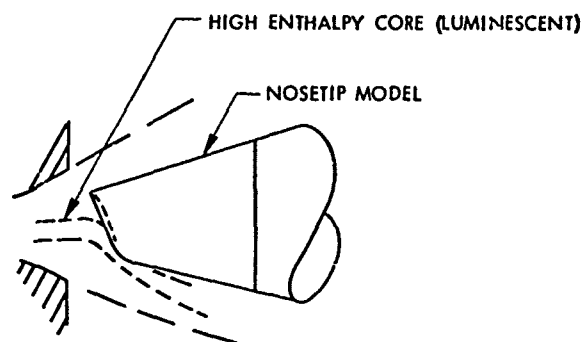
Figure 76. Flow deflection on flat-nose models.

Table 23. Recession data summary — segmented tungsten models.

Model No.	Overall Recession (inch)	Average[1] Recession Rate (in/sec)	Steady State[2] Recession Rate (in/sec)	Model Type[3]	Observations
1-1	0.607	0.334	0.427	Solid Tungsten	
1-2	0.781	0.431	0.465	0.120 Segments	
1-3	0.828	0.434	0.445	Infiltrated Core	
1-4	0.750	0.381	0.366	Infiltrated Segments	Concave angular face
2-1	0.553	0.299	0.350	0.120 Segments	
2-2	0.765	0.407	0.483	Solid Tungsten (S)	
2-3	0.715	0.376	0.371	0.045 Thin Sheet	
2-4	0.764	0.391	0.417	Infiltrated Core (S)	
3-1	0.340	0.189	0.281(4)	Infiltrated Segments	Hot enthalpy core deflected by highly angular concave face
3-2	0.499	0.287	0.319	0.120 Segments (S)	
3-3	0.808	0.425	0.433	0.010 Thin Sheet	Segments billowed out w/loss of several at nozzle exit
3-4	0.750	0.380	0.432	0.045 Thin Sheet (S)	
3-5	0.670	0.351	0.380	Infiltrated Core	
4-1	0.768	0.405	0.410	0.120 Segments	
4-2	0.626	0.335	0.428	0.010 Thin Sheet (S)	Single partial segment lost at nozzle exit
4-3	0.629	0.337	0.343	0.045 Thin Sheet	
4-4	0.904	0.486	0.528	Infiltrated Segments (S)	
4-5	0.654	0.350	0.358	0.010 Thin Sheet	Segments billowed out w/loss of several at nozzle exit

(1) Overall recession divided by dwell time.
(2) Recession rate after initial transient; obtained from motion picture data.
(3) (S) After model type designates model was spinning.
(4) Rate before hot enthalpy core was completely deflected (see test).
    Final overall recession rate was almost zero.

3.2.3.2 Thermostructural Performance

No gross thermostructural failures occurred on any of the models. However, close inspection revealed a fine crack in one of the 0.045-inch segments of Model 4-3; the crack occurred in one of the partially ablated segments exposed on the face of the model. A similar crack was found in one of the badly distorted 0.010 segments of Model 4-5. Inspection showed the fracture surfaces were bright and free of oxidation. Metallographic examination revealed that the fractures were intergranular and ductile in nature, indicating that they occurred during cooldown or, possibly, as the model left the jet.

3.2.3.3 Instrumentation Data

Three types of instrumentation data were obtained: 1) segmented model thermocouple temperature histories, 2) calorimeter data, and 3) ultrasonic ablation gage data. The reduced thermocouple data for each segmented model are given in Figures B-19 through B-23 of Appendix B. (The thermocouples adjacent to the ultrasonic transducers were included for diagnostic purposes only. As the transducers did not change temperature during the test, data for these thermocouples are not presented.)

PDA has now run several 50 MW tests with the same basic model configuration as in the present tests (15° half-angle cone with a 0.25-inch nose radius). As no sidewall heating data were available for this configuration, calorimeter model tests were included in an earlier facility entry (Reference 24). However, only one run was made with the 10138 nozzle, and the data for that run are doubtful because the null-point calorimeters were not flush with the model surface.

Thus, for the present series, the null points were replaced and a total of four new runs were completed. (Two of the four runs were made in a contiguous series of PDA 50 MW tests (Reference 28). However, the data for all four runs are presented here.)

The calorimeter model geometry is shown in Figure 69. For the present runs, the model was oriented with the three-sensor ray facing up as indicated in the figure. In the run of Reference 24, the sensor ray faced down.

The mean and range of the stagnation point heat flux measured for all four of the present runs was $11,350 \pm 1400$ Btu/ft^2-sec. The sidewall heat fluxes are plotted in Figure 77. The circles represent the data means for each location, while the vertical bars indicate the range. As can be seen, the single calorimeter on the bottom ray recorded a higher heat flux than the corresponding sensor on the top ray. The data of Reference 24 also indicated higher heating along the bottom ray. To complete the bottom ray curve, two data points from Reference 24 are also plotted on Figure 77; however, because of the null-point problem mentioned previously, these points must be accepted with caution.

The ultrasonic gage data were recorded on magnetic tape. Detailed quantitative analysis of these data required computer processing using a program available at the Aerospace Corporation. However, a qualitative evaluation could be obtained from an oscilloscope display of the signal. The results of such an evaluation were given in Reference 30. The principal conclusions were:

1. The compression wave pulse/echo signal decayed in a manner similar to the shear wave signal in previous tests. It was not possible to obtain useful recession measurements from the data.

2. The resonance peak for the sensor on Model 3-1 moved erratically and indicated little recession. As noted in Section 3.2.3.1, Model 3-1 ablated in a peculiar manner and, in fact, little overall recession occurred.

3. The resonance peak for the sensor on Model 2-1 generally behaved as expected.

Thus, the output from the Model 2-1 sensor was selected for detailed processing.
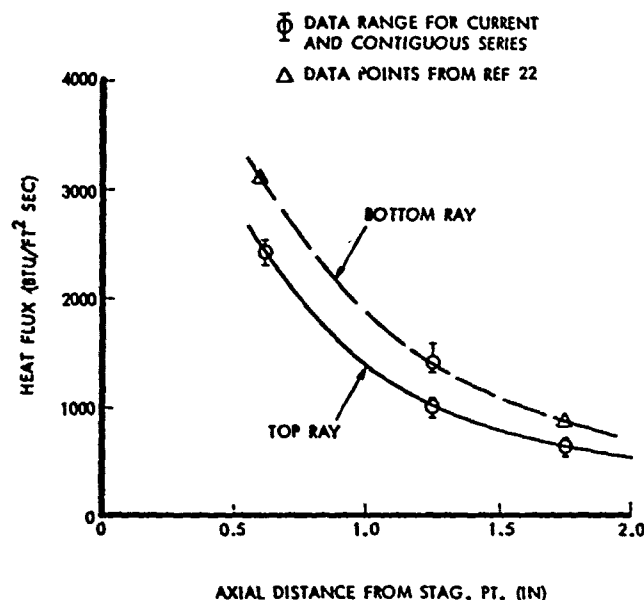
Figure 77. Sidewall heat flux data, AFFDL 50 MW arc-jet.

The computer processing was completed under the direction of S. Howell of the Aerospace Corporation. Figure 78 shows the processed data for the time interval of interest. The frames, each covering a time interval of 0.1 second, are arranged in a vertical display. The left boundary corresponds to a frequency of 50 kHz, the right boundary to 150 kHz. Several resonances are visible in this interval. Pre-test experiments indicated that the 3/2 wave resonance, initially at a frequency of approximately 100 kHz, gave the clearest indication of recession. A dashed line on Figure 78 traces the history of this resonance.

3.2.4   Data Analysis and Evaluation

3.2.4.1   Ablation Performance

For a convenient comparison by model type, the steady-state axial recession rate data from Table 23 are plotted in bar-graph form in Figure 79. The data from the rotating models are considered to be the more reliable indicators of the relative ablation performance expected in flight, since possible coupled effects of nose asymmetries on the test environment are precluded. Such effects were particularly evident on the non-rotating infiltrated segment models (Section 3.2.3.1 and Figure 74).

111

Figure 78. Resonant frequency sensor data frames.

Figure 79. Steady-state recession rates of tungsten models.

The obvious conclusion from Figure 79 is that the ablation performance of the segmented concepts was at least as good as for the solid tungsten models. The infiltrated segment concept is a possible exception, since Model 4-4 receded slightly more than the rotating solid model (No. 2-2).

With the exception of the infiltrated segment models, the recession rates for all of the tests lie within a band of 0.4 inch/second ±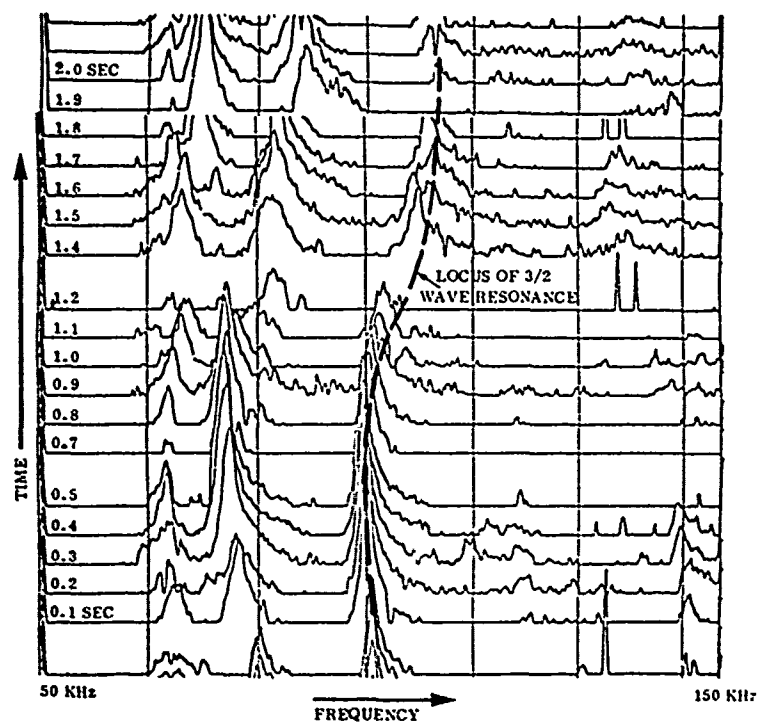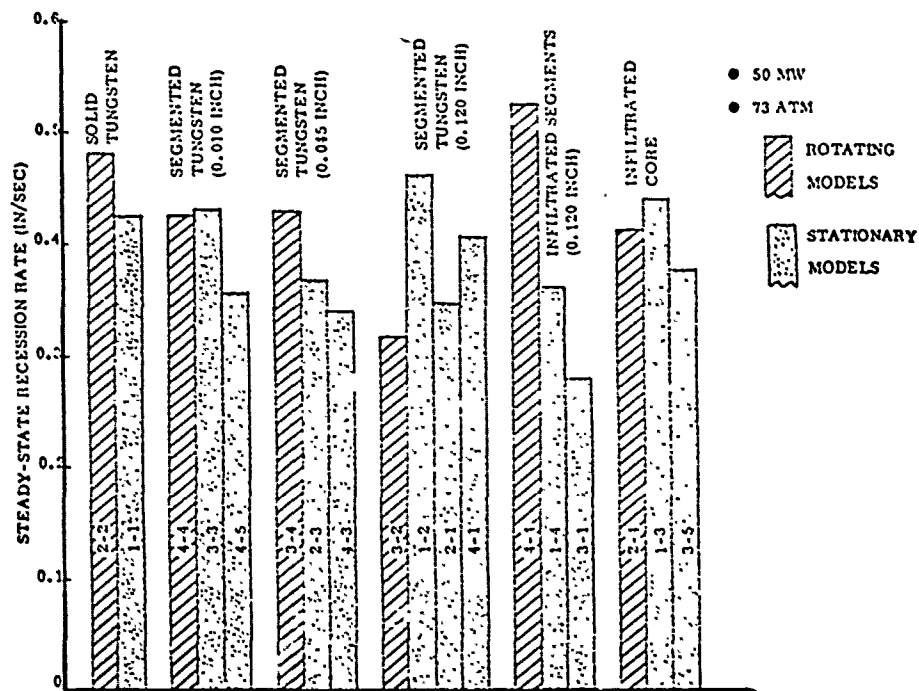 20 percent. The data suggest that the ± 20 percent scatter is random in nature and unrelated to the model type (i.e., normal scatter for this test facility). The scatter in the recessions of the four 0.120-inch segment models, for example, is nearly as great as the scatter for the entire data set (again excluding the infiltrated segment models). The spread in the data for the spinning models also is of the same order as the scatter for the entire population. Thus, it is concluded that, with the possible exception of the infiltrated segment models, all of the segmented models ablated the same as the solid tungsten specimens within experimental error.

It may be noted that even the 0.010-inch thin-sheet models ablated at the same steady-state rate as solid tungsten; all mechanical material loss and distortion occurred at the end of the test, as the models left the jet. However, as the 0.010 sheets are apparently fragile at high temperatures, and may be subject to mechanical loss at angle-of-attack, the thin-sheet concept was down rated.

The infiltrated segment concept is difficult to evaluate. Since the recession rates of the non-spinning models were affected by the flowfield/nose shape coupling (Section 3.2.3.1), there is, in effect, only one recession rate data point available. The recession rate of the spinning infiltrated segment model (4-4) was only 9 percent higher than the recession rate of the spinning solid tungsten model, hardly a statistically meaningful difference. Still, Model 4-4 did recede faster than any other model tested, 31 percent faster than the average. Thus, as the concept offers no particular advantage over the segmented tungsten designs, further development does not seem warranted.

The three infiltrated core models all ablated at close to the nominal rate (0.4 inch/second), with very little scatter. Scallop patterns and a "turbulent shape" did form on these models; however, the axial recession rate apparently was not affected. The satisfactory ablation performance of these models is significant, since a copper-infiltrated core has the potential of improving the thermostructural margin of segmented tungsten nosetip designs.

The 0.045-inch and 0.120-inch segment concepts both performed satisfactorily. The spinning versions of these designs, in particular, ablated very smoothly and evenly.

3.2.4.2   Instrumentation

The three types of instrumentation evaluated were: 1) thermocouples, 2) the pulse/echo acoustic gage, and 3) the resonant frequency ablation gage. The potential application of all three is to measure the in-flight recession rate of tungsten nosetips.

Encouraging test results were obtained only for the resonant frequency gage. As noted in Section 3.2.3.3, the signal from the compression wave pulse/echo gage attenuated to unacceptable levels before any measurable recession occurred. Attempts to correlate the thermocouple temperature histories (Appendix B) with recession also were unsuccessful. In general, the thermocouples either failed or reached maximum calibration temperature well before becoming exposed by ablation. Neither the failure times nor the rate of temperature rise could be related to recession. The data suggest that hot gas leakage may have been the dominant source of run-to-run temperature variations.

As stated in Section 3.2.3.3, only the resonance gage data for Model 2-1 were analyzed in detail. The steps in the analysis, following the theory outlined in Section 6.1, were:

1. The 3/2 wave resonant frequency history was obtained from Figure 78 (dashed line).
2. From the resonant frequency history (f), the history of the acoustic wave round trip time $\left(\tau_0\right)$ was computed from the formula $\tau_0 = 3/f$.
3. The "apparent length" $\left(L_0\right)$ history of the tungsten stud was obtained from $\quad C_0 \tau_0$, where C_0 is the room temperature

$$L_0 = \frac{C_0 \tau_0}{2}$$

speed of sound in tungsten.
4. The actual length history was obtained by adding an analytically determined "temperature correction" to the apparent length.

To obtain the temperature correction, the internal nosetip temperature distributions were calculated for the 50 MW environment using the NOSEC computer code (described in Reference 7). Figure 80 shows the degree of correlation between the actual model shape change history (from the motion picture data) and the shape change calculated with the NOSEC code. Figure 81 (a) shows the calculated axial temperature profiles, while Figure 81 (b) gives the tungsten speed of sound variation with temperature (from References 2 and 31). The resultant temperature correction history is given in Figure 82.
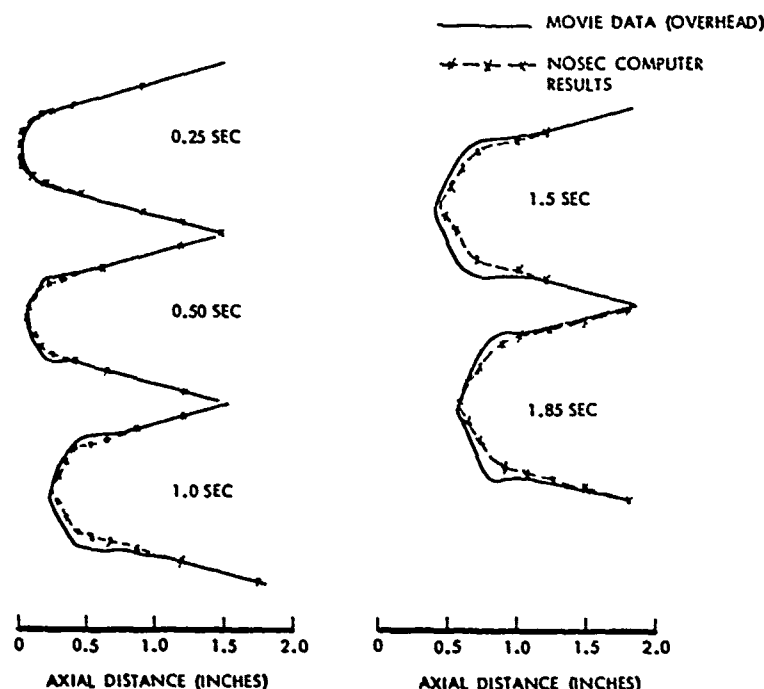
Figure 80. Comparison of measured and computed model shapes.

114

(a) COMPUTED AXIAL TEMPERATURE DISTRIBUTION

1.85 SEC
1.5
1.0
0.5
0.25 SEC

TEMPERATURE (°F)

AXIAL STATION (INCHES)

(b) EFFECT OF TEMPERATURE ON SPEED OF SOUND IN TUNGSTEN (EXTENSIONAL WAVES)

SOLID LINE SUPPORTED BY LABORATORY DATA •

DASHED LINE BASED ON SAMS FLIGHT CORRELATION (REF 7)

• LOWRIE & GONAS (REF 15) AND PANAMETRICS RESISTANCE HEATED FILAMENT DATA (UNPUBLISHED)

NORMALIZED SPEED OF SOUND

TEMPERATURE (°F)

Figure 81. Data for temperature correction calculation.
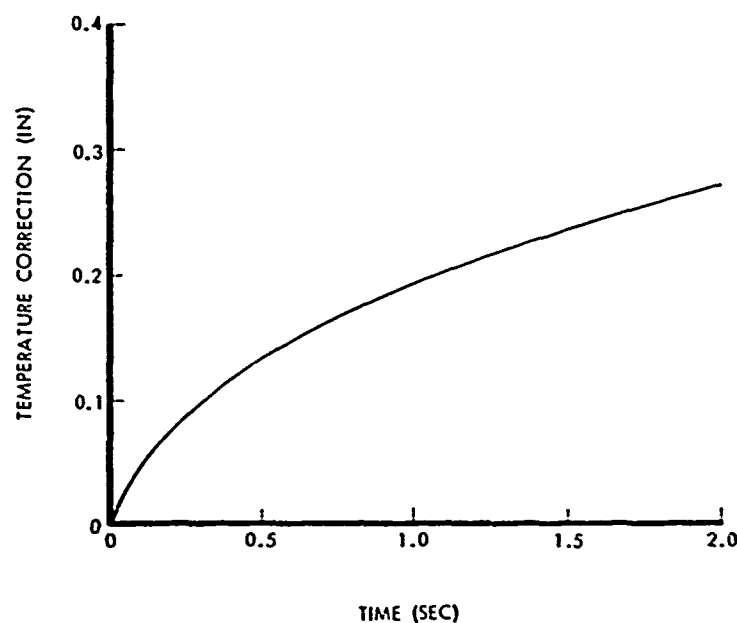
Figure 82. Temperature correction history.

The final result of the resonance gage data analysis is presented in Figure 83. The corrected ablation gage data (solid circles) are compared with the motion picture recession data of Figure B-11 (Appendix B). As can be seen, the agreement is excellent.
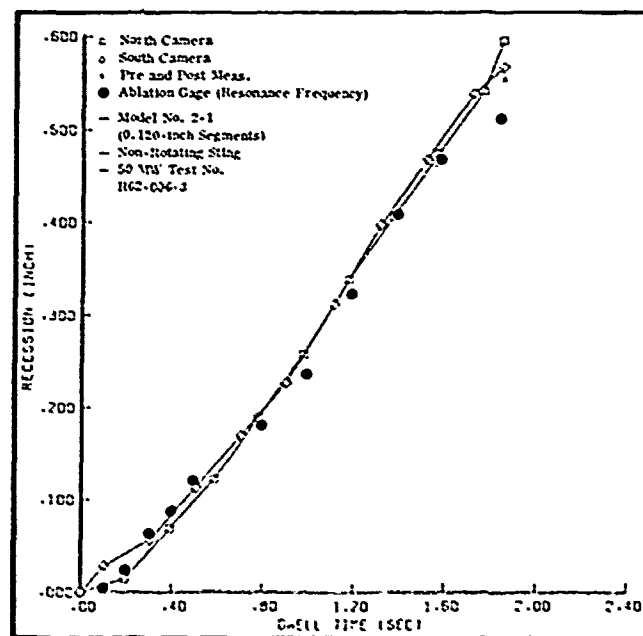
Figure 83. Comparison of measured and actual recession
histories of segmented tungsten ablation model.

116

3.2.5   Conclusions

The principal conclusions from the test series are:

1. Segmentation of tungsten nosetips has no detrimental effect on ablation performance.

2. All of the segmented designs ablated satisfactorily when the models were on flow centerline. However, the 0.010-inch thick "thin-sheet" segments used in one design deformed and tore under the side loads generated during flow exit.

3. All of the models exhibited satisfactory thermostructural performance in the test environment.

4. The resonant frequency ablation gage successfully measured the recession of a segmented tungsten model.

5. The compression wave pulse/echo gage is unsatisfactory as a tungsten ablation sensor.

6. The in-depth thermocouple temperature histories could not be correlated with ablation.

4.0 HEARTS/ERN DESIGNS

Tungsten nosetips were flight-tested on HEARTS (Hydrometeor Erosion And Recession Test System) reentry vehicles as an intermediate evaluation step prior to full-scale ICBM flights on A.N.T. reentry vehicles. Other ERN flight tests were performed in the SAMS program (Reference 2) and in the FLAME program (Section 5.0). The HEARTS vehicles (Reference 32) were launched on Athena C and D boosters and attained entry velocities (V_e) of approximately 18,000 ft/sec at flight path angles (γ_e) of around 35 degrees.

Two monolithic tungsten nosetips and one segmented tungsten nosetip were built for the flight test program. One monolithic nosetip was destroyed in a vehicle launch malfunction, and the other two nosetips experienced successful flight tests. Each nosetip was covered with a teflon glove designed to burn through and expose the tungsten at an altitude of approximately 35 kft, thereby simulating anticipated conditions for flight through erosive weather environments.

This section describes the thermal and structural design analyses of the two HEARTS/ERN configurations and briefly summarizes the flight results. The basic objectives of these flights were to: 1) evaluate the thermal and structural performance of tungsten nosetips in actual flight environments, and 2) evaluate the effect of the segmented construction on thermostructural performance. However, it was recognized that the thermostructural environment in the HEARTS flights would be less severe than on a full-scale ICBM flight (such as the A.N.T. vehicles). Therefore, the main emphasis of these designs was to evaluate the effect of the segmented boundaries on nosetip recession characteristics. It also should be noted that the design was compromised somewhat to accommodate an acoustic recession gage and thermocouples installed between the segments. Consequently, the designs were not optimized for thermostructural performance, and margin-of-safety comparisons between the two designs should not be taken as an indication of the maximum improvement obtainable with the segmented construction technique.

The HEARTS monolithic and segmented tungsten nosetip designs are shown in Figures 84 and 85, respectively. Both designs were sphere-ogive-cone configurations to duplicate the shape of a proposed erosion-resistant insert being designed by the General Electric Company as a potential Mark 12 nosetip modification. The monolithic nosetip was machined from a 2.62-inch diameter extruded billet of Sylvania "fine-grain" tungsten (the proposed Mark 12 material). The segmented nosetip was fabricated from 3.0-inch diameter extruded billets of 2 percent thoriated tungsten. Each segment was machined from sections of an extruded billet, as opposed to the upset-forging and coining method used to fabricate the FLAME nosetip segments (Section 5.0). Both nosetips utilized a tantalum-10 percent tungsten alloy sleeve for structural attachment to the vehicle. The sleeves were shrink-fitted onto the shank of the plug nosetip with a nominal interference of 0.002 inch. The stud and segment stack assembly in the segmented design were retained by a tantalum nut threaded to the aft end of the stud. The nut was reacted against a spring washer to provide limited movement to accommodate thermal expansion of the segment stack relative to the stud.

4.1   DESIGN ANALYSES

4.1.1   Thermal Analysis

Calculations were performed to predict the aerothermal response of the solid and segmented HEARTS/ERN designs illustrated in Figures 84 and 85. The calculations assumed a clear air environment and used the two design trajectories shown in Figures 86 and 87 (from Reference 32).
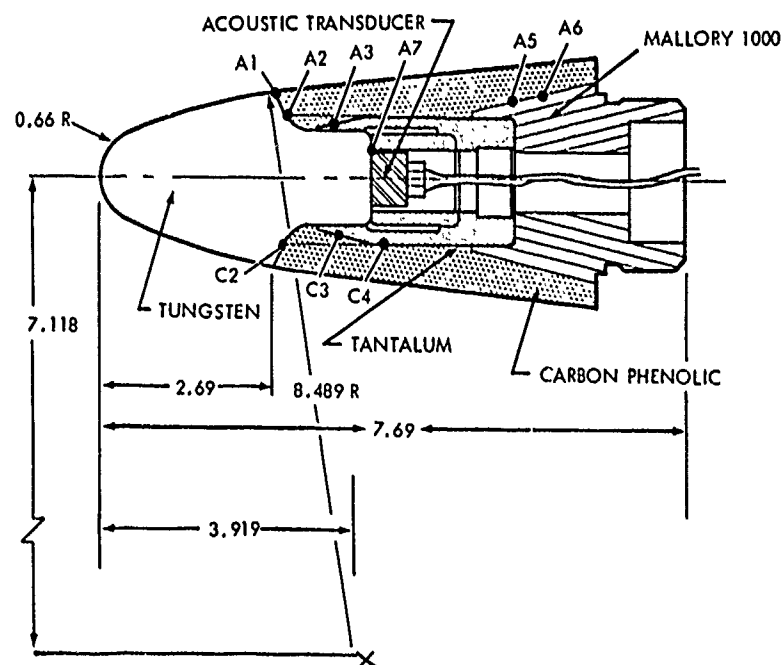
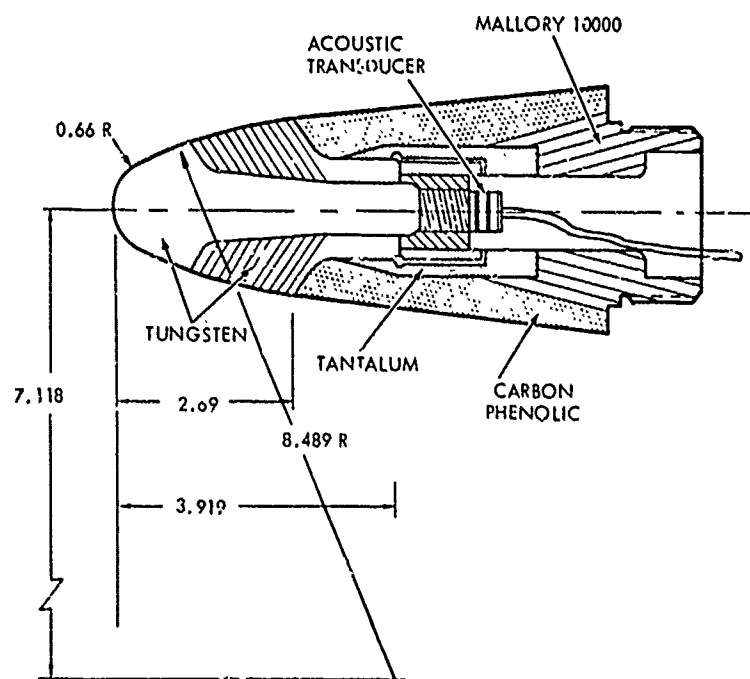Figure 84. HEARTS monolithic tungsten nosetip.
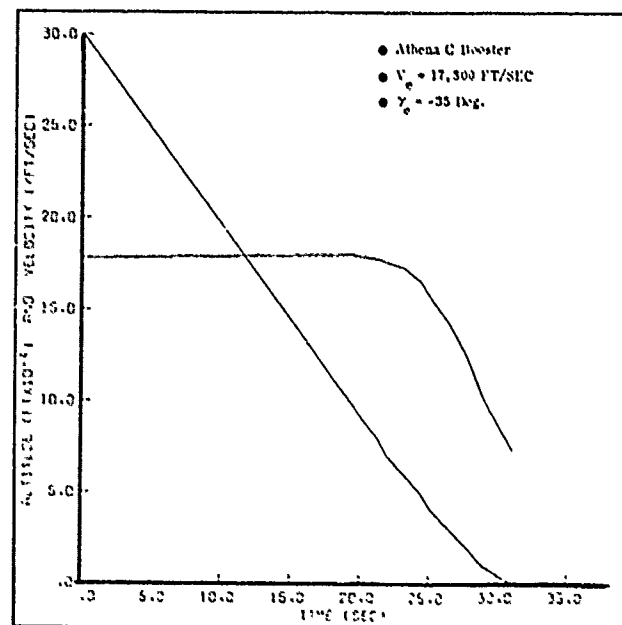

Figure 85. HEARTS segmented tungsten nosetip.

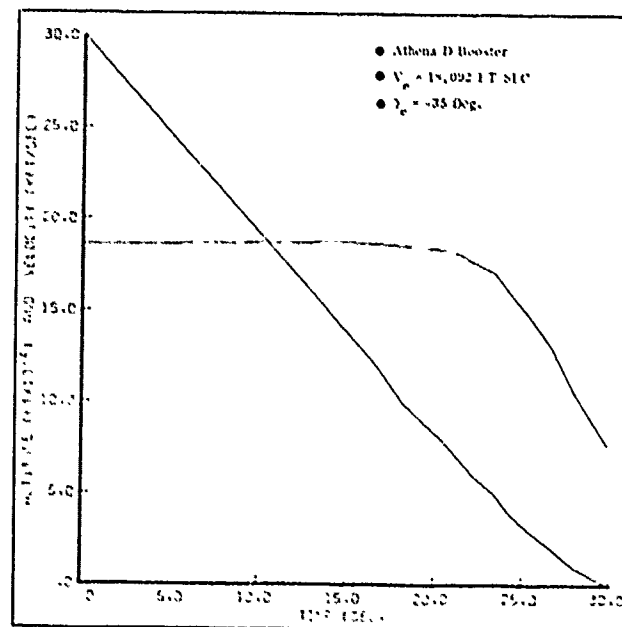**Figure 86. HEARTS design trajectory number 1.**

Figure 87. HEARTS design trajectory number 2.

Both trajectories had planned entry flight path angles (γ_e) of 35 degrees, with the small difference in entry velocities (V_e) corresponding to the two different boosters used in the HEARTS II program. Most of the design calculations used the slightly more severe Trajectory No. 2 (Figure 87).

Two-dimensional nodal networks were constructed to represent the two nosetips for the heat conduction calculations. The networks for the solid and segmented designs are illustrated in Figures 88 and 89, respectively. Two thermal models were considered to describe heat conduction in the segmented nosetip. In the first model, perfect thermal contact was assumed between all components. This, of course, is equivalent to the solid nosetip network (Figure 88) and produces the maximum temperature gradients in the nosetip. For the second model, the segments and collar were assumed to be in perfect thermal contact, and this assembly was considered to be perfectly insulated from the center retention stud (although radiation between the segments and the stud was permitted). This second network model (Figure 89) is believed to be more representative of actual conditions since the segments are maintained in axial compression throughout the flight, but are free to expand or move relative to the stud.

The thermophysical properties of tungsten used in the thermal response calculations are summarized in Table 24. The density, melt temperature, specific heat, and heat of fusion were obtained from Reference 33, and the thermal conductivity data are from Reference 34. The total hemispherical emissivity data were obtained from Reference 35 and are based on measurements made in a vacuum. No attempt was made to account for the possible effects of a surface oxide on the emissivity.

The ablation and heat conduction calculations were performed with the NOSEC (NOsetip Shape change, Erosion, and Conduction) computer code, which is described in Reference 7. The thermochemical ablation model for tungsten, described previously (References 22 and 36), assumed chemical equilibrium in the gas phase with kinetic effects occurring only at the ablating surface.
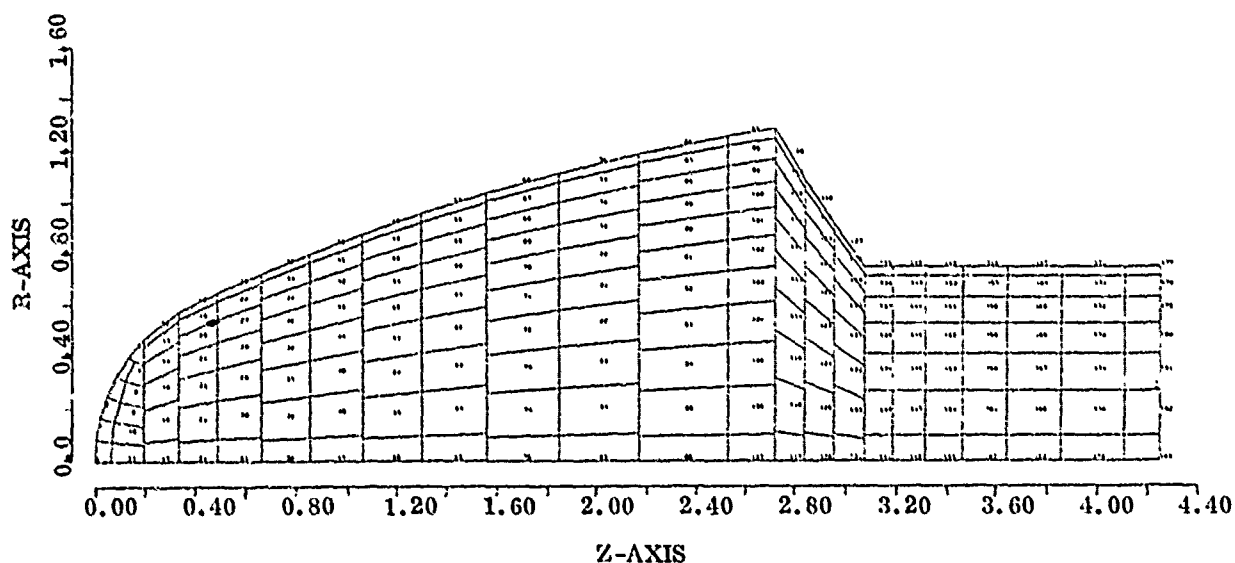
Figure 88. Thermal nodal network for solid HEARTS/ERN nosetip.
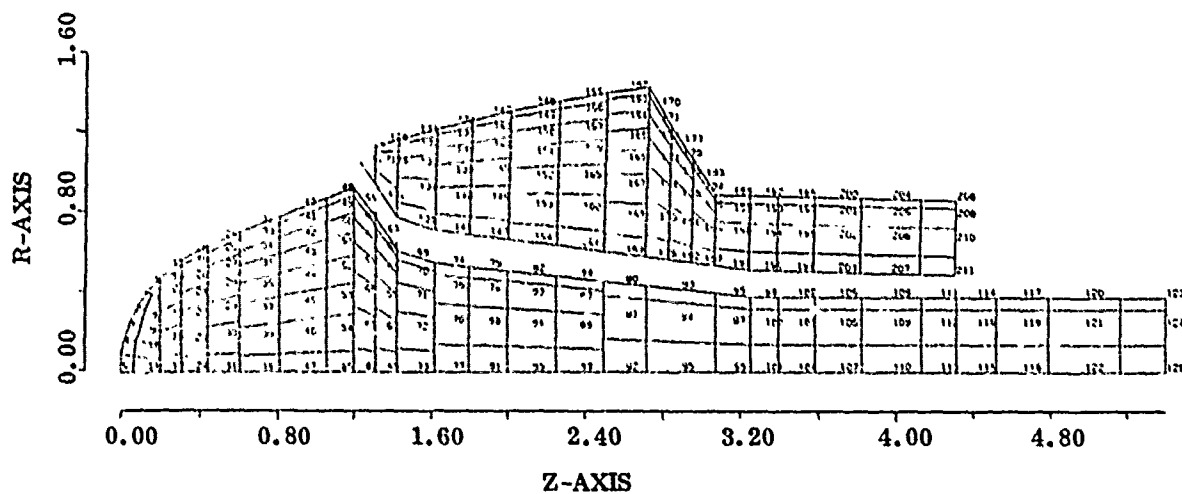
Figure 89. Thermal nodal network for segmented HEARTS/ERN nosetip.

Table 24. Thermal properties of tungsten.

Density: 1198 lb/ft^3
Heat of Fusion: 82.4 Btu/lb
Melt Temperature: 6110°F

TEMPERATURE (°F)	CONDUCTIVITY (Btu/ft-sec-°F)	SPECIFIC HEAT (Btu/lb-°F)	EMISSIVITY
-10.	0.02985	0.0310	---
32.	0.02921	0.0313	---
80.	---	---	0.043
260.	0.02600	0.0320	0.053
620.	0.02231	0.0333	---
980.	0.02054	0.0344	0.086
1340.	0.01942	0.0358	---
1880.	0.01814	0.0375	---
2240.	---	---	0.195
3140.	0.01605	0.0419	---
4040.	---	---	0.300
4580.	0.01485	0.0487	---
6020.	0.01436	0.0802	---
6740.	---	---	0.360
10000.	0.01436	0.0802	---

The basic assumptions and methods used in the convective heating calculations were the same as were used in the A.N.T./ERN detailed design analyses (References 2 and 22). The surface heat transfer distributions were computed by standard smooth-wall methods and then modified to account for: 1) the effects of surface roughness on the onset and progression of boundary layer transition, and 2) the development and increased heating effects of surface roughness.

Boundary layer transition was predicted by the PANT criterion (Reference 37) using a characteristic surface roughness height of 0.5 mil. The effects of uniformly distributed (sand-grain) surface roughness on the laminar heating distribution was included using the method of Reference 38. These laminar calculations used the same effective roughness height as that used in the boundary layer transition predictions.

After transition is predicted, the local surface roughness height increases and can be characterized either by a larger sand-grain roughness or by the crosshatched/scallop pattern type of surface roughness. The sand-grain roughness was assumed to increase at a rate equal to 20 percent of the local surface recession rate, to a maximum value of 2 mils, and the smooth-wall turbulent heat flux was augmented by the expressions of Powars (Reference 38). The formation and augmented heating effects of crosshatching and/or scallop patterns were described by the methods of Grabow and White (Reference 39). The scallop pattern type of roughness generally was used for tungsten in turbulent flow. Sand-grain roughness was used if the scallop formation criterion of Reference 39 was not satisfied. However, the calculations indicated that scallop patterns would be predicted in the forward nose region for all reentry cases of interest. (This may represent a deficiency in the analytical modeling for tungsten, since the SAMS/ERN flight results, described in Reference 2, indicated that the scallop patterns would form only in flight through erosive environments. However, the higher heating augmentation factors associated with scallop patterns represents a conservatism in the design calculations. Furthermore, it remained to be proven if there would be a greater tendency for scallop pattern formation in higher performance flight regimes.)

The thermal response of the monolithic design was computed for both design trajectories (Figures 86 and 87), while the segmented configuration was analyzed only for the more severe Trajectory No. 2 (Figure 87). For all three cases, the tungsten was assumed to be exposed suddenly at an altitude of 35,000 feet. Since the tungsten was covered with a teflon glove prior to the exposure altitude, the nosetips were assumed to be at a uniform temperature of 70°F at the time of initial exposure.

The computed stagnation point recession histories for the three cases are shown in Figure 90. Figures 90 (a) and 90 (b) compare the monolithic nosetip recession histories for the two design trajectories; as indicated, the difference is very small. The predicted recession history for the segmented design is presented in Figure 90 (c). The corresponding nosetip profile histories are illustrated in Figure 91 for all three cases.

Internal temperature distribution histories were computed for use in the nosetip thermo-structural response predictions (Section 4.1.2). The computed in-depth temperatures are illustrated in Figures 92 and 93 for the solid nosetip and the segmented nosetip stud, respectively. The results are shown in the form of lines of constant temperature (isotherms) at several different altitudes. (Note that the scales of the nosetip coordinates are different in different portions of Figures 92 and 93. This is a result of the response of the automatic plot routine as the nosetip shape changed due to recession.) These temperatures, along with the computed histories of the nosetip shapes and surface pressure distributions were output on magnetic tapes for direct input to the structural analysis computer codes.
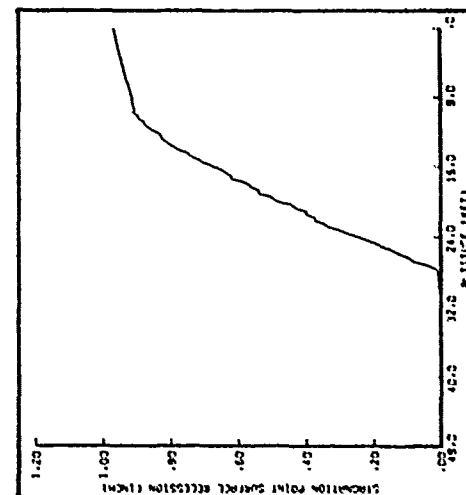
(a) Solid design, trajectory 1   (b) Solid design, trajectory 2   (c) Segmented design, trajectory 2
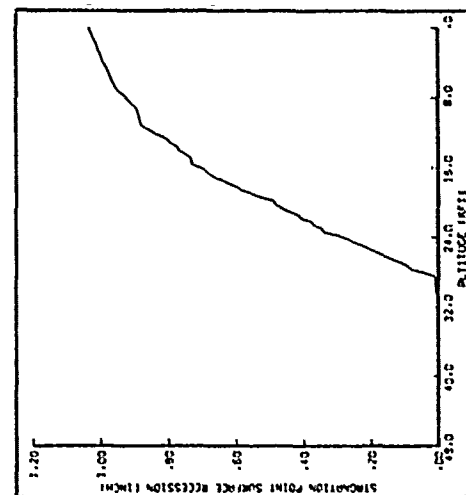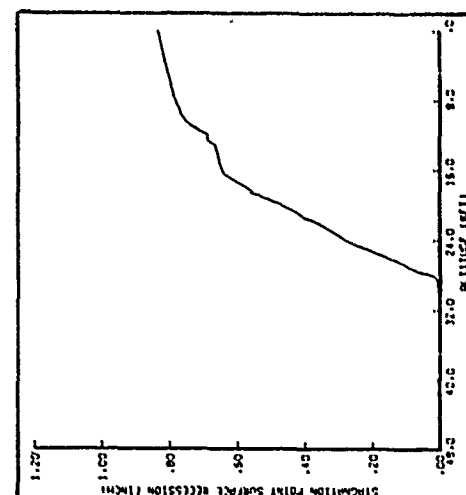
Figure 90. HEARTS/ERN predicted stagnation point re ession histories.

124

(a) Solid design, trajectory 1
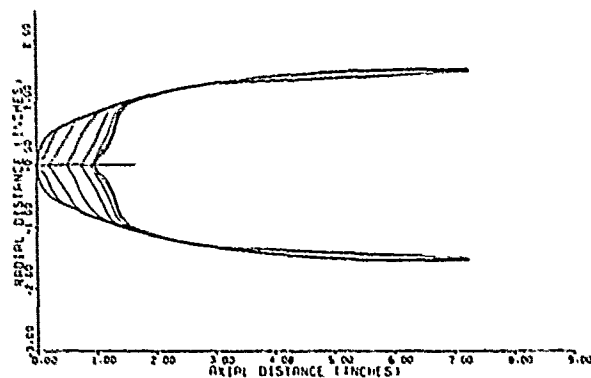
TIME (SEC)	ALT (KFT)
24.750	35.00
25.359	29.55
25.996	24.64
26.643	19.67
27.291	14.69
27.956	9.71
28.895	4.76
29.800	0.00

(b) Solid design, trajectory 2
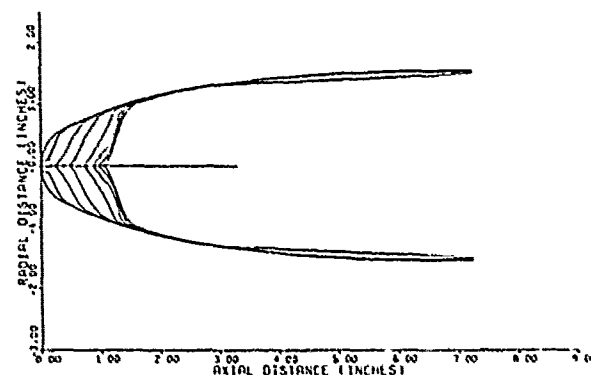
TIME (SEC)	ALT (KFT)
25.800	35.00
26.428	29.79
27.096	24.64
27.715	19.88
28.312	14.90
28.910	9.95
29.992	4.80
31.000	0.00

(c) Segmented design, trajectory 2
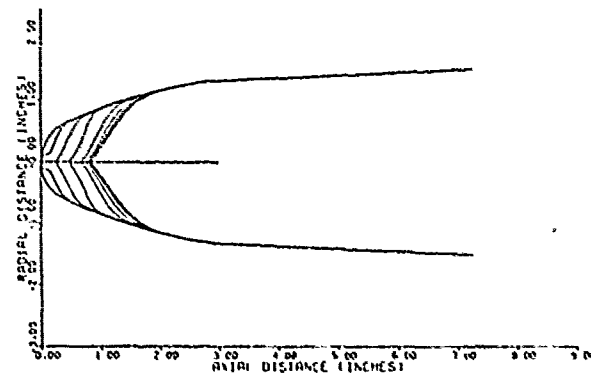
TIME (SEC)	ALT (KFT)
25.800	35.00
26.428	29.79
27.096	24.64
27.715	19.88
28.312	14.90
28.910	9.95
29.992	4.80
31.000	0.00

Figure 91. HEARTS/ERN predicted ablation profile histories.
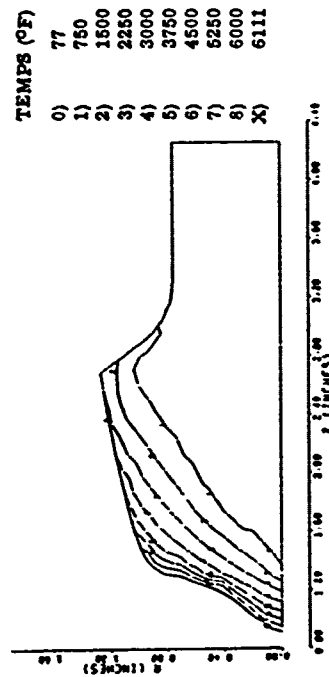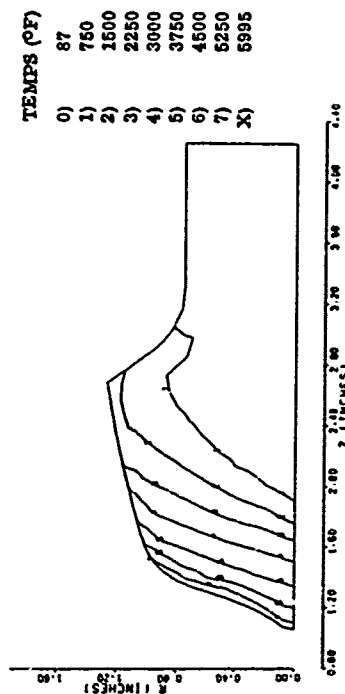
Figure 92. Predicted internal temperature distributions, HEARTS/ERN solid nosetip.

(a) 25.5 kft

(b) 20.2 kft

(c) 10.3 kft

(d) 1.9 kft

Figure 93. Predicted internal temperature distributions, HEARTS/ERN segmented nosetip stud.

127

4.1.2   Structural Analysis

4.1.2.1   Monolithic Design

The results of the preceding nosetip thermal response predictions were used as inputs to a finite element thermostructural analysis. Mechanical, physical and s'rength properties required for the analysis were taken from References 2, 20 and 21.

The predicted minimum margins-of-safety are plotted as functions of altitude in Figure 94, which also shows the location history of the critical elemei. .elative to the original (unablated) geometry. The analysis was completed initially with a data base and material model developed for 3-inch diameter extruded billets of thoriated tungsten. Three time points were subsequently repeated using a material and strength model developed specifically for the Sylvania "fine-grain" material from which the nosetip was machined. These results are also given in Figure 94 and show little difference from the previous results.
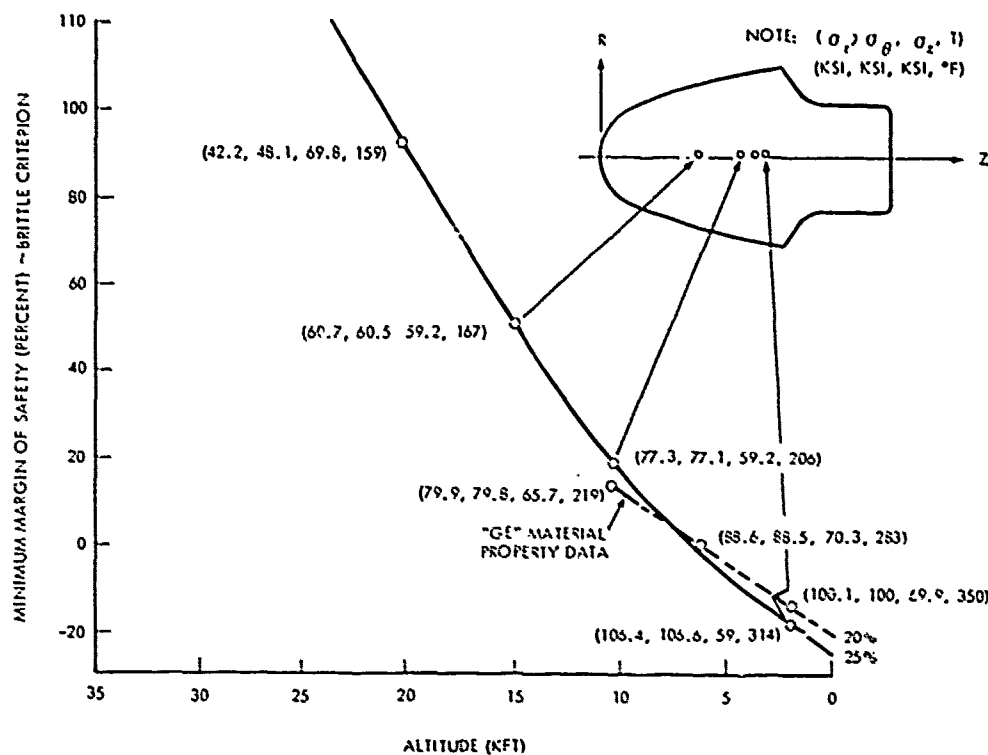
Figure 94.   Minimum brittle margin-of-safety versus altitude,
HEARTS/ERN solid nosetip.

Two important aspects of tungsten material behavior were omitted from the analysis. First, the brittle material volume effect would probably indicate much lower margins-of-safety than determined, since the stressed volume is higher than that of the tensile test coupons from which the strength data were derived. The other consideration is that of crack propagation. Late-time negative margins, which are measures only of the probability of crack initiation, may not be indicative of an observable flight failure. A crack initiating in flight may only propagate through the brittle zone to the boundary of the ductile zone. This case becomes catastrophic only when, later in flight, the

ablation front reaches the crack and material is removed. If the crack forms late in flight, as indicated by this analysis, the crack may never be exposed prior to successful impact.

4.1.2.2   Segmented Design

The thermal heat conduction analysis of the segmented design concept assumed that the boundary between the segment stack and the stud was insulated. As discussed in Section 4.1.1, this was judged to be the most realistic model of the nosetip. The $1500^\circ F$ isotherm at 20,200 ft altitude is shown in Figure 95 for the segmented design for both the insulated boundary condition and for a condition of perfect thermal contact. The figure illustrates the effect of the insulated boundary. It also shows that the isotherm is essentially perpendicular to the segment boundaries, indicating that little heat flows across segment boundaries. Consequently, the thermal contact boundary condition between individual segments is not important.

(a) Non-insulated

- 20.2 KFT
- 1500°F ISOTHERM

(b) Insulated along stud-segment boundary
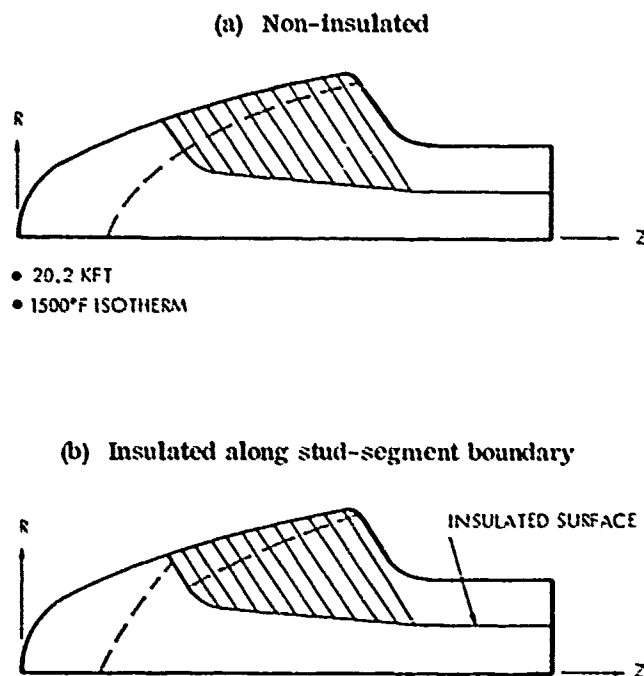
Figure 95.   Internal temperature comparison of insulated
and non-insulated segmented nosetips.

The computed minimum margins-of-safety in the stud and segments are shown as functions of altitude in Figures 96 and 97, respectively. The results indicate a significant improvement over the solid (monolithic) design. In addition, the volume of stressed material is much less in individual components than in the monolithic design. If the brittle material volume effect had been taken into account, the improvement in probability of failure would have been more dramatic.

4.2   FLIGHT TEST RESULTS

Tungsten nosetips were flight-tested successfully on two HEARTS II reentry vehicles. The solid (monolithic) design was flown on HEARTS Vehicle 106, which was launched on an Athena C
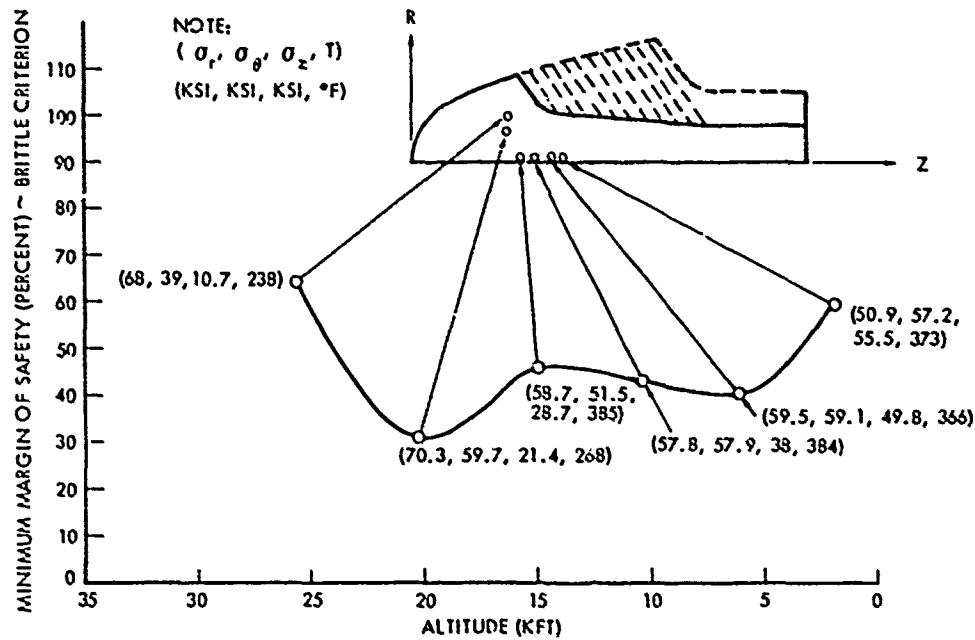
Figure 96. Minimum brittle margin-of-safety versus altitude.
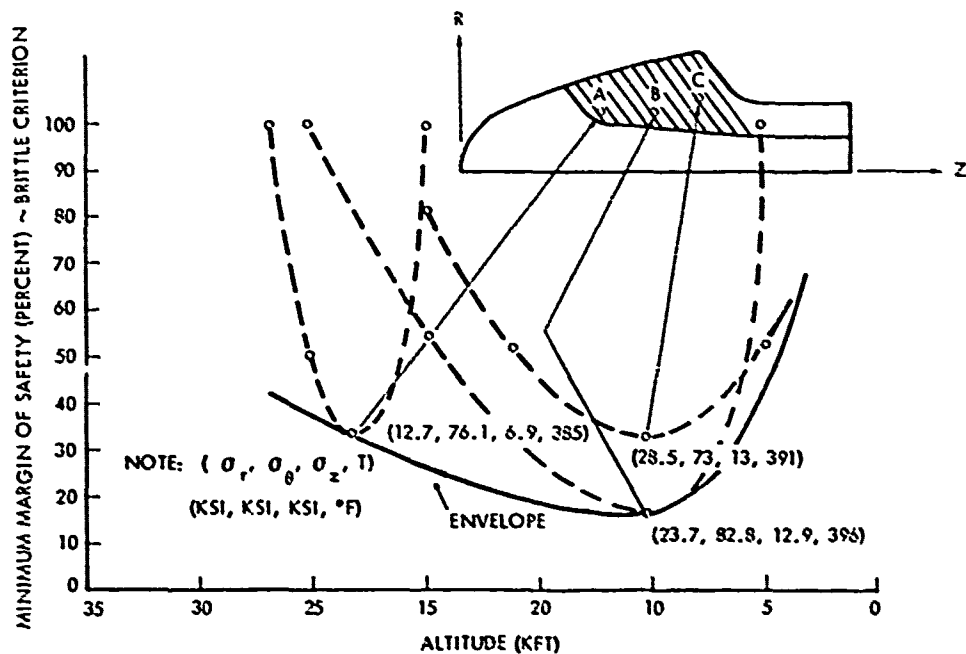
Figure 97. Envelope of minimum brittle margins-of-safety versus altitude.

130

booster from Wallops Island, Virginia on 20 January 1975. The segmented design was flown on Vehicle 112, which was launched on an Athena D booster, also from the Wallops Island facility, on 2 April 1975. Vehicle 112 was flown in a clear air environment, while Vehicle 106 encountered a very light (and undefined) cloud environment at low altitudes (below 16,000 ft).

Both nosetips survived to impact with no evidence of thermostructural failure or asymmetric ablation. The flights were considered to be completely satisfactory demonstrations of the feasibility of the ERN concept in a moderately severe clear air reentry flight environment. In particular, it was noted that the performance of the segmented design was identical to that of the monolithic design in all respects. There was no measurable evidence that the segmented construction caused any change in the nosetip flow or ablation characteristics.

Each nosetip was instrumented with a K West pulse/echo ultrasonic ablation sensor and with 16 thermocouples. The monolithic nosetip used a shear wave transducer (the baseline A.N.T./ERN sensor), while the segmented design was equipped with a compression wave transducer that was being evaluated as an alternate sensor. In both flights, the return echo disappeared within one second after removal of the teflon glove, and no usable recession measurements were obtained. The 16 thermocouples were positioned at various locations within the nosetip and heatshield to provide materials performance data and diagnostic information. Nearly all of the thermocouples performed satisfactorily in the flights.

Detailed post-flight analyses were conducted only for the monolithic nosetip flown on Vehicle 106. The results of these analyses are presented in this section. The derived performance of the tungsten nosetip is described in Section 4.2.1, and the nosetip skirt heatshield performance is discussed in Section 4.2.2.

4.2.1   Nosetip Performance

The tungsten nosetip, illustrated in Figure 54, was a sphere-ogive configuration with an initial radius of 0.66 inch. The nosetip was of monolithic (i.e., solid) construction and was fabricated from a 2.62-inch diameter extruded billet of Sylvania "fine-grain" tungsten. The skirt heatshield was a conical frustum of 5055A tape-wrapped carbon phenolic, with a wrap angle of 26 degrees from the axis of symmetry. The plies were oriented in an aft-facing direction. The forward portion of the nosetip was covered with a teflon glove, designed to burn through and provide sudden exposure of the tungsten at an altitude of approximately 35 kft. The initial spherical nose radius of the teflon cap was 0.75 inch.

The HEARTS II reentry vehicles are conical frusta with a half-angle of 6.43 degrees. The heatshield material is the same type of carbon phenolic used for the nosetip skirt heatshield (described above). The nosetip/vehicle interface is located at vehicle station 16.69 inches, measured from the theoretical cone apex. The overall dimensions of the HEARTS II vehicles are summarized below:

HEARTS II RV 106 DIMENSIONS		
Weight	61.891	lbs
Length	34.01	inches
Base Diameter	9.112	inches
Cone Half-Angle	6.43	degrees

Vehicle instrumentation that were utilized in the post-flight analysis of the trajectory were the axial, pitch, and yaw accelerometers.

Nosetip instrumentation consisted of 16 thermocouples and a K West ultrasonic ablation sensor (Figure 84). One thermocouple (A1) was designed to provide an indication of teflon cap removal; eight thermocouples were allocated to measure the response of the carbon phenolic skirt heatshield (the post-flight evaluation of the heatshield instrumentation is discussed in Section 4.2.2); one thermocouple (A7) measured the temperature of the ablation gage transducer; and one thermocouple (A8) was designed to provide an indication of possible catastrophic failure of the tungsten by measuring the internal gas temperature. The remaining five thermocouples measured the thermal response of the tungsten nosetip and tantalum holder at three different axial locations in the shank region. All 16 thermocouples functioned satisfactorily during the flight.

The ultrasonic ablation gage used a pulse/echo shear wave transducer with a frequency of 1.5 mHz. During the flight the return echo decreased suddenly soon after tungsten exposure and became undetectable. No useful data were obtained from the ablation gage.

The flight trajectory was nominal with two exceptions: 1) separation imposed a periodic motion on Vehicle 106 (but not on Vehicles 104 or 105, which were launched on the same booster) that produced maximum angles-of-attack in excess of 20 degrees at altitudes above 150 kft; and 2) the clouds were at lower altitudes than desired so that the weather environment was encountered at lower-than-planned velocities.

Trajectories for the three vehicles were reconstructed by Xonics, Inc. (Reference 40) using digitized axial accelerometer data. While pitch and yaw accelerations also provide contributions to total vehicle acceleration, they are important only for large pitch and yaw angles and were not included in the Xonics reconstructions. In view of the large pitch and yaw angles seen by Vehicle 106, it was believed necessary to examine this simplification. To provide an upper bound for the influence of pitch and yaw accelerations, the trajectory was reconstructed by PDA using a normal acceleration history obtained from the envelope of the peak values recorded by the yaw accelerometer. The following expressions were used to account for angle-of-attack effects:

$$\dot{V} = \dot{V}_{AXIAL} \cos\alpha + \dot{V}_{NORMAL} \sin\alpha$$

$$= \frac{1}{2} \rho_{\infty} V^2 \left(C_A \cos\alpha + \frac{dC_N}{d\alpha} \alpha \sin\alpha \right) \qquad (3)$$

$$\alpha = \frac{\dot{V}_{NORMAL} M_{VEHICLE}}{\frac{1}{2} \rho_{\infty} V^2 \frac{dC_N}{d\alpha} A_{BASE}} \qquad (4)$$

in which $\dot{V}_{NORMAL}$ and $\dot{V}_{AXIAL}$ are the measured accelerations, and $\frac{dC_N}{d\alpha}$ is given in Figure 98.

Since the Xonics trajectory was reconstructed using digitized data, while the PDA reconstruction described above was based on data extracted manually from the oscillograph records, the
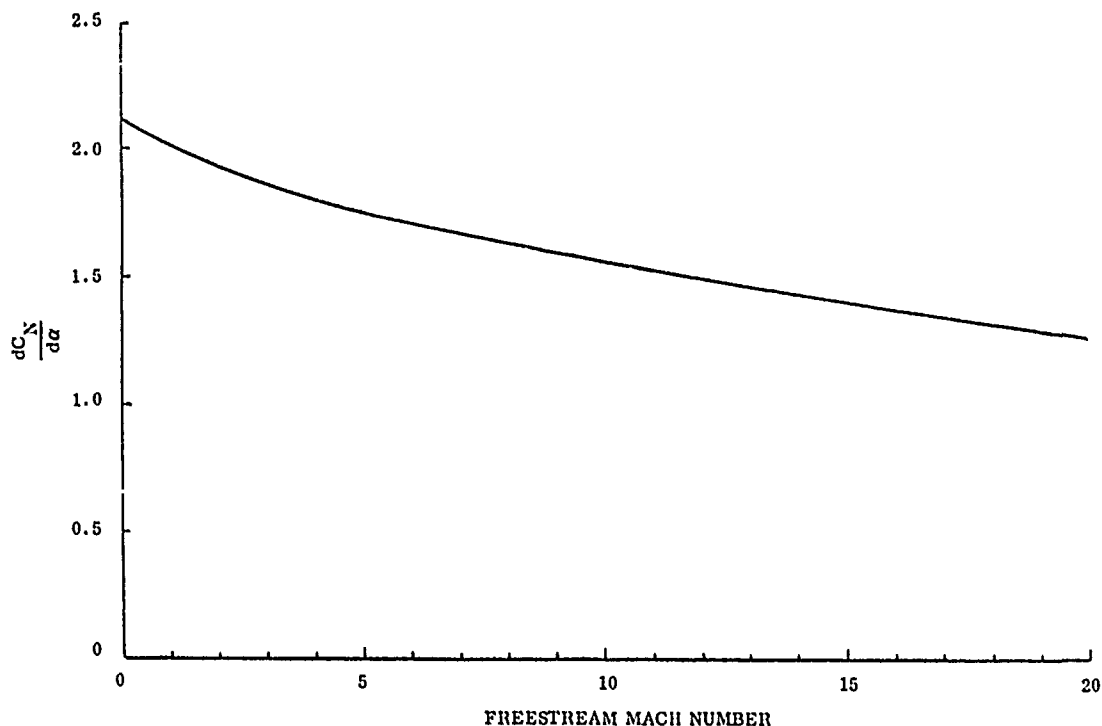
Figure 98. HEARTS/ERN normal force coefficient derivative.

Xonics trajectory was believed to be inherently more accurate (excluding angle-of-attack effects). Consequently, trajectories were reconstructed by PDA both with and without angle-of-attack contributions, and the Xonics trajectory was then modified by the computed differences in the velocity and altitude histories caused by the angle-of-attack. Figures 99 and 100 show these four trajectories. It is seen that inclusion of the angle-of-attack contribution to drag in the trajectory reconstruction produces an altitude difference of 3200 feet at 100 kft. This would imply that, for Vehicle 106, the Xonics trajectory reconstruction should have predicted an altitude at loss-of-signal 3200 feet lower than the altitudes predicted at loss-of-signal for Vehicles 104 and 105. This altitude difference is actually only 315 feet, indicating that the above analysis provides, as intended, an upper bound on the influence of angle-of-attack on the trajectory, since the envelope of peak angles was used. It also indicates that the true trajectory is probably closer to the baseline trajectory given in Reference 40 than that modified above to account for angle-of-attack effects. Therefore, the trajectory reported by Xonics (Reference 40) was used as the baseline trajectory for all subsequent calculations.

No quantitative cloud density data were obtained because the clouds were below the aircraft flight sampling altitude of 16,000 feet in the region of the vehicle flight path.

The ablation of the teflon glove was calculated using an effective heat of ablation, Q^*, given by

$$Q^* = \text{J} + \eta\left(h_r - h_w\right) \quad \text{Btu/lb} \tag{5}$$
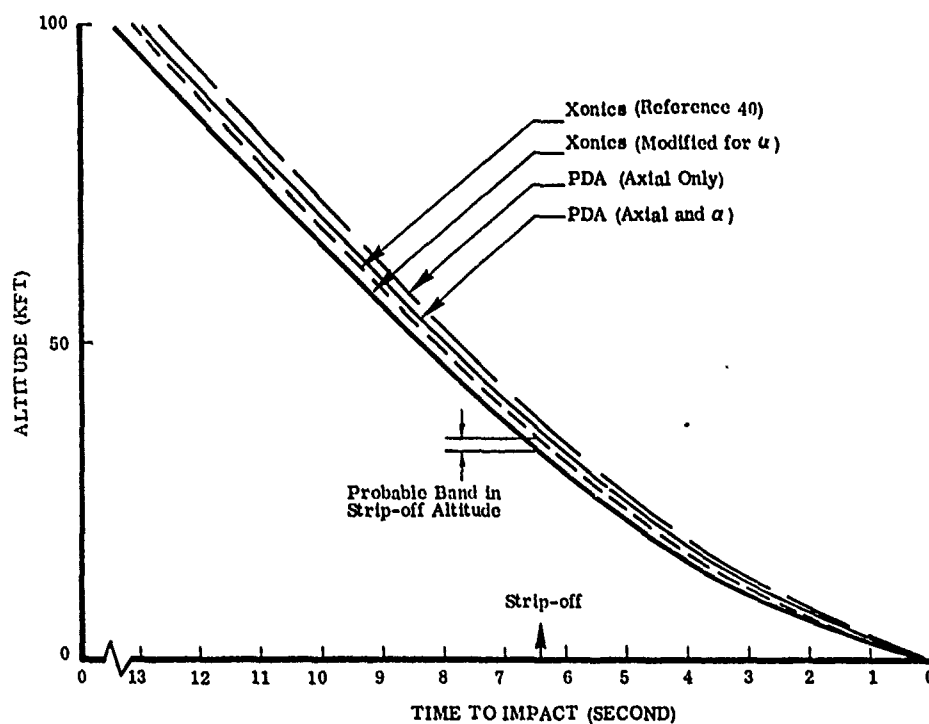
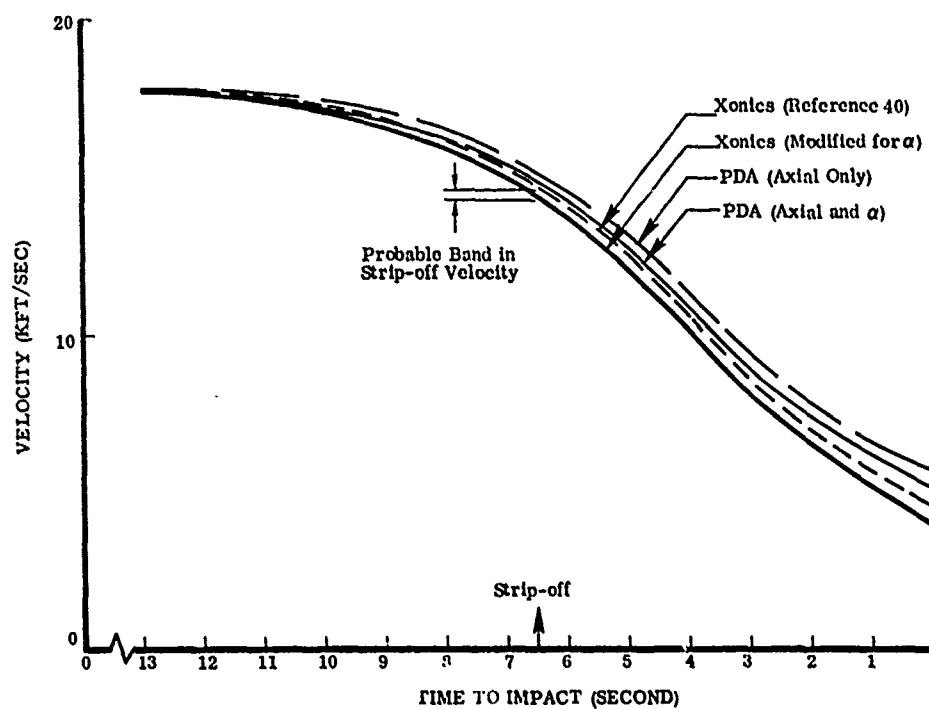Figure 99. Reconstructed HEARTS/ERN altitude histories.

Figure 100. Reconstructed HEARTS/ERN velocity histories.

134

along with the following material properties:

Thermal Conductivity, $k = 3.89 \times 10^{-5}$ Btu/ft-sec-$^{\circ}$R
Heat Capacity, $C_p = 0.25$ Btu/lb-$^{\circ}$R
Density, $\rho = 137$ lb/ft^3
Laminar Blowing Parameter, $\eta_{LAM} = 0.44$
Turbulent Blowing Parameter, $\eta_{TURB} = 0.175$
Ablation Temperature, $T_a = 1660^{\circ}$R

   A series of ablation and shape change calculations was performed to determine the sensitivity of the teflon glove removal altitude to the expected error band in entry angle and velocity for trajectories predicted both with and without angle-of-attack effects. These calculations, which were performed in conjunction with the angle-of-attack analysis discussed previously, used a NOHARE code option in which a spherical earth ballistic trajectory prediction is combined with the ablation and shape change calculations so that the analysis represents full coupling between vehicle shape and weight change, drag, and the trajectory. The same boundary layer transition and rough surface heating assumptions used in the pre-flight analysis (Section 4.1.1) were used in these calculations.

   The results of these analyses are shown in Figure 101, along with the cap removal conditions obtained from the trajectory reconstruction. In the NOHARE analysis, cap removal was assumed to occur when the teflon burned through at the sonic point. Actual removal was seen in the telemetry data as a sudden rise in the response of Thermocouple A1 and as a spike and a change in the shape of the curves of all three accelerometer traces 6.40 seconds before loss-of-signal (vehicle impact).
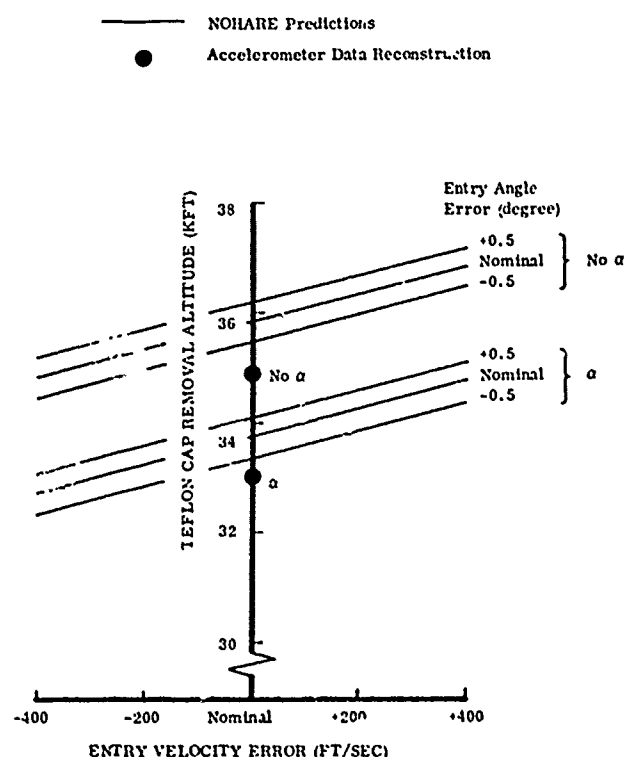

Figure 101. HEARTS/ERN teflon cap removal map.

135

The altitudes corresponding to 6.40 seconds before impact were obtained from Figure 99. It can be seen in Figure 101 that the cap removal altitude is relatively insensitive to errors in entry conditions. It also is seen that the removal altitude predicted for the nominal entry conditions is within 1000 feet of the removal altitude determined from trajectory reconstructions, with or without the inclusion in the analysis of angle-of-attack effects. Figure 102 shows the predicted teflon cap profiles for nominal entry conditions, including the effects of angle-of-attack.
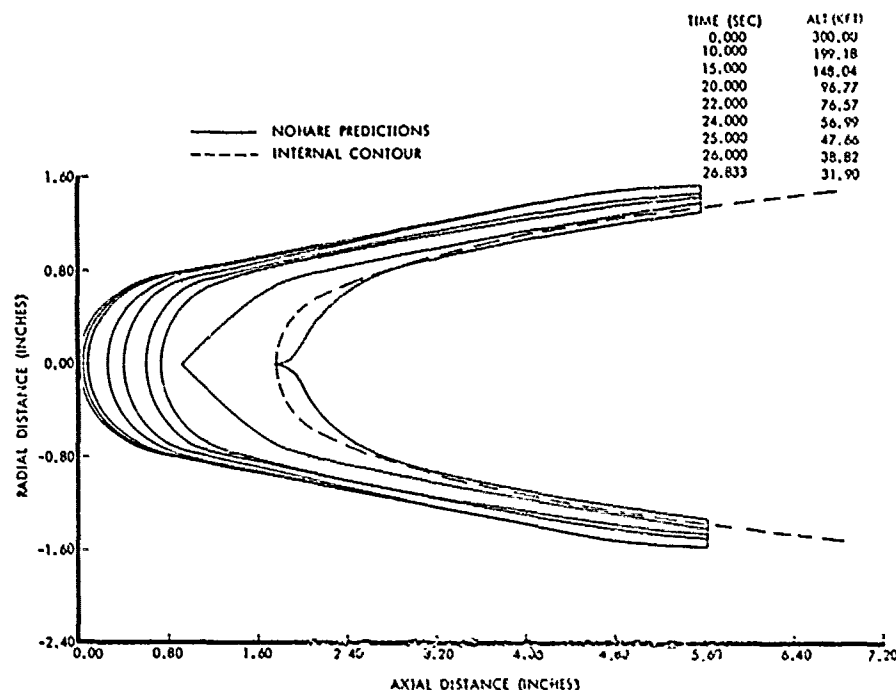
Figure 102. Computed teflon cap shape history.

The tungsten nosetip and tantalum holder were analyzed using the NOSEC code with the coupled trajectory calculation option. The nodal network used in these calculations is shown in Figure 103. This network is the same as the pre-flight network (Figure 88), with the exception that the tantalum-10 percent tungsten holder was modeled to permit correlation of the measured temperature histories in the shank region. The influence of angle-of-attack on the trajectory after teflon cap removal was studied and found to be negligible due to the low pitch and yaw angles experienced. The following conditions for the analysis were taken from the Xonics trajectory reconstruction for a time 6.40 seconds before loss of signal:

$$V_0 = 14,650 \text{ ft/sec}$$
$$Z_0 = 34,700 \text{ ft}$$
$$\gamma_0 = 35.56 \text{ degrees}$$

It has been found from SAMS flight tests (Reference 36) that the primary effect of weather on tungsten nosetips is to trigger the formation of surface scallop patterns in the region of turbulent flow melting ablation. Since almost all of the nosetip ablation on this vehicle occurred above 16,000 feet and since no weather was encountered above 16,000 feet, the flight was analyzed using the clear air methodology outlined in Reference 36. Figure 104 shows the predicted nosetip profile history.
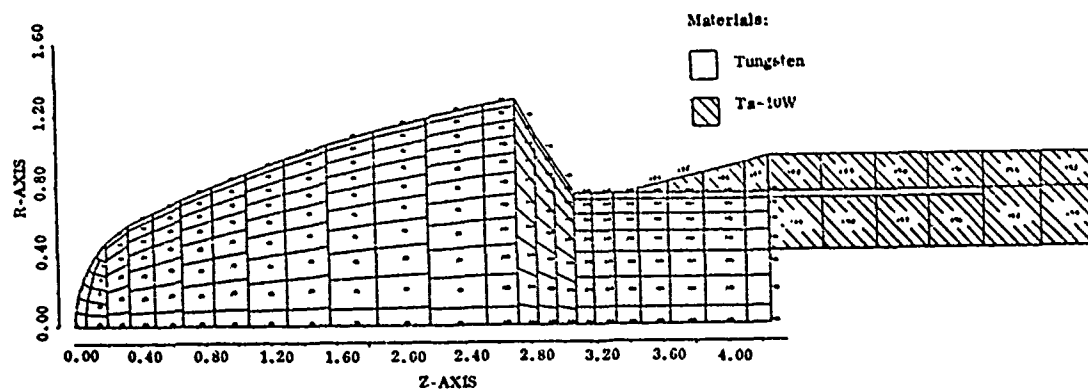
Figure 103. HEARTS/ERN tungsten nosetip post-flight nodal network.

TIME (SEC)	ALT (KFT)
0.000	34.70
1.001	26.57
2.001	19.41
3.002	13.46
4.002	8.70
5.001	4.90
6.001	1.87
6.760	0.00
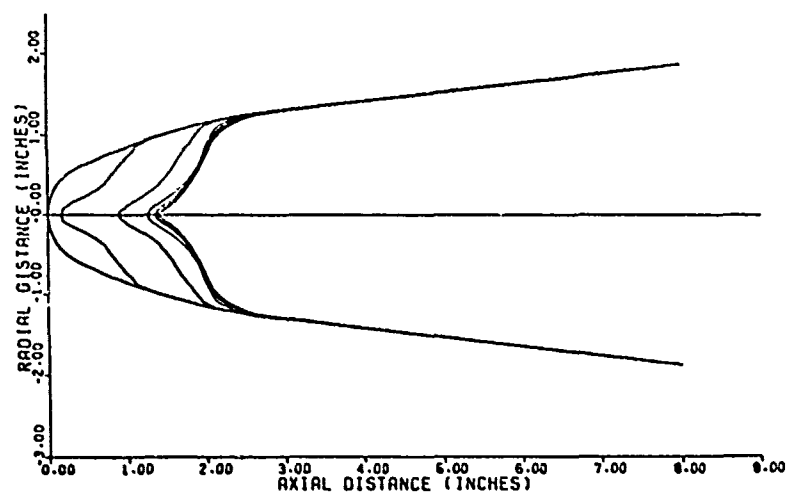
Figure 104. Computed HEARTS/ERN tungsten nosetip ablation profile history.

Figures 105 through 107 compare the telemetered thermocouple data to the predicted tungsten or tantalum surface temperatures at the points closest to the thermocouple junctions. It is seen that in each case the predicted surface temperature exceeds the recorded thermocouple response. The following three causes were considered to explain this lack of agreement: 1) poor thermal contact between the thermocouple junction and the nosetip, 2) actual recession of the tungsten that was lower than predicted, and/or 3) lower thermal diffusivity $\left(K/\rho C_p\right)$ than that used in the analysis.
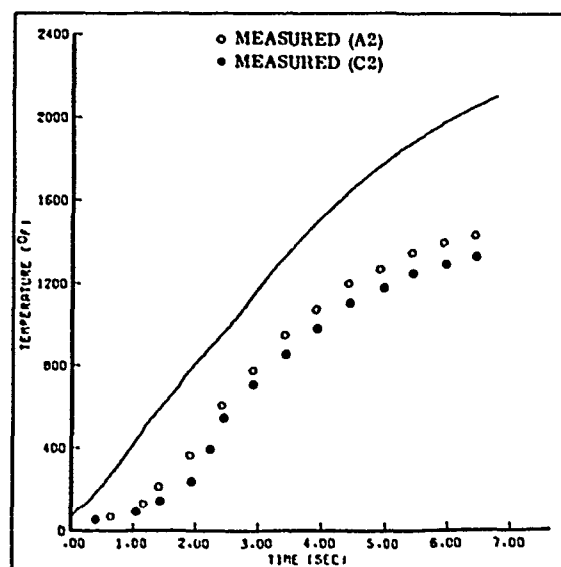
Figure 105. Comparison of measured and computed temperature histories, HEARTS/ERN solid nosetip location 2.
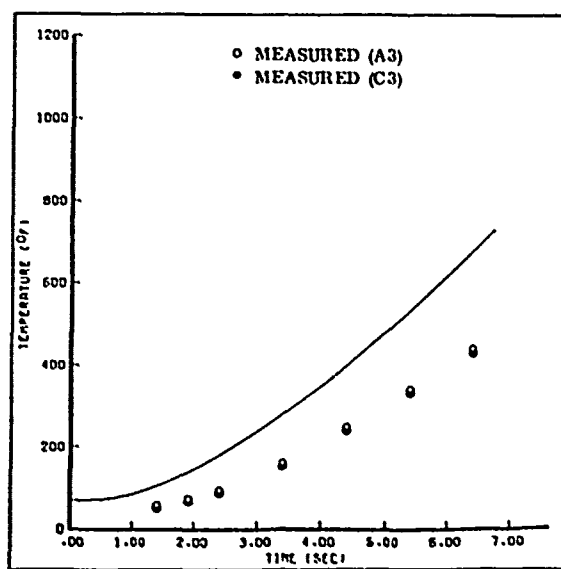
Figure 106. Comparison of measured and computed temperature histories, HEARTS/ERN solid nosetip location 3.
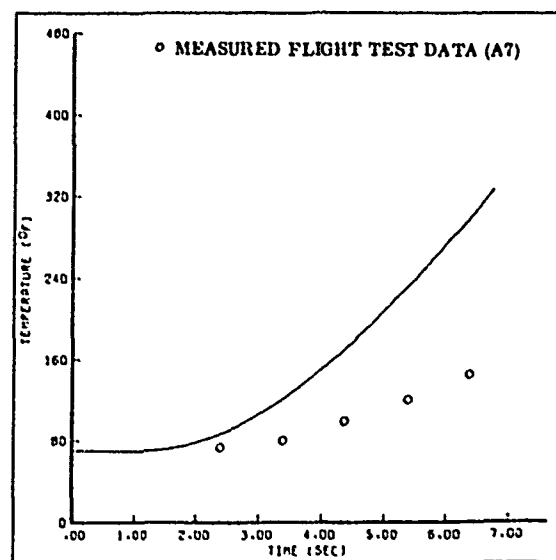
Figure 107. Comparison of measured and computed temperature
histories, HEARTS/ERN solid nosetip location 7.

After surveying the thermocouple installation techniques and the measured electrical
resistance between the thermocouple and the nosetip, it was decided that the thermal contact error
should have been much less than the observed differences between predicted and measured tempera-
tures. The pre-flight resistance measurements showed that thermocouples A7 (bonded in position)
and A3 and C3 (peened in position) were in good electrical (hence, thermal) contact with the nosetip
prior to the flight. Thermocouples A2 and C2 were not in electrical contact with the tungsten when
the vehicle was assembled for flight (although they had been in contact before the bond cured). Con-
sequently, the physical separation between the junctions of A2 and C2 and the tungsten surface appar-
ently was due only to the very slight expansion that the bond undergoes during curing.

To provide an economical method for evaluating the influences of recession and diffusivity,
the nosetip was idealized as a one-dimensional slab with constant diffusivity. It was found that the
temperature histories predicted by the two-dimensional NOSEC analysis for thermocouples A2, A3,
C2, and C3 could be matched quite accurately using the one-dimensional analytical solution of Ref-
erence 41. This one-dimensional method predicts higher temperatures than the NOSEC analysis for
thermocouple A7 at the back surface of the nosetip, but this is felt to be due primarily to the fact
that the one-dimensional solution ignores the presence of the tantalum holder, while the NOSEC anal-
ysis includes it. A summary of the one-dimensional model is:

Physical Model: 2.32-inch thick slab

Material Properties: $K = 0.0258$ Btu/ft-sec-$^{\circ}$R

$C_p = 0.0290$ Btu/lb-$^{\circ}$R

$\rho = 1192$ lb/ft^3

$\alpha = K/\rho C_p$

$= 0.000747$ ft^2/sec

Boundary Conditions: $T(x) = 70^{\circ}$F $(t = 0)$

$T(x = 2.32) = 5000^{\circ}$F $(t > 0)$

Adiabatic surface at $x = 0$

139

Figure 108 shows the one-dimensional model superimposed on maps of the isotherms predicted with the NOSEC code. It is seen that the one-dimensional model appears to provide a reasonable physical representation of the NOSEC model, and it is noted that the heat conduction predicted by the NOSEC code is very nearly one-dimensional during the latter portions of the flight, as illustrated in Figures 108 (b) and 108 (c).

To examine the sensitivity of the thermocouple responses to changes in recession, the temperature histories at the thermocouple locations predicted by the one-dimensional model were calculated for slabs 0.25 inch and 0.50 inch thicker than the nominal. Note that if these differential thicknesses were applied to the stagnation point recession, they would represent reductions in recession of 17.5 percent and 35 percent, respectively. Figures 109 through 111 compare the NOSEC two-dimensional predictions, the measured temperatures, and the one-dimensional predictions for the three slab thicknesses. It is seen that the one-dimensional temperature predictions match the measured temperatures quite well for the analysis in which the slab was increased in thickness by 0.25 inch. (It also should be noted that the one-dimensional results are in generally good agreement with the two-dimensional results for the nominal thickness.)

To examine the sensitivity of the thermocouple responses to changes in diffusivity, the thermocouple histories predicted by the one-dimensional model were calculated for diffusivities 17.5 and 35 percent lower than the nominal value. Figures 112 through 114 compare the NOSEC predictions, the measured temperatures, and the one-dimensional predictions for the three diffusivities. It is seen that the one-dimensional temperature predictions match the measured temperatures quite well for the analysis in which the diffusivity was 35 percent lower than nominal.

Thus, it has been shown that the temperature histories can be matched either by assuming a 17.5 percent reduction in nosetip recession or by a 35 percent reduction in diffusivity by using a one-dimensional idealized model with an effective length and diffusivity chosen to best match the NOSEC predictions. Due to the well-documented and regular behavior of the diffusivity of solid tungsten, a 35 percent error in diffusivity (averaged over all temperatures) appears unlikely. Consequently, it is concluded that the ablation model used in the NOSEC code overpredicted the recession by a factor on the order of 17.5 percent. This overprediction could be due to any one of several factors. Additional analyses and data correlations would be required to determine the specific cause (or causes) more precisely.

Figure 115 compares the axial acceleration history predicted by the coupled nosetip ablation and shape change trajectory analysis with the telemetry data. It is seen that the agreement is excellent. To show the influence of shape and weight change on drag, this trajectory was recalculated for a vehicle with constant (initial) shape and weight. It can be seen in Figure 115 that this calculation underpredicts the drag by nearly 30 percent and results in a predicted impact time nearly one second early. This comparison tends to verify the ablation and shape change techniques used. Note that the analysis of the thermocouples on the tungsten tip indicated that recession probably was slightly overpredicted. The fact that peak drag also is slightly overpredicted supports this conclusion.

4.2.2   Heatshield Performance

The forebody heatshield (forward of vehicle station 16.69) was FM 5055A carbon phenolic with a 26-degree (aft-facing) wrap angle, and it was designed and fabricated by PDA. The monolithic nosetip assembly showing the heatshield configuration is presented in Figure 84. The heatshield was instrumented with six in-depth thermocouples and two heatshield/substructure bondline thermocouples.

(a) 2.0 seconds after exposure
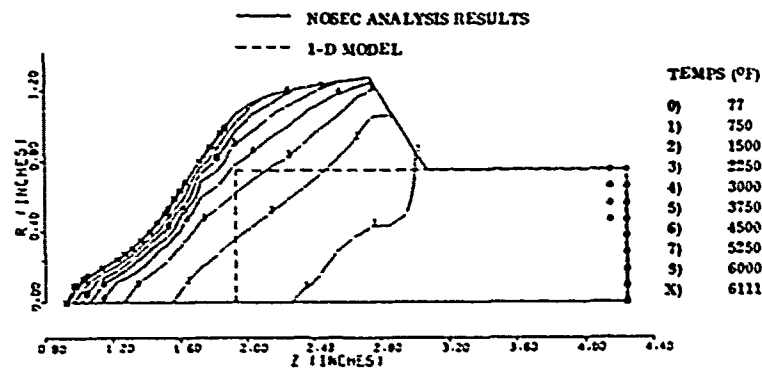
(b) 4.0 seconds after exposure
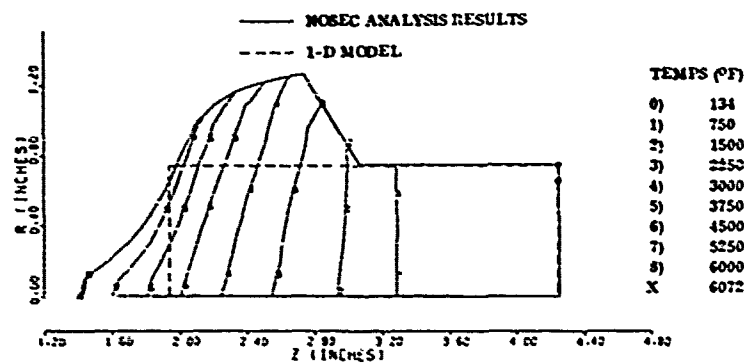
(c) 6.7 seconds after exposure
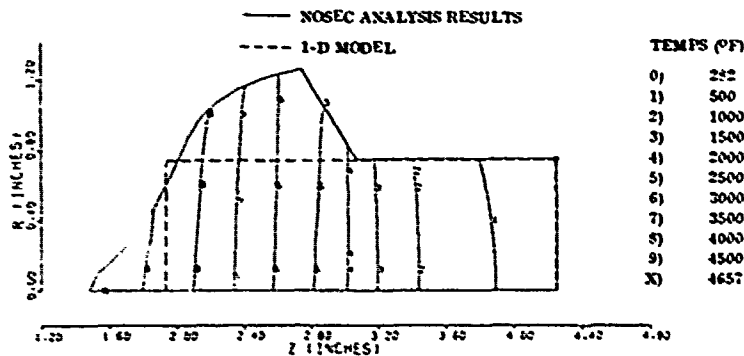
Figure 108.   Predicted post-flight temperature distributions
in solid tungsten nosetip.
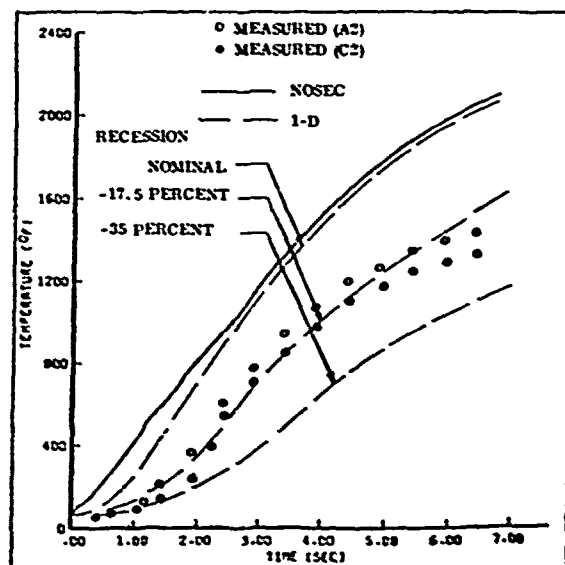
Figure 109. Effect of surface recession on temperature histories, HEARTS/ERN solid nosetip, location 2.
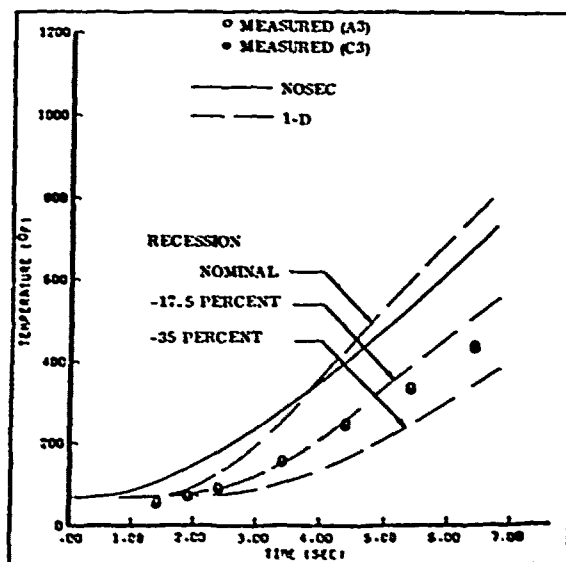
Figure 110. Effect of surface recession on temperature histories, HEARTS/ERN solid nosetip, location 3.

142
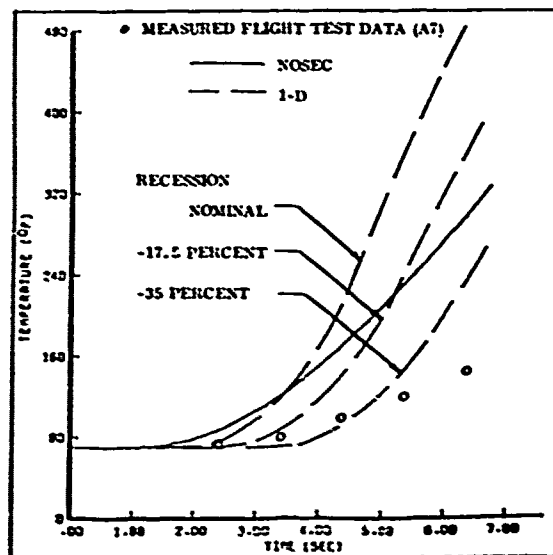
Figure 111. Effect of surface recession on temperature histories, HEARTS/ERN solid nosetip, location 7.
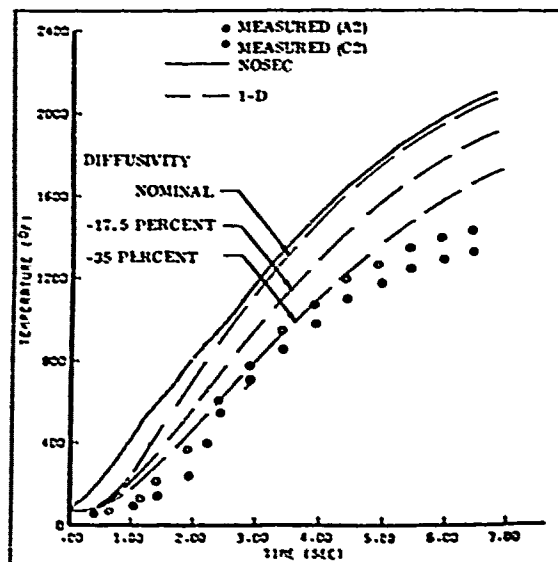
Figure 112. Effect of thermal diffusivity on temperature histories, HEARTS/ERN solid nosetip, location 2.
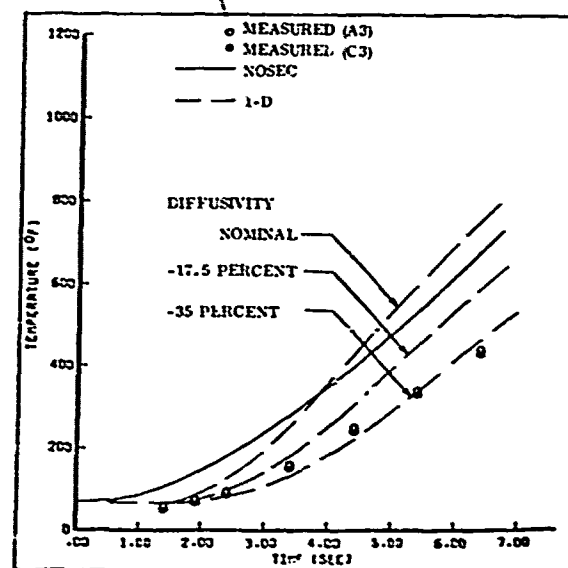
Figure 113. Effect of thermal diffusivity on temperature histories, HEARTS/ERN solid nosetip, location 3.
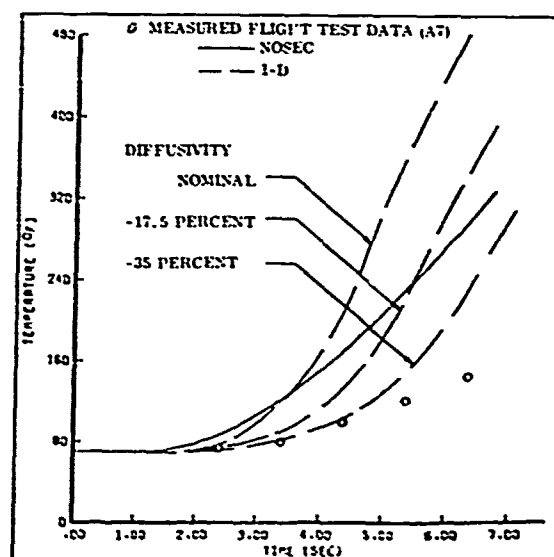
Figure 114. Effect of thermal diffusivity on temperature histories, HEARTS/ERN solid nosetip, location 7.
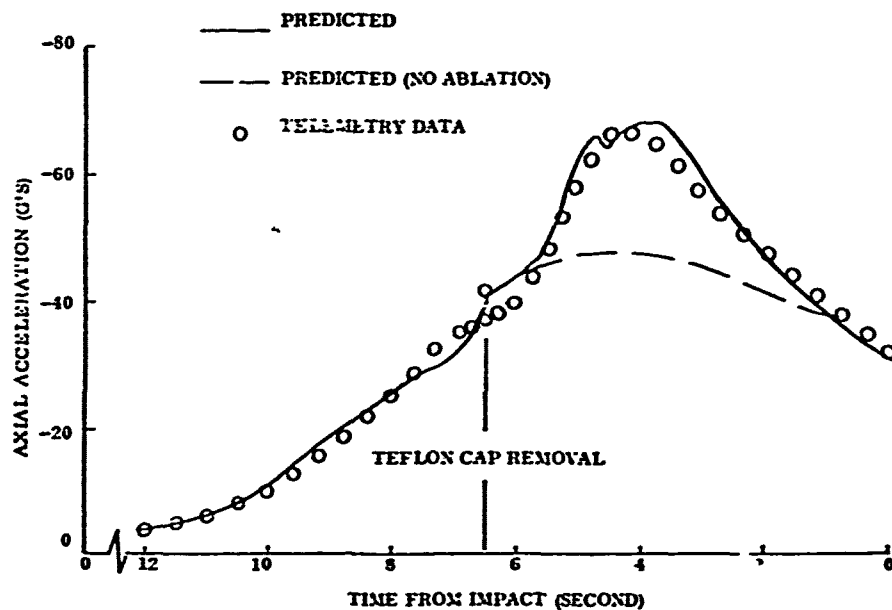
Figure 115. Axial acceleration history correlation.

The thermocouple types and positions are shown in Figure 84. Thermocouples B1, B2, D1, and D2 were tungsten/tungsten-26 rhenium, sheathed in 0.008-inch diameter (outside diameter) tantalum tubing; thermocouples B3 and D3 were Chromel-Alumel, sheathed in 0.032-inch diameter steel tubing; and thermocouples A5 and A6 were glass-wrapped Chromel-Alumel.

The in-depth heatshield thermocouples were installed so that, from the junctions, a minimum of 0.35 inch of lead wire was located in an isothermal zone. This was done to minimize temperature differences between the junction and the heatshield induced by heat conduction along the lead wire. The thermocouples were installed by cutting the heatshield along the ply direction, running the lead wire along the plies to the desired radial position, and then making a 90-degree bend and routing the lead wire circumferentially (at a constant vehicle radius) so that the junction was a minimum of 0.35 inch from the 90-degree bend. Figure 116 is a sketch showing the routing of the lead wires. After the thermocouples were installed, a mating aft heatshield was bonded to the forward heatshield. This installation method was selected over a thermocouple plug assembly since plugs cause interruptions in the plies which, in turn, can induce vortex shedding and/or aggravated ablation at vehicle positions near the plug. Inserting thermocouples along the plies does not cause interruptions in the plies, and the method does not induce aggravated ablation (Reference 2).

The tungsten nosetip and a portion of the forebody heatshield were covered with a teflon glove. The teflon glove was designed to burn through at 35 kft. The teflon glove and its position relative to the in-depth thermocouples are shown in Figure 116. As can be noted, thermocouples B2, B3, and D3 lay beneath the teflon glove and are insulated from direct aerodynamic heating prior to glove removal.

A one-dimensional charring ablation analysis was performed at the vehicle station corresponding to the location of thermocouples B1 and D1 (see Figure 116) using the PDA Ablation-Conduction-Erosion (PACE) computer code. The heatshield thermal properties used in the analysis are presented in Table 25. All properties except the char conductivity are the same as those used in

145

Reference 2. The char conductivity for 0-degree and 90-degree fiber orientations was obtained from Reference 42 and modified for the 26-degree wrap angle according to the following expression from Reference 43:

$$k = k_0 \left[1 \div \left(\frac{k_{90}}{k_0} \right) \sin \theta \right]$$

(6)

T/C	x (inch)	Δx (inch)	$R_{T/C}$ (inch)	$R_{H/S}$ (inch)	φ (deg)	ΔR (inch)
B1	3.971	0.230	1.371	1.422	138	0.049
B2	3.701	-0.037	1.275	1.353	98	0.134
B3	3.513	-0.225	1.141	1.372	145	0.239
D1	3.524	0.183	1.381	1.413	322	0.048
D2	3.752	0.011	1.275	1.390	278	0.134
D3	3.446	-0.295	1.161	1.362	327	0.230
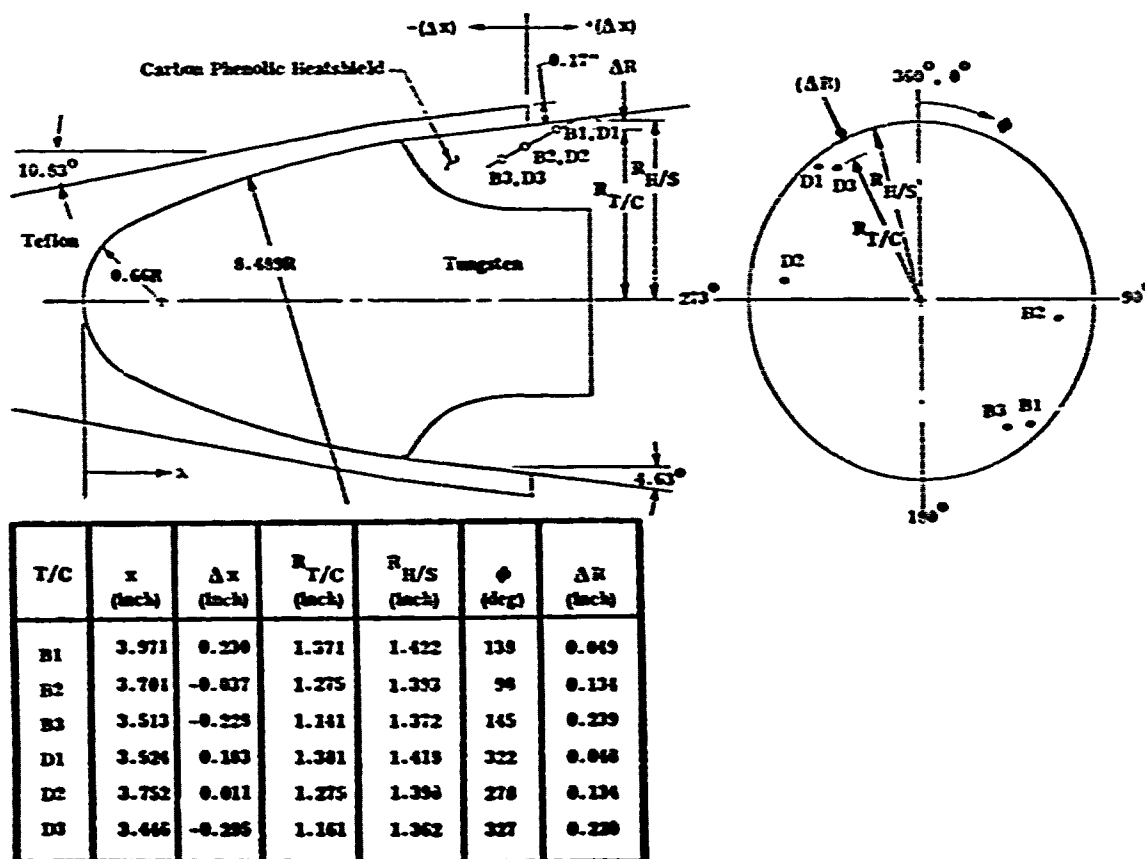
Figure 116. HEARTS/ERN solid nosetip heatshield thermocouple locations.

The convective boundary conditions used in the heatshield analysis were obtained from the NOsetip Heating And REcession (NOHARE) code for the axial location of thermocouples B1 and D1 (station 12.99). These conditions were used to predict the response of all six heatshield thermocouples. The trajectory used in the calculations was obtained from Reference 44 and is illustrated in Figure 117. Boundary layer transition was assumed to occur according to the roughness-modified "LORN" transition criterion described in Reference 2, using a characteristic roughness height of 0.0004 inch for laminar flow. Roughness-augmented heating was used for both laminar and turbulent flow. The turbulent flow surface roughness could be of either the uniformly distributed (i.e., sand-grain) type (with a maximum height of 0.002 inch) or the scallop type of surface patterns.

Table 25. Thermal properties of carbon phenolic.

Temperature (°R)	Conductivities (Btu/ft.-sec.-°R)		Specific Heats (Btu/lbm-°R)	
	Char	Virgin	Char	Virgin
400	0.148×10^{-3}	0.874×10^{-4}	-	0.235
660	0.156×10^{-3}	0.112×10^{-3}	-	0.310
860	0.163×10^{-3}	0.124×10^{-3}	0.0602	0.352
1060	0.175×10^{-3}	0.130×10^{-3}	0.0794	0.547
2000	0.247×10^{-3}	0.201×10^{-3}	0.274	0.070
3000	0.381×10^{-3}	-	0.341	-
4000	0.603×10^{-3}	0.340×10^{-3}	0.3715	1.4??
5000	0.977×10^{-3}	-	0.364	-
6000	1.509×10^{-3}	0.481×10^{-3}	0.400	1.560

Arrhenius Constants

For the expression:

$$-\frac{1}{w_o}\left(\frac{dw}{dt}\right) = \left(\frac{w - w_f}{w_o}\right)^n \sum_{i=1}^{m} A_i \exp\left(\frac{-E_i}{RT}\right)$$

i	A_i (lbm/ft²-sec)	E/R (°R)
1	0.001815	420
2	248.	12,700
3	3.009 E6	28,200

$n = 2$ (for all i)

General Information

Densities (lbm/ft³)

- Virgin   -90.4
- Char   -74.0

Char Temperature: $1060°R$

Specific Heat of Pyrolysis Gas: $0.4 \text{ Btu/lbm}_{gas}$

Heat of Pyrolysis: $1650 \text{ Btu/lbm}_{gas}$

As can be noted in Figure 116, thermocouples B1 and D1 are positioned just ¼ft of the teflon cap. At this station it is anticipated that the flow will be separated and the convective heating prior to cap removal will correspond to separated cavity heating induced by a rearward-facing step. To model the separated cavity heating, the correlations of Reference 45 were used to correct the attached flow predictions from the NOHARE code. The correlations of Reference 45 are summarized in Figure 118, where the ratio of the separated flow heat transfer coefficient (H) to the attached flow coefficient (H_o) is presented as a function of the downstream distance-to-step height ratio (X/Z). The convective heating at station 12.99 prior to cap removal was computed with the NOHARE code by modelling the teflon cap ablation in the vicinity of the thermocouples. The teflon configuration and ablation properties used in the analyses were described in Section 4.2.1. The instantaneous teflon cap thickness (Z) and attached flow heating coefficient (H_o) were used in conjunction with Figure 118 to find the separated flow heating coefficient (H). The predicted teflon thickness (Z) history is presented in Figure 11J. The resultant convective heating condition computed for the heatshield station
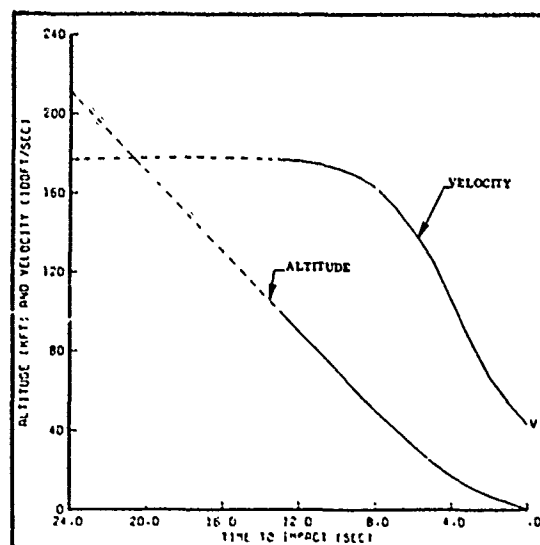
Figure 117. HEARTS/ERN R/V 106 flight trajectory.
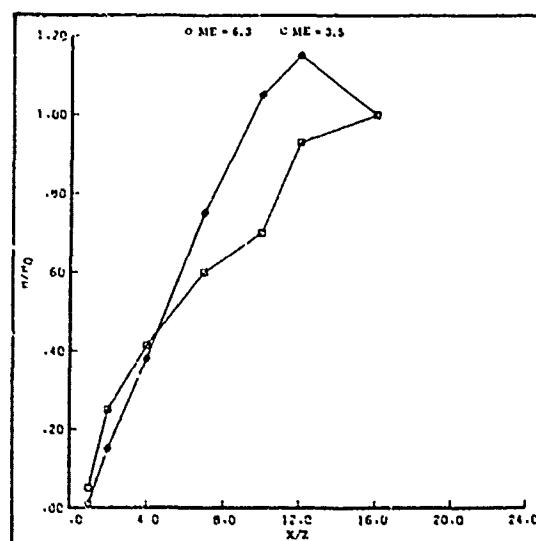
Figure 118. Relative heat transfer downstream of a
rearward-facing step (Reference 45).

is presented in Figure 120. For comparison, the attached flow convective heating condition also is shown in the figure. As can be noted in Figure 119, the heatshield originally under the cap was exposed to direct aerodynamic heating at 6.8 seconds prior to impact, which corresponds to an altitude of 40 kft. Complete cap removal was predicted to occur at 34.7 kft (Section 4.2.1).
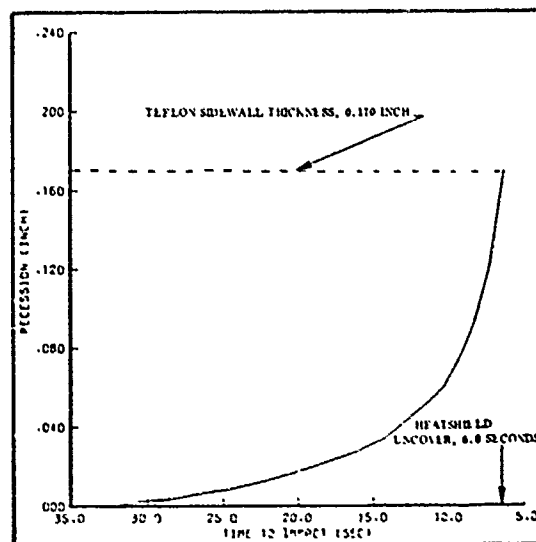
Figure 119. Sidewall recession history of teflon glove, HEARTS/ERN R/V 106, Station 12.99.
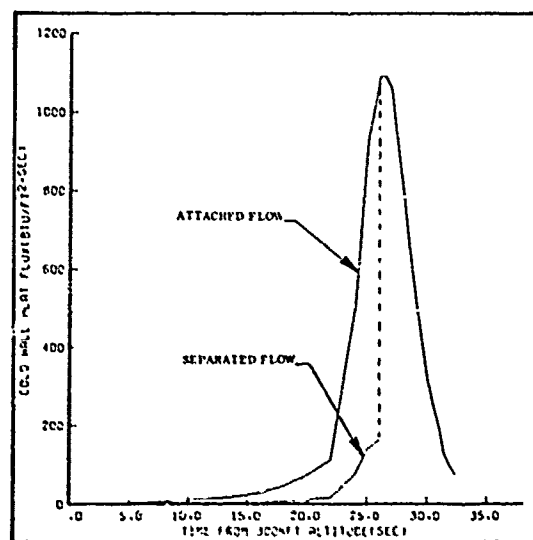
Figure 120. Sidewall convective heating history, HEARTS/ERN R/V 106, Station 12.99.

149

The predicted heatshield surface and char front recession histories are presented in Figure 121. The total surface ablation depth at vehicle station 12.99 inches is predicted to be approximately 0.042 inch. The predicted heatshield temperature response histories are compared with flight data in Figure 122. The agreement between the measured and computed temperature histories is seen to be reasonably good at the three thermocouple depths.
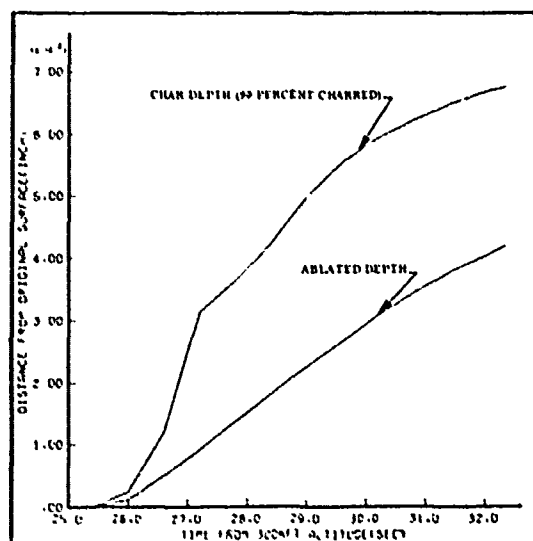
Figure 121. Computed heatshield surface recession and char depth histories, HEARTS/ERN R/V 106, Station 12.99.
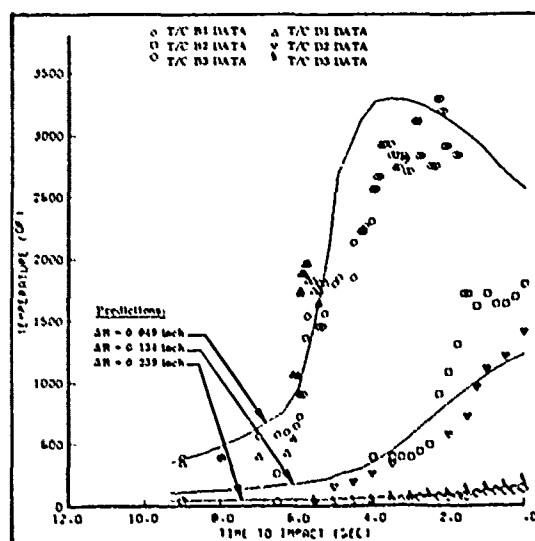
Figure 122. Comparison of measured and computed heatshield temperature histories, HEARTS/ERN R/V 106, Station 12.99.

Thermocouples A5 and A6, both of which measure heatshield-to-substructure bondline temperatures, did not measure any temperature change during flight. Thermocouple A3, which is on the tantalum holder below thermocouples B2 and B3, reached a maximum temperature of 450°F during flight. Comparing the in-flight responses and positions of thermocouples B3 and D3 (neither of which showed any significant temperature rise) with A3, it is concluded that A3 was heated conductively from the tungsten nosetip rather than by conduction through the heatshield. From the responses of these thermocouples, together with the computed results of Figure 121, it is concluded that the heatshield maintained the substructure at temperatures well below their upper operating temperature levels (~3000°F for tantalum and ~1500°F for Mallory).

5.0 FLAME/ERN DESIGNS

The last step in the evaluation of tungsten nosetips at sub-ICBM conditions was a series of two flight tests on FLAME (Fighter-Launched Advanced Materials Experiment) vehicles. FLAME is an aircraft-launched vehicle consisting of a two-stage rocket and a payload (i.e., "reentry" vehicle). The assemblies were launched supersonically from F-4 aircraft at altitudes of approximately 60 kft. The rockets then boosted the payload to a peak velocity of around 14,000 ft/sec at altitudes of 35 - 40 kft, thereby providing reasonably good simulation of the low altitude portion of reentry flight (Reference 46). The payload was designed (Reference 47) so that portions of the vehicle, including the nosetip, could be recovered intact for post-flight examination and evaluation.

One monolithic tungsten nosetip and one segmented tungsten nosetip were designed, built, and flight-tested in the FLAME program. Both nosetips were of the same external shape, as shown in Figures 123 and 124. The initial spherical nose radius was 0.60 inch, the cone half-angle was 9.3 degrees, and the tungsten overhang length was 3.25 inches. Both nosetips were made from 3.0-inch diameter extruded billets of 2 percent thoriated tungsten, as described in Sections 5.1.2.1 and 5.1.2.2. No thermal instrumentation was used on the segmented nosetip, while the monolithic design contained only a compression wave pulse/echo type of acoustic recession sensor.

The following paragraphs summarize the thermal and structural design analyses of the two FLAME/ERN configurations and briefly summarize the flight results.

5.1   DESIGN ANALYSES

5.1.1   Thermal Analysis

The thermal response of the two FLAME/ERN designs illustrated in Figures 123 and 124 was predicted for use in the structural design calculations (Section 5.1.2). The calculations assumed a clear air environment and used the design trajectory illustrated in Figure 125. The trajectory assumed ballistic flight to impact, although it was planned to initiate the recovery sequence at an altitude of approximately 16 kft.

All of the assumptions and methods used to compute the thermal response of the nosetips were the same as described previously (Section 4.1.1) for the HEARTS/ERN nosetips. The two-dimensional nodal networks used to represent the nosetips are shown in Figures 126 and 127 for the solid and segmented designs, respectively. As with the HEARTS designs, two limiting thermal models were used to describe heat conduction in the segmented nosetip. In the first model (Figure 127 [a]) perfect thermal contact was assumed between all components. This model is equivalent to the solid model network (Figure 126), with the exception of the slightly different tantalum-10 percent tungsten holders used to attach the nosetips to the aft structure. In the second model (Figure 127 [b]), all of the segments are in perfect thermal contact, and this segment assembly was considered to be perfectly insulated from the center retention stud. Thus, radiation was the only mode of heat transfer between the segments and the stud in this thermal model. This second network model was believed to be more representative of actual conditions since the segments are maintained in axial compression throughout the flight, but are free to expand or move relative to the stud.

Originally it was intended that the FLAME/ERN tungsten nosetips would be covered with teflon gloves, similar to the HEARTS/ERN designs, sized to burn through and provide sudden exposure of the tungsten at 35 kft. Because of this requirement, the nosetip design calculations assumed a uniform initial temperature of 70°F at 35 kft. Although it later was decided, because of the
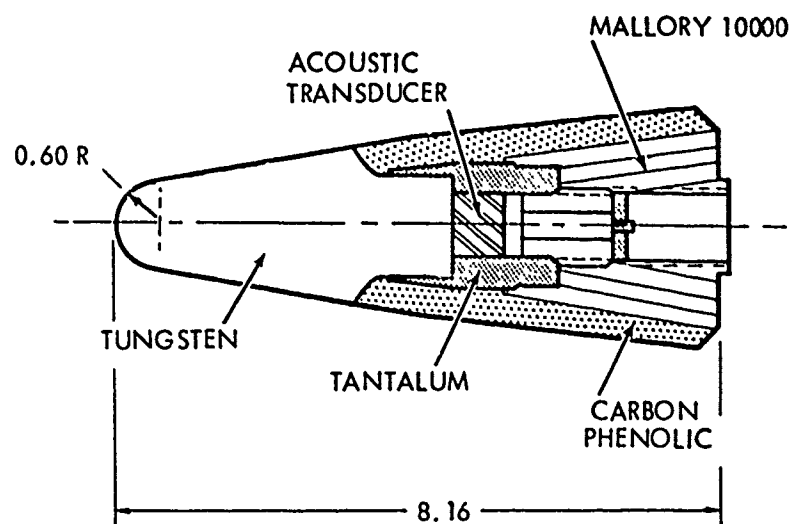
Figure 123. FLAME solid tungsten nosetip.
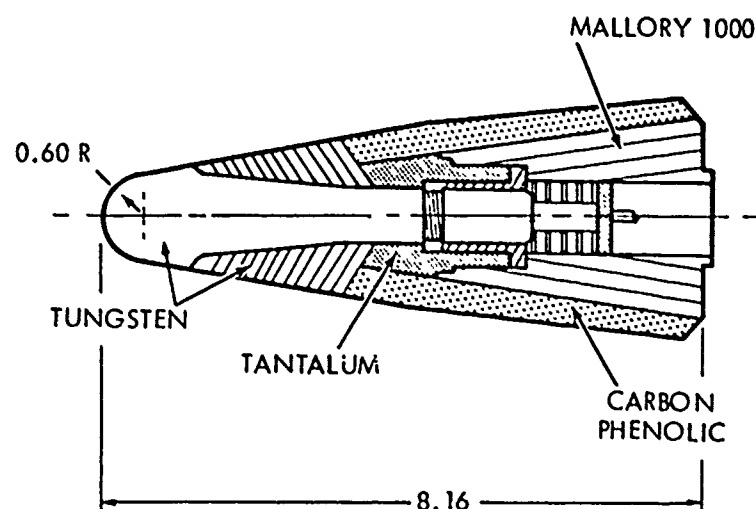
Figure 124. FLAME segmented tungsten nosetip.
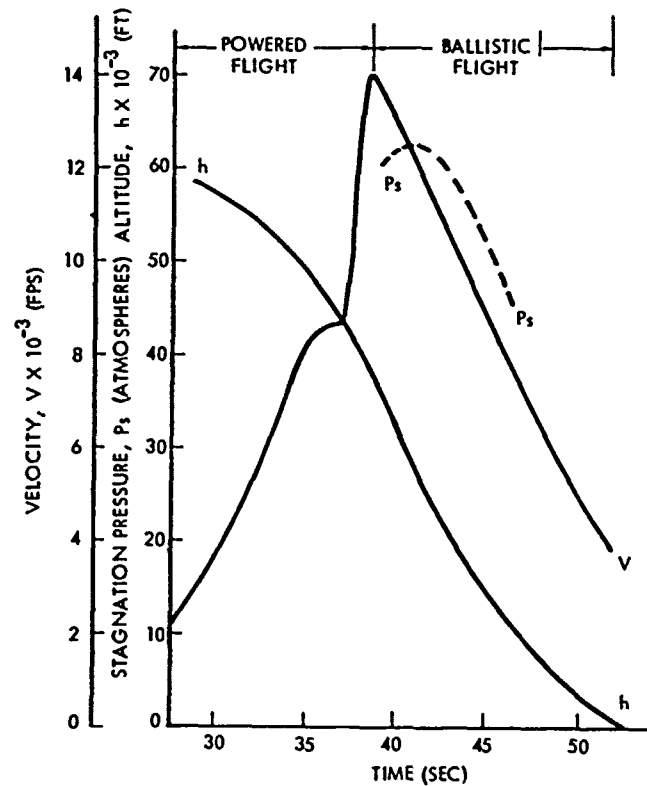
Figure 125. FLAME design trajectory.
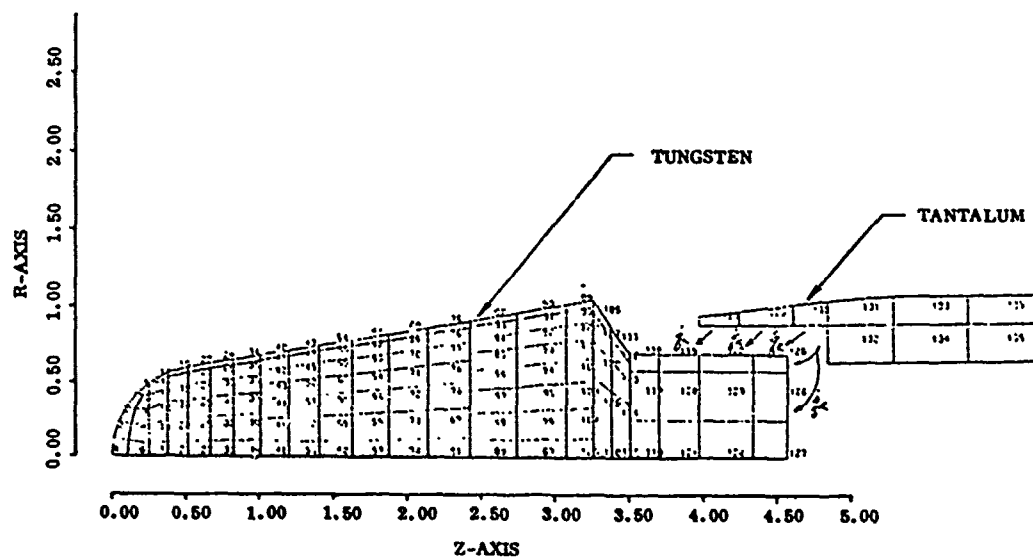
Figure 126. Thermal nodal network for solid FLAME/ERN nosetip.

(a) Perfect thermal contact model
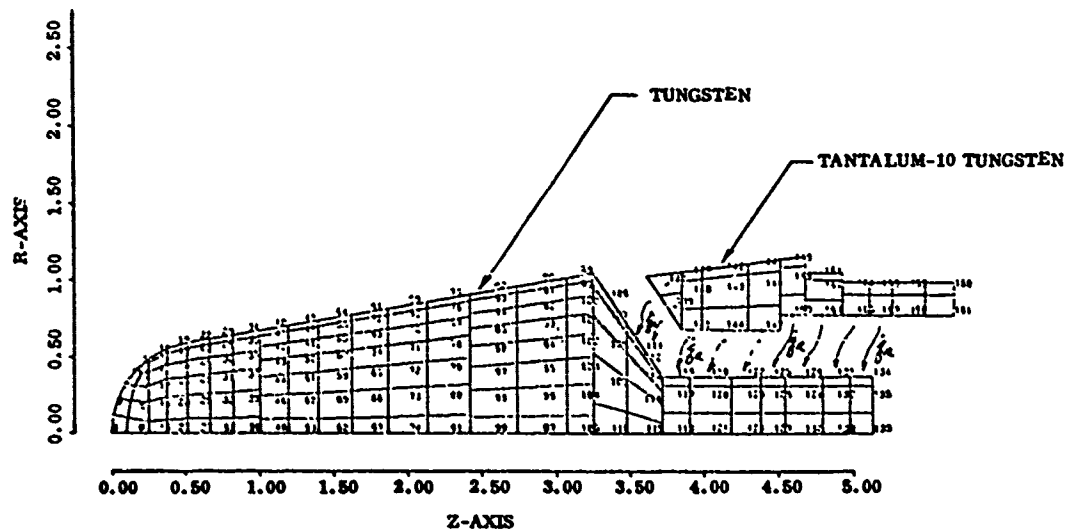
(b) Insulated segments model
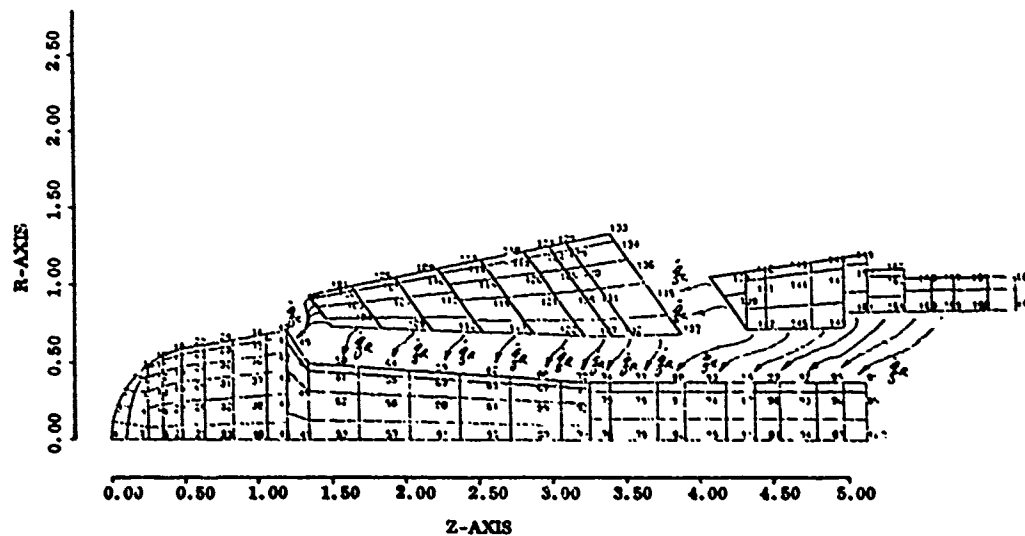
Figure 127.   Thermal nodal networks for segmented
FLAME/ERN nosetip.

comparatively mild (relative to conventional reentry flight) "high altitude" flight environment, that it was not necessary to use the teflon glove, the analysis was not repeated using the extended heating period. It was believed that the assumption of sudden exposure at 35 kft provided a conservative boundary condition for the thermostructural response calculations.

The computed nosetip recession profiles at various altitudes are shown in Figure 128. These profiles are essentially identical for all three analytical models, since the surface recession histories are nearly independent of differences in the internal heat conduction paths. The corresponding stagnation point axial recession history is shown in Figure 129. The computed histories of the internal temperature distributions, surface pressure distributions, and external shapes for the three cases were output on magnetic tapes for direct input to the structural analysis codes (Section 5.1.2).

Since the FLAME nosetips were to be recovered, additional design analyses were performed to evaluate the adequacy of the nosetip retention structure during the recovery deceleration loads and during water soak following splashdown.

Initiation of the recovery sequence was planned to occur at an altitude of 16 ± 4 kft. Therefore, the initial nosetip shape and temperature distribution for this phase of the flight were taken from the results of the preceding "reentry" calculations at an altitude of 12 kft. This should represent a worst-case condition, since it provides the maximum aerodynamic heat input prior to recovery initiation. A two-dimensional nodal network, illustrated in Figure 130, was constructed to represent the nosetip shape at 12 kft. This shape, a.   'h the initial temperature distribution and temperature-dependent material properties, were inpu. . the NOSEC computer code (Reference 7). The thermal response of the nosetip assembly then was calculated by allowing the temperatures to equilibrate with surface radiation as the only mode of heat transfer (i.e., convective cooling was ignored).

TIME (SEC)	ALT (KFT)
39.200	35.15
40.001	31.78
41.001	27.84
42.001	24.15
43.001	20.73
44.001	17.53
45.001	14.59
45.229	13.96
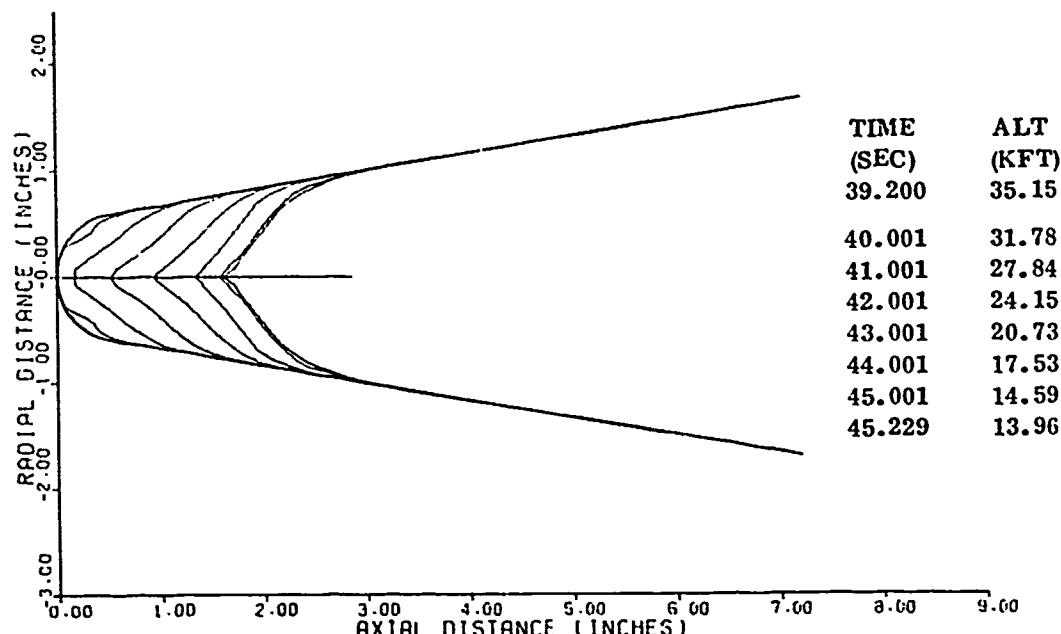
Figure 128. Computed FLAME/ERN tungsten nosetip ablation profile history.
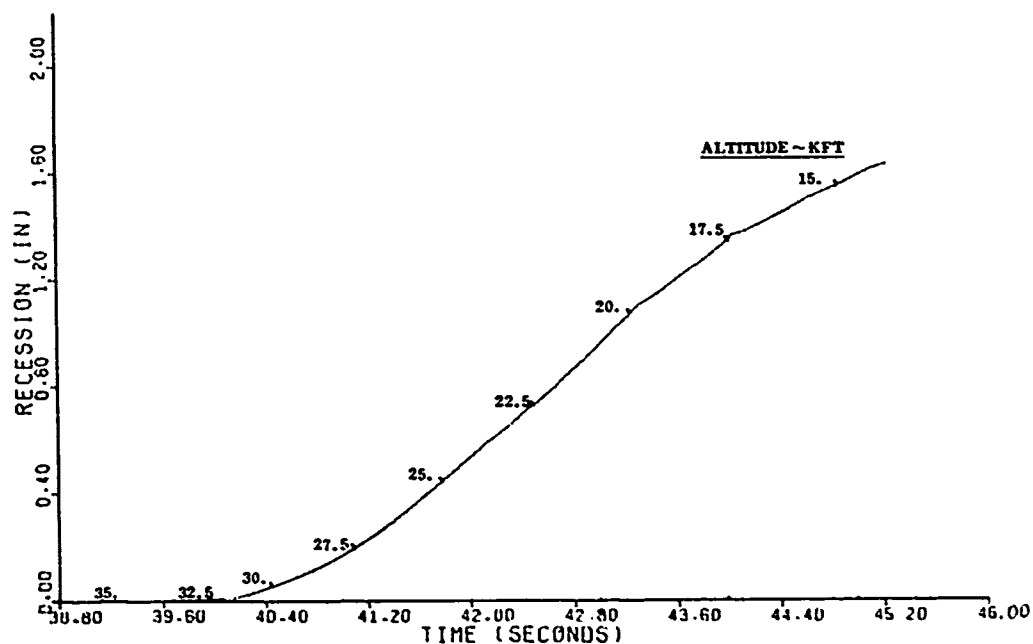
Figure 129. Computed FLAME/ERN tungsten nosetip axial recession history.
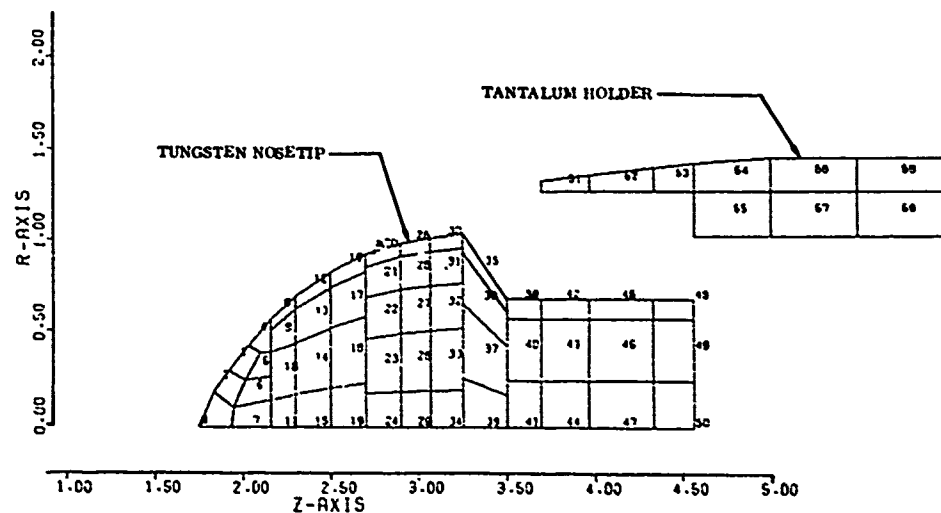
Figure 130. Nodal network for solid FLAME/ERN
nosetip during recovery flight.

157

A similar procedure was used to predict the temperature response following splashdown. For this case, the surface nodes were assigned a constant temperature of 50°F to simulate the external environment (infinite heat transfer coefficient between the water and the tungsten). The nosetip was then allowed to equilibrate to this 50°F temperature condition.

The computed temperature histories at several critical locations in the shank interface region are illustrated in Figures 131 and 132. The temperature response along the surface of the tungsten shank is presented in Figure 131, while the temperatures in the tantalum holder are shown in Figure 132. These results were stored on magnetic tape for use in the structural design analyses described in the following section.

5.1.2   Structural Analyses

Analyses were performed to compare the relative thermostructural responses of the two tungsten nosetip design concepts. Of particular interest was the isolation of potential thermostructural failure modes of the nosetip segments and the stud in the segmented concept and the sensitivity of failure predictions to heat conduction boundary condition assumptions. The segmented design was intended principally as an experiment for determination of ablation characteristics on the segmented boundary. The nosetip was not optimized for thermostructural response and, consequently, comparisons of failure probabilities between the segmented and monolithic (solid) designs may not be indicative of the relative thermostructural performance of the segmented concept.

In addition to thermostructural analyses, calculations of the probabilities of failure of the two nosetips in modes specifically related to the FLAME recovery experiment were conducted. These potential failure modes included interface mechanical loading on segments and tensile loads on the stud attachment resulting from recovery deceleration. The shrink-fit attachment of the monolithic design was checked for pull-out resistance during the period of vehicle deceleration, parachute descent (with coincident heat soak), and the splashdown condition where rapid cooling would occur.
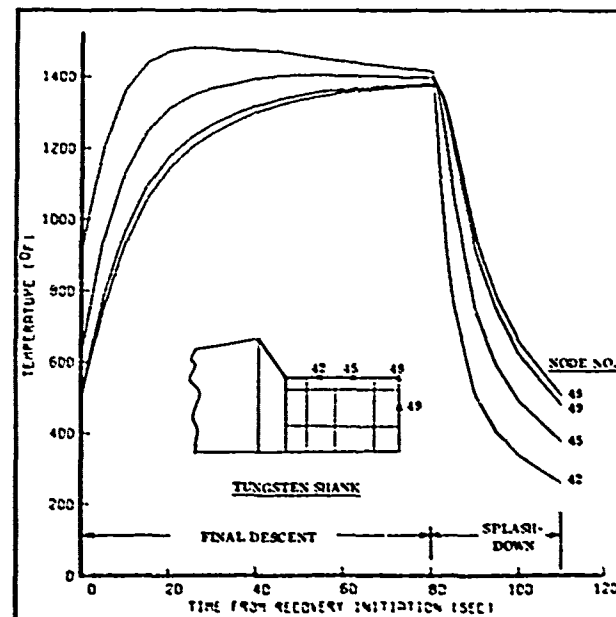
Figure 131.   Predicted temperature histories in FLAME/ERN
solid nosetip during recovery, tungsten shank.

158
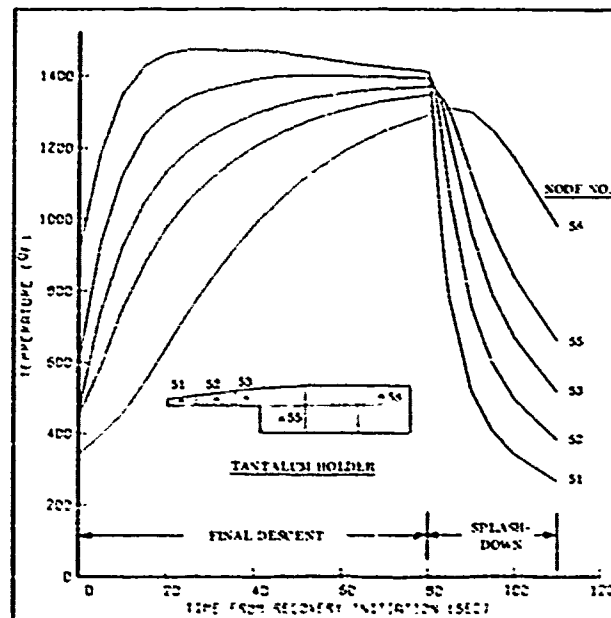
Figure 132. Predicted temperature histories in FLAME/ERN solid
nosetip during recovery, tantalum holder.

The design trajectory was shown in Figure 125 for ballistic flight from second stage burn-out to impact (no recovery). The entire trajectory was evaluated for thermostructural response to determine if the most critical response would occur above the intended upper-bound recovery initiation altitude of about 20,000 feet. Parachute deployment was programmed for 12,000 feet. Maximum deceleration loading during recovery was estimated to be 150 g's at 20,000 feet.

5.1.2.1 Monolithic Design

The monolithic nosetip (Figure 123) was fabricated from a 3-inch diameter extruded billet of 2 percent thoriated tungsten. The mechanical and physical properties necessary for thermostructural analyses are given in References 2, 20, and 21. The ductile-brittle transition temperature (DBTT) was assumed to be 400°F, based on the available test data (Reference 20).

Two-dimensional finite-element stress analyses were performed to determine instantaneous stress distributions in the tungsten nosetip. The analyses used the ablated shapes and internal temperature distributions as functions of altitude as predicted by the preceding thermal analyses.

The minimum margins-of-safety of material in the brittle zone (at temperatures below the DBTT) are plotted in Figure 133 as functions of altitude. The figure also shows that the minimum margins occur on the centerline and progress aftward as the nosetip ablates and heat soaks in the axial direction. The stress states and temperatures of critical elements at representative altitudes are given and show that, in all cases, the largest stress component is the axial stress. However, the extruded billets are transversely isotropic and the critical stresses in the monolithic nosetip are the equal biaxial hoop and radial stresses.

159
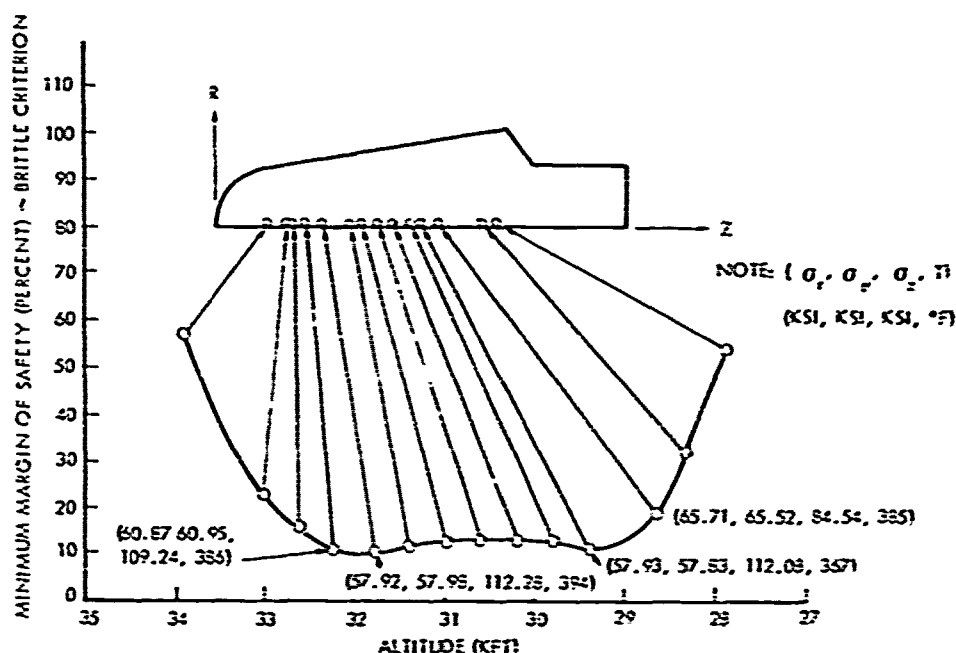
Figure 133. Minimum brittle margins-of-safety
in FLAME/ERX solid nosetip.

A nonconservative factor in the thermostructural analysis was the lack of recognition
of volume effects. In the monolithic nosetip, considerably larger volumes of brittle material are
stressed than in the biaxial flexure specimens used for derivation of the failure criterion (References 2 and 20). Consequently, the margins-of-safety for the design may be significantly lower
than those shown in Figure 133.

5.1.2.2 Segmented Design

The segmented nosetip design is shown in Figure 124. The stud was machined from a
3-inch diameter extruded billet of 2 percent thoriated tungsten. The segments were machined from
blanks which were coined from short upset-forgings of lengths of thoriated tungsten extrusions. In
this manner, a more desirable grain structure giving better in-plane strength properties was obtained
in the segments.

Two coupled ablation heat transfer analyses were conducted with the PDA NOSEC code.
As described in Section 5.1.1, the first case assumed perfect thermal contact at each internal boundary between segments and between the segment stack and the stud. The second case assumed no
thermal contact between the stud and the segments while retaining perfect contact between segments.
The latter case is judged to best represent reality because the segments do expand away from the
stud due to thermal gradients. The degree of thermal contact between segments is of lesser importance because the principal direction of heat flow is essentially parallel to the segment boundaries.
That is, the isotherms are nearly normal to the segment surfaces and little heat is transferred
across segment boundaries, regardless of the actual thermal resistance.

The results of the finite-element thermostructural analyses are given in Figures 134 through 137, where the minimum predicted margins-of-safety are plotted as functions of altitude. The minimum margins in the stud are not affected significantly by the degree of thermal contact at the segment boundary until the critical element has moved near the station of the forward segment. After this occurs, the case with no thermal contact effectively isolates the stud from the large radial thermal gradients and the probability of thermal stress failure becomes very low.

The margins-of-safety of the segments are affected more significantly by thermal contact at the stud boundary. As shown in Figures 136 and 137, the envelope of minimum margins is reduced by the assumption of no thermal contact. This results from the stud soaking heat away from the segments and, thus, increasing the radial thermal gradient in each individual segment.

The thermostructural analysis of the segmented nosetip is conservative in two important aspects. First, the strength properties of large-diameter (3 inch) extrusions were used for the failure analysis. As discussed in Section 3.1, it is believed that very large improvements in strength and DBTT characteristics will result from forging and coining segments in the manner used to produce the FLAME components. Secondly, the volume of stressed material is much lower in the stud and segments than in the monolithic nosetip. In any brittle material, the volume effect is significant, with smaller components having lower probabilities of failure than large components with the same applied stress level.

5.1.2.3   Structural Response to Recovery Loads

Monolithic Design

During the recovery phase of the flight test, the tungsten nosetip was retained by the shrink-fitted tantalum-10 percent tungsten alloy sleeve. The sleeve was originally shrunk onto the tungsten shank with a 0.0028-inch minimum interference fit. This condition produced clamping pressures at the interface which, when combined with a reasonable estimate of the friction coefficient, provided an estimated resistance to pull-out of 6000 lbs. In this condition, the maximum hoop stress in the tantalum sleeve was calculated to be 55,000 psi.

The critical load for nosetip retention was evaluated at the recovery initiation altitude by taking into account the temperatures in the components at that time. Some reduction of clamping pressure due to thermal expansion differences between the tungsten and tantalum components occurred relative to the original assembly condition, but the critical pull-out load was still 5500 lbs. This provides a capability to withstand about 900 g's axial deceleration. The maximum estimated deceleration for the recovery phase was 180 g's, indicating a large positive safety margin.

Calculations of the temperature distributions in the attachment region during parachute descent indicated the shank and tantalum sleeve would soak out to about 1450°F, as illustrated in Figures 131 and 132. Consideration of the free thermal expansion behavior of the two metals indicated that the shrink-fit preload decays to zero as the temperature of the sleeve and shank rises uniformly to 1500°F. The computed free thermal strains of the two materials (References 48 and 49) are shown in Figure 133 with the tantalum offset by the amount of the shrink-fit interference. The temperature across the attachment was assumed to be uniform because of the relatively long soak period during parachute descent and because of the intimate thermal contact between the components.
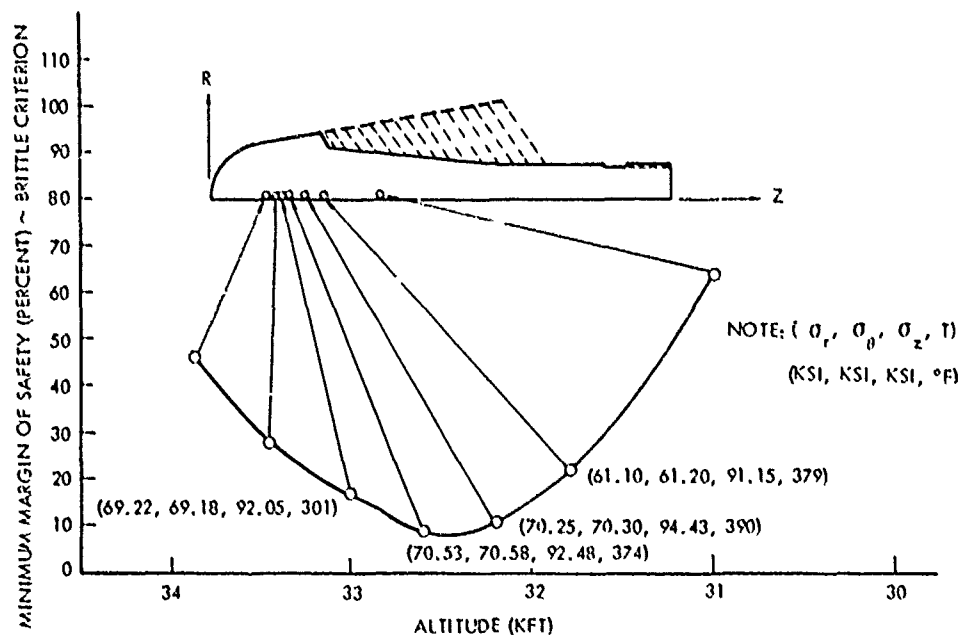
Figure 134. Minimum brittle margins-of-safety in stud, FLAME/ERN segmented nosetip with good thermal contact.
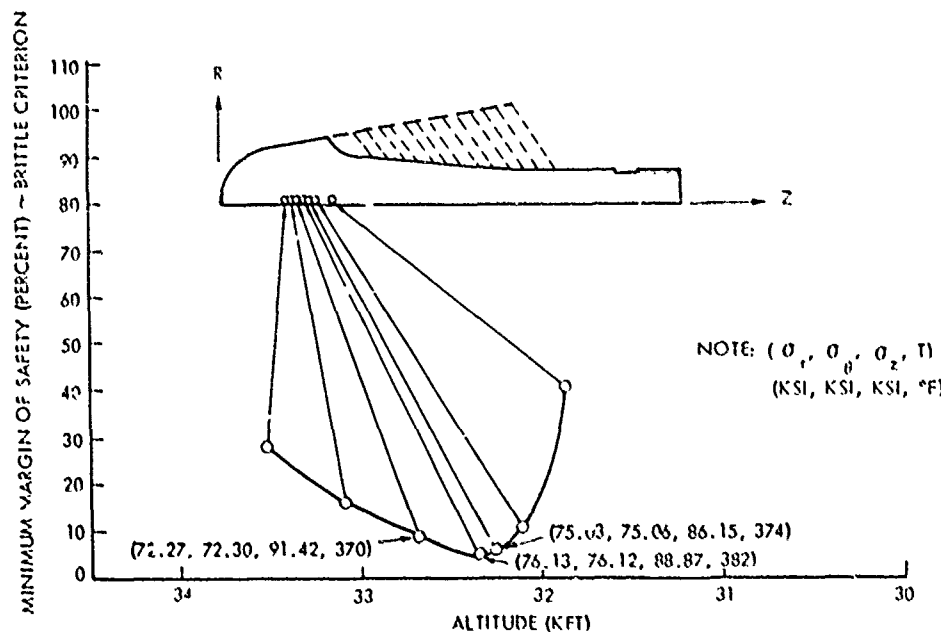
Figure 135. Minimum brittle margins-of-safety in stud, FLAME/ERN segmented nosetip with no thermal contact.
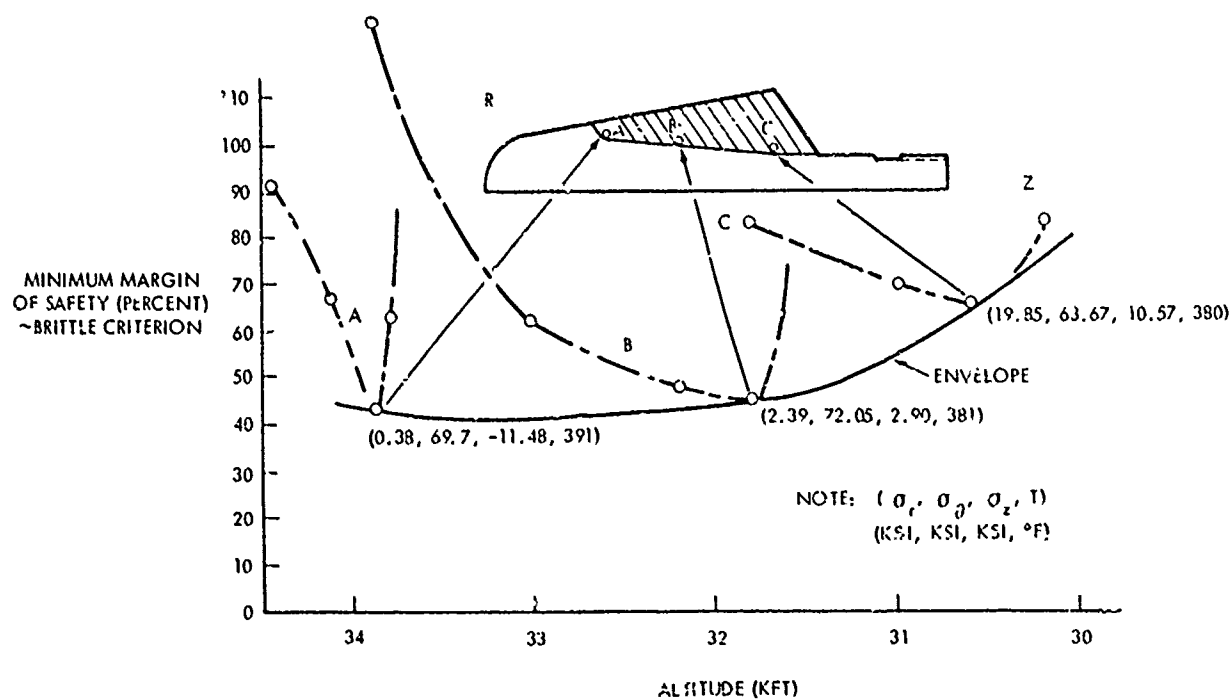
Figure 136. Minimum brittle margins-of-safety in segments, FLAME/ERN segmented nosetip with good thermal contact.
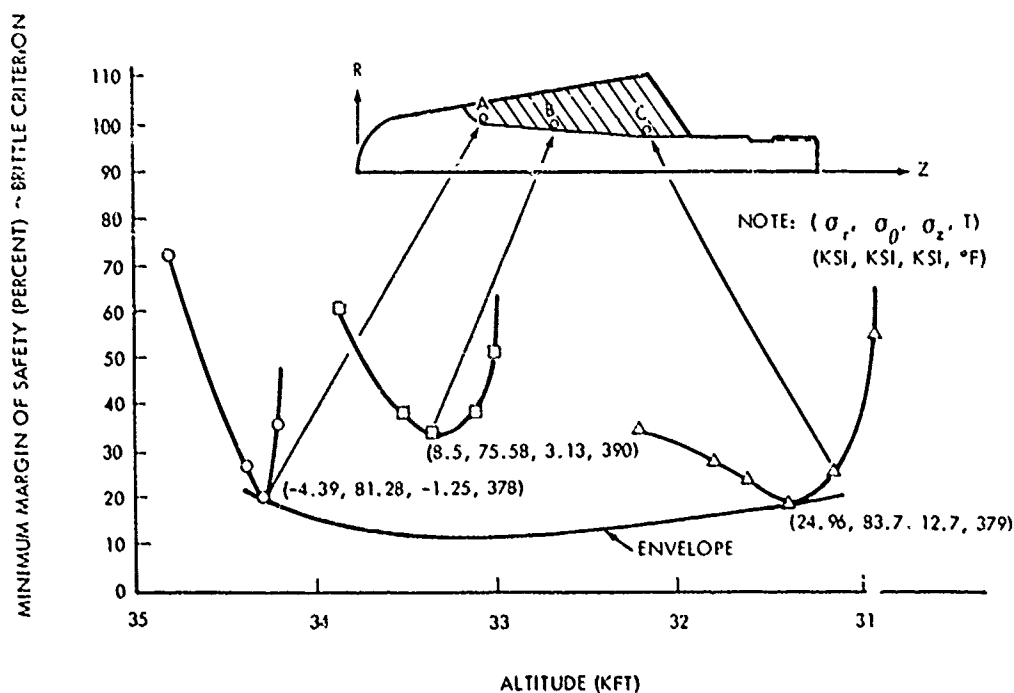
Figure 137. Minimum brittle margins-of-safety in segments, FLAME/ERN segmented nosetip with no thermal contact.
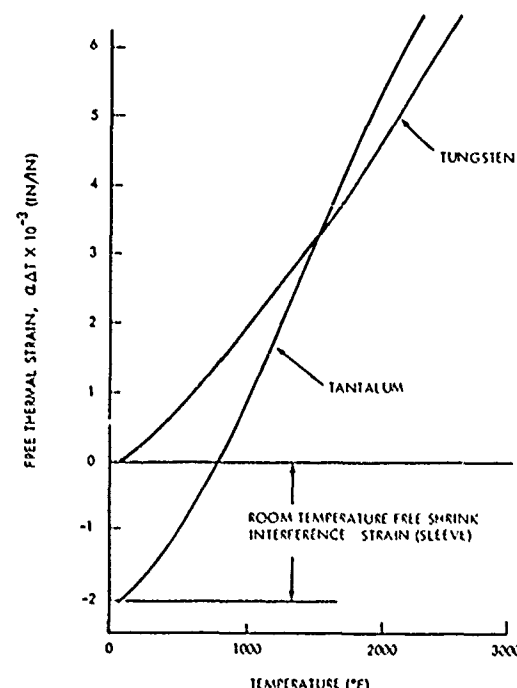
Figure 138. Free thermal strain including initial room
temperature shrink interference strain.

As a result of the soak-out analysis and consideration that the tungsten shank may cool much faster than the tantalum sleeve after splashdown in the originally planned water recovery, the design was modified to add two retention pins through the sleeve and shank.

Segmented Design

Axial deceleration causes inertial loading of the segment stack against the forward segments. This loading tends to push the segments up the tapered stud, thereby causing a hoop tension stress at the segment internal diameter. A finite-element analysis was conducted to determine the magnitude of this stress. The segment was modeled with a uniform pressure on the aft surface representing the inertia of the segment stack aft of that location. The load was reacted by combined pressure and shear at the inside diameter representing friction and pressure loading on the stud. The analysis included temperatures at the initiation altitude. The resulting critical stresses are:

$$\sigma_z = 2310 \text{ psi}$$
$$\sigma_\theta^z = 13090 \text{ psi}$$
$$\sigma_z = 1370 \text{ psi}$$
$$\sigma_{Rz}^z = -410 \text{ psi}$$

at a temperature of 3000°F. Since the critical element is ductile (temperature above the DBTT), the von Mises failure criterion was used along with tensile strength data at the critical temperature (Reference 20). The resulting margin-of-safety was determined to be 95 percent.

164

Margins-of-safety were also calculated for the threaded stud attachment. The stud is retained at the aft end by a threaded sleeve which bears against a spring washer. The washer allows the stud to move forward to accommodate thermal expansion at the segment stack and limit the axial tensile loads in the stud. However, during recovery deceleration, the spring washer bottoms out and higher loads may be imposed. These loads were calculated from the estimated weight of the nosetip at recovery and the anticipated recovery deceleration. Stresses in the tungsten threads and in the shank were calculated including a factor of 2.0 on the loading to account for shock dynamic effects. Very large margins-of-safety were determined for both failure modes.

5.2 FLIGHT TEST RESULTS

Both tungsten nosetips were flight-tested successfully on FLAME vehicles. The segmented design was flown on FLAME Vehicle F-003 on 28 March 1975 at Wallops Island, Virginia. The flight occurred in an undefined (i.e., no measurements were made) weather environment characterized by low altitude clouds and rain. The burn-out velocity was approximately 12,800 ft/sec at an altitude of 41,100 ft. Payload recovery was not accomplished because of an ordnance system malfunction that resulted in incomplete removal of the vehicle centerbody ballast sections. However, the measured axial and lateral vehicle acceleration histories prior to initiation of the recovery sequence indicated that the nosetip performance was nominal in all respects. In particular, very small lateral accelerations were measured, which implies symmetrical recession of the nosetip. The axial acceleration history was smooth and within predicted bounds, suggesting nominal recession with no removal of segments or other solid material.

The monolithic tungsten nosetip was flight-tested on FLAME Vehicle F-005 on 3 June 1965 at the Tonopah, Nevada test range. The flight was in clear air, and the vehicle reached a maximum velocity of 13,200 ft/sec at an altitude of approximately 46,000 ft. The return echo from the compression wave acoustic sensor disappeared prior to burn-out so that no in-flight recession measurements were obtained.

The recovery experiment was completely successful, and the entire nosetip was recovered intact for post-flight examination and evaluation. As illustrated in the photograph shown in Figure 139, the recovered nosetip had a smooth, rounded shape with no evidence of scallop patterns. The measured total axial recession of the stagnation point was 0.37 inch. As with the monolithic design discussed previously, the vehicle experienced no significant angle-of-attack or axial acceleration anomalies prior to initiation of the recovery sequence.

A brief analysis was performed to evaluate the recession characteristics (i.e., total recession and shape) of the recovered tungsten nosetip. The calculations used the derived flight test trajectory (Table 26) and were performed with the NOHARE code (Reference 7) using the same methods and assumptions described previously for the design analyses of the HEARTS and FLAME tungsten nosetips (Sections 4.1.1 and 5.1.1). The only parameter varied in the analysis was the assumed value of the characteristic laminar surface roughness height, which is used to define: 1) the onset and location of boundary layer transition (as described by the PANT criterion, Reference 37), and 2) the roughness-augmented laminar heat flux (Reference 38).

The computed stagnation point recession depth is presented in Figure 140 as a function of the assumed laminar roughness height. Also shown in Figure 140 is the measured total recession of the recovered nosetip. As indicated, agreement between the measured and computed values is achieved with a laminar roughness height of about 0.51 mil. This value then was used in a NOHARE computer code calculation to compare the computed shape with the shape of the recovered nosetip.
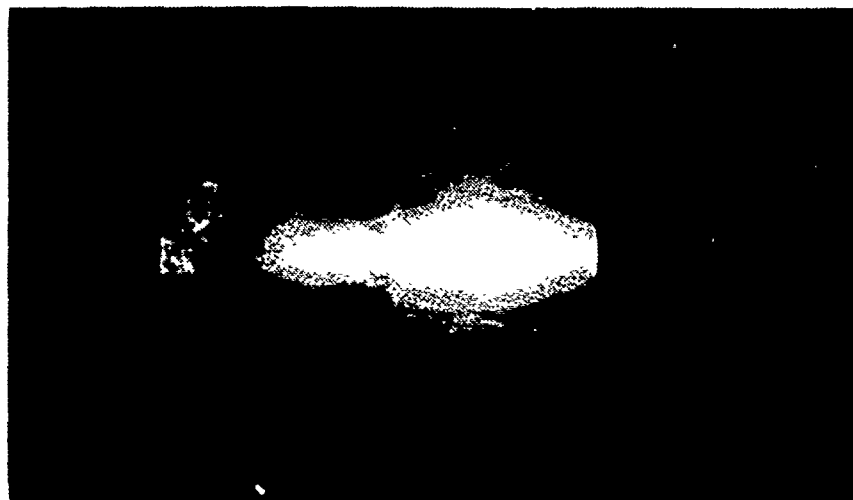
Figure 139. Photograph of recovered FLAME/ERN nosetip.

The results of this calculation are illustrated in Figure 141, where it can be seen that agreement between the two shapes is very good. Thus, it was concluded that the basic methodology used to predict the recession and shape change histories of melting tungsten nosetips is adequate for use in design calculations. (Additional verification is, of course, required at more severe flight conditions.)

The FLAME/ERN flight tests also provided additional indirect evidence that the segmented construction technique does not cause any measurable effect on the surface ablation characteristics of tungsten nosetips. Since neither design was expected to be critical thermostructurally in the FLAME flight environment, additional tests in more severe environments are necessary to verify the improved thermal stress resistance of the segmented design concept.

Table 26. FLAME/ERN flight test trajectory F-005.

TIME (SEC)	VELOCITY (FT/SEC)	ALTITUDE (FT)
.000	1000.	60000.
2.000	2050.	59500.
4.000	3200.	58500.
6.000	4610.	57000.
8.000	6210.	55000.
10.090	7650.	52200.
11.000	8000.	50500.
12.000	10800.	48750.
13.200	13200.	46000.
14.020	12841.	44000.
14.820	12459.	42000.
15.660	12055.	40000.
16.520	11627.	38000.
16.950	11409.	37016.
17.430	9815.	36000.
17.640	9205.	35600.
17.980	8322.	35000.
18.360	7469.	344'0.
19.080	6104.	33400.
19.970	4850.	32400.
20.820	3912.	31600.
21.590	3223.	31000.

Figure 140. Effect of laminar roughness height on total stagnation point recession of FLAME monolithic tungsten nosetip.

Figure 141. Recession profiles of FLAME monolithic tungsten nosetip.

6.0 TUNGSTEN ABLATION GAGE DEVELOPMENT

Design of a suitable ablation gage for obtaining in-flight recession measurements proved to be a major problem associated with the development of erosion-resistant nosetips (ERN). The susceptibility of tungsten to brittle thermostructural failure precludes the use of concepts requiring drilled holes for the in-depth insertion of sensors or radioac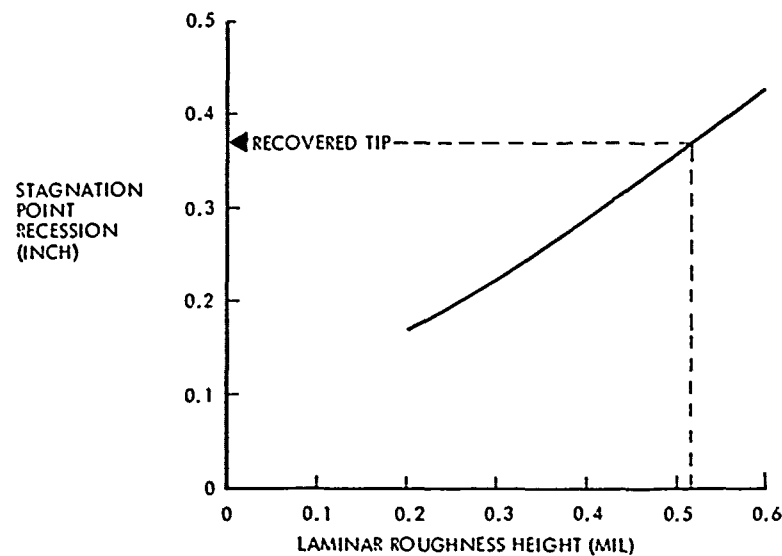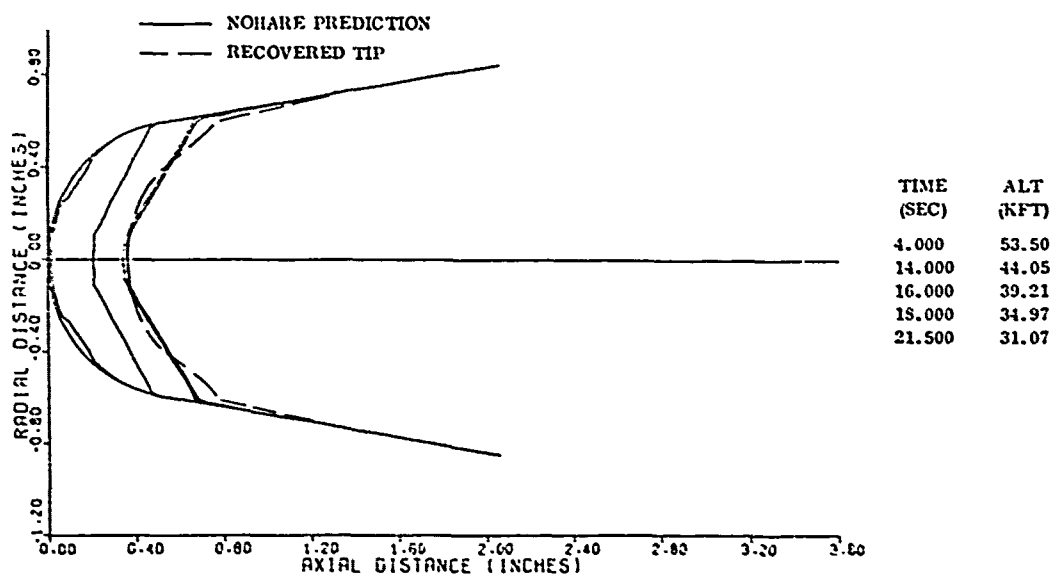tive sources. Moreover, the high density of tungsten severely limits the potential of conventional gamma-ray backscatter gage concepts. The one concept that seemed promising initially was a pulse/echo acoustic ablation gage.

The acoustic gage had been flown successfully on a number of vehicles with graphite nosetips and there seemed to be no theoretical barriers to its application to metals. Thus, despite some anomalous results in early tests with tungsten, it was decided to proceed with development of the gage for the A.N.T./ERN program (Reference 2).

Further ground and flight test results for the sensor, however, were discouraging. The shear wave mode had been selected initially, based on successful ablation tests with melting stellite alloy subtips in an erosive rocket motor exhaust. In tungsten, however, the echo pulse decayed to the noise level within about 0.5 second of exposure to high heating rates. Little or no improvement occurred after a change to a pulse/echo compression wave mode. In fact, to date, no successful measurements of tungsten ablation histories in ground tests have ever been obtained with a pulse/ echo gage.

Because of the early problems with the acoustic sensors, efforts were initiated to investigate and develop alternate sensor concepts for tungsten. A radioactive backscatter sensor utilizing neutrons (which are not attenuated by tungsten as readily as are gamma rays) was designed and tested and found to offer a promising, though limited, measurement capability (Reference 2). However, the neutron backscatter gage presented difficult safety and handling problems and required more development work to be suitable for flight.

In the present study, two additional sensor concepts were investigated. One of the concepts was another type of acoustic gage that measures the resonant frequencies in the nosetip to obtain an indication of the remaining length. The second concept was another radioactive sensor that uses Bremsstrahlung radiation to activate the tungsten. The work accomplished in the development of these two ablation gages is summarized in this section.

6.1 RESONANT FREQUENCY ACOUSTIC ABLATION GAGE

The first ground test with the compression wave acoustic sensor occurred as an add-on experiment in a series of AFFDL 50 MW arc-jet tests of segmented tungsten nosetip concepts (Section 3.2). The segmented designs all included a central tungsten stud which ran axially the length of the nosetip and held the separate segments together. The stud provided the continuous acoustic path required by the sensor.

In planning discussions for the tests, it was noted that the rod-like geometry of the studs suggested a different type of acoustic sensor. The resonant frequencies in a rod are well separated and can be used to measure length. Furthermore, the low frequencies corresponding to the resonances would be expected to have relatively low attenuation coefficients. Thus, when some simple bench tests proved promising, it was decided to incorporate a test of the resonant frequency concept, along with the compression wave pulse/echo tests, in the 50 MW series.

While the compression wave pulse/echo signal vanished in manner similar to the shear wave signal in previous 50 MW tests, the resonant frequency gage provided the first measurements of tungsten recession ever obtained with an acoustic ablation sensor. Thus, it was decided to proceed with development of a flight-qualified resonance gage for A.N.T./ERN nosetips.

This section summarizes the current development status of the K West resonant frequency ablation gage concept. The sensor is still considered a promising solution to the tungsten ablation gage problem, particularly for segmented tips.

6.1.1 Concept Description

For a simple rod, free at both ends, resonances occur when the rod length is an integral multiple of one-half wave length. One physical interpretation of this fact is that reinforcement occurs when return waves reflect from the drive end boundary in phase with the outgoing driven wave. When the reflections at both rod ends are of the same type (zero strain type for free ends), a corresponding condition is that the round trip time for a stress wave be an integral multiple of the wave period. Thus, the resonant frequencies are

$$f_n = \frac{n}{\tau_o}, \quad n = 1, 2, 3, \cdots \cdots \tag{7}$$

where the round trip time, τ_o, is defined by

$$\tau_o = 2 \int_0^L \frac{dX}{C(T[X])} \tag{8}$$

where L is the rod length
    X is the length coordinate
    C(T) is the speed of sound in the rod as a function of temperature.

It may be noted that the temperature distribution in the rod, $T(X)$, must be known to evaluate the integral.

Conceptually, a resonant recession gage for a rod would include: 1) transmitter and reciever acoustic transducers, both fixed to the non-ablating end of the rod; and 2) an electronic package that would drive the rod at frequencies near resonance for a given mode and, in some manner, define the resonant frequency history. The round trip time history $\tau_o(t)$ could then be obtained from Equation (7).

The "apparent length" history of the rod is defined by

$$L_o(t) = \frac{C_o \tau_o(t)}{Z} \tag{9}$$

where C_o is the room temperature speed of sound in the rod. To obtain the actual length history, a "temperature correction" would be added to L_o; from Equation (8) the temperature correction is given by

$$\Delta L(t) = \int_o^{L(t)} \frac{d}{\overline{C} \ (t\{X\})} - L(t) \qquad (10)$$

where $\overline{C} = C/C_o$.

Of course, L(t) is not know a priori and the temperature distribution in the rod would not normally be available from measurements. Thus, ΔL must be calculated by an iterative process. From the L_o history and other flight measurements, an appropriate ablation model (transition criterion, surface roughness, etc.) would be selected. The ablation and internal temperature distribution histories conforming to this model would then be calculated. Next, the temperature correction would be computed and applied to the apparent nosetip length. Finally, the corrected measured recession history would be compared to the computed ablation rates. If necessary, the process could be repeated until agreement is obtained. Fortunately, the temperature correction will be a small fraction of the nosetip recession for most cases of interest. Thus, convergence should be rapid and errors in the computed temperatures would not be too important.

For a rod, the resonances are well defined and easily correlated with length. For a real nosetip, the picture is complicated in several ways. Some of the more important of these are:

1. The curved stagnation region, together with the beam divergence characteristic of the low resonance frequencies, leads to a spreading of the resonance peak. In effect, the nosetip may be modeled as a bundle of rods of varying lengths, all excited simultaneously, even when consideration is restricted to one-dimensional stress wave propagation.

2. Because the stress wave propagation is three-dimensional, many resonances exist other than the length resonances. The frequencies of some of these resonances will vary with nosetip ablation while others will remain fixed or will vary with temperature only.

3. As there will be many oblique reflections in a three-dimensional nosetip, stress wave mode conversions (from compression to shear and vice versa), with changes in stress wave velocity, will occur. These mode conversions complicate the interpretation of resonances.

4. The base of the nosetip (where the transducer is mounted) is modeled imperfectly as a "free end." Thus, some phase shift of the reflected wave, with a corresponding shift in the resonant frequencies, can be expected.

The first three of these conditions waste power while contributing structure to the frequency response curve, making it more difficult to identify and track a "length resonance." They are all less important for a segmented tip design with a central stud than they are for a solid plug tip. The fourth condition affects the calibration of the gage, but otherwise should not be important.

To help assess the potential of an ablation gage based on the resonant frequency principal, some early bench tests were performed on a Mallory (copper-infiltrated tungsten) replica of the studs used in the segmented 50 MW models. A vertical stack of two transducer chips was bonded to the rear end of the stud. The chip bonded directly to the stud was excited with a wave generator while the aft-most chip was used as a listening device. In a series of experiments, the excitation frequency was varied in sawtooth curves covering several different sweep rates and frequency ranges. It was found that the first resonance (n = 1 in Equation [7]) was very difficult to identify. The peak was so narrow (i.e., the resonance was of such high Q) that it was completely obscured at all but the very slowest sweep rates (less than 1 kHz/second). The second resonance (n = 2) was easier to find, but was still highly attenuated at sweep rates above 50 kHz/second. The third resonance, on the other hand, was readily identifiable at sweep rates in excess of 500 kHz/second and was located at frequencies in agreement with theory. Thus, it was decided to continue with a 50 MW test of the resonance gage concept.

At a later date, similar bench experiments were performed on a full-scale unsegmented subtip. While the frequency response curve for the subtip had more structure than the response curve for the stud (as would be expected), the third length resonance was still readily identifiable. Thus, it would appear that a resonance ablation gage is feasible for both segmented and unsegmented tips.

6.1.2 Signal Conditioning Concept

Two basic signal conditioning concepts were considered: 1) a system analogous to the bench tests described above in which the drive frequency is varied in a sawtooth curve over the range of interest and the entire response curve is transmitted to the ground, and 2) a phase-lock loop system. The considerations in the evaluation of these alternatives included data rate capabilities, noise rejection capabilities, reliability, and hardware development schedule. The evaluation was made for the A.N.T./ERN program in which an in-weather recession measurement capability was desired.

The advantages of the phase-lock loop approach include: 1) a continuous output which may be correlated directly with apparent recession, 2) simpler data reduction and interpretation, and 3) adaptability to high noise rejection designs. These are attractive attributes and it was found later that Acurex Corporation is developing a resonance gage with a phase-lock loop (Reference 50).

The major disadvantage of a phase-lock loop is that if lock is lost at any time during reentry, ablation measurements would be lost for the remainder of the flight. Two uncertainties make it difficult to assess the probability of lock loss in advance. The first of these is that a typical nosetip frequency response curve has considerable structure with different resonance peaks that may cross as the nosetip ablates. For an unsegmented tip in particular, the changes in the response curve structure are unpredictable and could lead to a shift in the lock from one resonance to another.

The second uncertainty is in the background acoustic noise to be expected during reentry. No flight data are presently available in the resonance gage band. This lack of data presents problems to the designer. If too much noise rejection capability is built into the signal conditioner, lock loss may occur because of the resulting degradation in response time. If too little noise rejection capability is included, lock loss may occur due to the resulting degradation in signal-to-noise ratio. For ordinary clear air reentries, the noise rejection compatible with maximum predicted recession rates is quite high and probably satisfactory. However, for weather flights, in which it is anticipated that exceptionally high acoustic noise will be combined with very high ablation rates, a satisfactory design compromise may not be possible.

The alternate signal conditioning concept (in which the complete response curve is transmitted) has definite design limitations, at least with the data rates available from the A.N.T. vehicle telemetry system. In the system selected, for example, only ten nosetip length measurements per second could be obtained. Noise rejection is obtained through the use of a tracking filter. Again, the designer is confronted with a problem for weather flights. If the filter bandwidth is narrow enough to reduce particle impact noise to an acceptable value, tracking would probably be lost at high erosion rates.

Despite these limitations, the full response curve type signal conditioner was selected for development for the A.N.T. vehicle. The rationale was as follows:

1. For initial flight tests, the system providing the most information is to be preferred. The complete response curves could be subjected to analysis and, if desired, further processing on the ground. Once the behavior of the response curve is fully evaluated, the potentials and pitfalls of a phase-lock loop system can be assessed.

2. Even though both systems would have difficulty in a severe weather environment, the complete response system would recover after the vehicle leaves the cloud cover. Thus, the total recession in the weather, if not the details of the history, would be measured. With the phase-lock loop system, on the other hand, once lock is lost, no further valid measurements can be made.

The full response curve system had one further advantage. Existing pulse/echo type signal conditioners fabricated for the A.N.T. program could be adapted readily to that system on a short schedule and for minimum cost. It was necessary to replace only one module and modify two others in each unit. Figure 142 shows a block diagram of the system.
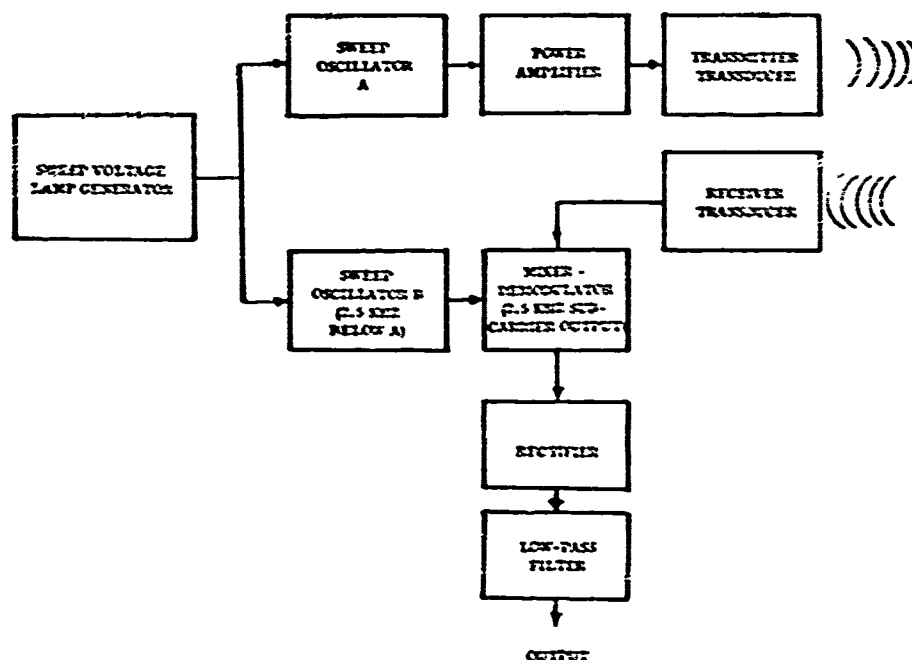

Figure 142. Block diagram of signal conditioner module for resonant frequency ablation gage.

6.1.3 Test Experience

Two ground tests of the resonance gage were performed: the 50 MW test mentioned earlier, and an RPL rocket motor test of an unseg ᵣ ted tungsten tip. The results of these tests were presented in Sections 3.2 and 2.6, respectively. Thus, the following is a very brief review of the results.

Two models in the 50 MW series were instrumented with resonance sensors. In one case, however, almost no stagnation point recession occurred due to an unusual model/flowfield interaction. Thus, only one set of data was reduced.

The basic model configuration was shown in Figure 64. A vertical stack of two transducer chips was bonded to the rear end of the central tungsten stud as in the case of the bench tests described in Section 6.1. The method used to drive and monitor the transducer also was the same as in the bench tests.

Figure 83 showed a comparison of the actual recession history, as measured from motion picture films, with the recession history obtained from the ablation gage. As can be seen, the agreement is excellent. The ablation gage data points were corrected for temperature using Equation (10). The temperature distributions required for the calculations were obtained from a three-dimensional ablation code which gave an excellent prediction of the model shape change and recession histories.

A single solid tungsten plug tip with a resonance sensor was tested in the RPL rocket motor ablation facility. Figure 143 shows a schematic of the test setup. Unfortunately, however, the transducer failed before any significant recession could be measured. Post-test analyses indicated that a vibration-induced failure of a wire terminal was the probable cause of the failure (Section 2.6).
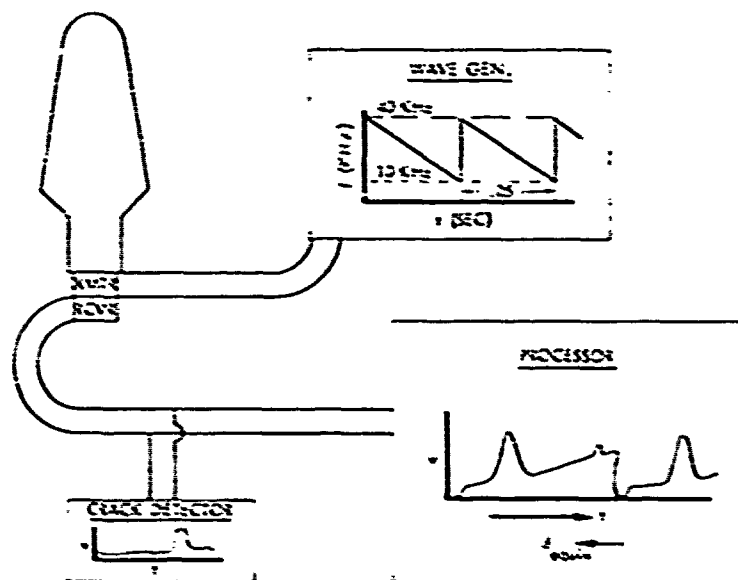

Figure 143. RPL test setup for resonance sensor.

6.2 BREMSSTRAHLUNG-ACTIVATION ABLATION GAGE

The Bremsstrahlung-Activation Ablation Gage (BAAG) was designed to measure the recession of a tungsten nosetip. The gage requires no physical alterations or changes to the nosetip and measures ablation by monitoring the change in nosetip radioactivity. The gage was designed by Intelcom Rad Tech (IRT) under subcontract to PDA. The design analyses and demonstration tests that were performed on the gage are presented in the following subsections. Additional data and design information on the BAAG system are contained in Reference 51.

6.2.1 Concept Description

The BAAG system is a radioactive gage that uses bremsstrahlung radiation to activate a tungsten nosetip. The nosetip is activated by high energy electrons which produce high energy bremsstrahlung photons. The bremsstrahlung photons convert the nosetip material, tungsten, into ^{182}Ta by the following two reactions:

$$^{182}W(\gamma, p) \; ^{182}Ta \text{ and } ^{183}W(\gamma, pn) \; ^{182}Ta.$$

Because of the conversion of tungsten directly into the ^{182}Ta isotope by bremsstrahlung photons, no physical alterations are required to activate the nosetip. Since the attenuation coefficients for the bremsstrahlung photons and the 1.2 MeV gamma rays emitted by th ^{182}Ta source are approximately equal, a nearly linear gage count rate versus nosetip thickness can be obtained by proper nosetip irradiation and detector placement.

A potential limitation to the BAAG system could be the sensitivity of the system to possible background counting rates caused by nosetip radioactive material that has migrated from the forward portion of the nosetip and deposited on the vehicle sidewall. The importance of source migration will depend on: 1) the ability to collimate and shield the detector, 2) the radioactive strength and amount of nosetip material irradiated, and 3) the amount and location of radioactive material deposited on the sidewall. To minimize the effect of source migration, two detectors are proposed for the BAAG system. One will be collimated to measure nosetip radiation and the other will be shielded from the nosetip to measure background radiation. The shielded detector output will be subtracted from the collimated detector output to obtain nosetip recession.

A preliminary design application of the BAAG instrumentation system is shown in Figure 144. The system consists of a tungsten nosetip that has been nondestructively activated along the centerline by bremsstrahlung photons. A detector is collimated and placed at a convenient location aft of the nosetip. The detector consists of two scintillators coupled to one or more photomultiplier tubes.

6.2.2 Tungsten Nosetip Activation

The tungsten nosetip is activated by bremsstrahlung radiation produced by a beam of high-energy electrons. Two methods of producing bremsstrahlung radiation were investigated for the irradiation of tungsten nosetips. One method utilized a collimated beam of bremsstrahlung radiation produced by a tantalum target and a tungsten collimator. The second method produced bremsstrahlung radiation directly in the nosetip. The first method will produce a more concentrated amount of ^{182}Ta along the centerline (i.e., minimum bremsstrahlung dispersion and subsequent activation in the radial direction) than the second method. However, the first method requires more electron

beam energy to produce reasonable activity levels because a significant amount of the energy is lost in the tantalum target and collimator. Both methods were investigated for the purpose of determining the radial and axial distributions of the ^{182}Ta activity and the electron energy required to achieve reasonable counting rates for a flight 'stem.
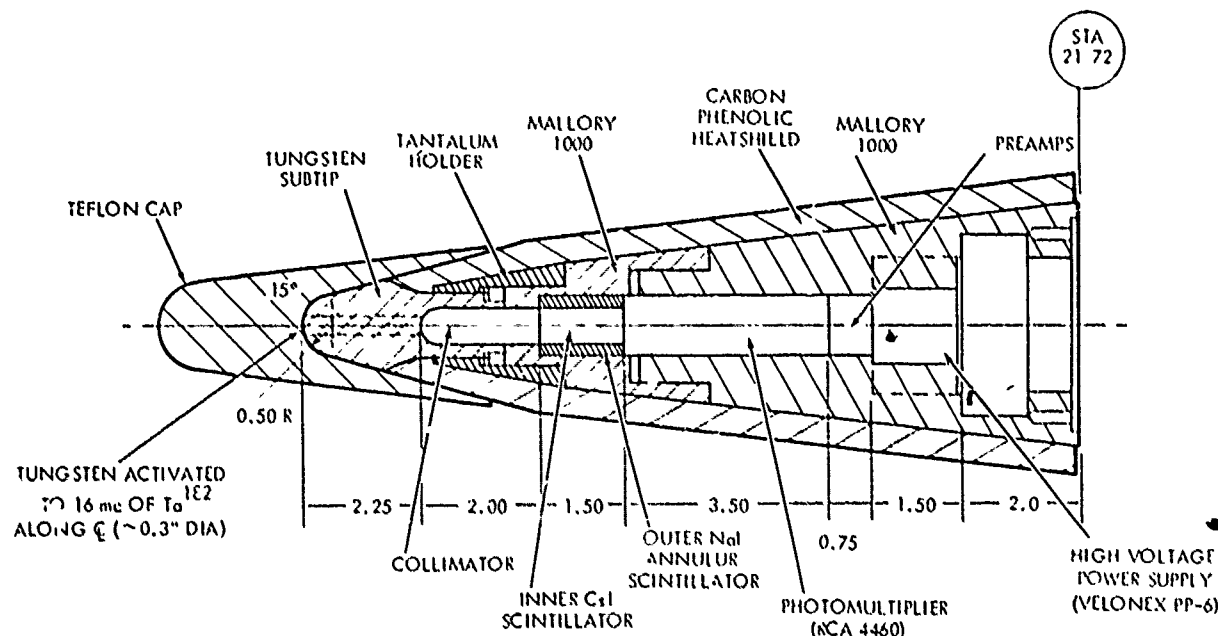

Figure 144. Preliminary tungsten nosetip design with radioactive recession sensor.

6.2.2.1 Tungsten Activation With Collimated Bre sstrahlung

A schematic of the hardware use' ω produce the collimated bremsstrahlung radiation is presented in Figure 145. A 60 MeV electron beam was passed through a graphite collimator to irradiate a water cooled tantalum target. Behind the tantalum was an electron beam attenuator consisting of several layers of water-cooled aluminum discs. The forward-directed bremsstrahlung beam produced by electron bombardment of the tantalum target was collimated by a hollow cylinder. A stack of tungsten discs simulating a nosetip were placed in the collimated bremsstrahlung beam for irradiation.

The tungsten discs were irradiated at IRT for five hours at an electron energy of 60 MeV and an average current of 70 μA. The measured axial distribution of ^{182}Ta activity is presented in Figure 146. The axial distribution was obtained by measuring the absolute activation of each disc from the end facing the beam. The radial measured distribution of ^{182}Ta activity in each disc is shown in Figure 147.
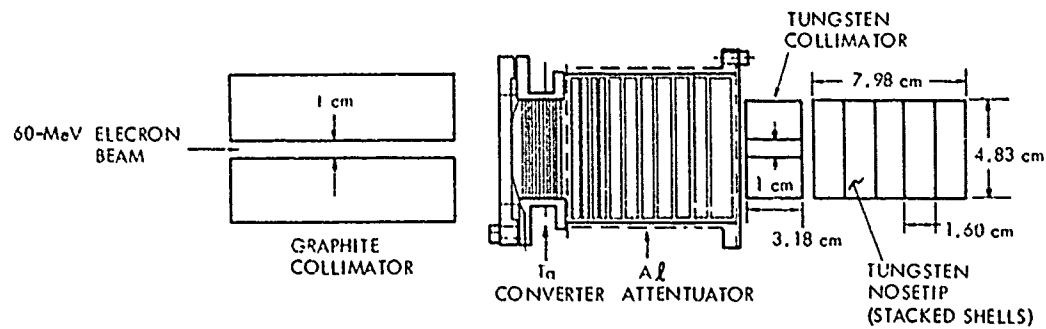
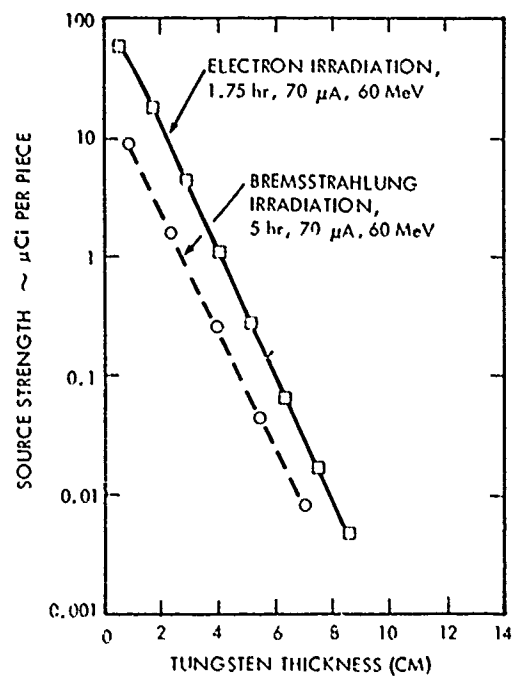Figure 145. Geometry for irradiation of tungsten with collimated bremsstrahlung beam produced by 60 MeV electrons.

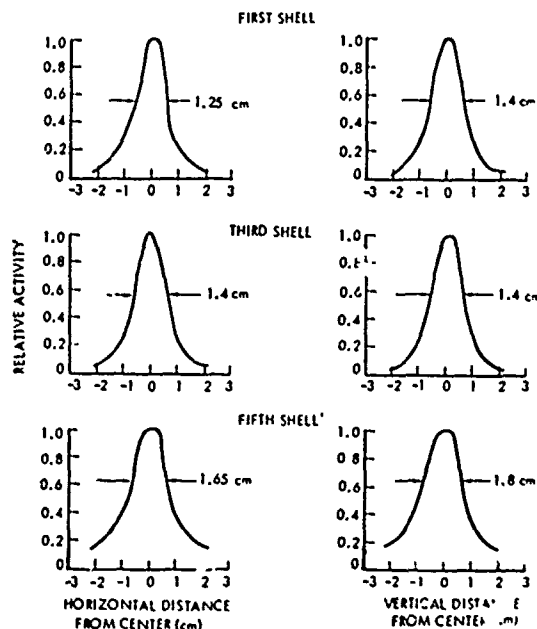

Figure 146. Measured axial distribution of [182]Ta activity.

Figure 147. Radial distribution of ^{182}Ta activation in the discs
irradiated with a collimated bremsstrahlung beam.

A nosetip, collimator, and detector assembly was fabricated to determine the ablation measurement sensitivity of the instrumentation system. A schematic of the assembly is presented in Figure 148. The stack of irradiated tungsten discs shown in the figure was used to simulate a nosetip. The initial overhang of the nosetip was varied by removing the aft discs and the ablated depth was varied by removing the forward discs. The measured sensitivities of the count rate to nosetip thickness are presented in Figure 149 for initial nosetip overhangs of 4.65 cm and 6.20 cm. As can be noted, the count rate is nearly a linear function of nosetip thickness.

For an actual nosetip irradiation, the electron beam current would be run at 350 μA (typical for the IRT LINAC) instead of the 70 μA used in the present study. For flight, a counting rate of approximately 5,000 cps would be a lower limit of the desired counting rate. For a nosetip overhang of 6.20 cm, the data of Figures 146 and 149 indicate that the irradiation time to achieve a 5,000 cps counting rate would be over 1300 hours. This irradiation time is undesirable because of the LINAC costs that would be involved in supporting a flight test.

6.2.2.2   Tungsten Activation With Direct 60 MeV Electrons

Because of the excessive time required to irradiate a nosetip using a collimated bremsstrahlung beam, direct irradiation of the nosetip with electrons was investigated to establish the savings in irradiation time that would result. Direct irradiation will result in uncollimated bremsstrahlung in the nosetip and the radial distribution in ^{182}Ta activity may be expected to be more diffuse and not as centrally concentrated as the activity produced by collimated bremsstrahlung. To determine the irradiation time and the radial distribution of activity, a stack of tungsten discs were irradiated and the ^{182}Ta distribution was mapped both axially and radially. A schematic of the

Pb (0.635 cm)

5.08 CM

7.62 CM

| 1 | 2 | 3 | 4 | 5 | 6 |

W

Pb

CsI (Na)

PCA 4460
PM TUBE

1.5 CM

Pb

TUNGSTEN
NOSETIP
STACK
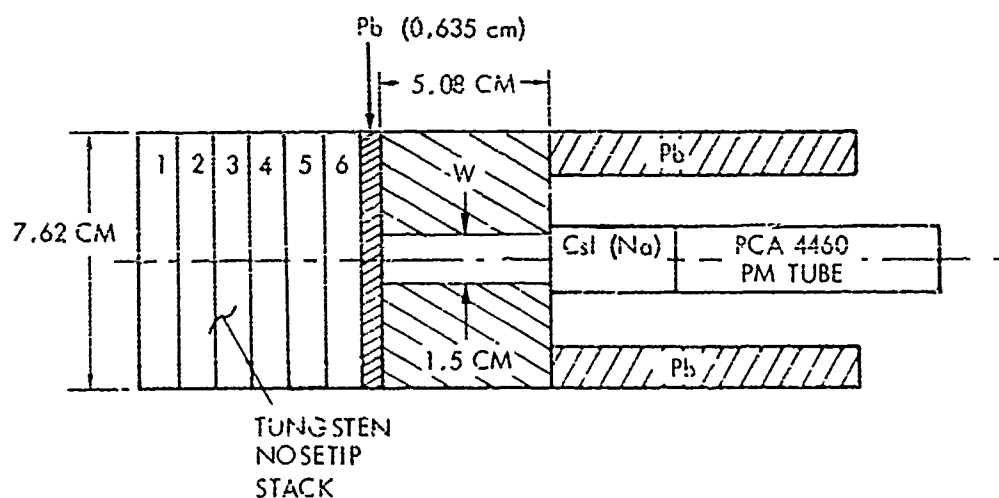
Figure 148. Hardware schematic for measuring
sensor ablation sensitivity.

COUNTS/400 SEC

10000

8000

6000

4000

2000

0

1   2   3   4   5   6

TUNGSTEN THICKNESS (CM)

4.45 CM
INITIAL THICKNESS
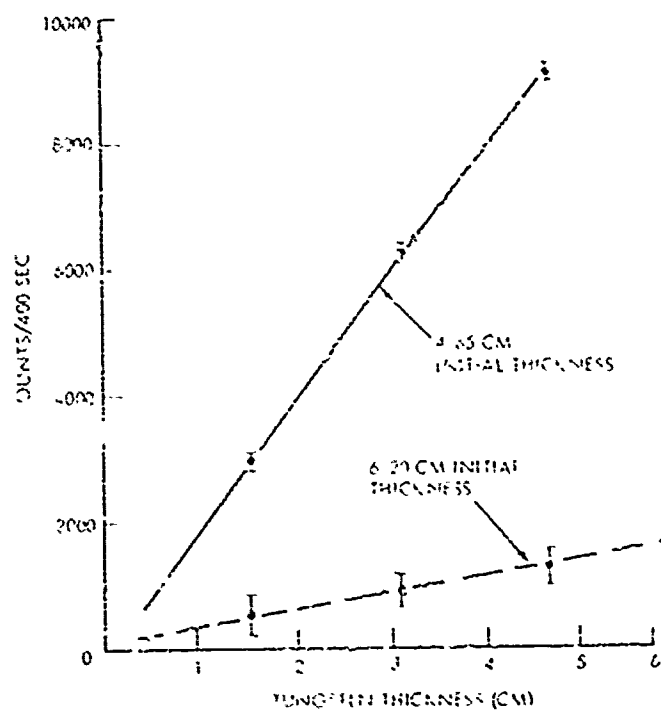
6.20 CM INITIAL
THICKNESS

Figure 149. Count rate versus nosetip thickness for the
first three pieces irradiated with a collimated
bremsstrahlung beam (Figure 145).

hardware used to irradiate the tungsten stack is presented in Figure 150. As was done in the collimated bremsstrahlung activation experiment, a 60 MeV electron beam was collimated by a hollow graphite cylinder. However, instead of having the electron beam impinge on a tantalum target, the electron beam was focused on the tungsten stack to form bremsstrahlung radiation directly in the tungsten. The tungsten stack was water-cooled to prevent material property changes that can occur in tungsten at temperatures above 1800°F. The cooling apparatus was simply an unpressurized water bath with the water inlet located at the forward face of the first tungsten disc. The first tungsten disc was separated from the other discs to allow both faces of the first disc to be water-cooled. In cooling an actual nosetip, a sophisticated, pressurized high velocity water-cooling system will be required to maintain reasonable tungsten temperatures during activation. The nosetip cooling analysis and the cooling system required for activation of a flight nosetip are described in Section 6.2.4.
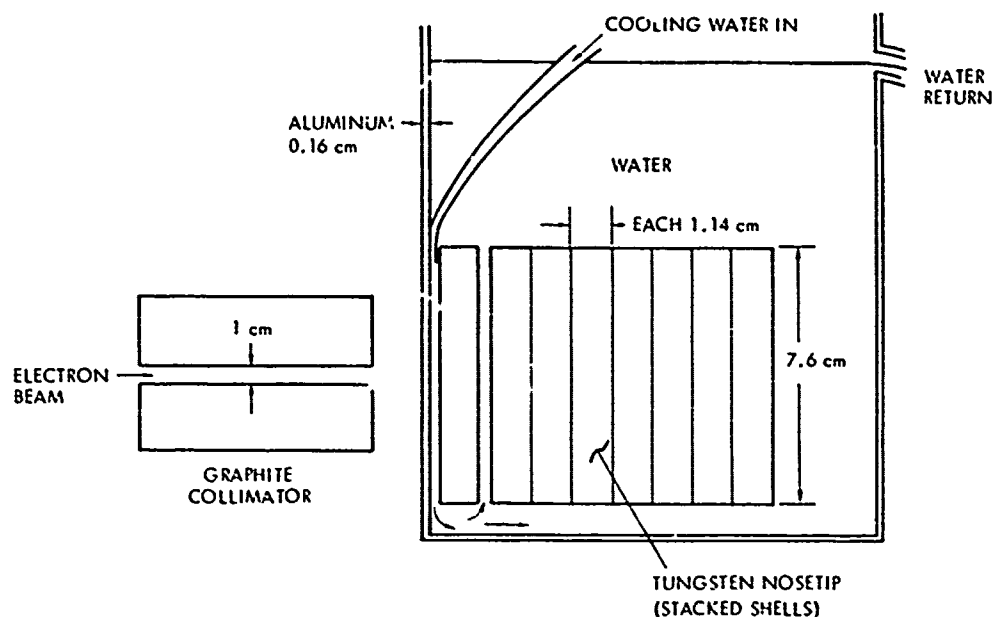

Figure 150. Geometry for irradiation of tungsten
with direct electron beam.

The tungsten discs were irradiated directly with electrons at IRT for 1.75 hours at an electron energy of 60 MeV and an average current of 70 μA. The axial distribution of ^{182}Ta activity is presented in Figure 146. As can be noted, direct electron irradiation results in a significantly higher activity level than was obtained by indirect (or collimated) bremsstrahlung irradiation. Comparing the activities obtained from each method for equal irradiation times, it can be shown that the activation obtained by direct irradiation is over 18 times the activation obtained by indirect irradiation.

The measured radial distribution of ^{182}Ta activity in each disc is shown in Figure 151. The "full-width-half-maximums" of the radial distributions, as shown in Figures 147 and 151, are compared in Figure 152. As can be noted, direct irradiation produces a slightly broader region of activation. At a depth of 2 inches, the width of activated tungsten induced by direct irradiation is
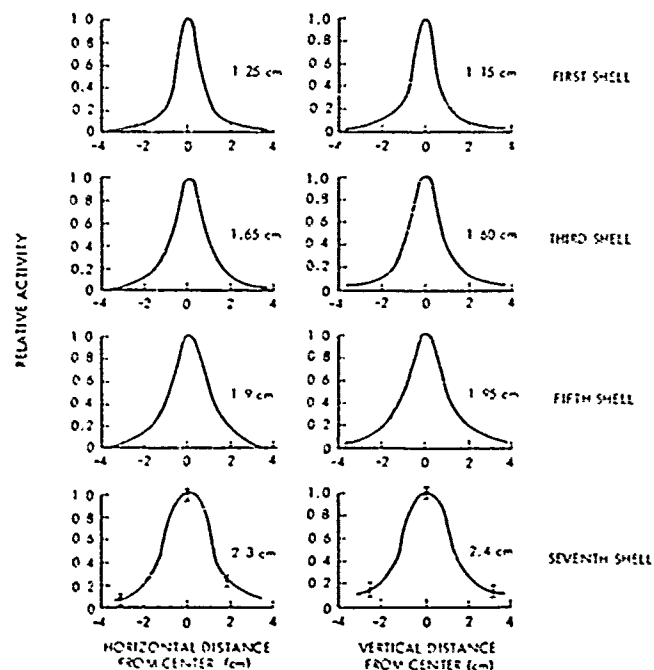
Figure 151. Radial activation profile of ^{182}Ta activation for 1.14-cm thick pieces of tungsten irradiation with 60 MeV electron beam.
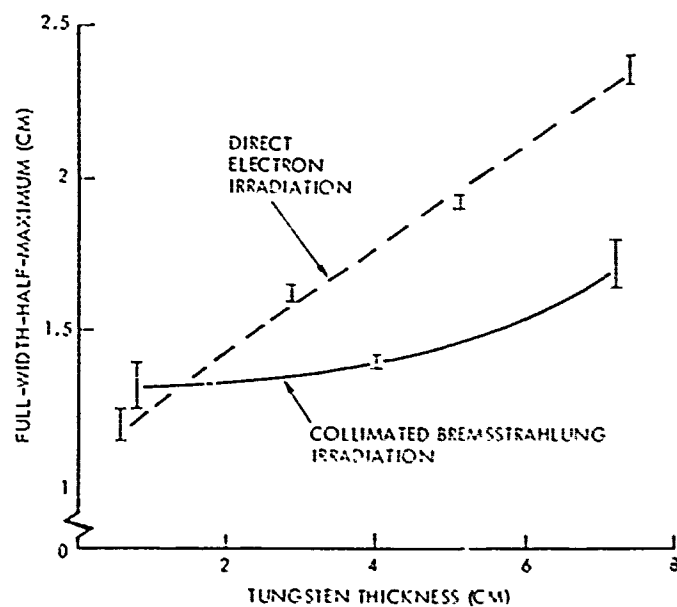

Figure 152. Comparison of radial source distributions.

35 percent greater than the width induced by indirect irradiation. For a flight nosetip, as will be indicated in Section 6.2.5, the activated width produced by direct irradiation appears to be acceptable. If desired, the width can be reduced further by using a small electron-beam collimator and a higher electron beam energy.

The activated tungsten discs (activated directly with electrons) were used in the assembly shown in Figure 148 to determine the count rate as a functior of nosetip thickness. The measured count rates are presented in Figure 153 for nosetip overhangs of 5.72, 6.86, and 8.00 cm. The count rate dependence on thickness is similar to that measured with tungsten discs activated by collimated bremsstrahlung, Figure 149. The count rate is nearly a linear function of thickness with a slightly increasing count rate per unit thickness (count rate versus thickness slope) as the tungsten thickness is increased.
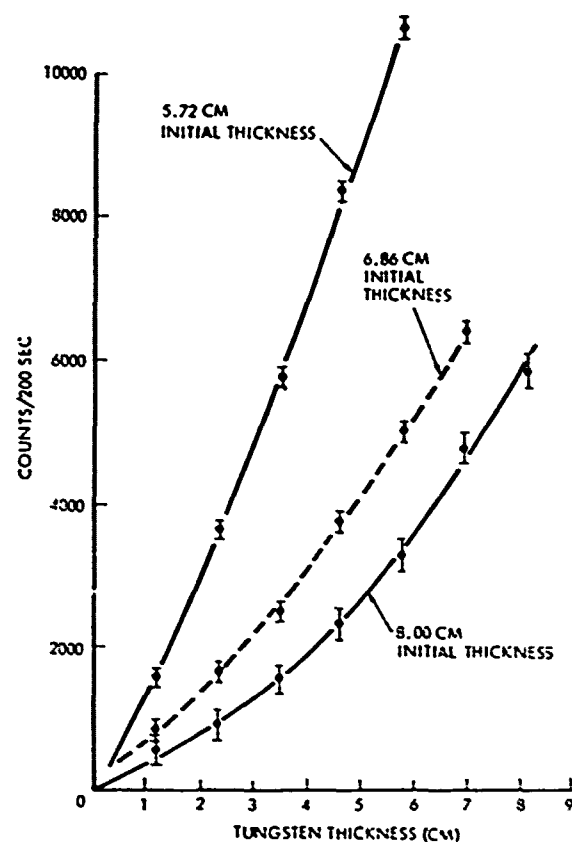
Figure 153. Count rate versus nosetip thickness for direct electron irradiation, 8 cm overhang.

The estimated count rates for a tungsten nosetip irradiated directly with 60 MeV electrons at 350 μA for 75 hours are presented in Figure 154. As can be noted, a count rate of over 10,000 cps will result for a thickness of 5.72 cm. The irradiation time and counting rate for direct irradiation, relative to indirect irradiation, are improved significantly with very little sacrifice in the radial distribution of activated tungsten. In view of these results, it is recommended that direct irradiation be used for flight activation.

182

Figure 154. Composite plot of count rate versus nosetip
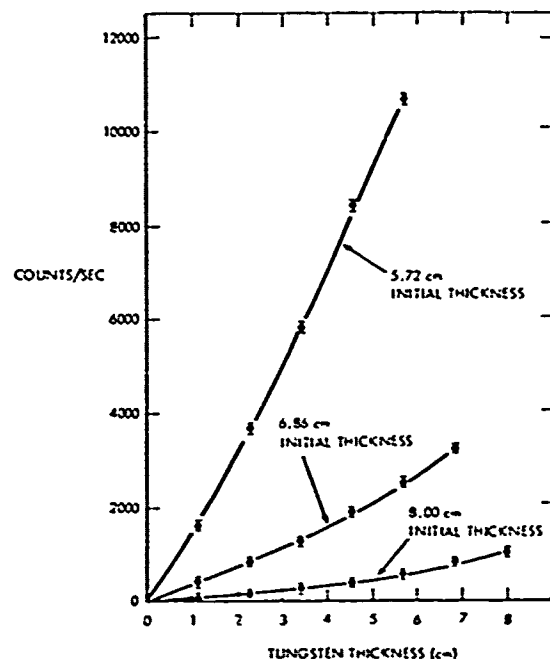thickness for direct electron irradiation of
75 hours of full Linac power; four different
nosetip overhangs.

6.2.3 Background Effects On Measurement Uncertainty

As has been noted, the BAAG system uses bremsstrahlung radiation to convert the nose-
tip material, tungsten, into the gamma-ray isotope ^{182}Ta. Because tungsten has good gamma-
attenuation characteristics, a relatively large amount of the ^{182}Ta isotope is required to obtain.
reasonable detector counting rate. The greater the amount of ^{182}Ta that is present in the nosetip,
the greater is the possibility of having a portion of the isotope migrate and deposit on the sidewall
heatshield (a phenomenon commonly referred to as source migration). The deposited sidewall iso-
tope will contribute to the counting rate by changing the background radiation, thereby introducing
an error in the ablation measurement. To estimate the error induced by possible source migratio. ,
measurements were made on ground test and flight test heatshields to determine the amount of tung-
sten nosetip material deposited on the sidewall. Assuming the amount of deposited ^{182}Ta is propor-
tional to the amount of deposited tungsten, an estimate was then made of the background rate that
would be expected for a particular instrumentation design.

Neutron activation analyses were utilized to measure the tungsten deposition thickness
on two test specimen heatshields. This was accomplished by wrapping the heatshield with a thin
layer of tungsten sheet, irradiating the assembly in a neutron field, and counting the 24-hour ^{186}W
radioactivity arising from neutron capture in tungsten. Several locations on the aft heatshield were
counted with and without the tungsten sheet. The ratio of the two counting rates can be related to
the amount of tungsten deposition on the heatshield. The heatshields that were analyzed included a
heatshield recovered from a SAMS tungsten nosetip flight test and a heatshield obtained from an
SO atm spiked enthalpy tungsten nosetip test in the 50 MW arc-jet facility. For the SAMS heatshield,

the mean deposited tungsten thickness was measured to be 0.15 micron with a variation of ±20 percent over the entire heatshield. For the 50 MW heatshield, a mean thickness of 0.6 micron was measured. The thickness variation over the heatshield was between 0.4 and 0.8 micron, and this variation apparently was caused by the nonsymmetrical ablation behavior of the nosetip.

  To estimate the importance of source migration, two tungsten sidewall deposition rates were assumed. In one case, the tungsten was assumed to be deposited and removed at equal rates so that a constant tungsten thickness of 0.6 micron was maintained during the entire portion of re-entry. In another case, the tungsten thickness was assumed to be dependent on the nosetip thickness as shown in Figure 155. The calculated ratio of background counts to nosetip counts is shown for an initial nosetip overhang of 5 cm and the detector shielding and collimator design of Figure 144. For a constant tungsten deposit thickness of 0.6 micron, the background counts reach a maximum of 8 percent of the signal when the nosetip has ablated 5 cm. Increasing the nosetip overhang or increasing the amount of sidewall activity will increase this ratio accordingly. Because of the unknown amount and behavior of sidewall deposition, it is recommended that two scintillators be used in the system. One will be shielded from the nosetip to measure background radiation. The other will be collimated to view the nosetip and will measure a combination of nosetip and background radioactivity.

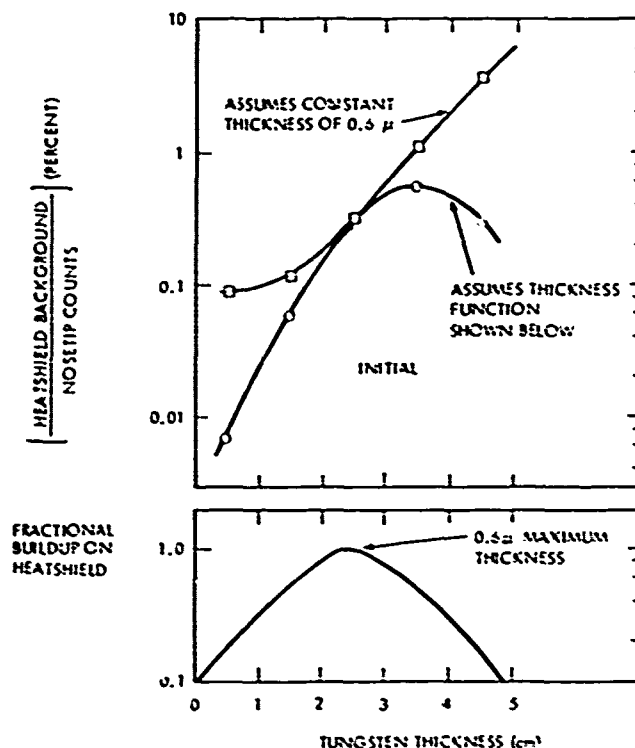Figure 155. Calculated background effects of 0.6 micron thick tungsten deposit on heatshield assuming instantaneous and slow build-up of tungsten layer. Lower figure shows tungsten-build-up function assumed.

6.2.4   Nosetip Cooling During Activation

  Thermal analyses were performed on a tungsten nosetip for the purpose of estimating the cooling requirements necessary to maintain the nosetip at a reasonable temperature level during

irradiation. Direct irradiation of the nosetip with electrons results in a large conversion of electron energy into thermal energy. For the electron beam energy estimated to produce the desired flight radioactive strength (Figure 154), approximately 21 kW of thermal energy is generated in the nosetip. To preclude changes in material properties that can occur in tungsten above 1800°F, a highly efficient cooling system will be required to maintain the nosetip at reasonable temperatures, and/or the electron beam energy must be reduced.

To estimate the requirements of the cooling system, analyses were performed at electron beam power levels of 21 kW and 10.5 kW. The 60 MeV electron beam currents at these levels are 350 μA and 175 μA, respectively. The nosetip that was analyzed is illustrated in Figure 144. The nose radius is 0.50 inch, with a 15-degree cone half-angle and a thickness of 2.25 inches along the centerline. The nosetip shank has a 0.50-inch diameter hole along the center to aid in gamma-ray collimation.

During irradiation in a linear accelerator, the nosetip was considered to be encapsulated in a pressure vessel (e.g., titanium) with high-pressure water forced through annular passages to extract heat. The estimated power dissipated in the nosetip as a function of nosetip depth is presented in Figure 156 for the 21 kW operating condition. The power dissipation was estimated by calculating the heat deposition due to electron ionization and attenuation of the bremsstrahlung photons.
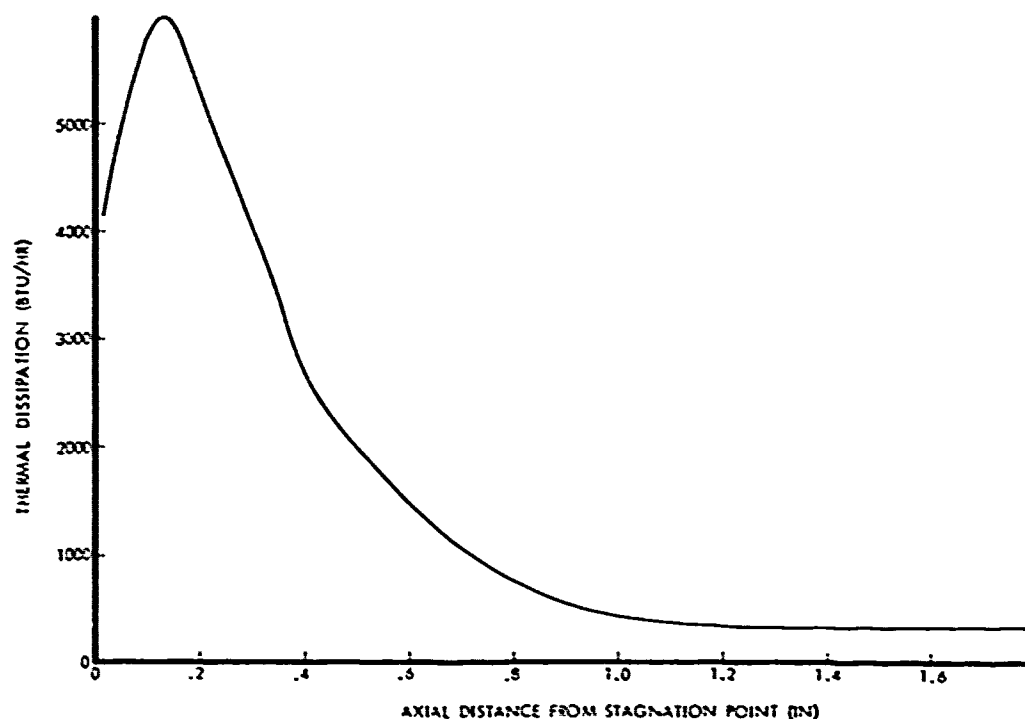

Figure 156. Thermal energy dissipation in tungsten for full-power direct electron irradiation.

For the power profile of Figure 156, it is estimated that the nosetip must be irradiated for 75 hours to achieve an initial flight count rate of approximately 10,000 cps for the geometry and detector assembly of Figure 144. Because of the long irradiation time, thermal transients will be

unimportant in defining the maximum nosetip temperature level. A steady-state, two-dimensional thermal analysis of the nosetip was performed using the nodal network of Figure 157. The thermal conductivity of tungsten that was used in the analysis was presented in Table 24.
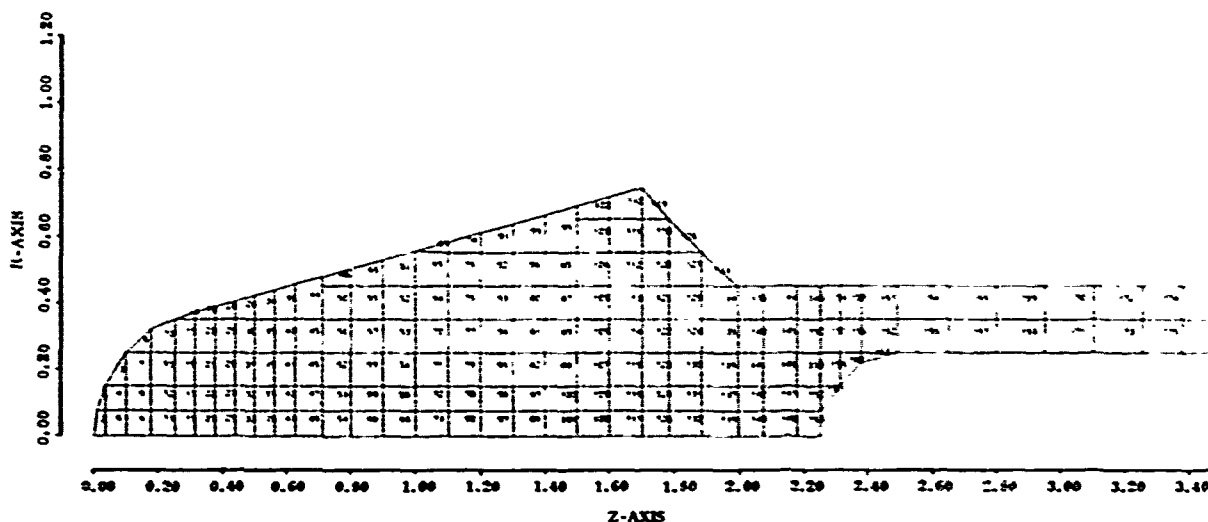

Figure 157. Nosetip nodal network.

The thermal boundary condition at the nosetip external surface was computed using the forced cooling and water boiling correlations of Reference 52 as a basis. The correlations of Reference 52 were extrapolated to a water velocity of 15 ft/sec with $150^{\circ}F$ subcooling, and these correlations are presented in Figure 15S. A maximum heat transfer rate of 2.5×10^6 Btu/ft^2-hr is estimated to occur at "burn-out."

For the 21 kW electron beam irradiation condition, noset'; ..nperatures over $4000^{\circ}F$ were predicted for the forced water cooling correlations of Figure 1' . With the same cooling correlations, a maximum nosetip temperature of $2125^{\circ}F$ was predicted for the 10.5 kW electron beam condition. The predicted temperatures for the nodes of Figure 157 are presented in Table 27 for a power level of 10.5 kW. As can be indicated by the temperature distribution, the major portion of the heating is occurring near the nosetip stagnation point. Because of the high concentration of thermal dissipation in the stagnation region, it is possible that "burn-out" will occur and temperatures higher than predicted may result. To ensure reasonable temperature levels, it is recommended that the electron beam energy be reduced below 7 kW. This power level would require approximately 230 hours for irradiation, compared to the 75 hours required with 21 kW.

The estimated 230 hours required for irradiation possibly could be reduced by using a thin tantalum section just forward of the nosetip. As can be noted in Figure 156, peak dissipation occurs at a depth of approximately 4 mm in the nosetip. By placing a 4 mm tantalum section forward of the nosetip, the peak dissipation will occur on the surface of the nosetip, rather than within the nosetip. This ill increase the ability to conduct heat to the surface of the nosetip. By forcing high-pressure water between the gap separating the tantalum and the tungsten, power levels higher than 7 kW may be possible. Use of this higher power level and the subsequent reduction in irradiation time will require further analysis for verification.
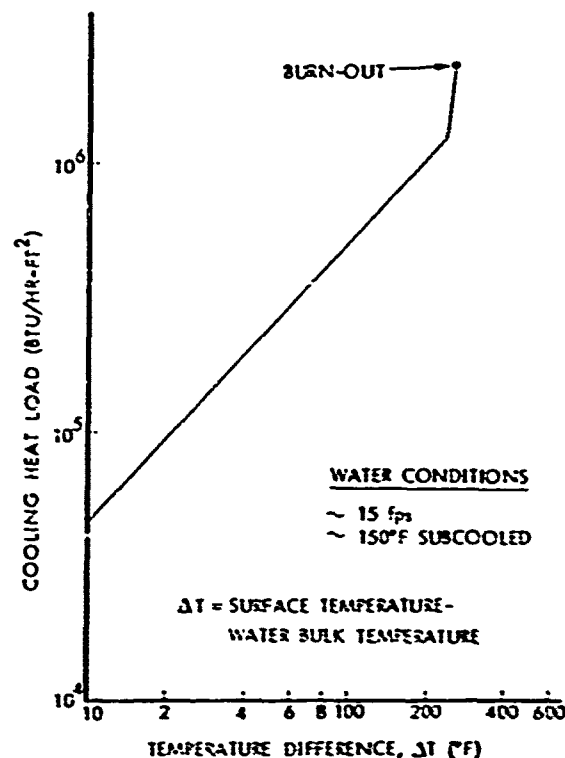
186

Figure 158. Boiling heat transfer data for water.

6.2.5 Description of Flight System

A schematic of a preliminary flight nosetip design utilizing the BAAG system was presented in Figure 144. The nosetip is 2.25-inches long with a 2.0-inch long collimator. A CsI scintillator is used to measure radiation from the nosetip. An annular ring of NaI scintillation material is used primarily to measure background radiation. The signal from the NaI scintillator is used to correct the CsI signal for variations that can occur in the background radiation. Both scintillation crystals are bonded to a common photomultiplier tube to form a "phoswitch" detector assembly. The phoswtich uses the difference in the phosphor's decay time to distinguish between the two scintillators. The phosphors generated in NaI (T() have a decay time of 0.23 msec versus a decay time of 0.7 μsec for CsI (T(). Using the large difference in decay time, the photomultiplier pulses can be screened electronically to differentiate between NaI and CsI interactions. The phoswitch technique has been used in space radiation experiments. In these experiments, a single photomultiplier tube was used to monitor the counting rate from two scintillators.

The sensor shown in Figure 144 is configured for a flight vehicle with the detector assembly located forward of Vehicle Station 21.72 inches. The photomultiplier is packaged with the preamps and the high-voltage power supply in a gas-sealed container. The nosetip source strength is approximately 16 millicuries with an initial detector count rate of about 10,000 cps. A teflon cap, placed over the tungsten nosetip, is designed to expose the tungsten at approximately 35 kft. This is the approximate altitude at which the primary nosetip would be removed when a high-altitude weather environment is encountered. The tungsten subtip has a 0.50-inch nose radius with a 15 degree cone

half-angle followed by the regular vehicle cone angle of 6.4 degrees. The biconic shape is required to provide adequate detector sidewall tungsten shielding to minimize the effect of background radiation on the ablation measurement.

Table 27. Predicted steady-state temperatures for half-power irradiation.

Node*	Temp. (°F)	Node*	Temp. (°F)	Node*	Temp. (°F)	Node*	Temp. (°F)	Node*	Temp. (°F)	Node*	Temp. (°F)
1	1515	37	625	73	200	109	207	145	122		
2	2125	38	691	74	112	110	110	146	145		
3	1456	39	271	75	126	111	110	147	155		
4	1760	40	410	76	151	112	115	148	161		
5	2074	41	646	77	152	113	125	149	110		
6	1277	42	715	78	227	114	115	150	117		
7	1575	43	770	79	251	115	175	151	125		
8	1837	44	277	80	204	116	152	152	140		
9	2014	45	358	81	110	117	209	153	142		
10	957	46	514	82	122	118	110	154	110		
11	1172	47	601	83	142	119	110	155	113		
12	1735	48	645	84	170	120	113	156	125		
13	1577	49	181	85	200	121	123	157	125		
14	537	50	221	86	220	122	141	158	110		
15	559	51	365	87	231	123	170	159	112		
16	1329	52	430	88	110	124	146	160	113		
17	1564	53	457	89	129	125	155	161	110		
18	1683	54	530	90	137	126	110	162	110		
19	577	55	156	91	161	127	112	163	110		
20	750	56	193	92	195	128	129	164	110		
21	1154	57	263	93	215	129	127	165	110		
22	1364	58	254	94	225	130	166	166	162		
23	1468	59	409	95	110	131	141	167	162		
24	431	60	431	96	114	132	199	168	96		
25	632	61	135	97	132	133	110	169	99		
26	955	62	176	98	56	134	116	170	91		
27	1146	63	225	99	185	135	121	171	91		
28	1235	64	254	100	285	136	130	172	44		
29	343	65	335	101	215	137	174	173	43		
30	534	66	353	102	110	138	141	174	54		
31	623	67	122	103	110	139	113	175	46		
32	573	68	133	104	117	140	125	176	45		
33	1056	69	162	105	129	141	152	177	45		
34	302	70	202	106	139	142	165				
35	463	71	255	107	151	143	172				
36	697	72	230	108	222	144	119				

*Node locations are identified in Figure 157

6.2.6 Conclusions

The BAAG system utilizes a nondestructive method to activate a tungsten nosetip for the purpose of measuring nosetip ablation with radioactive counters. The nosetips are activated with a high-energy electron beam to transform tungsten into the ^{182}Ta isotope. A highly efficient cooling system is required during irradiation to prevent the nosetip from exceeding 1800°F. At temperatures above 1800°F, undesirable material property changes occur in tungsten. An adequate amount of ^{182}Ta isotope can be formed in less than 230 hours of nosetip irradiation and result in a detector counting rate of over 10,000 cps. The count rate versus thickness curve for the BAAG system has been found to be nearly linear. The linear dependence and high count rate result in a detector system with good measurement accuracy.

Because of the possibility of nosetip source migration and subsequent deposition on the vehicle sidewall, it is necessary that two scintillators be used in the BAAG system. One scintillator will measure the background radiation that results from source migration and the other will measure both nosetip and background radiation. The count rate from the former is used to correct the count rate from the latter to minimize the measurement error induced by variable (or transient) background levels.

All electrical components in the BAAG system have been developed and the basic detector design has been extensively flight-tested. Additional development required for the system includes: 1) designing and testing the phoswitch detector assembly, 2) designing and verifying the cooling system and nosetip activation procedures, and 3) modifying for use on tungsten nosetips the calibration procedures currently used for graphite nosetips.

7.0 REFERENCES

1.

2.

3.   Miyazawa, E. T., Deleget, J. L., and Stetson, J. R., "A.N.T./ERN Design Verification Test Report," PDA TR 1031-27-54, May 1976.

4.   Fanciullo, Thomas J., and Phillips, Lt. T. D., "Reentry Nosetip Test Facility and Calibration Report - Final Report," AFRPL, Edwards AFB, California, AFRPL TR-75-71, February 1976.

5.   Gordon, S., and McBride, B. J., "Computer Program for Calculation of Complex Chemical Equilibrium Compositions, Rocket Performance, Incident, and Reflected Shocks, and Chapman-Jouquet Deformations," NASA SP-273, 1971.

6.   Fancuillo, T. J. (AFRPL), Personal communication with G. R. Nickerson (PDA), 7 May 1975, "AFRPL Combustor and Nozzle Contours."

7.   Smith, D. H., Haddock, R. L., and Sherman, M. M., "Computer Codes for Nosetip Recession and In-Depth Thermal Analysis: NOHARE, NOSEC, NODGEN," PDA TR 5002-00-01, January 1976.

8.   Personal communication from T. J. Fancuillo (AFRPL) to G. R. Nickerson (PDA), 17 September 1975.

9.   Cramer, F. B., and Baker, P. D., "Combustion Processes in a Bipropellant Liquid Rocket Engine," JPL Report No. 900-2, 15 January 1967.

10.   Pieper, J. L., ICRPG Liquid Propellant Thrust Chamber Performance Evaluation Manual, Performance Standardization Working Group, September 1969, CPIA No. 178.

11.   Priem, R. J., and Heidmann, M. F., "Propellant Vaporization as a Design Criterion for Rocket-Engine Combustion Chambers," NASA TR R-67, 1960.

12.   "A.N.T./ERN Ground Test Analysis - Presentation to SAMSO/Aerospace," Aerotherm Division of Acurex Corporation, 14 October 1975.

13.   Deleget, J. L., "Failure Analysis of Blunt Graphite Ablation Model in A.N.T./ERN Design Verification Test," PDA TM 1031-27-41, 10 July 1975.

14.   Crose, J. G., and Jones, R. M., "The SAAS III Computer Program," PDA TR 4001-02-05, November 1974.

15.   Schutzler, J. C., "Strain Allowables for 994 Graphite," PDA TM 1031-17-17, 3 March 1975.

16.

17.   Deleget, J. L., "Pretest Thermostructural Predictions for Design Verification Test of the A.N.T./ERN Blunt Primary Nosetip, Revision 2," PDA TM 1031-27-42, 15 July 1975.

18.   Priddy, T. G., "A Fracture Theory for Brittle Anisotropic Materials," Journal of Engineering Materials and Technology, April 1974.

19.   Starrett, H. S., "Probable Values for the Mechanical and Thermal Properties for 994-2 Graphite," SoRI rough draft dated 6 June 1975.

20.   Iannuzzi, F. A., Starrett, H. S., and Pears, C. D., "Thermal, Mechanical, and Brittle-to-Ductile Behavior of Thoriated Tungsten," AFML TR-75-203 (SoRI-EAS-75-513-3230-14), December 1975.

21.   Larsen, D. C., "Final Report - Generation of Baseline Thermal and Mechanical Property Data on Thoriated Tungsten," IITRI Project No. D6105, PDA Purchase Order No. 5001, 12 June 1975.

22.   "A.N.T./ERN Nosetip Final Design Summary and Report," PDA TR 1018-11-34, 11 November 1974.

23.   "Final Design Review, A.N.T./Graphite Nosetip Program," PDA, Inc., 20 February 1976.

24.   Smith, D. H., "Test Report - Segmented Stress-Resistant Tungsten Nosetip Test Program - AFFDL 50 Megawatt Arc-Jet Test Facility," PDA TR 1031-22-09, 14 January 1975.

25.   Groener, L. S., and Sherman, M. M., "Test Report: Segmented Tungsten Nosetip Ablation Test Program," PDA TR 1031-01-56, 20 September 1976.

26.   Smith, D. H., "Test Report - Materials Performance Program - AFFDL 50 Megawatt Arc-Jet Test Facility," PDA TR 1031-22-10, 23 January 1975.

27.   Bernstein, B. T., " Elastic Properties of Polycrystalline Tungsten at Elevated Temperatures," Journal of Applied Physics, Vol. 33, No. 6, p. 2140, June 1962.

28.   Groener, L. S., "Hardened Reentry Vehicle Development Program, Phase II: Rotating Ablative Sting Technology," DNA Report No. 4272F, PDA TR 1031-33-54, April 1976.

29.   Air Force Flight Dynamics Laboratory, "The 50 Megawatt Facility of the Air Force Flight Dynamics Laboratory, Information for Users," AFFDL TM-75-39-FXE, Third Edition, September 1975.

30. Olson, E., "Ablation Tests at WPAFB 50 MW Facility," K West No. ETR-1055, 12 June 1975.

31. Lowrie, R., and Gonas, A., "Dynamic Elastic Properties of Polycrystalline Tungsten, 24° - 1800^oC," Journal of Applied Physics, Vol. 36, No. 7, p. 2189, July 1965.

32. Roberts, T. R., "Flight Test Plan for Hydrometeor Erosion and Recession Test System II (HEARTS II) Program," General Electric RESD Document No. 74SD2158, 1 October 1974.

33. JANAF Thermochemical Tables, National Bureau of Standards Publication No. NSRDS-NBS 37, Second Edition, June 1971.

34. Touloukian, Y. S., ed., Thermophysical Properties of High Temperature Solid Materials, Volume 1: Elements, Thermophysical Properties Research Center, Purdue University.

35. Gubareff, G. G., et al., Thermal Radiation Properties Survey, Honeywell Research Center, Minneapolis, Minnesota, 1960.

36. Moody, H. L., et al., "Tungsten and Molybdenum Ablation Modeling for Reentry Applications," AIAA Paper 75-112 presented at the 13th Aerospace Sciences Meeting, January 20-22, 1975.

37. Anderson, A. D., "Interim Report, Passive Nosetip Technology (PANT) Program, Volume III," SAMSO TR-74-86, January 1974.

38. Powars, C. A., "Surface Roughness Effects on Reentry Heating," Aerotherm Report No. TM-71-10, July 1971.

39. Grabow, R. M., and White, C. O., "Surface Roughness Effects on Nosetip Ablation Characteristics," AIAA Journal, May 1975.

40. Pitts, Carl C., "HEART II Vehicle Numbers 104, 105, and 106, Vehicle Dynamics Data Package," Xonics, Inc., MDC 25633.07, March 1975.

41. Carslaw, H. S., and Jaeger, J. C., Conduction of Heat in Solids, Oxford University Press, 1959.

42. Clayton, W., et al., "Thermal Conductivity of Phenolic Carbon Chars," AFML-TR-69-313, December 1969.

43. Schaefer, J. W., et al., "Final Report - Studies of Ablative Material Performance for Solid Rocket Nozzle Applications," NASA CR-72429, March 1968.

44. Cline, P. B., "HEARTS RV 105 and 106 Trajectory Reconstruction," General Electric Letter to H. Moody of PDA, 7 March 1975.

45. Nestler, D. E., et al., "Heat Transfer to Steps and Cavities in Hypersonic Turbulent Flow," AIAA Paper 68-673, presented at AIAA Fluid and Plasma Dynamics Conference, June 24-26, 1968.

46.   Crenshaw, J. P., "Low Cost Flight Test Capabilities Study," PDA TR 5006-00-01, 19 January 1976.

47.   Kochendorfer, P. C., "HEART Recovery Vehicle (HRV) Test Program," Report No. DNA 3842F, PDA TR 1022-00-01, 10 November 1975.

48.   DMIC No. 189, "The Engineering Properties of Tantalum and Tantalum Alloys," 13 September 1963.

49.   DMIC No. 127, "Physical and Mechanical Properties of Tungsten and Tungsten-Base Alloys," 15 March 1960.

50.   Eichorn, R., Hartman, C., and Kelly, J., "A Resonant Acoustic Technique for Measuring Reentry Nosetip Recession," Instrumentation in the Aerospace Industry, Vol. 22, p. 147, proceedings of the 22nd International Instrumentation Symposium — San Diego, ISA, 1976.

51.   Verbinski, V. V., "Bremsstrahlung-Activation Ablation Gauge (BAAG) - Final Report," IRT Corp. Report No. INTEL-RT-0028-002, September 1975.

52.   Kreith, F., Principles of Heat Transfer, Scranton, Pennsylvania, International Textbook Company, 1965.

APPENDIX A

APPLICATION OF PRIDDY FAILURE
CRITERION TO 994-2 GRAPHITE

A1.0 DESCRIPTION OF FAILURE CRITERION

The Priddy failure criterion (Reference A-1) is a general macroscopic failure criterion applicable to brittle anisotropic materials. It consists of a cubic equation failure surface having the following properties:

1. Arbitrary stress states are accounted for, including effects of stress interaction and shearing stresses.
2. The failure surface is invariant with respect to the coordinate system used for stress-strain response calculations.
3. The failure surface is smooth, continuous and convex (but open in 1:1:1 compression).
4. The failure surface passes through measured strengths.

When this criterion is specialized to the case of an axisymmetric solid of revolution in a material having transverse isotropy, the failure surface is given by:

$$A1\tau_{rz}^2 + B1\sigma_z^2 + B2\sigma_r^2 + B3\sigma_\theta^2 + C1\sigma_z\sigma_r + C2\sigma_r\sigma_\theta + C3\sigma_\theta\sigma_z$$

$$- (E1\sigma_z + E2\sigma_r + E_3\sigma_\theta)(\sigma_z\sigma_r + \sigma_r\sigma_\theta + \sigma_\theta\sigma_z - \tau_{rz}^2) \qquad (A-1)$$

$$- D1\sigma_z - D2\sigma_r - D3\sigma_\theta - F(\sigma_r\sigma_\theta\sigma_z - \sigma_\theta\tau_{rz}^2)$$

The coefficients in Equation (A-1) are calculated from nine measured strengths defined below:

FTZ	tensile strength, Z direction
FCZ	compressive strength, Z direction
FTTH	tensile strength, θ direction
FCTH	compressive strength, θ direction
FSRZ	shear strength, RZ plane
QTHZ	biaxial tensile strength, θZ plane
PTHZ	biaxial compressive strength, θZ plane
QRTH	biaxial tensile strength, Rθ plane
PRTH	biaxial compressive strength, Rθ plane

The sequence of calculation to obtain the coefficients in Equation (A-1) is given by:

$$A1 = \frac{1}{FSRZ^2}$$

$$B1 = \frac{1}{FT? \cdot FCZ}$$

$$B2 = \frac{1}{FTTH \cdot FCTH}$$

$$B3 = B2$$

$$D1 = - \left[\frac{FCZ - FTZ}{FCZ \cdot FTZ} \right]$$

$$D2 = - \left[\frac{FCTH - FTTH}{FCTH \cdot FTTH} \right]$$

$$D3 = D2$$

$$P1 = PTHZ$$

$$P2 = PRTH$$

$$P3 - P1$$

$$Q1 = QTHZ$$

$$Q2 = QRTH$$

$$Q3 = Q1$$

$$C1 = - (B1 + B2) + \frac{1}{P1Q1} \left[\frac{Q1^3 + P1^3}{P1 \cdot Q1 \ (P1 + Q1)} + (D1 + D2)(P1 - Q1) \right]$$

$$C2 = - (B2 + B3) + \frac{1}{P2Q2} \left[\frac{Q2^3 + P2^3}{P2 \cdot Q2 \ (P2 + Q2)} + (D2 + D3) \ (P2 - Q2) \right]$$

$$C3 = C1$$

$$BB1 = \frac{1}{Q1} \ (B1 + B2 - C1) - \frac{1}{Q1^3} - \frac{1}{Q1^2} \ (D1 + D2)$$

$$BB2 = \frac{1}{Q2} \ (B2 + B3 - C2) - \frac{1}{Q2^3} - \frac{1}{Q2^2} \ (D2 + D3)$$

$$BB3 = BB1$$

$$E1 = \frac{1}{2} (BB1 - BB2 + BB3)$$

$$E2 = \frac{1}{2} \ (BB2 - BB3 - BB1)$$

$$E3 = E2$$

$$F = -3 \ (E1 + E2 + E3)$$

A2.0 STRENGTH DATA FOR TRUNCATED 994-2 GRAPHITE

Average strengths for truncated 994-2 graphite needed in the Priddy failure criterion were based primarily on tensile tests at 70°F and 2000 °F conducted at Southern Research Institute (SoRI) for the Material Requirements Definition (MRD) program (Reference A-2).

For temperatures above 2000°F and for compressive values, average failure stresses were based upon SoRI data for non-truncated 994-2 graphite in Reference A-3. These results are summarized below:

Average strengths (psi) for truncated 994-2 graphite.

	Temperature (°F)			
	70	2000	2500	3000
Across Grain Tensile Strength (FTZ)				
Sample Size	53	90	7	7
Average	4274	4807	5127	5217
Across Grain Compressive Strength (FCZ)				
Sample Size	4	---	---	4
Average	11840	12679*	13523*	13760
With Grain Tensile Strength (FTTH)				
Sample Size	41	55	7	7
Average	5677	6551	6730	7250
With Grain Compressive Strength (FTTH)				
Sample Size	6	---	---	9
Average	10270	11295*	11603*	12500

*Estimated from ratio of compressive strength to tensile strength
at 3000°F

To estimate the equal biaxial tensile strength in the θZ plane, off-axis test results described by Jortner on ATJ-S graphite (Reference A-4) were used. These results at 70°F and 2000°F (Figure A-1) show that a smooth curve passing through the centroid of uniaxial and biaxial strengths also goes through the following equal biaxial strength:

$$QTHZ = 0.90 \ FTTZ.$$

Biaxial failure stresses at 70°F (ATJ-S).
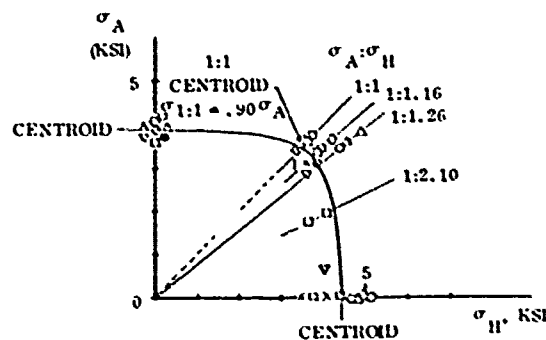
Biaxial failure stresses at 2000°F (ATJ-S).
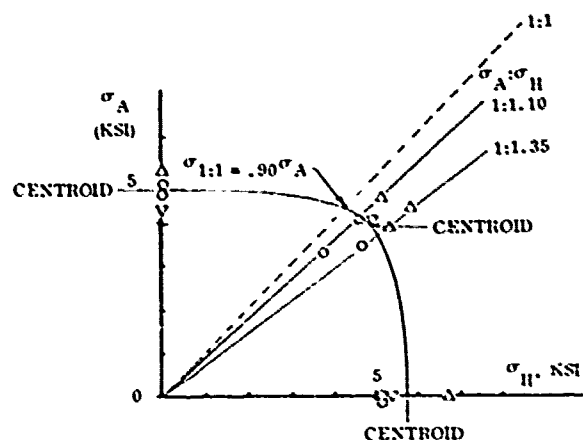
Figure A-1. Biaxial failure stresses for ATJ-S graphite.

It is reasonable to assume a similar result for equal biaxial strength in the θR plane:

$$QRTH = 0.90\ FTTH.$$

The equal biaxial compressive strengths were estimated as the smaller of the two uniaxial compressive strengths:

$$PTHZ = MIN\ (FCZ,\ FTTH)$$
$$PRTH = MIN\ (FCTH,\ FCTH).$$

To determine the RZ shear strength, it was assumed that off-axis uniaxial strength predicted as a function of off-axis angle:

1. should be a smooth-shaped, slowly varying curve in compression
    that follows measurements on ATJ-S graphite (Reference A-5) and,
2. should have 45-degree tension values close to measured strengths
    for non-truncated 994-2 graphite (Reference A-3).

199

Using assumed values for average shear strength together with average strengths previously assigned, off-axis compressive strength, σ, was calculated from Equation (A-1) by trial and error. For this purpose:

$$\sigma_r = \frac{1}{2}\sigma(1 - \cos2\phi)$$

$$\sigma_\theta = 0$$

$$\sigma_z = \frac{1}{2}\sigma(1 - \cos2\phi)$$

$$\tau_{rz} = \frac{1}{2}\sigma \cdot \sin2$$

where ϕ is the off-axis angle ($\phi = 0$ AG; $\phi = 90$ WG). These results in Figures A-2 through A-5 show that, as expected, off-axis compressive strength is sensitive to the assumed shear strength. The best estimate of shear strength required to satisfy the two requirements described above is summarized below:

Estimated shear strength for screened 994-2 graphite.

Temperature ($^\circ$F)	FSRZ (psi)
70	4000
2000	4500
2500	4750
3000	5000

It should be noted that these shear strengths:

1. are a smooth function of temperature, and
2. give 45-degree tensile strengths predictions within 200 psi of measured strengths for non-truncated 994-2 graphite at 70°F and 2000°F.

To summarize, the nine strengths required in the Priddy criterion for truncated 994-2 were determined as follows:

1. Uniaxial tensile strengths at 70°F and 2000°F were based upon MRD test results for truncated 994-2 in Reference A-2.
2. Uniaxial tensile strengths at 2500°F and 3000°F were based upon non-truncated 994-2 graphite in Reference A-3.
3. Uniaxial compressive strength were based upon non-truncated 994-2 graphite in Reference A-3.
4. Biaxial tensile strengths were calculated as 90 percent of the smaller of the uniaxial value based on ATJ-S data (Reference A-4).

200

5. Biaxial compressive strengths were assumed equal to the smaller of the two uniaxial compressive strengths.

6. Shear strengths were estimated from off-axis uniaxial compression tests on ATJ-S graphite (Reference A-5).
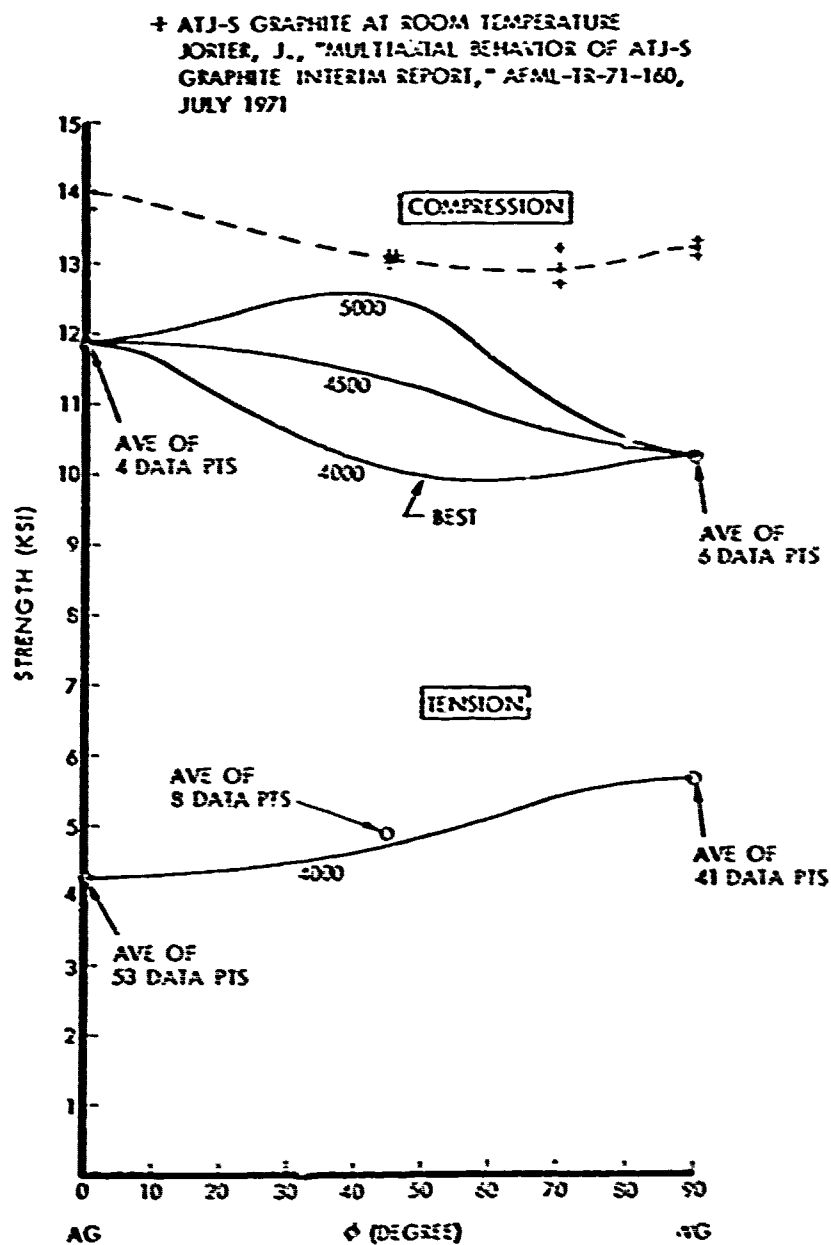
Figure A-2. Off-axis strength predicted by Priddy theory for 994-2 graphite as a function of RZ shear strength.

Figure A-4. Off-axis strength predicted by Priddy theory for 994-2 graphite as a function of RZ shear strength – 2500°F.

Figure A-3. Off-axis strength predicted by Priddy theory for 994-2 graphite as a function of RZ shear strength – 2000°F.
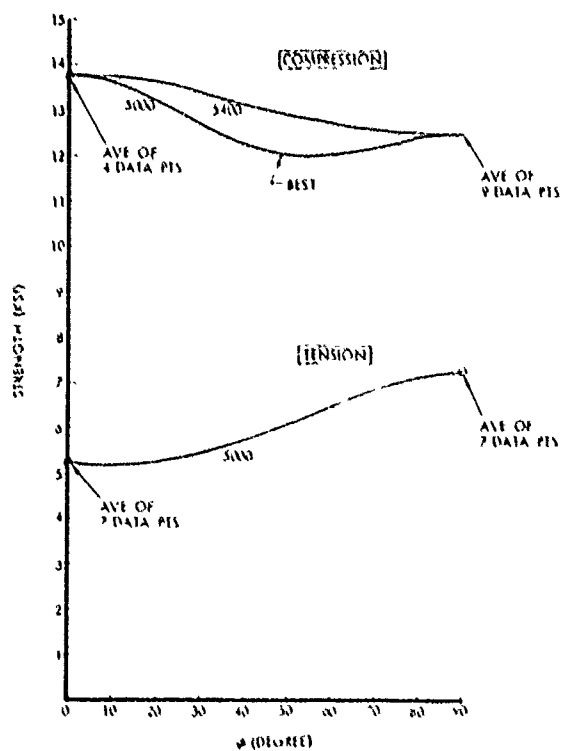
Figure A-5. Off-axis strength predicted by Priddy theory for 994-2 graphite as a function of RZ shear strength ~ 3000°F.

A3.0 MARGINS-OF-SAFETY FOR STRUCTURAL ANALYSES

Margins-of-safety are calculated for each finite element from the proximity of the applied stress vector to the Priddy failure surface as indicated in Figure A-6.
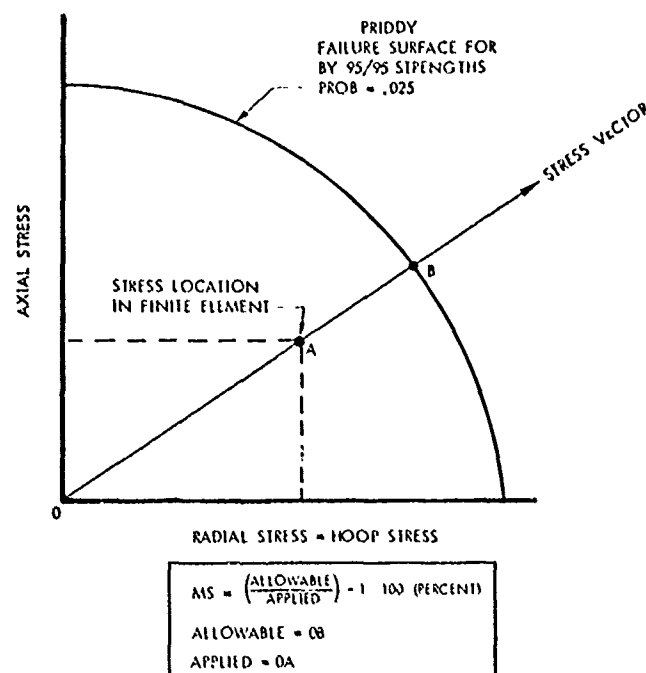
Figure A-6. Priddy margin-of-safety calculation.

For thermostructural analyses of nosetips, margins-of-safety are calculated with 95 95 allowable strengths for a fictitious finite element having the same volume as the volume of the Reference A-2 data base (0.038 in^3) so that margins-of-safety are not dependent on mesh size. The data base used to estimate statistical variation in the referenced strengths consists of at least 90 samples in each of the with-grain and across-grain directions. For a sample size of 90, the 95/95 allowable corresponds to strengths of approximately 2.5 percent failure probability. To reduce average strengths in Table A-1 to 95/95 level strengths, Weibull distributions were fit through with-grain and across-grain strengths at 70°F and 2000°F (Figures A-7 and A-8):

$$F(R) - 1 - EXP \left(- \Gamma^{\beta}(1 + \frac{1}{\beta}) \quad R^{\beta} \right)$$

where

F(R) is the cumulate probability of failure for a normalized strength, R
R is strength divided by average strength
Γ is the Gamma function.

Table A-1. Average strengths and Weibull statistics
for truncated 994-2 graphite (psi).

STRENGTH	WEIBULL STATISTIC	TEMPERATURE			
		70	2000	2500	3000
FTZ	32	4274	4807	5127	5217
FCZ	32	11840	12679	13523	13769
FTTH	16	5677	6551	6730	7250
FCTH	16	10270	11295	11603	12500
FSRZ	16	4000	4500	4750	5000
QTHZ	16	3847	4326	4614	4695
PTHZ	16	10270	11295	11603	12500
QRTH	16	5109	5896	6057	6525
PRTH	16	10270	11295	11603	12500

According to Figures A-7 and A-8:

β = 16 for with-grain strengths at any temperature
β = 32 for across-grain strengths at any temperature.

The required multiplying factor, RFAC, used for obtaining any failure strength probability, PROB, from average streng h is given by (Table A-2):

$$RFAC = \frac{\left[-\ell n(1 - PROB)^{\frac{1}{\beta}} \right]}{\Gamma\left(1 + \frac{1}{\beta}\right)}$$

Figure A-7. Weibull distribution of strength for truncated 994-2 graphite (WG direction).

Figure A-8. Weibull distribution of strength for truncated 994-2 graphite (AG direction).

Table A-2. Multiplying factors, RFAC*, for calculating strengths at various probabilities of failure.

CUMULATIVE PROBABILITY OF FAILURE	WITH GRAIN $\beta = 16$	ACROSS GRAIN $\beta = 32$
0.50	1.01010	1.00581
0.40	0.99101	0.99626
0.30	0.96901	0.98514
0.20	0.94102	0.97081
0.10	0.89791	0.94831
0.05	0.85840	0.92721
0.025	0.82135	0.90698
0.01	0.77526	0.88117
0.001	0.67116	0.81987
0.0001	0.58119	0.76294

$$* \quad RFAC = \frac{[-\ell n \, (1 - PROB)]^{\frac{1}{\beta}}}{\Gamma\left(1 + \frac{1}{\beta}\right)}$$

$$\Gamma\left(1 + \frac{1}{16}\right) = 0.96758$$

$$\Gamma\left(1 + \frac{1}{32}\right) = 0.98290$$

A4.0 PROBABILITIES OF FAILURE FOR STRUCTURAL ANALYSES

In calculating the probability of failure for a finite element, the average strengths in Table A-1 are scaled to the finite element volume using the Weibull statistics fitted to the 994-2 data base. The volume correction used for this purpose is given by:

$$S(V) = \left(\frac{VREF}{V}\right)^{\frac{1}{\beta}} \cdot S(VREF)$$

where

        S(V) is the average strength for a finite element of volume V
        S(VREF) is the average strength for a reference volume (0.038 in^3) .
            shown in Table A-1
        β is the Weibull statistic for strength.

The probability of failure for a finite element is obtained as follows:

1.   Average strengths for the finite element are calculated using the volume correction described above.
2.   Trial-and-error failure strength probabilities are used to find the Priddy failure surface that passes through the applied stress vector (Newton-Raphson root extractor).

The overall probability of failure for a nosetip is then calculated from the conservative assumption that failure in any one finite element constitutes an overall failure in the nosetip:

$$P_F = 1 - \prod_{i-1}^{i=n} \left(1 - P_{F_i}\right)$$

where

        P_F is the overall probability of failure
        P_{F_i} is the probability of failure in finite element i

        i=1,n are the finite elements with temperatures below 3500°F.

A4.1   SUMMARY

The Priddy failure criterion was developed for 994-2 graphite using tensile test data obtained for the Materials Requirements Development (MRD) program. Using a statistical treatment of the referenced strength data base, the criterion can be used to account for volume effects in nosetips and to predict probabilities of failure. The resulting biaxial and triaxial failure surfaces for 994-2 graphite are shown in Figures A-9 through A-12. The influence of applied shearing stress on the θ-Z biaxial failure surface is shown in Figure A-13.

SHEAR STRESS = 0
ELEMENT VOLUME = .028 IN^3

Figure A-9. θ-Z biaxial allowable for 994-2 at 70°F.

SHEAR STRESS = 0
ELEMENT VOLUME = .035 IN^3

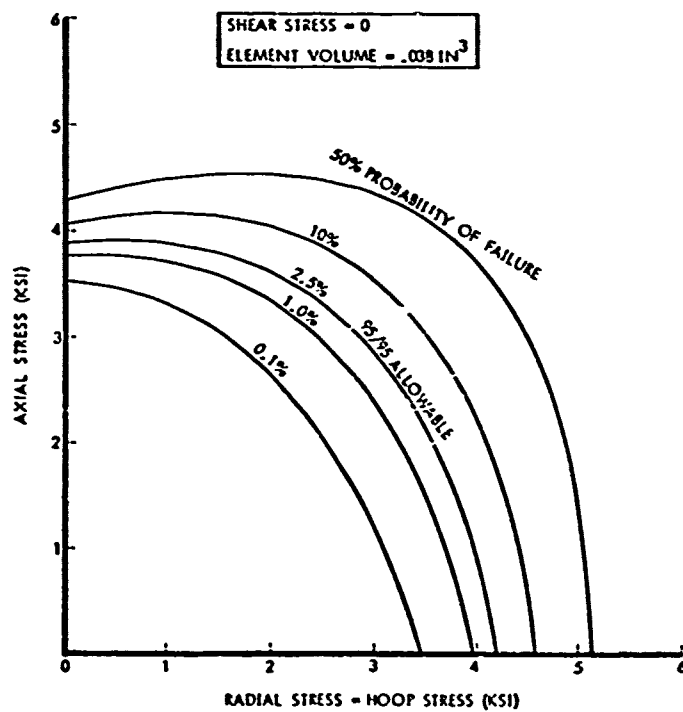Figure A-10. θ-Z biaxial allowable for 994-2 at 2000°F.

209
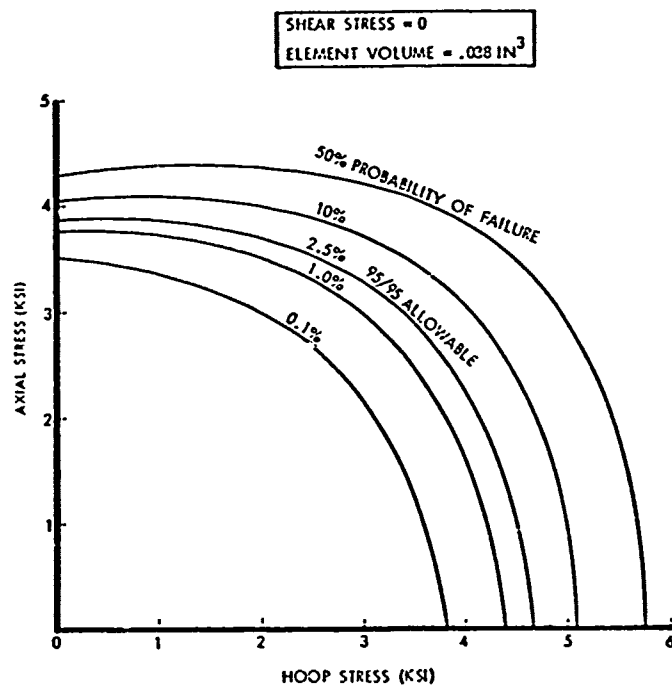
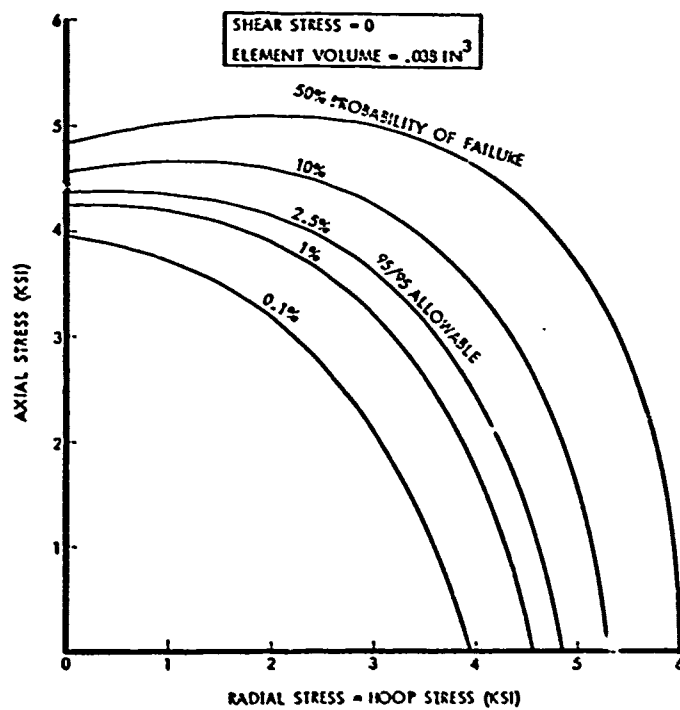Figure A-11. $R\theta$-Z spline allowable for 994-2 at 70°F.

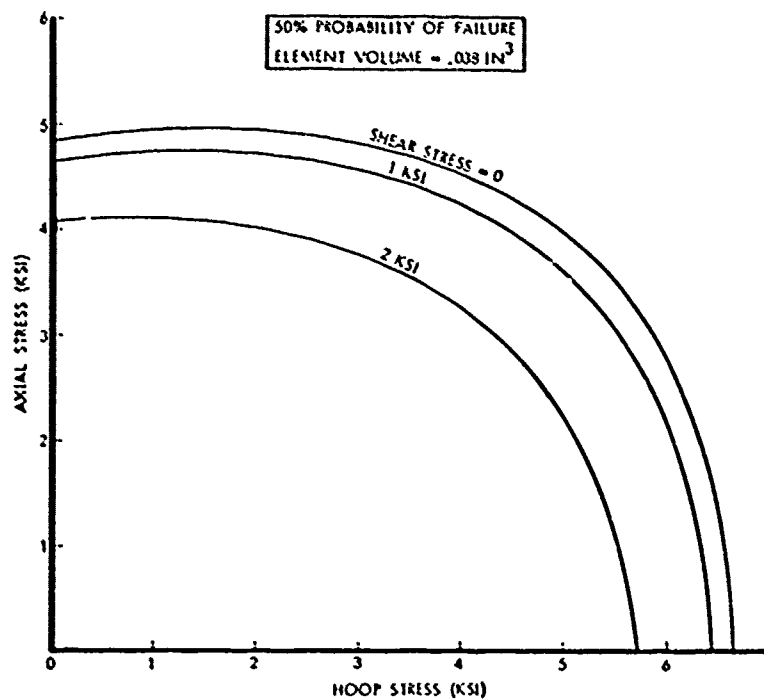Figure A-12. $R\theta$-Z spline allowable for 994-2 at 2000°F.

Figure A-13.   Effect of shear stress on θ-Z biaxial
allowable for 994-2 at 2000°F.

A5.0 REFERENCES

A-1. Priddy, T. G., "A Fracture Theory for Brittle Anisotropic Materials," *Journal of Engineering Materials and Technology*, April 1974.

A-2. Starrett, H. S., "Probable Values for the Mechanical and Thermal Properties of 994-2 Graphite," SoRI rough draft dated 6 June 1975.

A-3. Pears, C., and Littleton, H., "Status of 994-2 Per 8/1/74," SoRI Report, 12 November 1974.

A-4. Jortner, J., "Multiaxial Behavior of ATJ-S Graphite," McDonnell Douglas Astronautics Company, Technical Report AFML-TR-71-253, December 1971.

A-5. Jortner, J., "Multiaxial Behavior of ATJ-S Graphite, Interim Report," McDonnell Douglas Astronautics Company, Technical Report AFML-TR-71-160, July 1971.

APPENDIX B

RECESSION AND TEMPERATURE HISTORIES
OF SOLID AND SEGMENTED TUNGSTEN
ABLATION MODELS IN AFFDL 50 MW ARC-JET
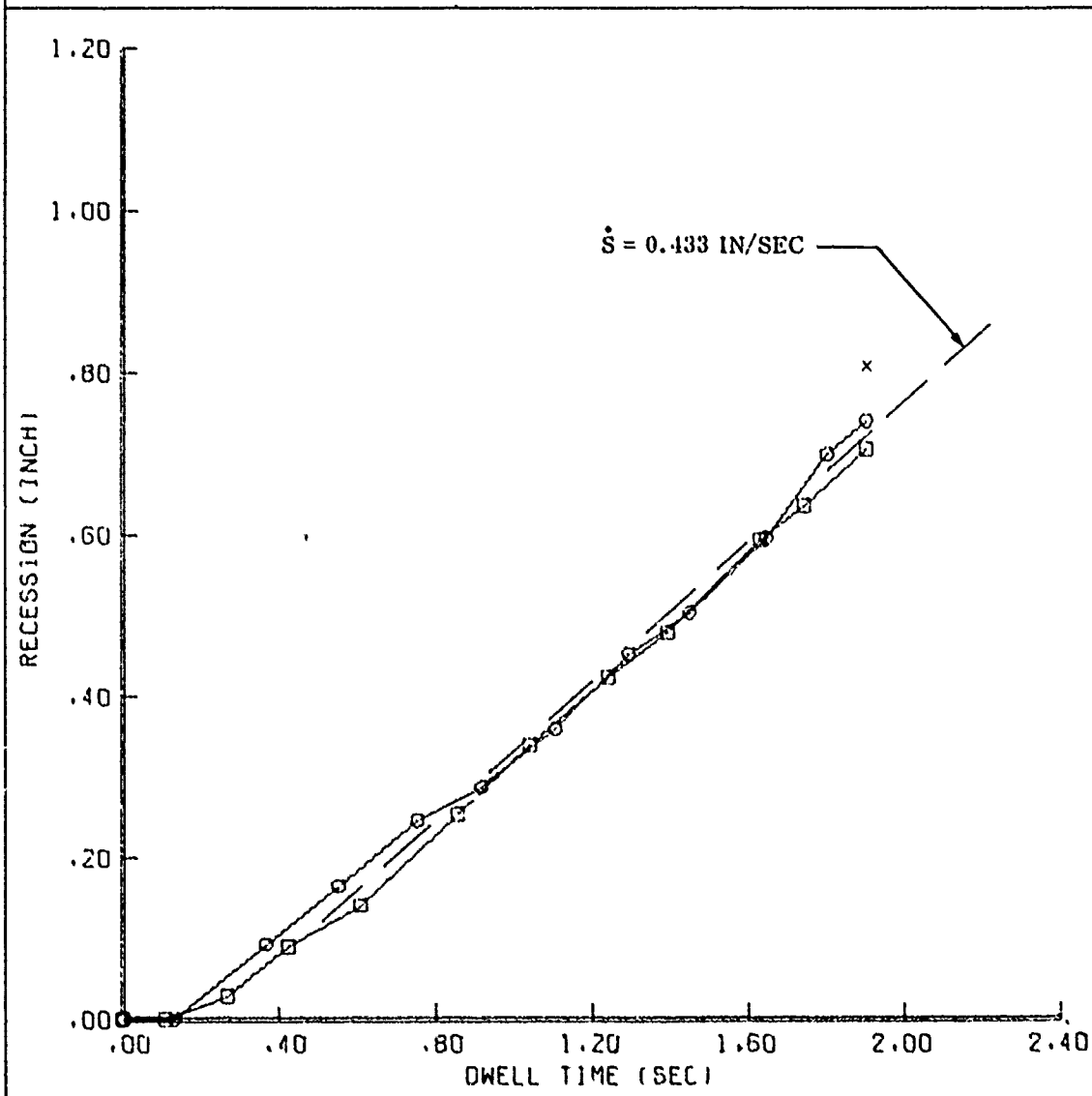
-

FIGURE B-1 . ABLATION HISTORY FOR SEGMENTED NOSETIP AT 50MW FACILITY

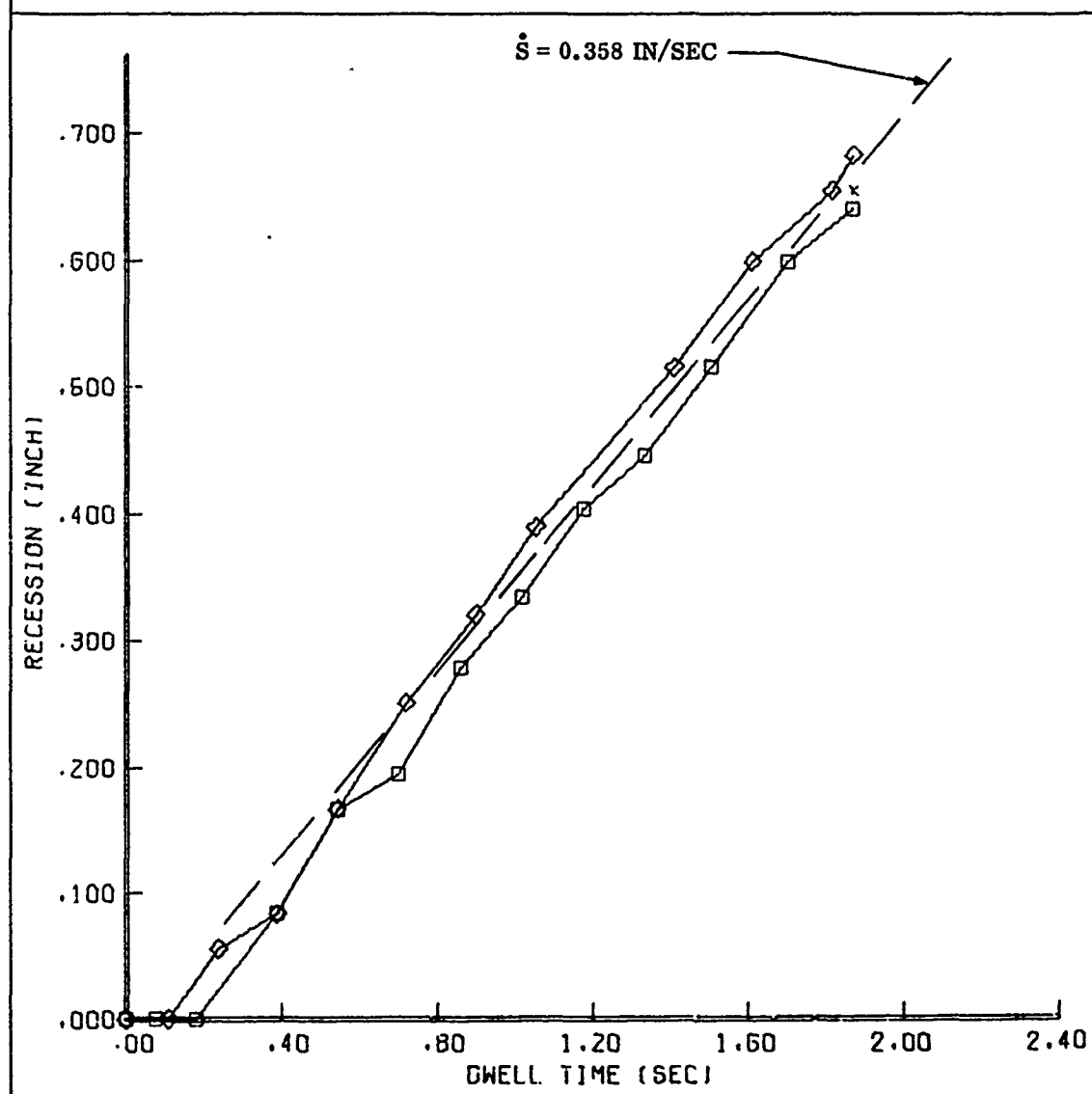MODEL NO. 2-2 SOLID TUNGSTEN
RS2-007-2 ROTATING STING DWELL TIME=1.850SEC

O OVERHEAD CAMERA   □ NORTH CAMERA
x PRE AND POST MEAS.

$\dot{S} = 0.483$ IN/SEC
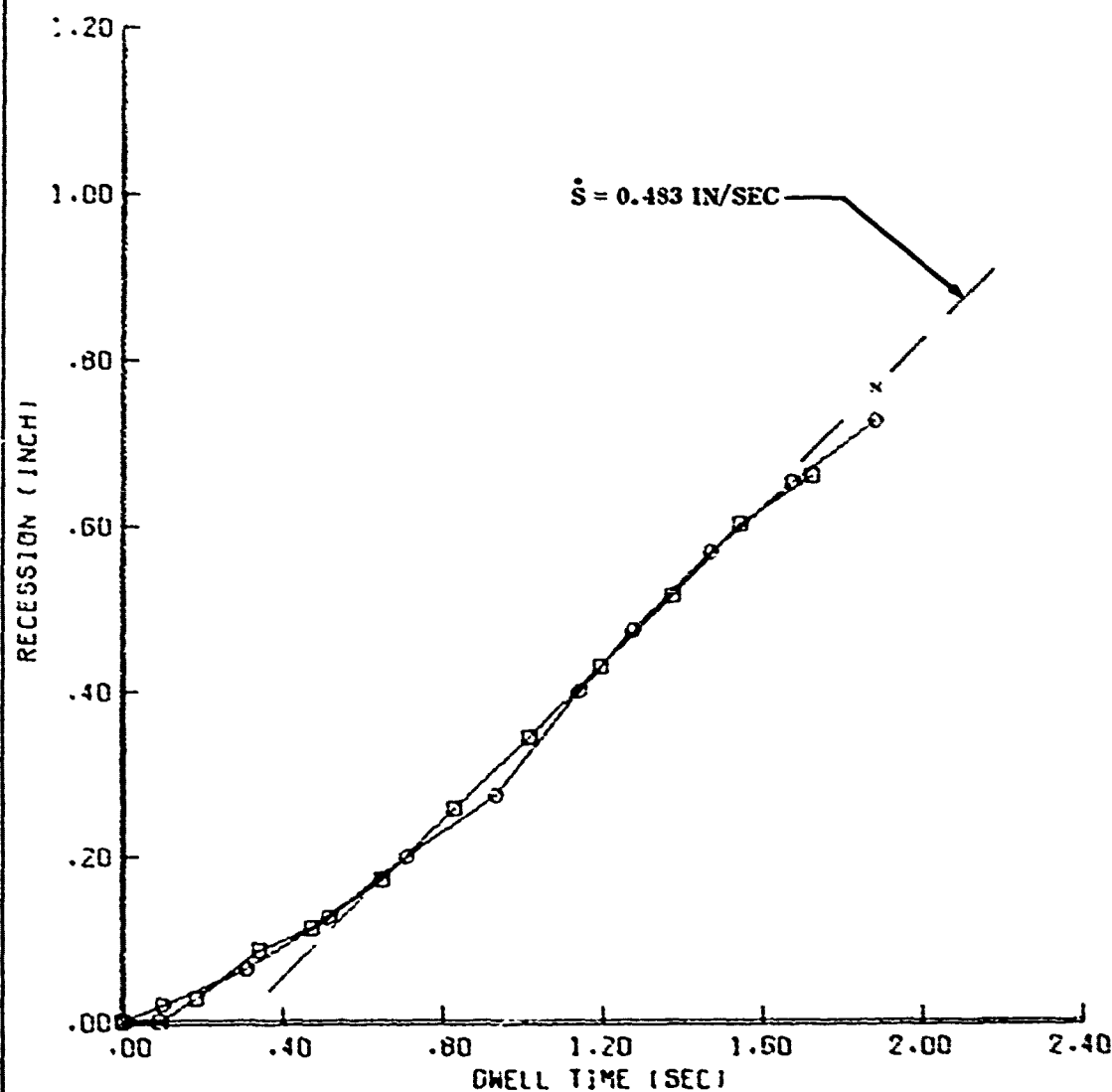
FIGURE B-2. ABLATION HISTORY FOR
SEGMENTED NOSETIP AT 50MW FACILITY

MODEL NO. 1-1   SOLID TUNGSTEN
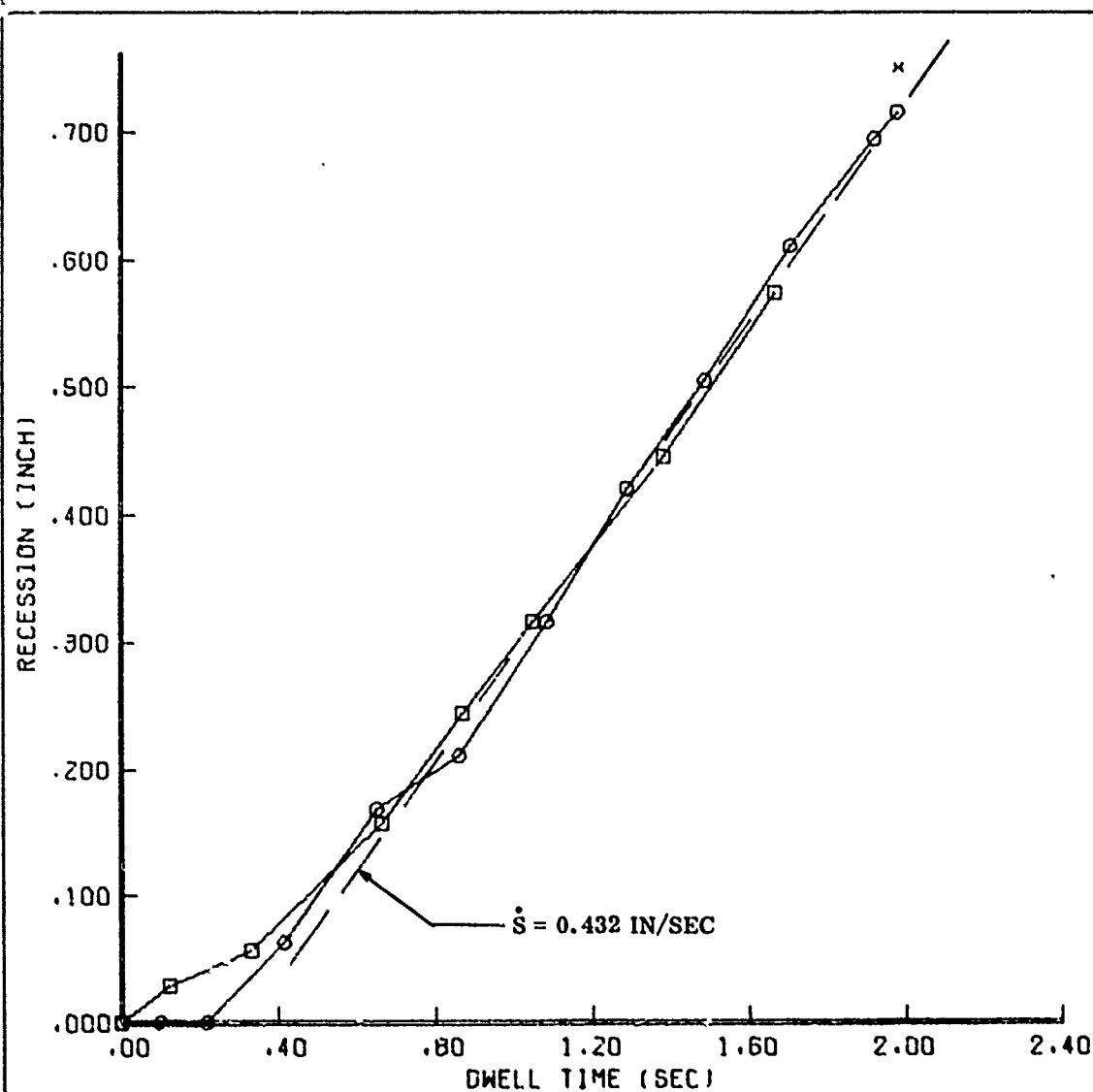RSZ-007-1   NON-ROTATING STING   DWELL TIME=1.820SEC

O OVERHEAD CAMERA   O SOUTH CAMERA
× PRE AND POST MEAS

$\dot{S} = 0.427$ IN/SEC

FIGURE B-3. ABLATION HISTORY FOR SEGMENTED NOSETIP AT 50MW FACILITY

MODEL NO. 4-2   SEGMENTED TUNGSTEN(0.010-INCH)
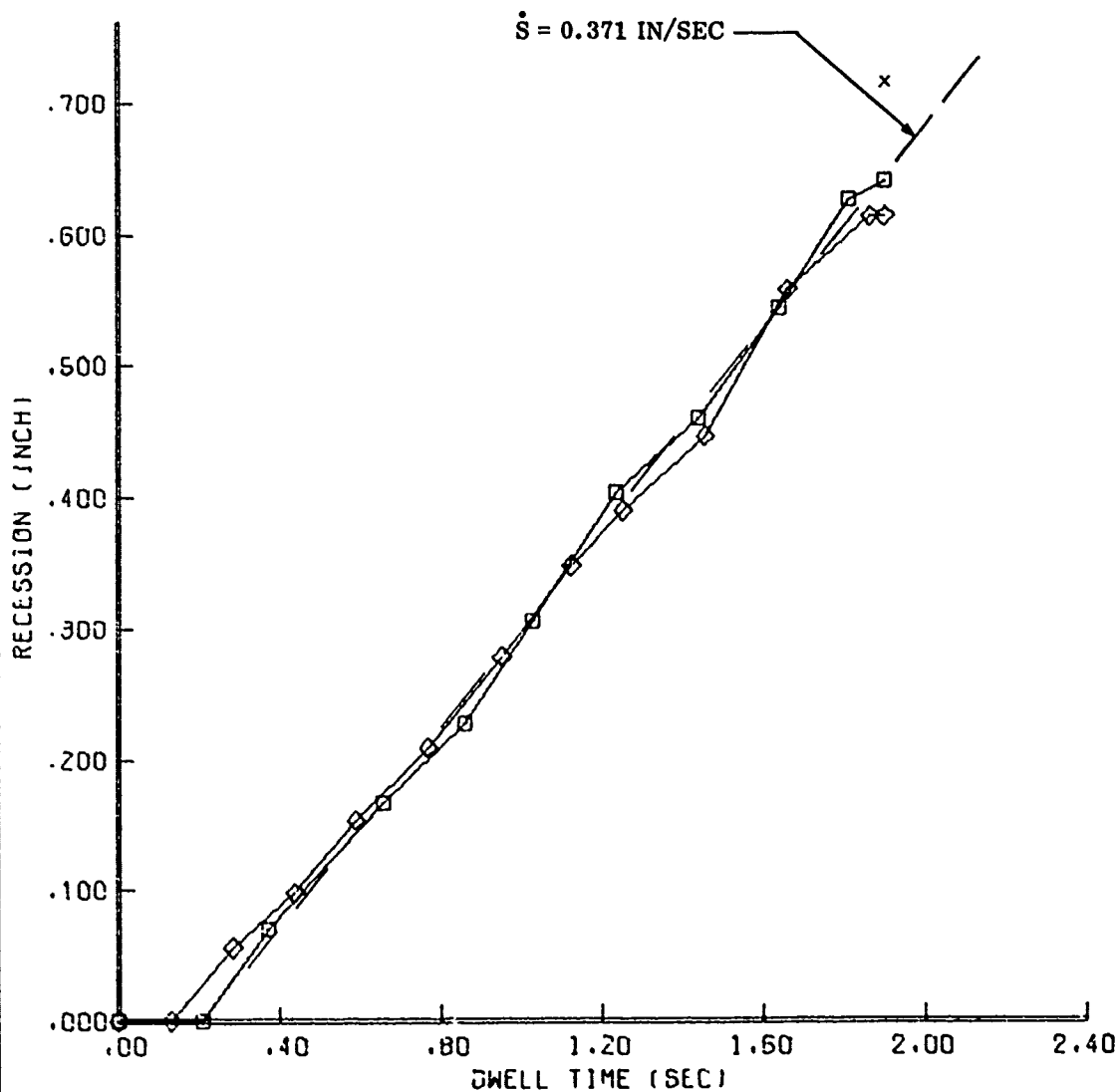R62-006-2   ROTATING STING   DWELL TIME=1.870SEC

O OVERHEAD CAMERA   ◇ SOUTH CAMERA
□ NORTH CAMERA   × PRE AND POST MEAS.

$\dot{S} = 0.428$ IN/SEC

216
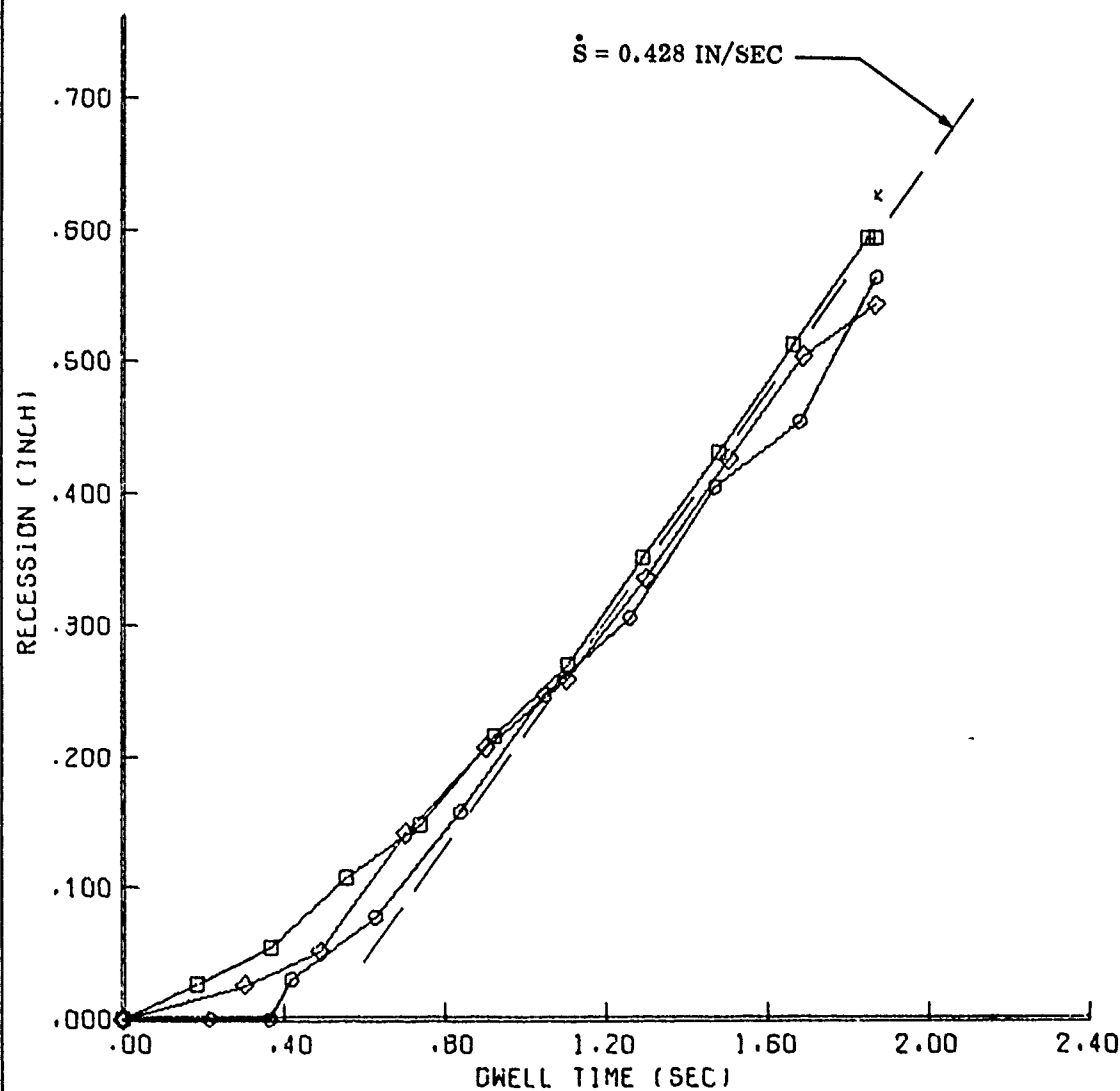
FIGURE B-4. ABLATION HISTORY FOR SEGMENTED NOSETIP AT 50MW FACILITY

MODEL NO. 3-3 SEGMENTED TUNGSTEN(0.010-INCH)
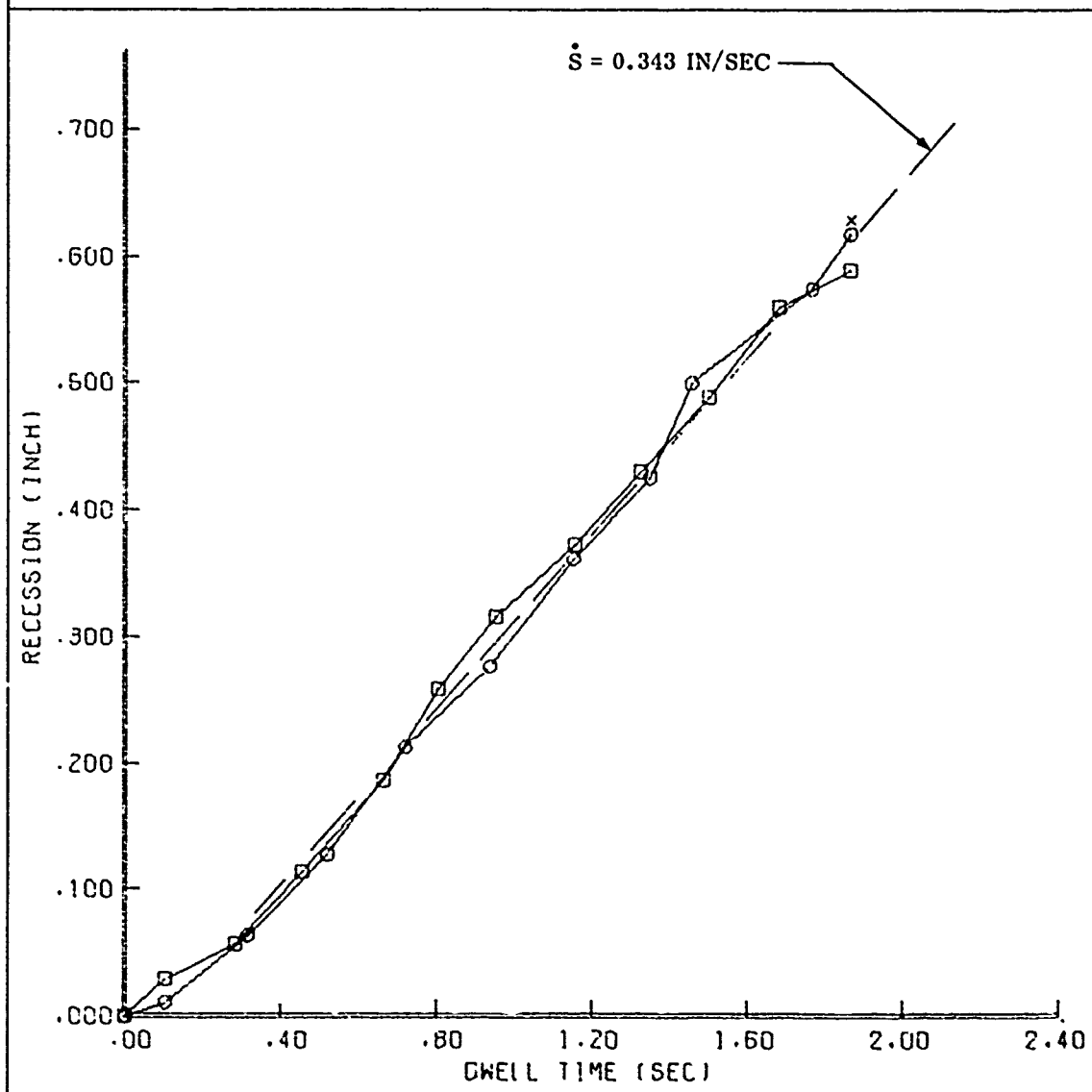R62-009-2 NON-ROTATING STING DWELL TIME:1.900SEC

O OVERHEAD CAMERA   □ NORTH CAMERA
× PRE AND POST MEAS.

$\dot{S} = 0.433$ IN/SEC

FIGURE B-5. ABLATION HISTORY FOR SEGMENTED NOSETIP AT 50MW FACILITY

MODEL NO. 4-5 SEGMENTED TUNGSTEN(0.010-INCH)
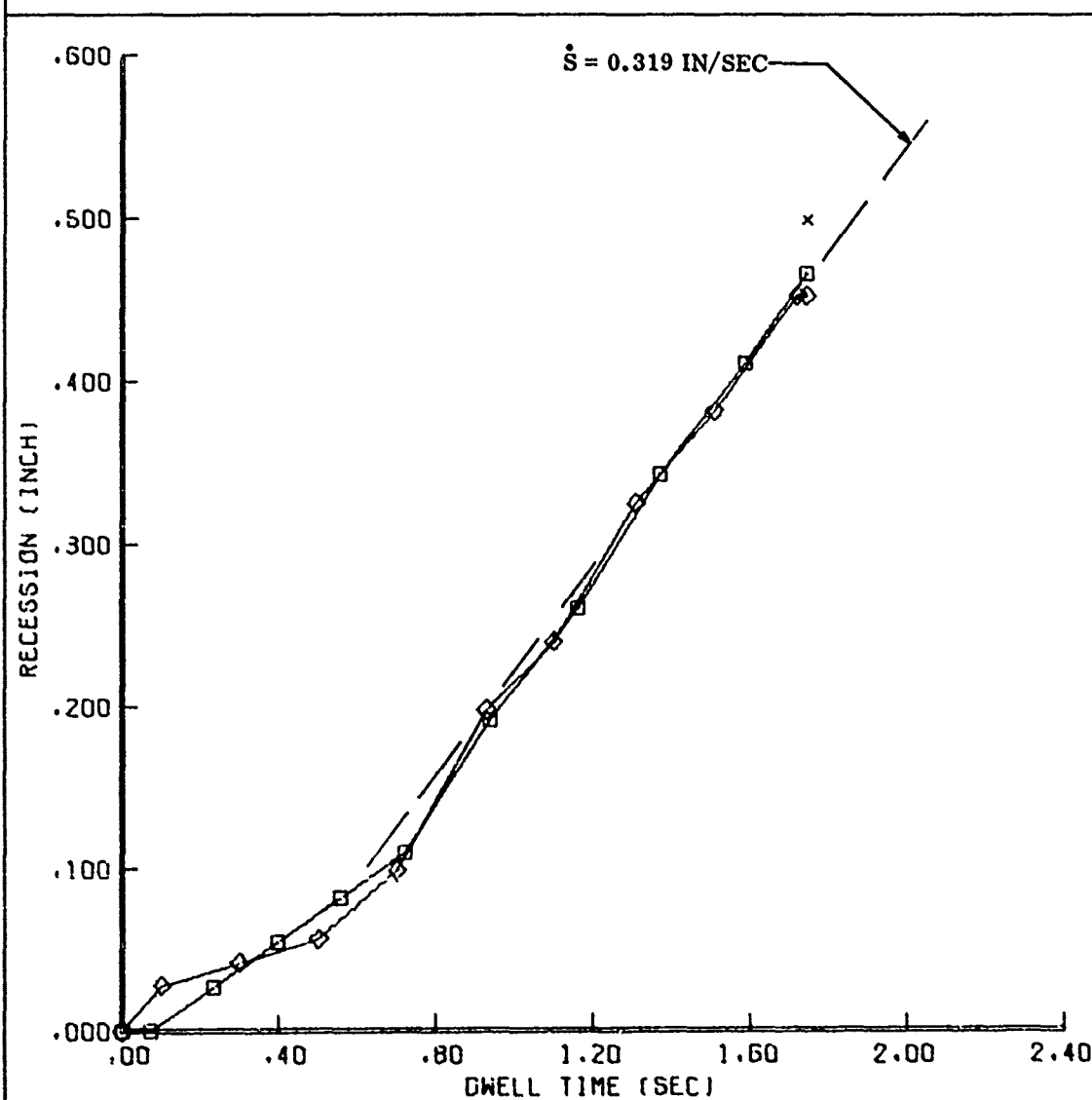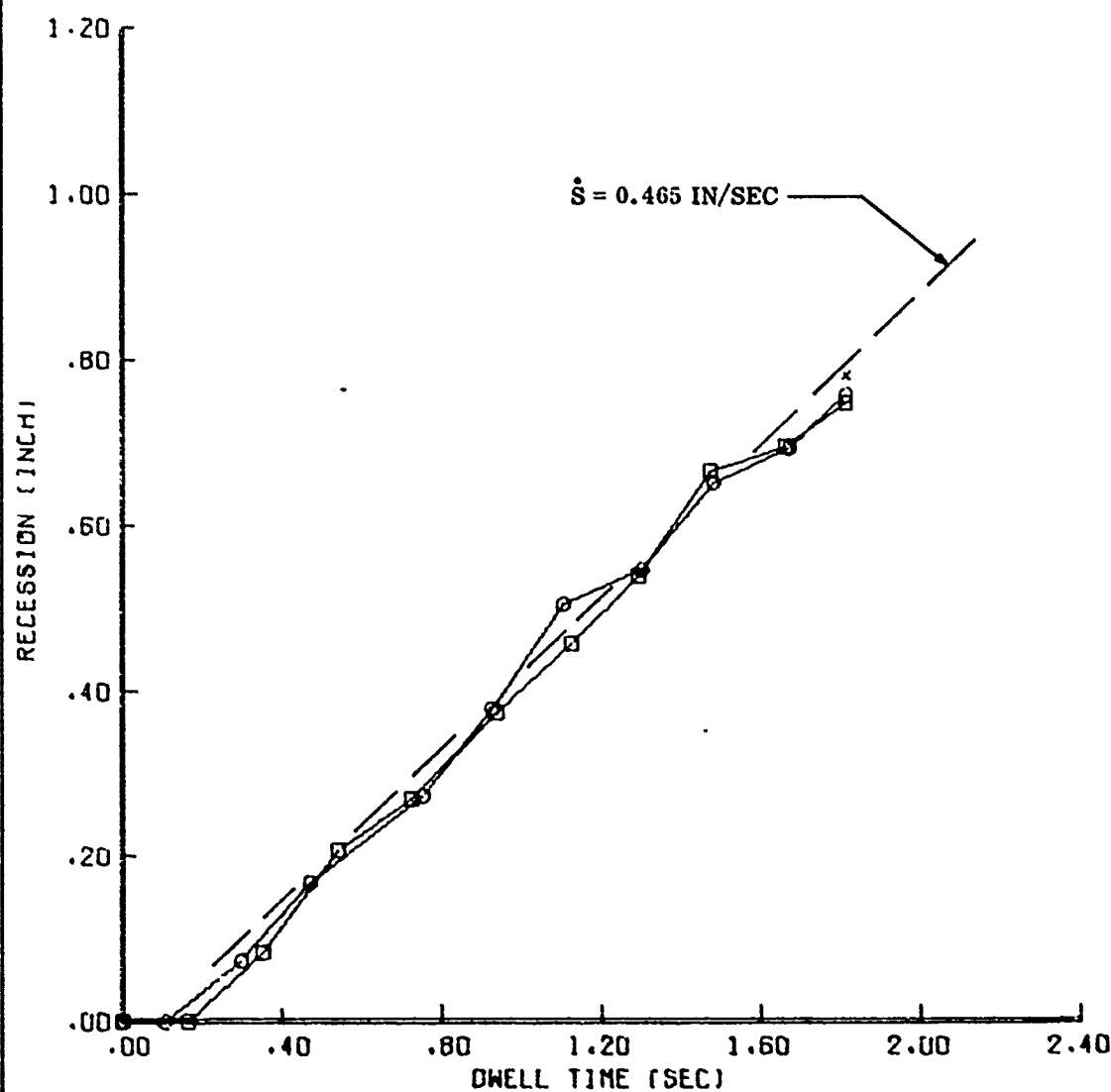R62-009-1 NON-ROTATING STING DWELL TIME=1.870SEC

□ NORTH CAMERA   ◇ SOUTH CAMERA
× PRE AND POST MEAS.

FIGURE B-6 . ABLATION HISTORY FOR SEGMENTED NOSETIP AT 50MW FACILITY

MODEL NO. 3-4 SEGMENTED TUNGSTEN(0.045-INCH)
R62-007-4 ROTATING STING DWELL TIME.:1.975SEC

O OVERHEAD CAMERA   □ NORTH CAMERA
x PRE AND POST MEAS.

$\dot{S} = 0.432$ IN/SEC

FICURE B-7. ABLATION HISTORY FOR SEGMENTED NOSETIP AT 50MW FACILITY

MODEL NO. 2-3 SEGMENTED TUNGSTEN(0.045-INCH)
R52-009-3 NON-ROTATING STING DWELL TIME-1.900SEC

□ NORTH CAMERA   ◇ SOUTH CAMERA
× PRE AND POST MEAS.

FIGURE B-8. ABLATION HISTORY FOR
SEGMENTED NOSETIP AT SOMW FACILITY

MODEL NO. 4-3 SEGMENTED TUNGSTEN(0.045-INCH)
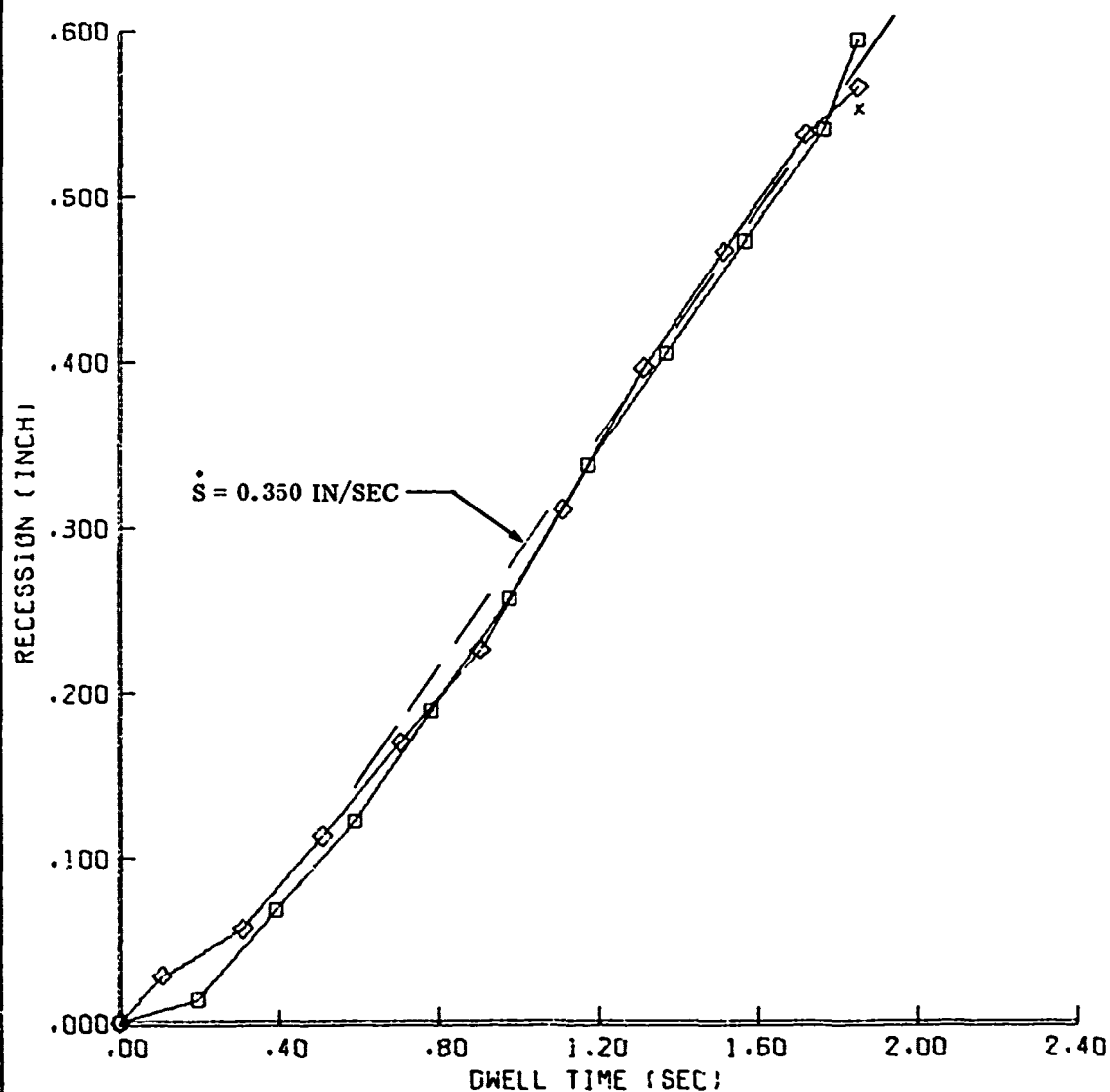R52-007-3 NON-ROTATING STING DWELL TIME.-1.865SEC

O OVERHEAD CAMERA   □ NORTH CAMERA
× PRE AND POST MEAS.

$\dot{S} = 0.343$ IN/SEC

FIGURE B-9. ABLATION HISTORY FOR
SEGMENTED NOSETIP AT 50MW FACILITY

MODEL NO. 3-2   SEGMENTED TUNGSTEN(0.120-INCH)
R62-006-4   ROTATING STING   DWELL TIME:1.740SEC

□ NORTH CAMERA   ◇ SOUTH CAMERA
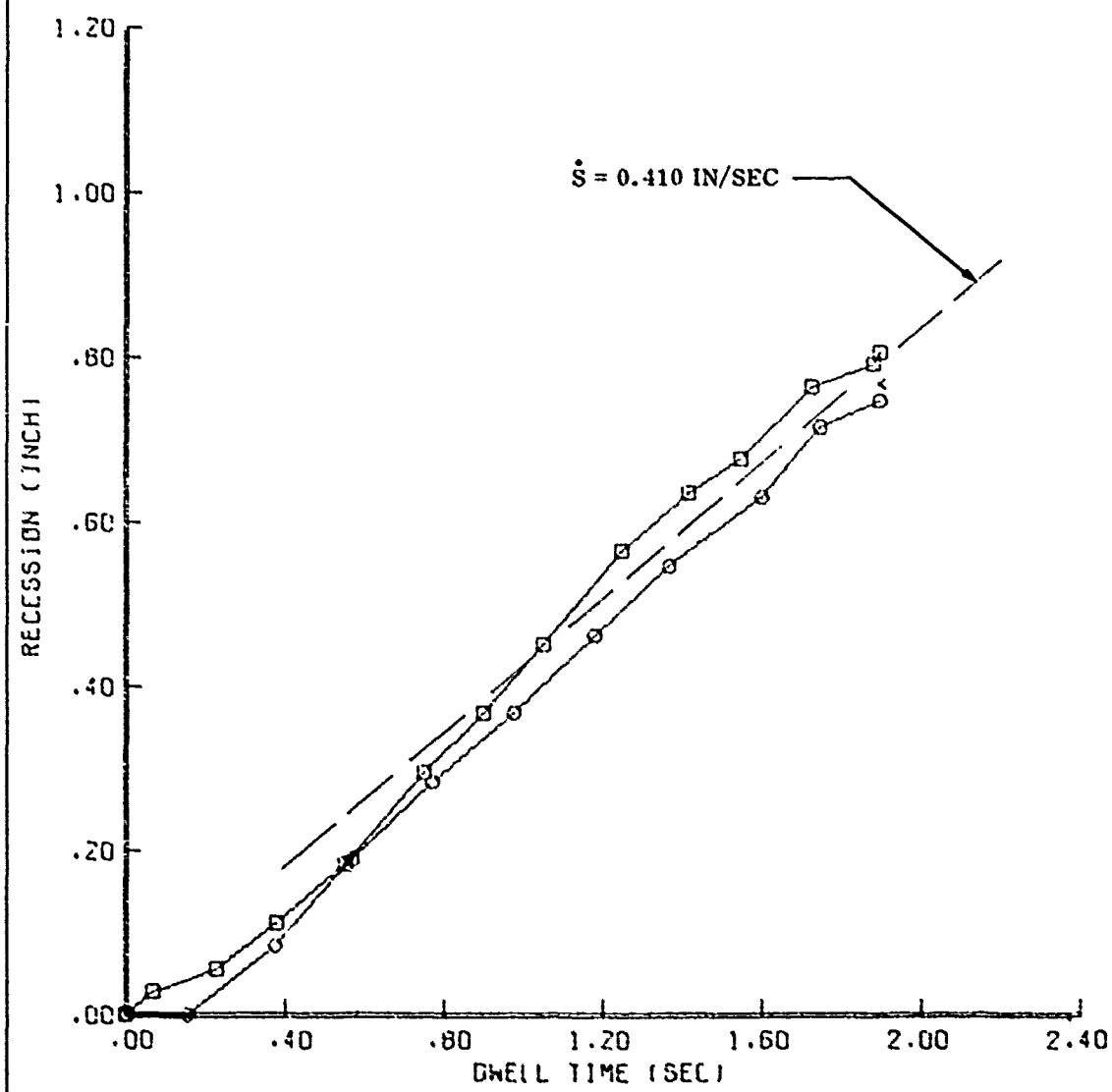× PRE AND POST MEAS.

$\dot{S} = 0.319$ IN/SEC

222

FIGURE B-10. ABLATION HISTORY FOR SEGMENTED NOSETIP AT 50MW FACILITY

MODEL NO. 1-2 SEGMENTED TUNGSTEN(0.120-INCH)
R62-008-5 NON-ROTATING STING DWELL TIME=1.810SEC

O OVERHEAD CAMERA   □ NORTH CAMERA
x PRE AND POST MEAS.

$\dot{S} = 0.465$ IN/SEC

RECESSION (INCH)

DWELL TIME (SEC)

FIGURE B-11. ABLATION HISTORY FOR
SEGMENTED NOSETIP AT 50MW FACILITY

MODEL NO. 2-1   SEGMENTED TUNGSTEN(0.120-INCH)
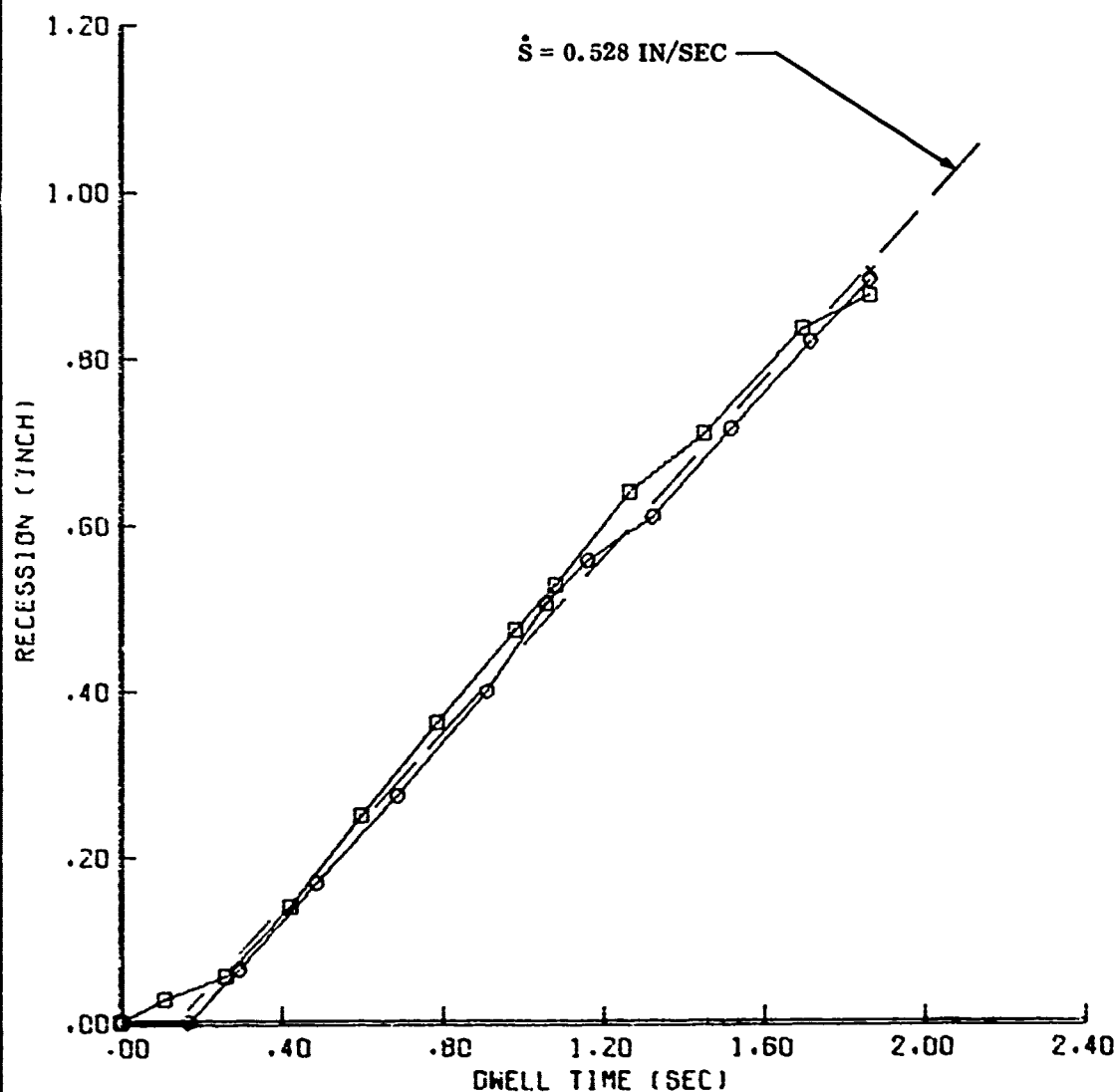R62-006-3   NON-ROTATING STING   DWELL TIME=1.850SEC

□ NORTH CAMERA   ◇ SOUTH CAMERA
× PRE AND POST MEAS.

$\dot{S} = 0.350$ IN/SEC

224

FICURE B-12. ABLATION HISTORY FOR
SEGMENTED NOSETIP AT 50MW FACILITY

MODEL NO. 4-1 SEGMENTED TUNGSTEN(0.120-INCH)
R62-005-3 NON-ROTATING STING DWELL TIME 1.895SEC

O OVERHEAD CAMERA   □ NORTH CAMERA
× PRE AND POST MEAS.

$\dot{S}$ = 0.410 IN/SEC

FIGURE B-13. ABLATION HISTORY FOR SEGMENTED NOSETIP AT 50MW FACILITY

MODEL NO. 4-4   COPPER INFILTRATED TUNGSTEN SEGMENTS
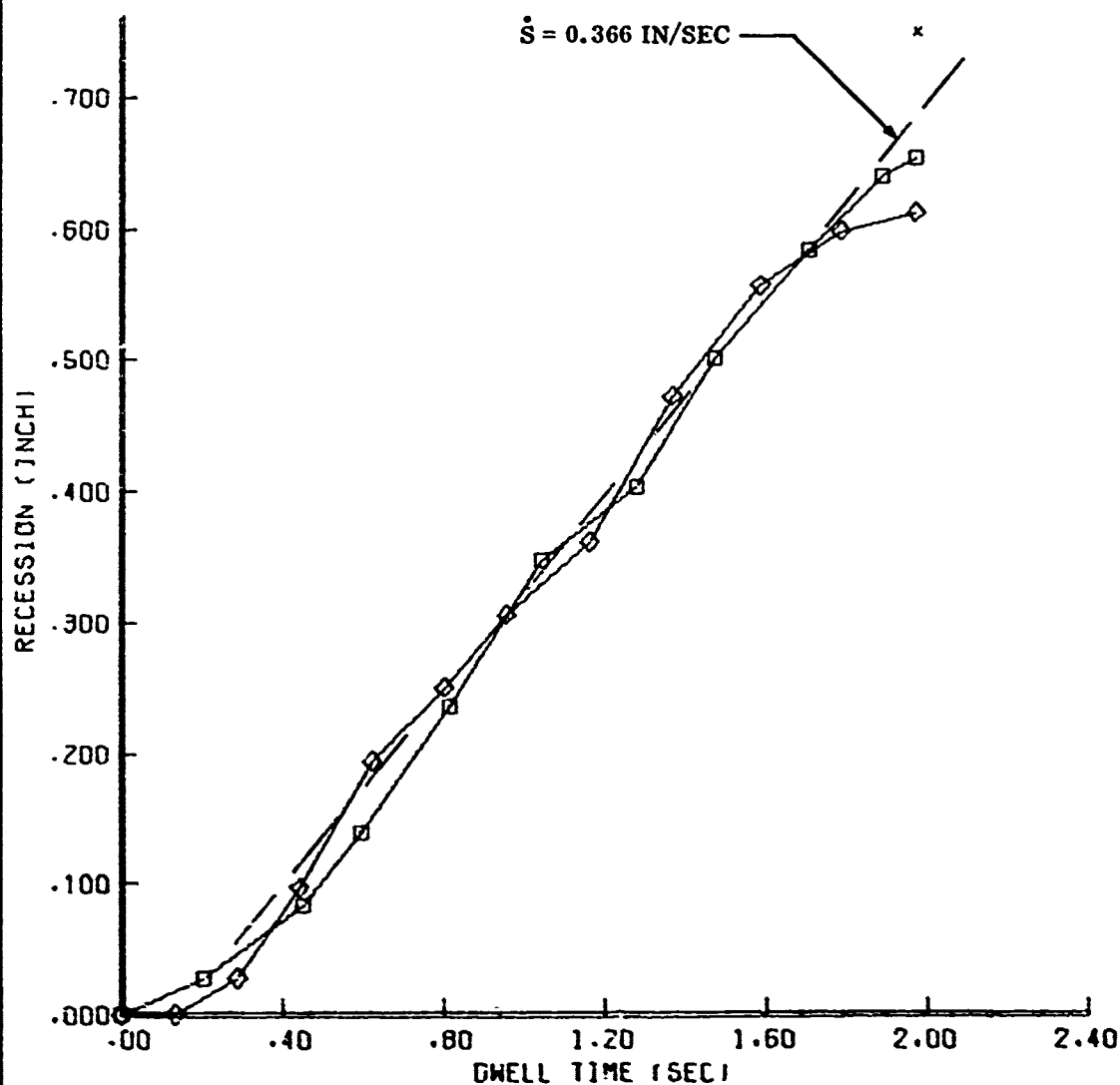R62-008-4 NON-ROTATING STING   DWELL TIME:-1.860SEC

O OVERHEAD CAMERA   □ NORTH CAMERA
× PRE AND POST MEAS.

$\dot{S}$ = 0.528 IN/SEC

FICURE B-14. ABLATION HISTORY FOR
SEGMENTED NOSETIP AT 50MW FACILITY

MODEL NO. 1-4 COPPER INFILTRATED SEGMENTS
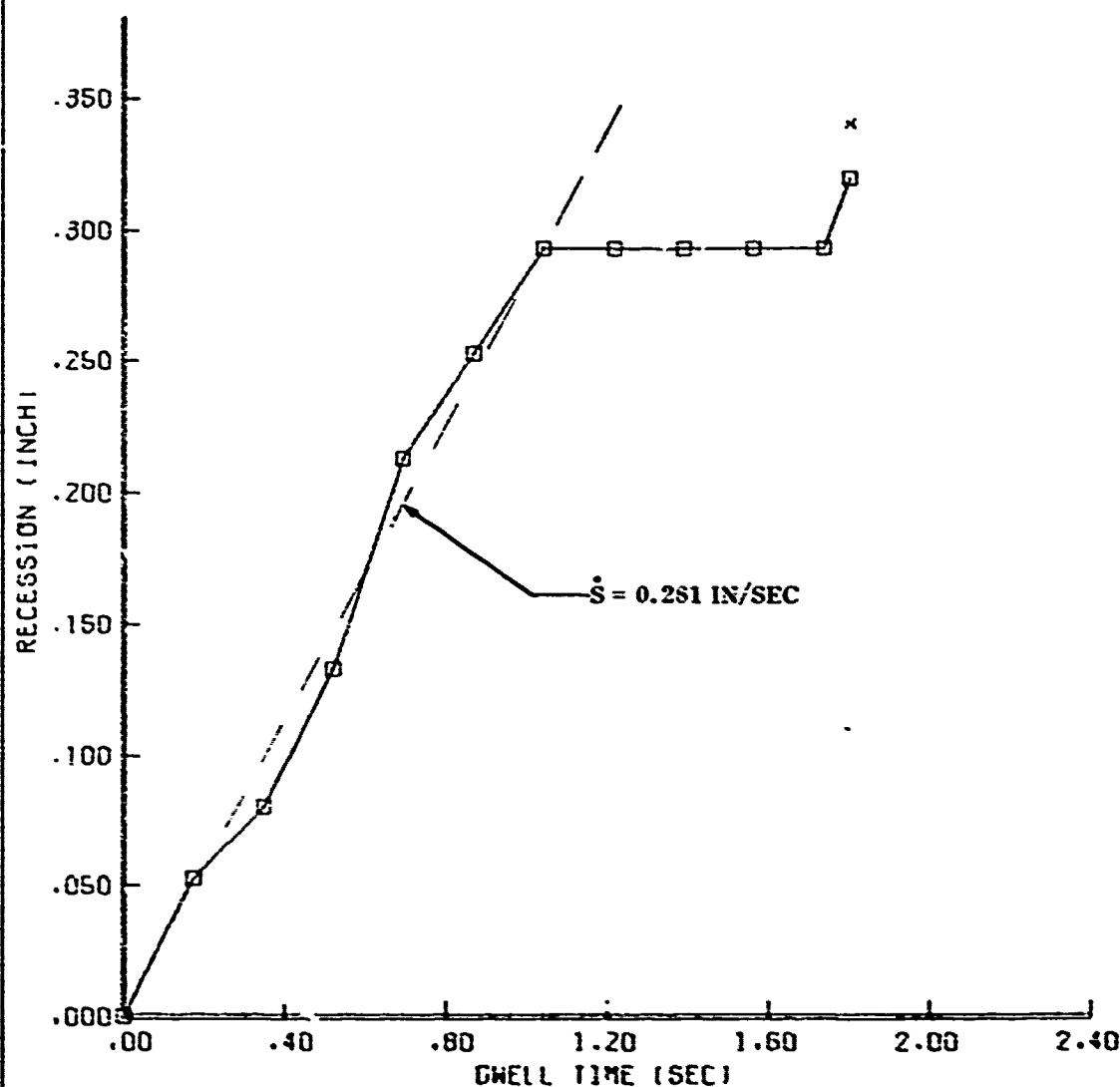R62-009-4 NON-ROTATING STING DWELL TIME=1.970SEC

□ NORTH CAMERA ◇ SOUTH CAMERA
× PRE AND POST MEAS.

$\dot{S}$ = 0.366 IN/SEC

227

FICURE B-15. ABLATION HISTORY FOR
SEGMENTED NOSETIP AT 50MW FACILITY

MODEL NO. 3-1 COPPER INFILTRATED TUNGSTEN SEGMENTS
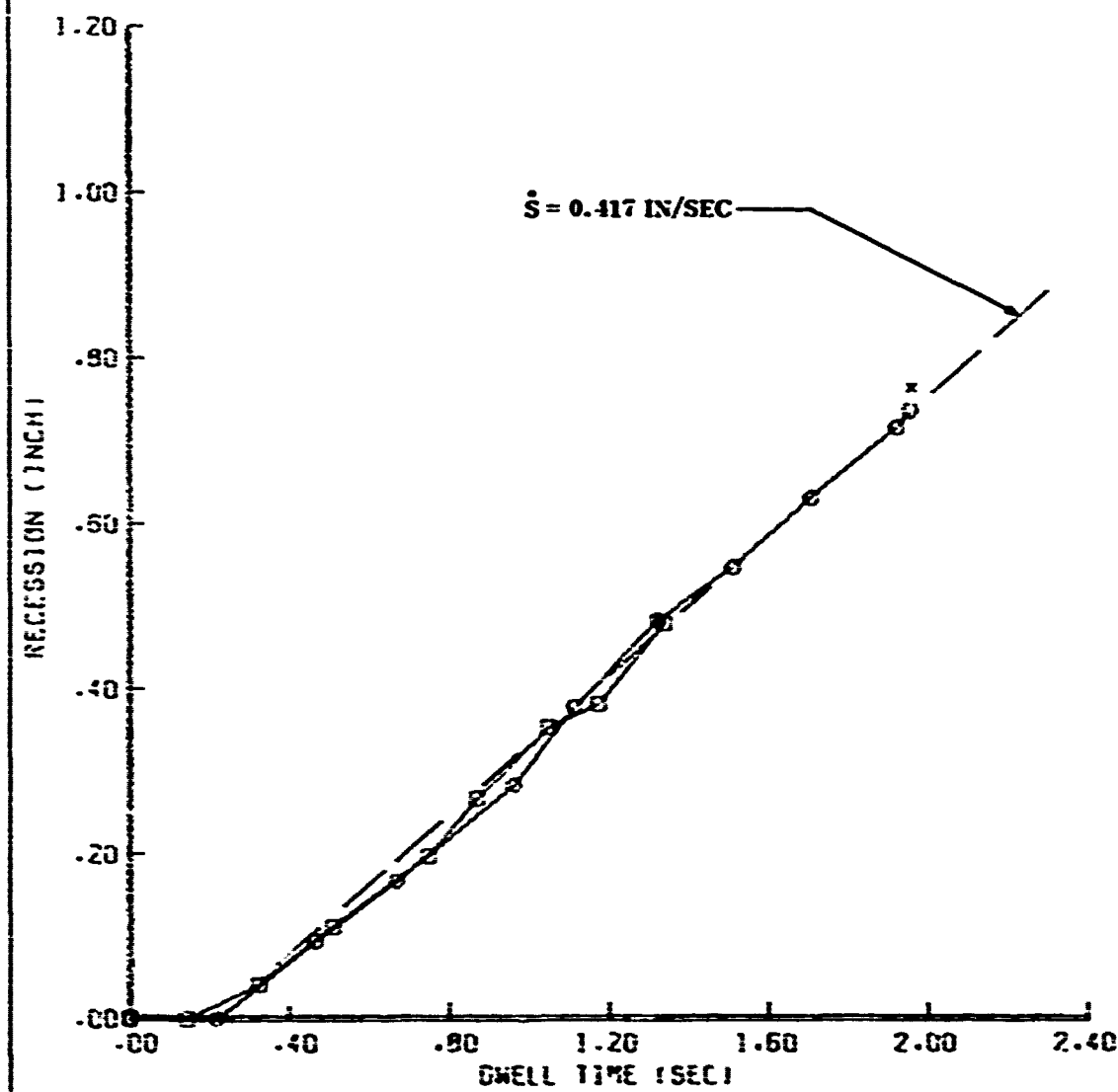RG2-006-1 NON-ROTATING STING DWELL TIME=1 800SEC .

□ NORTH CAMERA   x PRE AND POST MEAS.

$\dot{S}$ = 0.281 IN/SEC

RECESSION (INCH)

DWELL TIME (SEC)

FIGURE B-16. ABLATION HISTORY FOR SEGMENTED NOSETIP AT 50MW FACILITY

MODEL NO. 2-4 COPPER INFILTRATED TUNGSTEN CORE
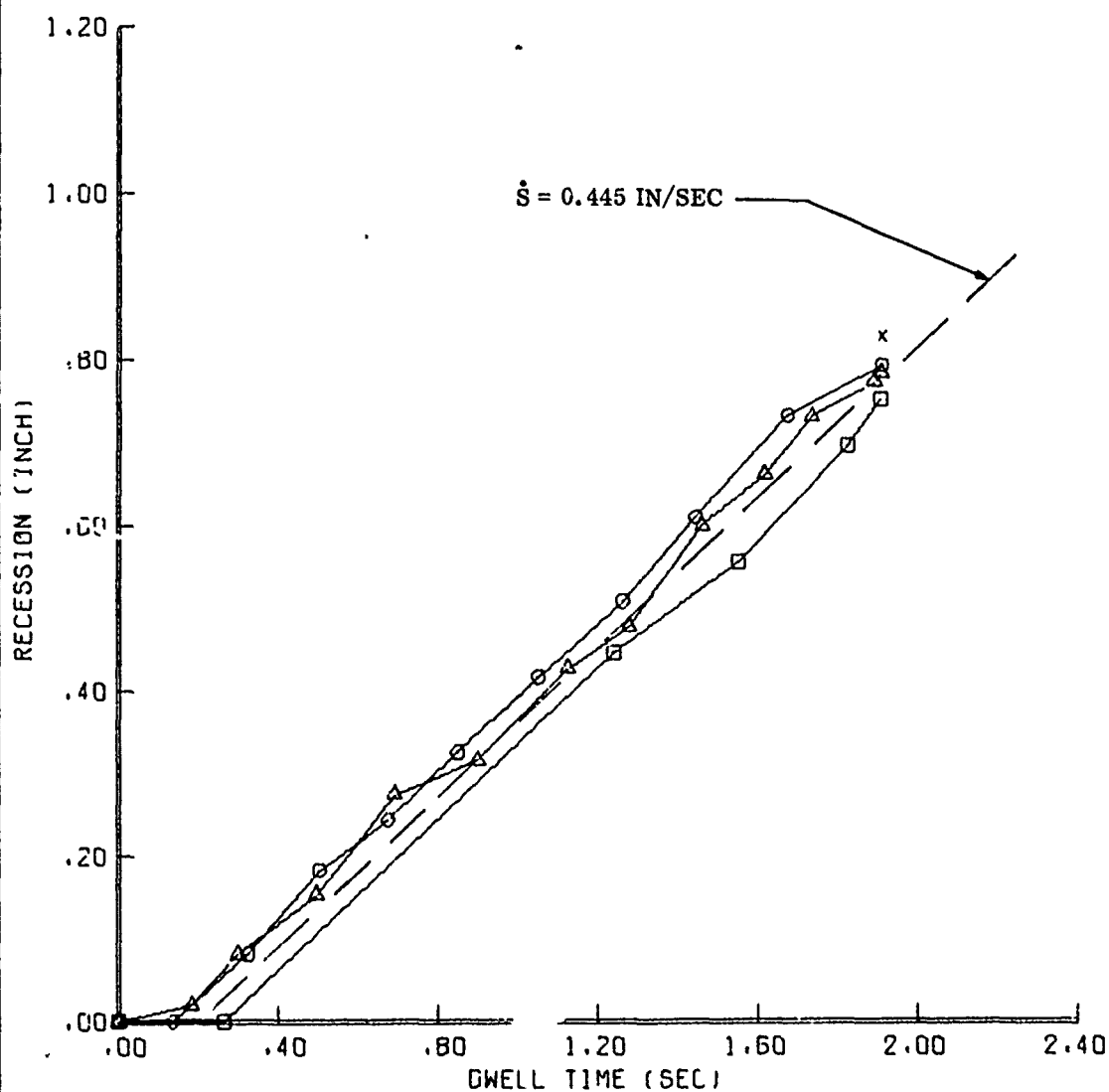R52-008-2 NON-ROTATING STING DWELL TIME=1.95SEC

O OVERHEAD CAMERA   □ NORTH CAMERA
× PRE AND POST MEAS.

$\dot{S} = 0.417$ IN/SEC

FICURE B-17. ABLATION HISTORY FOR
SEGMENTED NOSETIP AT 50MW FACILITY

MODEL NO. 1-3 COPPER INFILTRATED CORE
R62-009-5 NON-ROTATING STING DWELL TIME=1.910SEC

O OVERHEAD CAMERA   △ REPEAT OF OVERHEAD CAMERA
□ NORTH CAMERA   x PRE AND POST MEAS.

$\dot{S} = 0.445$ IN/SEC

RECESSION (INCH)

DWELL TIME (SEC)

FICURE B-18. ABLATION HISTORY FOR SEGMENTED NOSETIP AT 50MW FACILITY

MODEL NO. 3-5   COPPER INFILTRATED TUNGSTEN CORE
R62-008-1   NON-ROTATING STING   DWELL TIME=1.910SEC

O OVERHEAD CAMERA   □ NORTH CAMERA
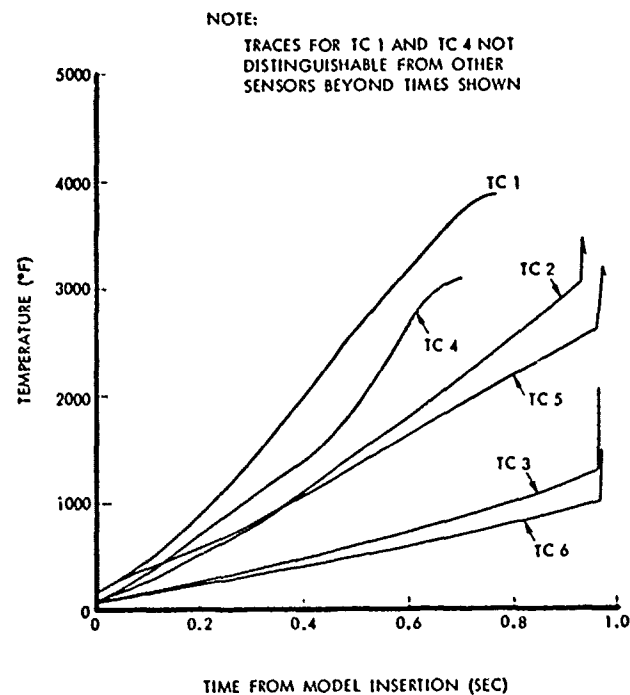x PRE AND POST MEAS.

$\dot{S} = 0.380$ IN/SEC
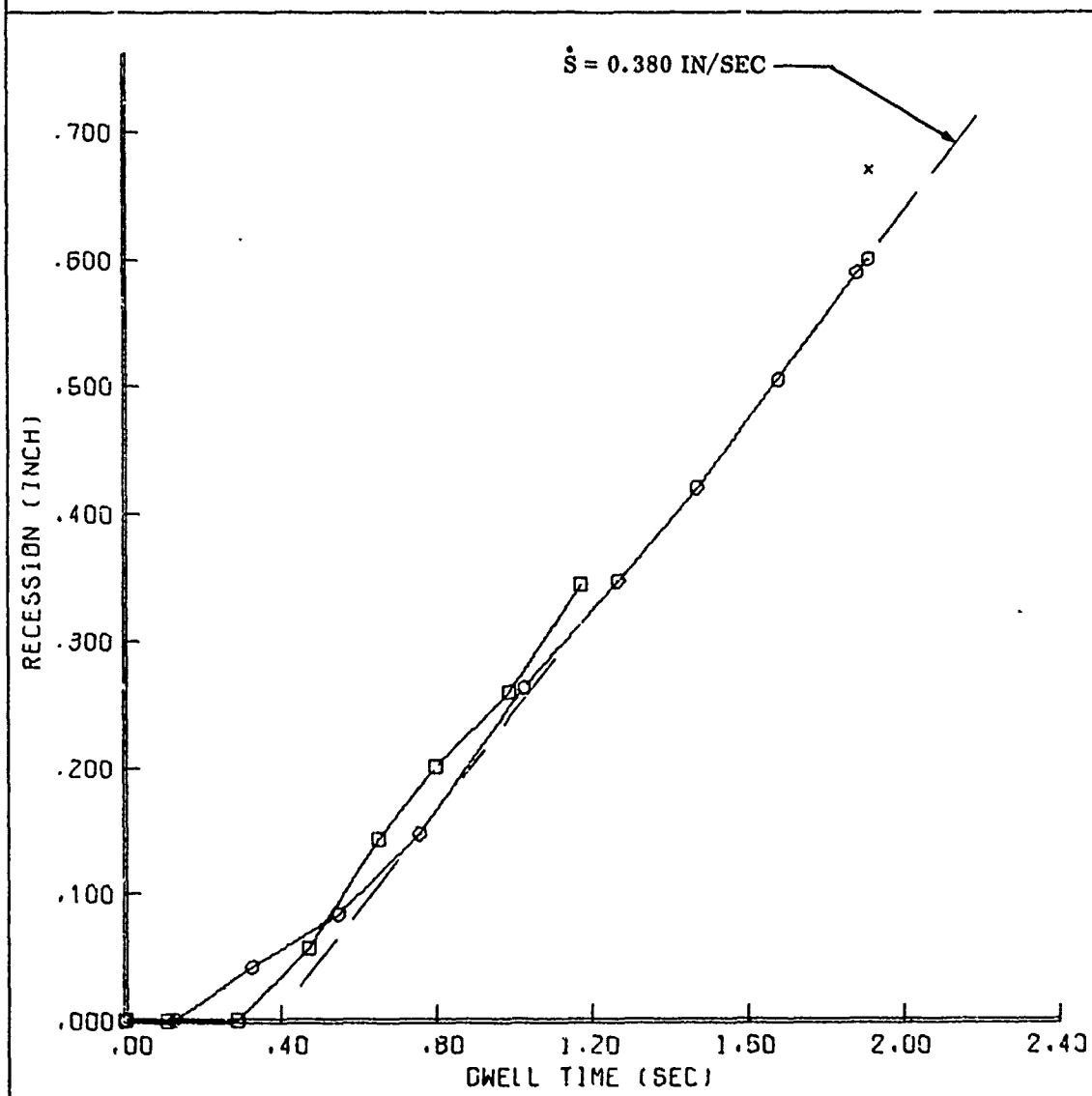
Figure B-19. Thermocouple data, model 1-2.

Figure B-20. Thermocouple data, model 1-3.

NOTES:
① TC 1 OPEN AT START
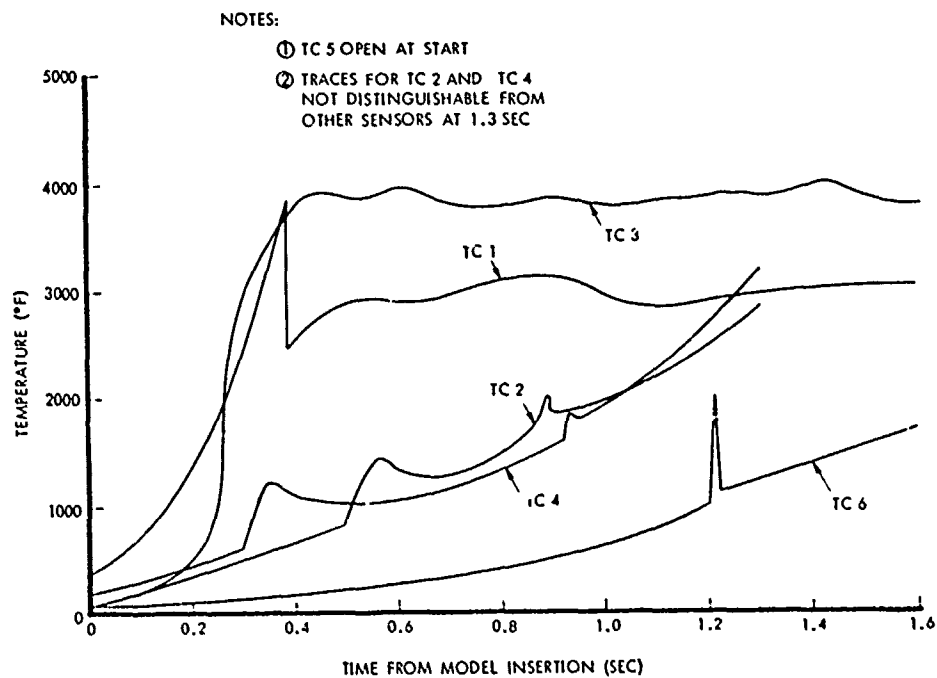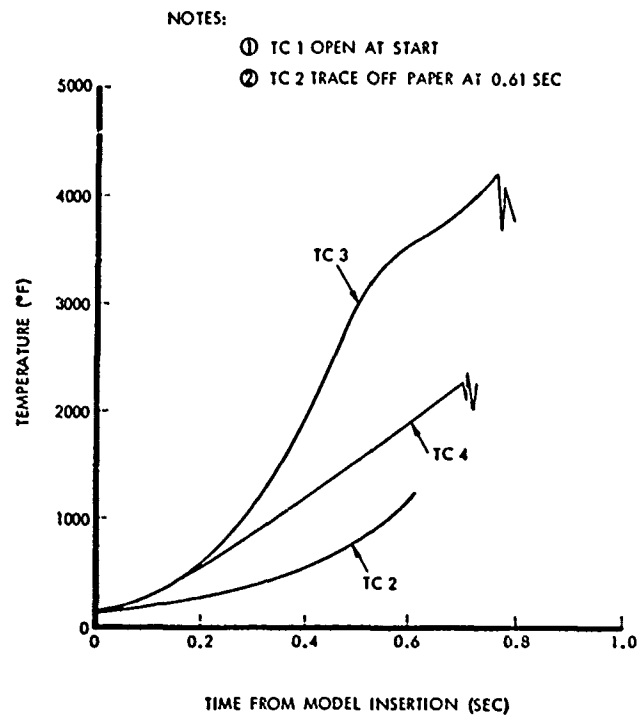② TC 2 TRACE OFF PAPER AT 0.61 SEC
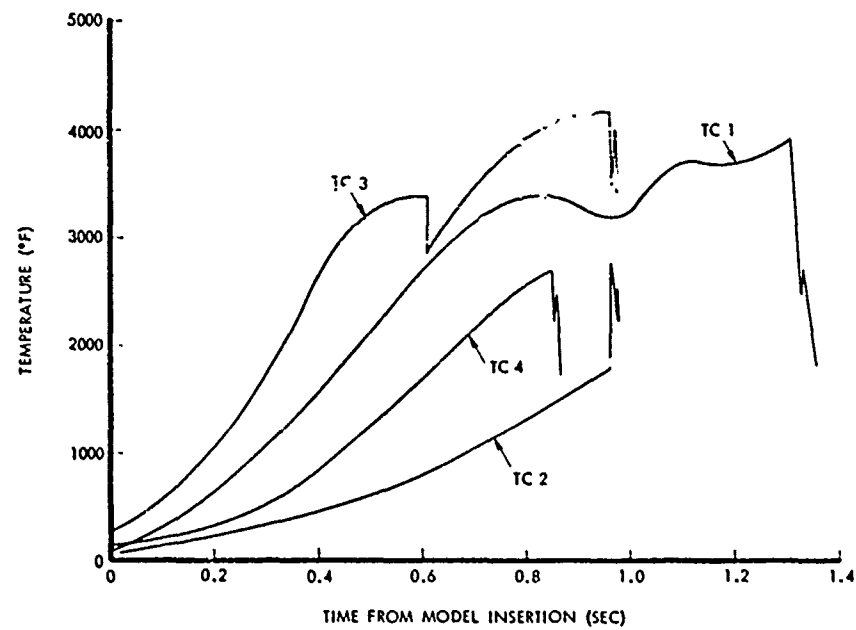

Figure B-21. Thermocouple data, model 1-4.
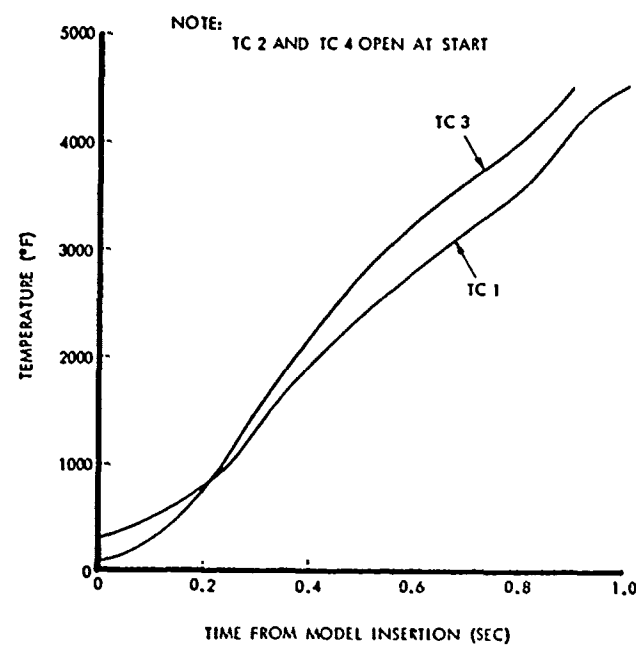

Figure B-22. Thermocouple data, model 2-3.

Figure B-23. Thermocouple data, model 3-3.

DISTRIBUTION LIST

DEPARTMENT OF DEFENSE

Director
Defense Advanced Rsch. Proj. Agency
 ATTN: Strategic Tech. Office

Defense Documentation Center
Cameron Station
12 cy ATTN: TC

Director
Defense Intelligence Agency
 ATTN: DT-2, Wpns. & Sys. Div.

Director
Defense Nuclear Agency
 ATTN: STSP
 ATTN: DDST
 ATTN: TISI, Archives
2 cy ATTN: SPAS
3 cy ATTN: TITL, Tech. Library

Commander
Field Command, Defense Nuclear Agency
 ATTN: FCPR

Chief
Livermore Division , Fld. Command, DNA
 ATTN: FCPRL

Under Sec'y of Def. for Rsch. & Engrg.
 ATTN: S&SS (OS)
 ATTN: AE

DEPARTMENT OF THE ARMY

Director
BMD Advanced Tech. Ctr.
 ATTN: ATC-M

Program Manager
BMD Program Office
 ATTN: Technology Division

Commander
BMD System Command
 ATTN: BMDSC-TEB

Commander
Harry Diamond Laboratories
 ATTN: DELHD-RBH
 ATTN: DELHD-RC

Director
US Army Ballistic Research Labs.
 ATTN: Robert E. Eichelberger

Commander
US Army Mat. & Mechanics Rsch. Ctr.
 ATTN: DRXMR-HH

Commander
US Army Nuclear & Chemical Agency
 ATTN: Library

DEPARTMENT OF THE NAVY

Chief of Naval Operations
 ATTN: OP 604C4

Director
Naval Research Laboratory
 ATTN: Code 2600, Tech. Library

Commander
Naval Sea Systems Command
 ATTN: Code 0351

Officer-in-Charge
Naval Surface Weapons Center
 ATTN: Code WA-07
2 cy ATTN: Code WA-43

Director
Strategic Systems Project Office
 ATTN: NSP-272

DEPARTMENT OF THE AIR FORCE

AF Materials Laboratory, AFSC
 ATTN: MBE
 ATTN: LTM
 ATTN: MXE
 ATTN: MBC
 ATTN: MXS

AF Office of Scientific Research
 ATTN: Paul Thurston

AF Weapons Laboratory, AFSC
 ATTN: SUL
 ATTN: DYV

Headquarters
Air Force Systems Command
 ATTN: DLCAM

Commander
Foreign Technology Division, AFSC
 ATTN: PDBG

HQ USAF/RD
 ATTN: RDQ
 ATTN: RDQSM

SAMSO/MN
 ATTN: MNNR
 ATTN: MNNH

SAMSO/RS
 ATTN: RSSR
 ATTN: RSS
7 cy ATTN: RSSE

DEPARTMENT OF ENERGY

University of California
Lawrence Livermore Laboratory
 ATTN: Hans Kruger, L-96
 ATTN: C. Joseph Taylor, L-92

DEPARTMENT OF ENERGY (Continued)

Los Alamos Scientific Laboratory
    ATTN: Doc. Con. for J. W. Taylor

Sandia Laboratories
Livermore Laboratory
    ATTN: Doc. Control for T. Gold

Sandia Laboratories
    ATTN: Doc. Con. for D. Rigali
    ATTN: Doc. Con. for Albert Chabai
    ATTN: Doc. Con. for R. Clem

DEPARTMENT OF DEFENSE CONTRACTORS (Continued)

Acurex Corporation
    ATTN: C. Powars
    ATTN: J. Huntington
    ATTN: C. Nardo

Aerospace Corporation
    ATTN: R. Hallse
    ATTN: D. T. Nowlan
    ATTN: W. Berry
    ATTN: R. Mortensen
    ATTN: D. Geiler
    ATTN: H. F. Dyner
    ATTN: Wallis Grabowsky
    ATTN: R. H. Palmer
    ATTN: P. Legendre
    ATTN: D. H. Platus
    ATTN: W. Portenier
    ATTN: M. Gyetvay

Aro, Inc.
    ATTN: G. Norfleet

Avco Research & Systems Group
    ATTN: V. Dicristina
    ATTN: A. Pallone
    ATTN: John E. Stevens, J100
    ATTN: William Broding

Effects Technology, Inc.
    ATTN: Robert Wengler

Ford Aerospace & Communications Operations
    ATTN: A. Demetriades

General Electric Company
Reentry & Environmental Systems Div.
    ATTN: Phillip Cline
    ATTN: B. M. Maguire

General Electric Company
TEMPO-Center for Advanced Studies
    ATTN: DASIAC

Institute for Defense Analyses
    ATTN: Joel Bengston
    ATTN: IDA Librarian, Ruth S. Smith

DEPARTMENT OF DEFENSE CONTRACTORS (Continued)

Kaman Sciences Corporation
    ATTN: Frank H. Shelton
    ATTN: Thomas Meagher

Lockheed Missiles & Space Co., Inc.
    ATTN: P. Schneider

Lockheed Missiles & Space Co., Inc.
2 cy ATTN: T. R. Fortune

Martin Marietta Corporation
Orlando Division
    ATTN: Laird Kinnaird
    ATTN: R. Cramer

McDonnell Douglas Corporation
    ATTN: L. Cohen
    ATTN: R. J. Reck
    ATTN: H. Hurwicz

National Academy of Sciences
    ATTN: National Materials Advisory Board for
            Donald G. Groves

Prototype Development Associates, Inc.
    ATTN: J. E. Dunn
    ATTN: M. Sherman

R & D Associates
    ATTN: F. A. Field

Science Applications, Inc.
    ATTN: K. Kratsch

Southern Research Institute
    ATTN: C. D. Pears

Spectron Development Laboratories
    ATTN: T. Lee

Science Applications, Inc.
    ATTN: A. Mortellucci

TRW Defense & Space Sys. Group
    ATTN: Thomas G. Williams
    ATTN: I. E. Alber, R1-1008
    ATTN: D. H. Baer, R1-2136
    ATTN: W. W. Wood
    ATTN: R. Myer

TRW Defense & Space Sys. Group
San Bernardino Operations
    ATTN: V. Blankenship
    ATTN: William Polich
    ATTN: E. Y. Wong, 527/712
    ATTN: L. Berger
    ATTN: Earl W. Allen, 520/141